Università degli Studi di Siena

Facoltà di Scienze Matematiche Fisiche e Naturali

Tesi di Dottorato in Fisica Sperimentale
PhD Thesis in Experimental Physics

Ciclo XX

Rare decays of B mesons and baryons at the Tevatron and the LHC

Candidato: **Dott. G. Volpi**

Relatore: **Prof. G. Punzi**
Tutor: **Dott. M. A. Ciocci**

Contents

Introduction

The experimental study of rare decays of hadrons containing the b quark has been a fertile ground for some time, and keeps being one of the most interesting subjects in high energy physics. It has improved our understanding of hadronic processes, and allows investigating various aspects of the Standard Model and searching for hints of physics beyond the Standard Model. Examples are the comparison of branching fractions of charmless modes with predictions of models, the constraints on CKM angles ($B^0 \to \pi^+\pi^-$, $B \to DK$, with D in suppressed modes), the observation of purely leptonic modes ($B^\pm \to \tau^\pm\nu$), the recently established difference in A_{CP} between $B^0 \to K^+\pi^-$ and $B^\pm \to K^\pm\pi^0$ [1], suspected to be a hint new physics. All of them came from a long and successful experimental activity with e^+e^- collisions at the $\Upsilon(4S)$ resonance.

With hadronic colliders now coming into play, the study of rare decays is reaching new heights. Given the high cross section for production of all kinds of B hadrons, the record luminosities now provided by the Tevatron collider, and the LHC program in view for the next years, there is the potential for a rich program of interesting new measurements, including even rarer modes as the $B^0_{(s)} \to \mu^+\mu^-$, strongly suppressed in the standard model but very sensitive to many NP scenarios.

The complexity of the hadronic collision environment, however, requires detectors with high precision and high quality tracking, and a trigger system capable of complex event selections at high rates. The CDF experiment, thanks to a fast trigger on impact parameter, has been able to reconstruct many rare B decays, including previously unobserved modes $B^0_s \to K^+K^-$ and $B^0_s \to K^-\pi^+$, the latter being particularly interesting for its relationship with the puzzling difference in CP asymmetry between neutral and charged modes.

In this thesis we go beyond B mesons, and present the first measurements of Branching fractions and CP asymmetries in charmless b-baryon modes. We study two-body Λ^0_b decays into final states with a proton and a charged pion or kaon. Their branching fractions can be significantly affected by New Physics contributions; under supersymmetric models with R-parity [2] violation, they can be increased by two orders of magnitude. Their CP-violating asymmetries are also

interesting to measure in search for possible further anomalies: then may reach significant size $\mathcal{O}(30\%)$ in the Standard Model [3], and are also sensitive to possible new physics sources.

This thesis is organized in the following way:

- Chapter 1 summaries the theoretical framework and underlines the motivations for studying rare decays, pointing out how the experiments at an hadronic collider can give an important contribution;
- in Chapter 2 the Tevatron accelerator and the CDF II detector are presented; here are underlined the accelerator and the detector characteristics that are the most important for the reconstruction and analysis of rare B-hadron modes;
- in Chapter 3 I describe the reconstruction of charmless B-hadron decays at CDF. Here I present the selection of the signals, both at trigger and analysis level, and the likelihood fit used to extract the Λ_b^0 parameters;
- in Chapter 4 I introduce a specialized Monte Carlo, that I developed to solve the problem of a reliable determination of the mass line-shapes. This is crucial both for the measurement of Λ_b^0 and for other channels, like the above-mentioned $B_s^0 \to K^-\pi^+$. Here I explain the motivation, the internal structure, and the tests performed using real-data control samples;
- in Chapter 5 I describe the determination of branching-ratios and CP asymmetries for the charmless Λ_b^0 modes $\Lambda_b^0 \to p\pi$ and $\Lambda_b^0 \to pK$
- finally, in Chapter 6 I discuss the prospects for a future program on rare decays at the LHC. The Tevatron experience has shown that the the most crucial resource for this is a track trigger: in spite of the similarities between CDF and D0, the lack of such trigger has made most of those channels completely inaccessible at D0. Here I describe my contribution to the development of the Fast TracK processor, that brings the same trigger ideas that have been successful at CDF to a new challenging system designed to work with the ATLAS detector at LHC.

Chapter 1

Rare b decays

1.1 Standard Model

The current description of the fundamental particles and their interactions is the result of the great effort that involved experimentalist and theoreticians over the last century. The result is the so called *Standard Model* (SM) of the fundamental interactions. The SM is a quantum-field theory composed by three different interaction: electromagnetic, weak, and strong. The electromagnetic and weak interactions are unified in the electro-weak interaction. The elementary particles forming the model, and experimentally verified, are four bosons: γ (photon), $W^{\pm}$, Z^0, and g (gluons); the other bricks are the twelve fermions, and the relative anti-particles, grouped in leptons and quarks. In the theory both fermions and quarks are organized in three generations as follow:

	1st	2nd	3rd	Q
Leptons	e^-	μ^-	τ^-	-1
	ν_e	ν_μ	ν_τ	0
Quarks	u	c	t	$+2/3$
	d	s	b	$-1/3$

the charged leptons carry electric and weak interaction, the neutrinos have only weak interaction, quarks all three interactions. The table above summaries the electric charge carried by the particles. The quarks with charge $+2/3$ are usually referred as u-like, while d-like are the ones with charge $-1/3$. An exhaustive explanations on the model can be found in many academic books [4, 5, 6].

Despite the great successes the model, there are parts still under investigation and need to be better understood. Some phenomena (dark matter, neutrino masses...) don't find an explanation in the current formulation of the SM. The topics discussed in this thesis don't involve the whole SM but a part of it, so in this chapter we will only touch on those parts.

1.1.1 Flavor sector in the Standard Model

The SM sustained, many tests of the accuracy of its predictions. The processes examined in this thesis involve the so-called "heavy-flavor" sector. Its experimental investigation is mostly based on the study of decays of hadrons containing heavy-quarks (c or b quarks) into lighter states. The t quark does not form bound states due to its very short lifetime, and makes a separate subject by itself.

The flavor-changing interactions in the SM are due to the weak interactions between quarks, mediated by the charged weak current and Cabibbo-Kobayashi-Maskawa matrix, with an Hamiltonian in the form:

$$\mathcal{H}_{ew} = \frac{g_2}{\sqrt{2}} \left(\bar{u}, \bar{c}, \bar{t}\right) V_{CKM} \begin{pmatrix} d \\ s \\ b \end{pmatrix} W^{\dagger} + \text{h.c.} \tag{1.1}$$

where g_2 is a constants the represents the coupling constants, the row-vector represents the three functions representing the u-like state, on the left of the product, and the column vector on the right the d-like. The V_{CKM} represents a 3×3 matrix that mediates the interactions magnitude. The Matrix was introduced by Kobayashi and Maskawa in 1973 [7], extending the Cabibbo mixing angle[8], proposed as the source of the different coupling between weak decays of kaon and Λ^0 particles with the respect to the β-decay of the neutron. The matrix can be written as:

$$V_{CKM} = \begin{pmatrix} V_{ud} & V_{us} & V_{ub} \\ V_{cd} & V_{cs} & V_{cb} \\ V_{td} & V_{ts} & V_{tb} \end{pmatrix} \tag{1.2}$$

where the V_{ij} elements are complex number. The SM formulation implies that the matrix must be unitary. This unitary constraint reduces the matrix observables to three Euler angles and a complex phase, the other phases being unobservable. This complex phase is the only source of CP violation in the quark sector allowed by the Standard Model. A commonly used parameterization is due to Wolfenstein[9]:

$$V_{CKM} = \begin{pmatrix} 1 - \frac{\lambda^2}{2} & \lambda & A\lambda^3(\rho - \imath\eta) \\ -\lambda & 1 - \frac{\lambda^2}{2} & A\lambda^2 \\ A\lambda^3(1 - \rho - \imath\eta) & -A\lambda^2 & 1 \end{pmatrix} \tag{1.3}$$

where $\lambda \equiv \sin(\theta_C)$, A is a real amplitude, η and ρ two numbers that represents the observable matrix phase. This parameterization is valid up to terms of $\mathcal{O}\left(10^{-4}\right)$.

The unitary of the CKM matrix yield the conditions:

$$\sum_k V_{ik} V_{jk}^{\star} = \delta_{ij} \qquad \sum_k V_{ki} V_{kj}^{\star} = \delta_{ij} \tag{1.4}$$

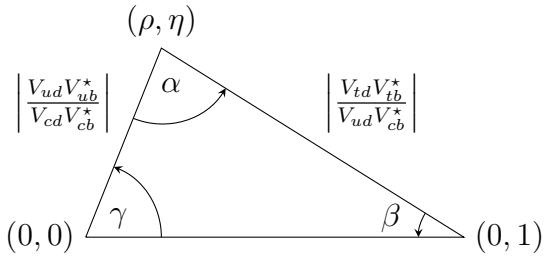

$$V_{cd}V_{cb}^\star + V_{td}V_{tb}^\star + V_{ud}V_{ub}^\star = 0$$

Figure 1.1: The figure shows the unitary triangle connected with the B hadron transitions. Each side represent the magnitude of a particular transition, the sides length are normalized to the $|V_{ud}V_{cb}^\star|$ element.

the previous conditions when $i \neq j$ can be graphically represented as 6 triangles in the complex plane, an example of unitary triangle is in Fig. 1.1

The last measured absolute values for the CKM matrix, within a 90% confidence level, are [10]:

$$V_{CKM} = \begin{pmatrix} 0.97383^{+0.00024}_{-0.00023} & 0.2272 \pm 0.0010 & (3.96 \pm 0.9) \times 10^{-3} \\ 0.2271 \pm 0.0010 & 0.97296 \pm 0.00024 & \left(42.21^{+0.10}_{-0.80}\right) \times 10^{-3} \\ \left(8.14^{+0.32}_{-0.64}\right) \times 10^{-3} & \left(41.61^{+0.12}_{-0.78}\right) \times 10^{-3} & 0.999100^{+0.000034}_{-0.000004} \end{pmatrix} \tag{1.5}$$

these values have been extracted from several experimental measurements, but some of them are particularly important ("golden channels"). This expression is used to indicate quantities that allow precise experimental measurements, and at the same time can be predicted with small theoretical uncertainties. Some example of channels used to determine the CKM elements are:

$|V_{ud}|$: the most precise determination of this element come from the super-allowed $0^+ \to 0^+$ nuclear transition.

$|V_{us}|$: the $K^+ \to \pi^0 e^+ \nu$ and other neutral decay are the main source of data for this element.

$|V_{ub}|$: this is extracted from the inclusive $B \to X_u l \nu$ decays, where is a light meson.

more details can be found in [10].

1.1.2 CP violation in the Flavor Changing Decays

The weak interaction in SM was proved to break the Parity symmetry (P) in conjunction with the charge symmetry (C), but also break the combined CP symmetry. The CP asymmetry can appear in different forms:

- CP violation in mixing. This happens when two neutral mass eigenstates are not CP-eigenstates. For this reason it's possible to observe both decays with $CP = 1$ or $CP = -1$ final states;

- direct CP violation. This happens when comparing the rate of a particular decay with respect to the CP-conjugate they have a different magnitude. This was observed both in neutral and charged states;

- CP violation in the interference. This happens when there is interference between mixing and direct CP violating phase;

We give few more details only for the direct CP violation. This is the only type of CP violation that can happen also in baryonic states, due to the baryonic number conservation.

Let's consider the decay of a generic heavy-flavor state B in a final state f. Under CP symmetry $CP\,|B\rangle = e^{\imath\phi_{CP}(B)}\left|\bar{B}\right\rangle$ and $CP\,|f\rangle = e^{\imath\phi_{CP}(f)}\left|\bar{f}\right\rangle$. The generic amplitude transition can be written as a sum of different terms, in the form:

$$\mathcal{A}(B \to f) = \sum_i e^{\imath\phi_i} A_i e^{\imath\delta_i} \tag{1.6}$$

$$\bar{\mathcal{A}}(\bar{B} \to \bar{f}) = e^{\imath(\phi_{CP}(B) - \phi_{CP}(f))} \cdot \left(\sum_i e^{-\imath\phi_i} A_i e^{\imath\delta_i}\right) \tag{1.7}$$

where A_i are the amplitudes of any different diagram that contributes to the transition, ϕ_i the relative weak phase, that changes under CP, and δ_i is the strong phase, unchanged under CP. The ratio of the two amplitudes:

$$\left|\frac{\bar{A}}{A}\right| = \left|\frac{\sum_i A_i e^{\imath(\delta_i - \phi_i)}}{\sum_i A_i e^{\imath(\delta_i + \phi_i)}}\right| \tag{1.8}$$

the result of this equation can be a value between -1 and +1, depending how the phases change. Using relation $\Gamma = |A|^2$ this ratio can used in the equation:

$$a_f = \frac{\Gamma(B \to f) - \Gamma(\bar{B} \to \bar{f})}{\Gamma(B \to f) + \Gamma(\bar{B} \to \bar{f})} = \frac{1 - |\bar{A}/A|^2}{1 + |\bar{A}/A|^2} \tag{1.9}$$

this suggests how the direct CP violation can be revealed by the measurement of a rate difference with respect to the particle and the anti-particle decays.

1.2 New Physics and Rare b-decays

The SM of the electroweak and strong interactions describes with an impressive accuracy all experimental data on particle physics up to energies of the order of the electroweak scale. On the other hand, we know that the SM should be viewed as an effective theory valid up to a scale $\Lambda \sim M_W$, since, among many other things, the SM does not contain a suitable candidate of dark matter and it does not account for gravitational interactions.

Many extensions to the standard model were proposed: SUSY, MSSM, Little Higgs, and others[11]. In this document we will refer generically to the extensions to the SM as New Physics (NP). These models are effective for energies greater than the SM cut-off, where a direct observation of new particles or interactions is expected. At a lower energy scale is therefore possible that the NP interactions are revealed indirectly trough correction to SM processes; these correction will be more important in processes suppressed in the SM.

It is possible to elaborate an effective weak interaction, that has an interaction Hamiltonian of the form

$$\mathcal{H}_{eff}^{int} \sim \sum_i C_i Q_i \tag{1.10}$$

the sum includes all the relevant physics processes at the highest order: the C_i coefficients represent the Wilson coefficients for each transition, Q_i are the operator representations of different transitions. Within the included effects there are all the well know SM processes and all possible NP processes that have a non-vanishing contribution in the energy range under analysis. Without loosing generalities, it is possible to use (1.10) in the calculation for a particular transition between two generic states $|i\rangle \to |f\rangle$. Separating the NP contributions from the SM terms, can be revealed the quantity:

$$\frac{\langle f|\, H_{eff}^{full}\, |i\rangle}{\langle f|\, H_{eff}^{SM}\, |i\rangle} = r_{fi} e^{i\theta_{fi}} \tag{1.11}$$

where H_{eff}^{full} is the full representation of the (1.10) and H_{eff}^{SM} is only the SM part that contains the processes with the coefficients as predicted by the current theory. The result represents the ratio between the amplitude transition in SM hypothesis with respect a NP generic scenario, the value is a complex number, suggesting as the NP effects can be identified in a modification of the expectation value for a transition rate, r_{fi}, or in a phase shift, θ_{fi}.

In the flavor sector, the initial and final state are identified by the number F, representing the number of quarks of the flavor F in a particular state. The transition are therefore grouped according the difference of the flavor value from the initial state and that final one, the ΔF.

In recent times, many efforts were spent in the analysis of the processes with $\Delta F = 1$ and $\Delta F = 2$. An example of a $\Delta F = 2$ process is the $B^0_{(s)}$-$\bar{B}^0_{(s)}$ mixing, observed and measured for both B^0 and B^0_s mesons. In these cases the current measurements agree with the theoretical expectation within experimental and theory uncertainties[12]. The agreement constraints the value of the operators that result in a $\Delta F = 2$ flavor variation.

Other interesting processes involve $\Delta F = 1$ variations. Many efforts are spent in the analysis involving "Charmless decays" of b-hadron and "Flavor Changing Neutral Current". The charmless decays have hadronic final states and are more abundant then FCNC, that have leptons in the final states. The full-hadronic final states however have larger theoretical uncertainties due to the QCD calculation. The FCNC decays are generally easier to study with current theoretical tools.

1.2.1 MSSM and R-parity

Putting aside the model independent approach, a model very often adopted to make quantitative predictions of the NP effect in the recent years is the Minimal Super Symmetric Model (MSSM), representing the simplest Super Symmetry (SUSY) extension to the the SM.

The MSSM represents a very simple, and promising, extension on the SM. It provides a good solution [13] to some inconsistency of the SM, as the Higgs Ultra-Violet divergence, and it is sufficient to produce a phenomenological model.

A principal aspect of the MSSM, in the most common representation, is the presence of an additional symmetry called R-parity. The conserved quantum number related to this symmetry is:

$$P_R = (-1)^{3(B-L)+2s} \tag{1.12}$$

where B and L are the baryonic and the leptonic numbers, s is the spin of the particle. For SM particle and Higgs boson it's easy to verify that have even R-parity eigen-value, $P_R = +1$,while all SUSY partners, the sparticles, have $P_R = -1$. The conservation of this number as many important consequences[13] limiting also processes with baryonic, or leptonic, number violation (e.g. proton decay). But it is in general possible to have SUSY model without R-parity conservation (R-Parity Violating (RPV) models). The possibility to have RPV in the heavy-flavor physics in many important processes is predicted to increase the NP amplitude[2] by orders of magnitude. In general, RPV models allow additional contributions in the loop or allow tree diagrams forbidden in the SM.

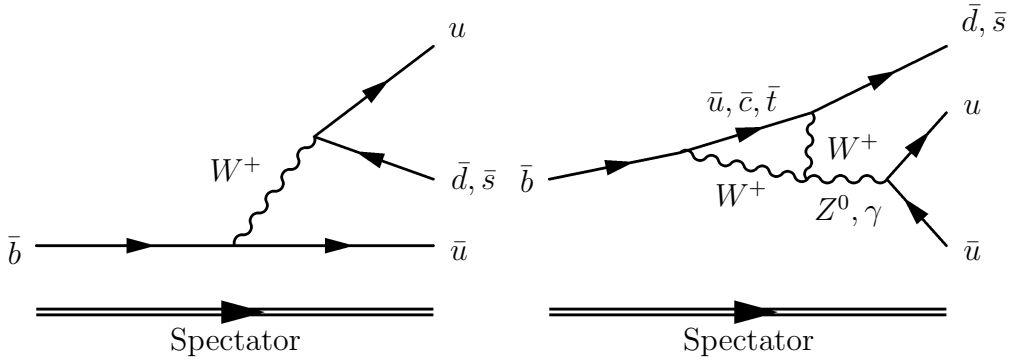

Figure 1.2: The figures show two kinds of flavor-changing currents. The left diagram shows the tree diagram for the $b \to u + h$ transition, the right diagram shows a penguin diagram that represent the 1-loop correction to the previous one. These diagrams are in both: B^0, B_s^0, and Λ_b^0 charmless decays.

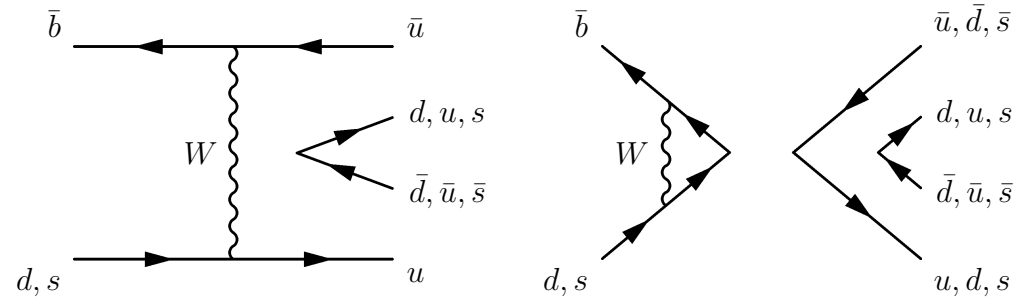

Figure 1.3: The figures show the W-exchange diagrams on the left and a generic penguin-annihilation diagram on the right. These diagrams contribute in some of to the B-meson charmless decays only.

1.3 Charmless decays

The CKM structure showed before in (1.5) favors the transition between $b \to c$ quark; as a consequence, transitions without a c-quark in the final state, charmless, are strongly suppressed. These decays were observed at the electron-positron and hadronic colliders, with Branching Ratios (BR) up to 10^{-5}, for both neutral and charged mesons, with d and s spectator quark, and recently, as will be reported in this Thesis also for Λ_b^0 .

In the SM these processes are mediated by tree, penguin, and W-exchange diagrams, as shown in Fig. 1.2 and 1.3. The phase difference between these processes induces a charge asymmetry between particle and anti-particle decays. Quantitative predictions are difficult, because they involve both short and long distance QCD effects.

It's important to note that it's possible to reduce some uncertainties by com-

B^0 Modes	HFAG Avg.	B_s^0 Modes	HFAG Avg.
$K^+\pi^-$	19.4 ± 0.6	$K^-\pi^+$	5.00 ± 1.25
$\pi^+\pi^-$	5.16 ± 0.22	$\pi^+\pi^-$	0.53 ± 0.51
K^+K^-	$0.15^{+0.11}_{-0.10}$	K^+K^-	24.4 ± 4.8

Table 1.1: The table shows the last results in unit $10^{-6}$for charmless decay of neutral B-mesons[14].

paring similar decays in B_d, B_s, but also Λ_b^0. This because many decays have similar diagram just changing the role of the quark flavor.

1.3.1 $B^0_{(s)}$ charmless decay modes

The phenomenology of the B-meson charmless decays is very rich, with many decay modes that provide multiple ways to test the SM predictions. The observables for each decay channel are the CP-averaged branching fraction, the direct CP-violating asymmetry, and the mixing-induced asymmetry for the CP-eigenstates.

The final states that is possible to reconstruct at CDF II contain charged mesons and are: $B^0 \to \pi^+\pi^-$, $B^0 \to K^+\pi^-$, $B^0 \to K^+K^-$, $B_s^0 \to \pi^+\pi^-$, $B_s^0 \to K^-\pi^+$, and $B_s^0 \to K^+K^-$. The B^0 and B_s^0 mode are linked by U-spin symmetry. This symmetry between d and s quark helps to reduce some uncertainties. All modes involve penguin and tree diagrams with different magnitudes (Fig. 1.2). The modes with $\pi^+\pi^-$ or K^+K^- in the final states also get penguin annihilation and W-exchange contribution (Fig. 1.3). In general the amplitude of a particular transition can be expressed as a sum of five different contributions:

$$\mathcal{A} \to T + P + P_{EW} + P_A + E \tag{1.13}$$

where T stands for the contribution from tree diagrams, P from QCD penguins, P_{EW} electroweak penguins, P_A penguin annihilation, and E the W-exchange contribution.

$B^0 \to K^+\pi^-$ decay mode

Amongst the two-body charmless decays for a B^0 meson, this is the most abundant one. It receives contributions from tree and QCD penguin decays, but the tree contribution is suppressed by the CKM mechanism and it's ruled by the QCD penguin.

The branching ratio was measured with great precision a BABAR and Belle B-Factories: $(1.88 \pm 0.07) \times 10^{-5}$. The interference between the different diagrams is a source of direct CP asymmetries. The measured value is 0.097 ± 0.012[14].

This decay in the charmless analysis at CDF II is a benchmark for the whole analysis; furthermore the BR of the other channels are quoted in relation to this mode.

$\mathbf{B^0 \to \pi^+\pi^-}$ decay mode

This is the second abundant decay for the B^0 meson, the amplitude has contribution from all five of diagram kinds. The final state is a CP eigenstate with an eigenvalue +1, and originates from the $\bar{b} \to \bar{u}u\bar{d}$ transition.

This decay channel is well studied at the B-Factory where both mixing and direct CP asymmetry were measured, obtaining the values [14]:

$$A_{\mathsf{CP}}^{DIR}(B^0 \to \pi^+\pi^-) = +\,0.38 \pm 0.07$$
$$A_{\mathsf{CP}}^{MIX}(B^0 \to \pi^+\pi^-) = -\,0.61 \pm 0.08$$

the central value for the direct CP asymmetry suggests a large penguin contribution. The Belle e BABAR measurements are not fully compatible, so a third independent should be desirable to solve the discrepancy.

$\mathbf{B_s^0 \to K^+K^-}$ decay mode

This decay modes is the most abundant one for the B_s^0 system. It has many analogies with both the $B^0 \to \pi^+\pi^-$, under U-spin exchange in the interacting quark $d \leftrightarrow s$, and $B^0 \to K^+\pi^-$, by the exchange of the spectator quark[15].

It was observed for the first time at CDF II an analysis similar to the one described in the present thesis [16]. The measured CP-averaged branching ratio is:

[17]:

$$\mathcal{B}(B_s^0 \to K^+K^-) = (33 \pm 5.7 \pm 6.7) \times 10^{-6} \tag{1.14}$$

was in good agreement with the theoretical expectation:

$$\mathcal{B}(B_s^0 \to K^+K^-) = (35 \pm 7) \times 10^{-6}$$

As in the $B^0 \to \pi^+\pi^-$, in this mode it is possible to observe both direct and mixing CP violation. When it will be measured, this will give useful information of the CKM γ angle [15].

$\mathbf{B_s^0 \to K^-\pi^+}$ decay mode

This rare channel has many analogies with the $B^0 \to K^+\pi^-$ decay mode. Its amplitude, following the example of (1.13), can be expressed as $\mathcal{A} = T + P + P_{EQ}$.

This mode was observed at CDF II for the first time[18], where the BR and A_{CP}were measured for the first time. The preliminary result quotes:

$$\mathcal{B}(B_s^0 \to K^-\pi^+) = (5.237 \pm 0.74 \pm 0.90) \times 10^{-6}$$
$$A_{\mathsf{CP}}\left(B_s^0 \to K^-\pi^+\right) = 0.39 \pm 0.15 \pm 0.08$$

There is an interesting connection between the CP asymmetries of $B^0 \to K^+\pi^-$ and $B_s^0 \to K^-\pi^+$ modes, that is valid only under the SM [19]. The CDF measurement:

$$R = \frac{\Gamma(B_s^0 \to K^-\pi^+) - \Gamma(\overline{B}_s^0 \to K^+\pi^-)}{\Gamma(B^0 \to K^+\pi^-) - \Gamma(\overline{B}^0 \to K^-\pi^+)} = 0.78 \pm 0.39 \pm 0.12$$

is consistent with $R = 1$, expected in SM hypothesis. However the current experimental precision is limited but seems to exclude NP scenario with large contribution in the flavor area.

$\mathbf{B_s^0 \to \pi^+\pi^-}$ and $\mathbf{B^0 \to K^+K^-}$ decay modes

These decay receives contribution only by W-exchange and penguin-annihilation diagrams. These kind of diagrams are difficult to predict with the current phenomenological model. Both decays are unseen and the theoretical prediction give expectation value of about $10^{-8} \div 10^{-7}$. The measurement of the branching ratios for these decay could reduce the theoretical uncertainties on diagrams common in other charmless decays.

1.3.2 Λ_b^0 charmless decay modes

No charmless decay of a b-baryon have yet been observed. Within the decays in two unflavored charged hadrons that are the subject of the analysis discussed in this thesis, we expect a possible contribution of $\Lambda_b^0 \to p\pi^-$ and $\Lambda_b^0 \to pK^-$. They are also the most abundant expected charmless decays of the Λ_b^0 baryon.

In a naive factorization approach, Λ_b^0 charmless decays can happen in a similar way as in b-mesons. The diagrams describing the transition are the same shown in Fig. 1.2, where the spectators in this case are a ud or $\bar{u}\bar{d}$ pair of quarks.

Using factorization, it is possible to write the transition as $\langle B_f P|\, O_i\, |\Lambda_b^0\rangle = \langle B_f|\, O_i\, |\Lambda_b^0\rangle\, \langle P|\, O_i\, |\emptyset\rangle$, where B_f is the unflavored baryonic state, P is the pseudoscalar particle that appears in the final state, and Q_i a generic weak operator. The sum over all possible operators that allow the transition will give the total amplitude.

The effective Hamiltonian describing both final state containing a baryon and a pseudo-scalar or a vector mesons, containing all the possible operators, can be written in the form[3]:

$$\mathcal{H}_{eff} = \frac{G_F}{\sqrt{2}} \left\{ V_{ub}V_{uq}^* \left[c_1(\mu)O_1^u(\mu) + c_2(\mu)O_2^u(\mu) \right] - V_{tb}V_{tq}^* \sum_{i=3}^{10} c_i(\mu)O_i(\mu) \right\} + \ h.c. \tag{1.15}$$

where $q = d, s$ and $c_i(\mu)$ are the Wilson coefficients for different transitions, evaluated at the renormalization scale μ. The first two elements are related to tree diagrams, the operators embedded within the sum represent both QCD and electroweak penguins.

Without entering in depth in the numeric calculation of the c_i coefficients, evaluated using numerical approximation, for the different $\Lambda_b^0 \to ph^-$ channels, where $h^- = \pi^-, K^-$, it's possible to give a naive estimation of the tree and penguins diagram contributions.

- the $\Lambda_b^0 \to p\pi^-$ is mediated by the $b \to u\bar{u}d$ tree or by the $b \to d$ penguin. In this case the tree transition dominates the decays;

- in the $\Lambda_b^0 \to pK^-$ the operator involved are the $b \to u\bar{u}s$ tree and the $b \to s$ penguin transition. In opposite with the previous case now the CKM matrix elements prefers the penguin QCD diagram.

The branching ratios expectation for the two processes are:

$$\mathcal{B}\left(\Lambda_b^0 \to p\pi^-\right) = 0.8 \div 1.2 \cdot 10^{-6} \tag{1.16}$$

$$\mathcal{B}\left(\Lambda_b^0 \to pK^-\right) = 1.4 \div 1.9 \cdot 10^{-6} \tag{1.17}$$

The interference between weak and strong phases is expect to induce also a direct CP symmetry violation in that decays, of order $\mathcal{O}(10\%)$ for the $\Lambda_b^0 \to p\pi^-$ and of order $\mathcal{O}(30\%)$ for the $\Lambda_b^0 \to pK^-$.

A detailed evaluation of the effect in a particular super-symmetric scenario, with large R-parity violation, was done in [2]. In this scenario is possible to see large effects both in the BR of the $\Lambda_b^0 \to p\pi^-$, that should be increased of two order of magnitude, while the asymmetry can be reduced. A similar effect is expected for the $\Lambda_b^0 \to pK^-$.

The previous search performed at CDF II for these decays resulted in a limit of 10^{-5} [20], at the boundary of the region where one could possibly observe new physics effect.

1.4 Flavor Changing Neutral Current

The charmless decays represent transition mediated by a charged current, where the $\Delta F = 1$ transition is coupled with an iso-spin variation $\Delta U = 1$, the Flavor Changing Neutral Current (FCNC) instead have instead $\Delta U = 0$. In the B-physics area the FCNC interaction involve the transitions $b \to s$ and $b \to d$. These processes are in general strongly suppressed in the SM, first of all because they cannot happen at tree level and require at least one-loop transition (Fig. 1.4).

Within the FCNC family of decays there are final states involving only leptons, i.e. $B^0_{(s)} \to \mu^+\mu^-$ decays, or mixed final states with both leptons and hadrons, i.e. $B^0 \to \mu^+\mu^- K^{*0}$ (seen at the B-Factories), or the never seen $B^0_s \to \mu^+\mu^-\phi$.

1.4.1 $\mathbf{B^0_{(s)} \to \mu^+\mu^-}$ modes

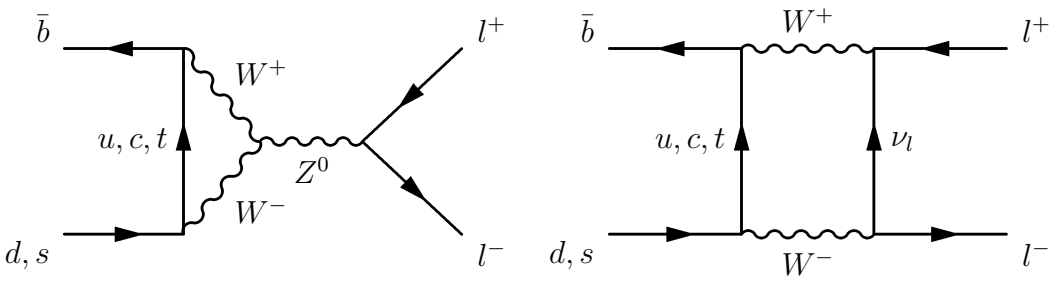

Figure 1.4: Two Feynman diagrams representing the FCNC for the $B^0_{(s)} \to l^+l^-$ process. These processes are a benchmark for the SM, in particular the processes with electron and muon in the final states are strongly suppress in the model.

The suppression is further increased by the CKM mechanism, due the insertion of the V_{ts} element for the B^0_s mode, and of the V_{td} element in the B^0 mode. The expected BR are [21]:

$$\mathcal{B}(B^0_s \to \mu^+\mu^-) = (3.42 \pm 0.54) \times 10^{-9} \tag{1.18a}$$
$$\mathcal{B}(B^0 \to \mu^+\mu^-) = (1.00 \pm 0.14) \times 10^{-9} \tag{1.18b}$$

In case of presence of physics beyond the SM, in the loop it is possible to introduce additional contribution. In a R-parity violating scenario it is also possible to have tree transitions. In all this scenarios, the BR of both decay modes are enhanced by many order of magnitude. Under very general conditions, in a SUSY scenario the BR is proportional to:

$$\mathcal{B}(B_q \to l^+l^-) \propto \frac{m_q^2 m_l^2 \tan^6\beta}{M^4_{A^0}} \tag{1.19}$$

where q is the down-type quark and l s a charged lepton, $\tan\beta$ and M_{A^0} are the usual super-symmetric parameters.

From the experimental point of view, the muon mode is preferred with respect to $B^0_{(s)} \to e^+e^-$ and $B^0_{(s)} \to \tau^+\tau^-$ modes: a muon trigger has usually a good efficiency, and background can be suppressed in more efficient manner with respect to the two other modes. The τ modes are the most challenging from the experimental viewpoint, due to the greater difficulty of triggering and reconstructing τ leptons.

1.4.2 $\mathbf{B^0_{(s)} \to \mu^+\mu^- h}$ modes

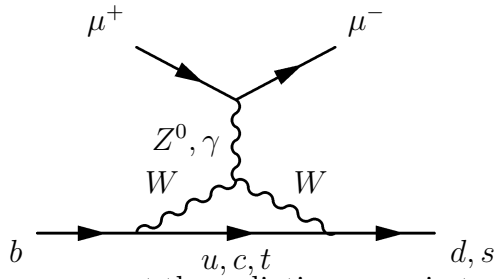

Figure 1.5: This diagram represent the radiative penguin transition between $b \to d$ or $b \to s$.

This decay modes in the SM are mediated by electroweak penguin decays $b \to s(d)l^+l^-$. They are only induced at the one-loop level, leading to small branching fractions and thus a rather high sensitivity to NP contribution.

Because of the small BR, these decays are experimentally challenging. In particular an excellent trigger and lepton identification could help to identify them within a large combinatoric background. The main background sources are the B and D semi-leptonic decays and the $B \to J/\psi X_s$ signal, where X_s is a generic strange-meson.

B^+ Decay	PDG 2006 Avg.	B^0 Decay	PDG 2006 Avg.
$K^+e^+e^-$	0.49 ± 0.10	$K^0e^+e^-$	$0.09^{+0.12}_{-0.09}$
$K^+\mu^+\mu^-$	$0.45^{+0.09}_{-0.08}$	$K^0\mu^+\mu^-$	$0.57^{+0.22}_{-0.18}$
$K^\star(892)^+e^+e^-$	$1.23^{+0.69}_{-0.62}$	$K^\star(892)^0e^+e^-$	$1.11^{+0.30}_{-0.26}$
$K^\star(892)^+\mu^+\mu^-$	$0.78^{+0.56}_{-0.44}$	$K^\star(892)^0\mu^+\mu^-$	$0.98^{+0.22}_{-0.21}$

Table 1.2: The table show the results for the observed transition $b \to sl^+l^-$[14].

Table. 1.2 lists the results of current measurements. The NP effect in these modes, as usual, can be revealed by an enhancement of the BR. The current measurement are in general in agreement with the SM but the results are limited by the large experimental error, mainly due to the statistic.

Other observables sensitive to the effect of NP are the CP asymmetry and the Forward-Backward (FB) asymmetry in the angular distribution of the two leptons. In particular the AFB in the SM is expected to be negligible, while it could be large in MSSM.

1.5 Heavy Flavor production in hadron collisions

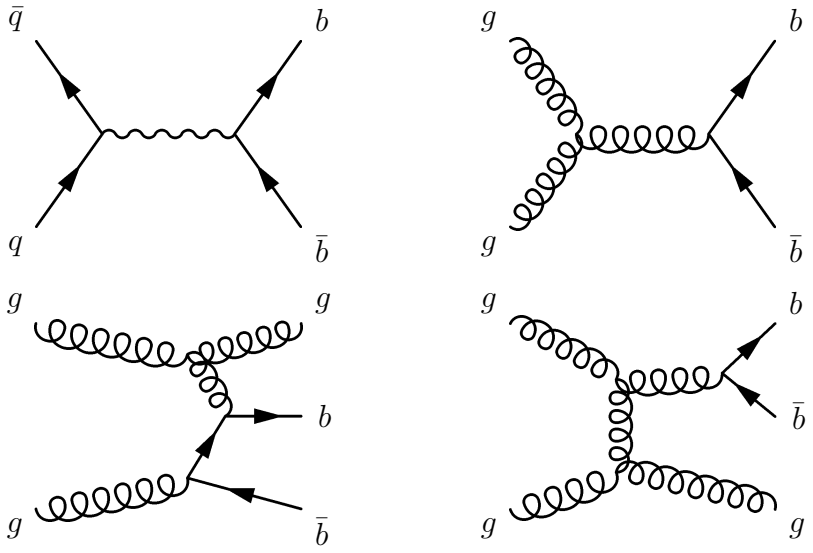

Figure 1.6: Example of $b\bar{b}$ production Feynman diagrams in a $p\bar{p}$ environments. The reported processes are known as direct production, gluon fusion, flavor excitation and gluon splitting.

	BaBar	Belle	CDF	LHC
Luminosity $cm^{-2}s^{-1}$	4.6×10^{33}	8.3×10^{33}	1×10^{32}	1×10^{34}
$\sigma_{b\bar{b}}$	1.15 nb	1.15 nb	100 μb	500 μb†
Production rate	5 Hz	10 Hz	1000 Hz	500 KHz
$\sigma_{b\bar{b}}/\sigma_{had}$	0.25	0.25	$\approx 10^{-3}$	

† prediction [22].

Table 1.3: This table compares the production rate of $b\bar{b}$ pairs in different environment. These numbers don't take into account experimental efficiencies.

Heavy-flavor studies in the past were done at different accelerator machine: e^+e^- general purpose collider, like LEP, fixed target experiment, as CLEO, hadronic

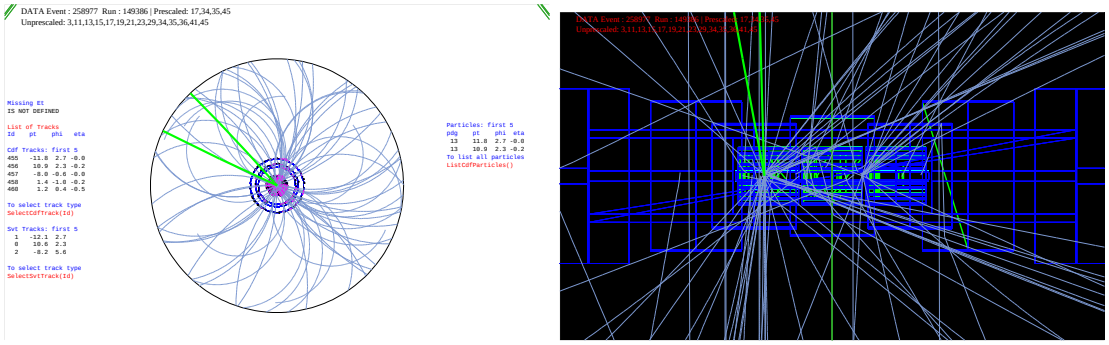

Figure 1.7: The pictures show a reconstruction of an event containing a $B^0_{(s)} \to h^+h'^-$ candidate in the CDF II detector. The left picture shows the reconstruction in the transverse plane, perpendicular to the beam line. Right plot shows a section of the inner silicon detector, projected in the plane that contains the beam.

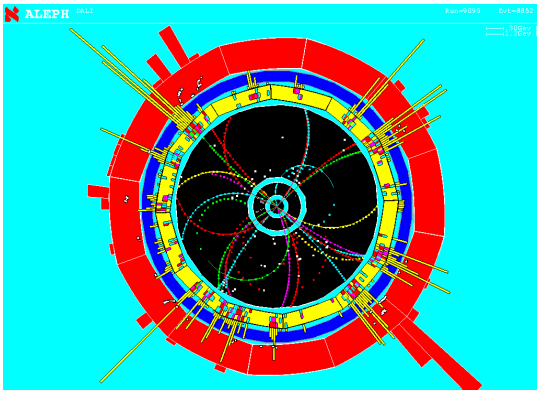

Figure 1.8: The plot shows a typical event in the ALEPH detector.

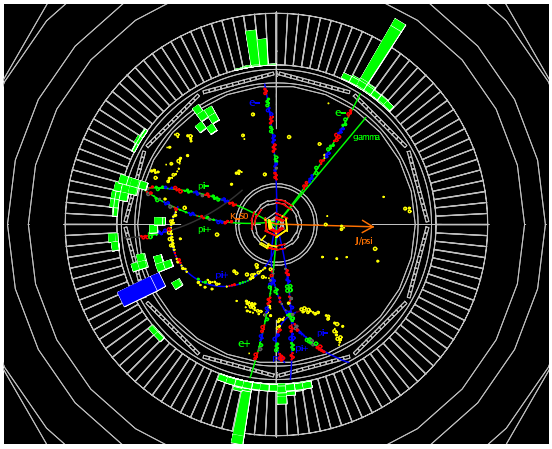

Figure 1.9: The plot show an event display of an event containing a $B^0 \to J/\psi K^0_S$ candidate in the BABAR detector.

colliders, as Tevatron, and e^+e^- colliders at the $b\bar{b}$ resonances, the so called B-factories. In Tab 1.3 are compared different values that describes the b-quark production at different machine.

In the recent years the Tevatron results and the prediction for the LHC on the rare-B decays have given support to the study of these processes at the hadronic colliders. The Fig. 1.6 shows the production diagrams at Tevatron, that are similar to the processes expected in other hadronic environment. Continuing to describe the Tevatron as example, the dominant production process is the non-resonant

inclusive b-quark pair-production of the type $p\bar{p} \to b\bar{b}X$. The corresponding cross section, multiplied by the detector efficiency to reconstruct at least one resulting b-hadron is $\sigma(p\bar{p} \to b\bar{b}X) \approx 50\,\mu$m[23]. This corresponds to roughly 5,000 b-hadrons within CDF acceptance per second (at typical current luminosities). The rate is large with respect to production cross-section at e^+e^- machines: 1 nb at Υ(4S) resonance and 7 nb at the Z^0 pole. As a consequence, experiments at the B-Factories require $\mathscr{O}(10^3)$ higher luminosity for collection comparable in size to the Tevatron samples.

A second important difference in hadron collisions is the available center-of-mass energy. At the Tevatron CM energy ($\sqrt{s} = 1.96\,$TeV) or at the LHC ($\sqrt{s} = 14\,$TeV) all species of b-hadrons: not only B^0 and B^+ mesons, produced in large quantities in Υ(4S) decays, but also B_s^0 and B_c^+ mesons and b-baryons has Λ_b, Σ_b, and others. In addition, the typical relativistic factors (i.e., Lorentz boost or $\beta\gamma$) of b-hadrons produced in $p\bar{p}$ are larger with respect to the B-Factories. This results in larger decay-length, which allow probing shorter scales in the time-evolution of heavy-flavors. This in particular was important i.e. for the measurement of B_s^0 oscillation frequency[12].

But one of the advantage cited above is also an important challenge to solve in the hadronic environment with respect to the B-Factories: while the $b\bar{b}$ production is large, the total $p\bar{p}$ cross section is very much larger. The b quarks couple production is 3 order of magnitude lesser than the total cross-sections, the interesting processes have a signal to background ratio respect to the total production of $\mathscr{O}(10^{-9})$. The search of a rare signal in this huge background is an important challenge in an hadronic collider, more than in Υ(4S) decays. In addition, the lack of knowledge of the total energy and longitudinal momentum of the system produced in the hard collision, due to the large spread in longitudinal momentum of the colliding partons, prevents the use of several kinematical constraints that are useful exploited at B-factories. Fig. 1.7 shows a candidate event used for a Flavor analysis at CDF, and should by compared to the figures 1.8 and 1.9, showing an event at ALEPH (at LEP II) and BABAR (at PEP-II), where a more clean event reconstruction is clearly possible.

In the next chapter, the Tevatron, the CDF detector and its trigger system will be described in more detail.

Chapter 2

CDF II detector at Tevatron

2.1 The Tevatron collider

The Tevatron collider is working in the Fermilab National Accelerator Laboratory. Until the start of the collision at LHC, it is the world's highest energy accelerator system. The accelerator started to collect interesting events at the end of the 1987. After this period, called *Run 0*, the accelerator undergo various changes and improvements. At the present time is operating the so called *Run II*. In this period the center-of-mass energy provided by the accelerator is 1.96 TeV, colliding proton and anti-protons beams, collected in bunches and spaced in time by 396 ns.

Together with energy another quantity is crucial on characterizing the performance of an accelerator: the instantaneous luminosity ($\mathcal{L}$). The value of $\mathcal{L}$ is related to the production of a particular physical state by the formula:

$$rate\left[\mathrm{s}^{-1}\right] = \mathcal{L}\left[\mathrm{cm}^{-2}\mathrm{s}^{-1}\right] \cdot \sigma\left[\mathrm{cm}^{2}\right] \tag{2.1}$$

where σ is the production cross-section for the interesting process. The instantaneous luminosity is a function of the accelerator parameters. It can be expressed with the formula:

$$\mathcal{L} = f\frac{n_1 n_2}{4\pi\sigma_x\sigma_y} \tag{2.2}$$

where f is the collision's frequency, n_i the number of particles in the two beams, $\sigma_{x,y}$ the transverse beam distribution using a Gaussian approximation for the beam shape. $\mathcal{L}$ is not uniform during the collisions: it has a maximum value at the start of the "store", then decreases because an increasing number of particle is lost from the orbits. In the Run II the largest value for instantaneous luminosity was $\mathcal{L} = 315\ \mathrm{cm}^{-2}\mathrm{s}^{-1}$, recorded in March 17, 2008.

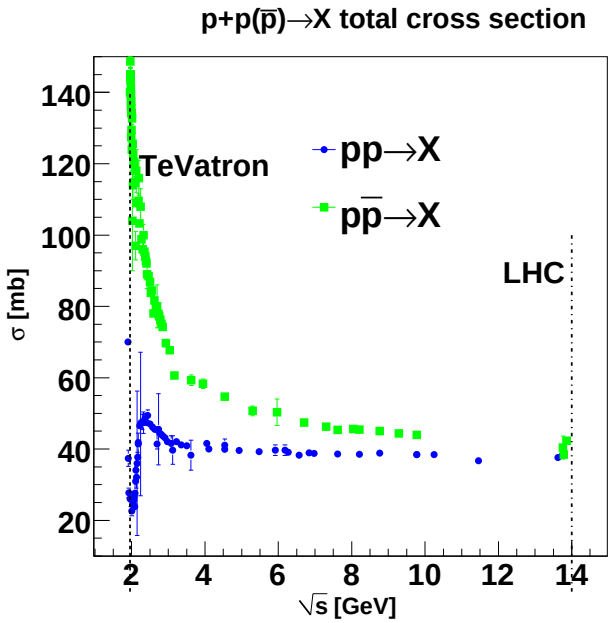

Figure 2.1: The figure compares the total cross-section as function of the $\sqrt{s}$ for $pp \to X$ and $p\bar{p} \to X$ collision [10]. That suggest how the choice to have a $p\bar{p}$ collider at the Tevatron energy gives a big advantage.

The integrated luminosity is defined as:

$$L = \int_{\Delta T} \mathcal{L}(t)dt \tag{2.3}$$

this quantity is derived from the $\mathcal{L}$. It is important because it relates both to the peak performances of the accelerator and to the duty cycle of the machine. Using this quantity is possible to know the amount of data expected to be collected for a particular process: time integrating eq. (2.1) $L \cdot \sigma$ is equal to the expected number of events.

2.2 Beams acceleration system

In the Tevatron the beam collisions are head-to-head; the two beams are composed by proton (p) and anti-protons ($\bar{p}$). This choice maximizes the total cross-section with respect to other possibilities, as p-p. Fig. 2.1 the total cross-section as function of Center Mass system energy is shown. The choice to have particle beams of opposite charge simplifies the design of the final stage with respect the proton-proton colliders.

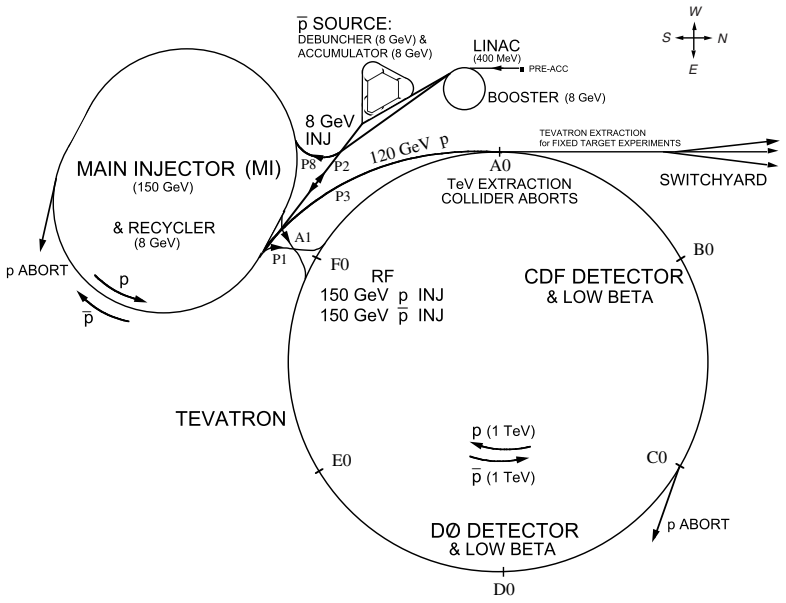

Figure 2.2: The figure shows the accelerator system operating at Fermilab National Accelerator Laboratory.

The Fig. 2.2 shows a sketch of the acceleration system. The beams are accelerated to the final energy using different techniques, combined to have the better performance. The first acceleration stage is the production of a proton and anti-proton.

2.2.1 Proton and anti-proton production

The proton are extracted using a gaseous hydrogen, in the molecular state $\mathcal{H}_2$, warmed and passed through a magnetron. The extraction current is 50-55 mA, with H^- ions in the energy range 15-22 keV. The ions are subsequently accelerated every 66 ms to 750 keV by three-staged diode-capacitor voltage multiplier (Cockroft-Walton) accelerator[24]. Then the H^- beams are segmented in bunched and a Linac and Radio Frequency cavity accelerate them up to 401.5 MeV[25]. At this step the beam can be injected in the Booster.

Before the injection within the Booster the H^- passed through a carbon foil, this process strips the two electrons to transform a negative ion into a single proton. The protons collected in the Booster are grouped in 84 bunches, if in accumulation mode have an energy of 8 GeV.

To produce anti-protons, the proton bunches are extracted to be injected in the Main Injector, where are accelerated up to 120 GeV. The beam of the Main Injector is directed against a target made of nickel alloys containing chromium,

iron and other metals.

The anti-protons are extracted from the particle produced in the proton collisions. The emerging anti-protons are spatially wide-spread, so the produced particles are collimated and then transferred to the Debuncher and cooled with various methods. Finally the anti-protons are collected into the Accumulator, where they are waiting for the collisions.

The anti-proton production rate is low mainly because the production efficiency is $21 \cdot 10^{-6}$, followed by other inefficiency in the transfers.

2.2.2 Injection and collision

The anti-proton accumulation process usually takes about 20 hours to collect a sufficient number of anti-protons, then the accumulation is stopped and the accelerator is prepared for a new injection. The first injection step is the extraction of the proton bunches from the Booster into the Main Injector[26], where they are accelerated up to 150 GeV. Within the Booster the protons are coalesced in a single bunch of $\approx 300 \cdot 10^9$. This process has an efficiency of 90%. When the proton bunches are ready, they are moved into the Tevatron. The whole process can be repeated every 12.5 seconds and has to be repeated for each of the 36 bunches. The transfer efficiency is 65%. The proton injection precedes the anti-proton injection, because if proton bunch losses are large this will point to tune the orbits. If this is the case the proton injection is aborted and restarted, at this stage the process can be quickly recovered, while a large anti-proton lost needs a new accumulation.

When the proton bunches are injected and stable, the anti-proton bunches are extracted from the Accumulator (or from the Recycler) to the Main Injector, accelerated to 150 GeV, then coalesced into four bunches with an efficiency of $\approx 80\%$. Finally each bunch has $80 \cdot 10^9$ anti-protons. The four bunches are injected into the Tevatron, where protons are counter-routing. The two beams have orbits spatially separated of 3-5 mm, that corresponds to $3 - 5\sigma$ of the beam size, to avoid beam interactions outside the collision points. The anti-proton process is repeated to have 36 anti-proton bunches.

After the end of anti-protons injection start a "store", defined as an interrupted period of collisions. A store lasts usually about 20-24 hours.

The proton and anti-proton bunches share the same magnets and Radio Frequency system. After the injection the beams are accelerated up to 980 GeV in about one minute.

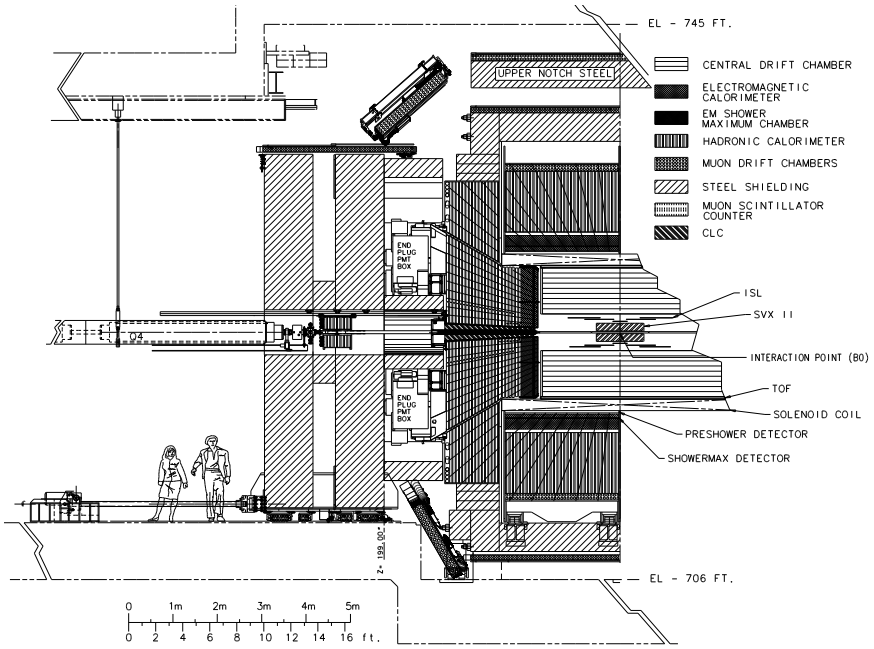

Figure 2.3: The illustration shows an half of the CDF II detector.

2.3 The CDF II detector

The upgraded CDF detector[27] is a large multi-purpose solenoidal magnetic spectrometer. The interaction points is surrounded by calorimeters and fine-grained muon detectors, covering most of the solid angle around the interaction point. It is installed in the B0 interaction point of the Tevatron, see Fig. 2.2.

The internal structure of the detector is shown in Fig. 2.3; the different subsystems have different role in the measurement of the properties for the particle produced in the 1.96 TeV collisions. The inner parts, the Silicon detectors and the Drift chambers, are devoted to measure the trajectories of the charged particles; the next part is composed by the electromagnetic and the hadronic calorimeters, that allow to measure the energy of the emerging particle. The outermost part is used to reveal the presence of muons, that are able to survive to the calorimeters.

2.3.1 Coordinates and notation

CDF adopts a left handed Cartesian coordinate system with origin at the nominal B0 interaction point, coincident with the center of the drift chamber (see Sec 2.4.5). The positive z-axis lies along the nominal beam-line and has the direction of the proton beam (east). The (x,y) plane is therefore perpendicular to the beam-

line, with the y-axis pointing upward and x-axis in the horizontal plane, pointing radially outward with respect the center of the accelerator ring.

In this thesis, as in most CDF publications, a cylindrical (r,ϕ,z) coordinate system is used. In this reference system the x-axis in the cartesian system has $\phi = 0$ and y-axis $\phi = \pi/2$. Throughout this document longitudinal means parallel to the z-axis, therefore parallel to the beams.

In hadron-collision environments it is customary to use also a different coordinate system, representing an extension of the polar system. The three variables used here are (R, y, ϕ), the variable that substitutes the polar angle θ is:

$$y = \frac{1}{2} \ln \left[\frac{E + p \cdot \cos(\theta)}{E - p \cdot \cos(\theta)} \right] \tag{2.4}$$

and it's called *rapidity*. This quantity has the property to be invariant under the effect of boosts along z-axis. Furthermore, many production cross-section are easily expressed in this variable: some important cross-sections are almost flat in a small y range. From the definition (2.4) it's possible to derive a more geometrical set of coordinate systems based on (r,ϕ,η), where η is the ultra-relativistic limit of the rapidity y:

$$\eta = \lim_{\frac{m^2}{p^2} \to 0} y = -\log \left(\tan \frac{\theta}{2} \right) \tag{2.5}$$

2.3.2 Sub-detector description

The CDF II detector is composed by a sequence of different systems, each devoted to a particular kind o measurement, with a shell structure that can be described starting from the level nearest to the beam-pipe, going through the detectors, until the outermost level. The sub-detectors related with the tracking system have a greatest impact on the Λ_b^0 analysis, these will be described more in depth in the next section (2.4), other detectors will be described less in depth to have only a minimal description of the whole experimental system.

Silicon detectors

The first sub-detector that a track is expected to cross, just outside the beryllium beam-pipe is the L00[28]. It consists of a single layer of single-sided, AC-coupled micro-strip silicon sensors mounted directly on the beam pipe. In the ϕ direction is segmented in twelve parts. The distance of each module from the beam pipe center is alternating in ϕ: 1.35 or 1.62 cm. It provides full azimuthal and $|z| \lesssim 47$ cm longitudinal coverage. The active modules are of size 0.84 (or 1.46) cm x 7.84, two longitudinal modules are combined into modules of 15.7 cm active length arranged into twelve partially-overlapping ϕ sectors and six longitudinal barrels.

The space from a radius of 2.45 to 10.6 cm is occupied by the Silicon VerteX, SVXII. It is a fine resolution micro-strip vertex detector which provides five three-dimensional samplings of tracks. The internal structure, as for the L00, is segmented in twelve wedges in the ϕ direction, six barrels along the z-direction (Fig. 2.6(a)). The layer distances from the beam are 2.45 (3.0), 4.1 (4.6), 6.5 (7.0), 8.2 (8.7) and 10.1 (10.6) cm, see fig. 2.6(b). The SVXII pseudo rapidity coverage is $|\eta| \lesssim 2$[29] that corresponds to a total length of 192 cm along the beam axis.

The Intermediate Silicon Layer (ISL) is a silicon tracker placed at intermediate radial distance between the SVXII and the drift chamber (see fig. 2.5), and covering the $|\eta| \lesssim 2$ pseudo-rapidity range for a total length of 174 cm along z[30]. In the $|\eta| \lesssim 1$ range a single layer of silicon sensors is mounted on a cylindrical barrel at radius of 22.6 cm (or 23.1 cm). In the region $1 \lesssim |\eta| \lesssim 2$ two layers of silicon sensors are arranged into two pairs of concentric barrels (inner and outer). In the inner (outer) barrel, staggered ladders alternate at radii of 19.7 and 20.2 cm (28.6 and 29.0 cm). One pair of barrels is installed in the forward region, the other one in the backward region.

Central Outer Detector

A large volume between a beam distance from 43.4 to 132.3 cm, with a longitudinal extension covering $|z| \lesssim 155$ cm in axial direction is occupied by the Central Outer Tracker (COT). This multi-wire, open-cell drift chamber, provides charged particle tracking at large radii in the central pseudo-rapidity region ($|\eta| \lesssim 1$, see fig. 2.7)[31]. The internal volume is occupied by a web of wire, with an intense electrical field between them. The signals collected by the wires permits a three-dimensional reconstruction of the tracks trajectories. This detector is very important to understand the tracking performance of the CDF tracking system, will be described in more details later in Sec. 2.4.5.

Time-Of-Flight detector

Outside the COT, in the space between it and the magnet cryostat, it is placed the Time of Flight (TOF) detector[32]. It has the capability to distinguish different kind of long-lived particles measuring the time elapsed between the collision time and when a particle is revealed by the detector. It's composed by a cylindrical array of 216 scintillating bars, 279 cm length and with a 4x4 cm^2 cross-section, oriented along the beam axis, installed in the 4.7 cm radial space between the outer surface of COT and the cryostat of the super-conducting solenoid at an average radius of 140 cm, which corresponds to 4.7 ns flight-time for a particle at light speed.

The light produced by the charged particles in the scintillator bars is collected

at both ends of each bar into 432 fine-mesh, 19-stage photon-multipliers. The design of the photon-multipliers permits them to maintain an adequate gain even in the 1.4 T magnetic field. The preamplified PMT signals follow two parallel paths: the timing signal is discriminated and digitized, while the charge signal is digitized to be eventually used at trigger level and for subsequent extraction of the off-line corrections.

Using the time measurement from this detector and the measured momentum from the COT is possible to deduce the particle mass by the formula:

$$m = \frac{p}{c}\sqrt{\frac{c^2t^2}{L^2} - 1} \tag{2.6}$$

where p is the momentum measured, L is the relative path length for the track, and t is the difference between the arrival time of the TOF signal with respect to the the bunch-crossing time.

The timing resolution of the sub-detector is $\sigma_t \approx 110$ ps. This resolution guarantees a separation power in the identification of pions and kaons with $p_T \lesssim 1.6$ GeV/c is greater than 2σ.

Calorimeters

The shells described up to this points are all contained within the CDF II solenoid, Sec. 2.4.1, and are devoted to the tracking. The sub-detectors external to the solenoid are dedicated to measure the energy carried by the particle produced during the proton anti-proton interactions: the calorimetric system.

The different system samples the "shower" evolution: each element is build alternating layers of passive material, containing atoms with high Z value, that compose the absorber, the other layers are composed by plastic scintillator. The calorimeters are finely segmented in solid angle around the nominal collision point and coarsely outward from the collision point (in-depth segmentation). Angular segmentation is organized in projective *towers*. Each tower is an independent read-out unit which subtends a portion of the solid angle, namely a rectangular cell in the (η - ϕ) space, with respect to the nominal interaction region. The in-depth segmentation of each tower consists of two independent compartments: the inner one samples the electromagnetic component of the shower, while the outer one samples the hadronic fraction of the deposited energy. Different fractions of energy release in the two compartments distinguish photons and electrons from hadrons. All the parts together cover the region with $|\eta| \lesssim 3.6$

The central calorimeters operate in the region $|\eta| \lesssim 1$, occupying the radial region between 173 and 208 cm[33, 34]. It is made of four arches, each sub-tending 180° and divided into 12 azimuthal 15°-sectors (see fig. 2.4(a)). Each sector consists of 31 layers of 5 mm thick polystyrene scintillator radially interleaved with 30

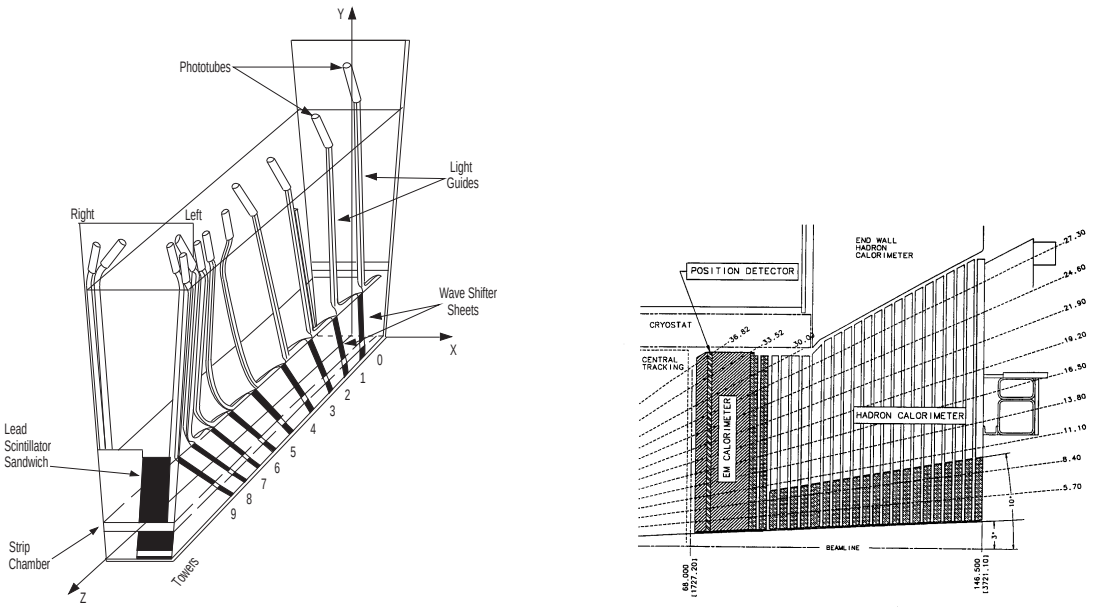

(a) CEM Wedge

(b) Plug calorimeters

Figure 2.4: The plot show one azimuthal electromagnetic calorimeter wedge (a), the second plot shows an elevation view of one quarter of the plug calorimeter (b).

aluminum-clad lead sheets, 32 mm-thick. Each sector is divided into ten projective towers with $\Delta\eta \cdot \Delta\phi \approx 0.11 \cdot 15^\circ$ per tower.

The hadronic compartment for the central part comprises two subsystems: the central ($|\eta| \lesssim 0.9$) and the end-wall ($0.7 \lesssim |\eta| \lesssim 1.3$) section[35]. Both consists of four "C"-shaped arches for a total of 48 azimuthal sectors. Each central wedge is segmented into nine η towers matching in size and position the electromagnetic towers, for 384 towers in total. The end-wall section has six additional towers, three of which matching central hadronic towers (see fig. 2.3) for a total number of 288 towers. A central hadronic tower is made of 32 layers of steel absorber, 2.5 cm thick, alternating radially with 1.0 cm-thick acrylic scintillator. The wall towers are similar but containing only 15 layers of 5.1 cm-thick absorber.

The total thickness of the central electromagnetic section corresponds approximately to $19\,X_0$, for a relative energy resolution per tower of $\sigma_E/E = 13.5\%/\sqrt{E\sin(\theta)} \oplus 2\%$. The total thickness of the hadronic section corresponds to approximately $4.5\,\lambda_{int}$, for an energy resolution of $\sigma_E/E = 50\%/\sqrt{E\sin(\theta)} \oplus 3\%$ for the central part, and $\sigma_E/E = 75\%/\sqrt{E\sin(\theta)} \oplus 5\%$ for the and-wall, $1\,\lambda_{\rm int}$ is the pion nuclear absorption length.

The large η extensions for the electromagnetic (hadronic) cover the region $1.10\,(1.30) \lesssim |\eta| \lesssim 3.64$ by a scintillating tile calorimeter (see Fig. 2.4(b))[36,

37, 38]. It is composed of two independent and identical devices, installed at longitudinally symmetric positions with respect to the interaction point (east and west). The absorber of the electromagnetic part consists of 23 annular lead plates, 2.77 m outer diameter, with a central hole to house the beam-pipe. Each one is made out of 4.5 mm-thick calcium-tin-lead sandwiched between two 0.5 mm-thick stainless-steel sheets. In between the absorber plates, 4 mm-thick scintillator tiles are organized azimuthally in 15° triangular sectors. A thicker (10 mm) amount of scintillator, independently read-out and installed in the first layer, acts as pre-shower detector. Shower-maximum sampling is available at a radial depth $\approx 6\,X_0$ using two tilted layers of scintillator strips with 5 mm pitch.

The hadronic section consists of 23 annular layers of 5 cm-thick iron absorber alternated with 6 mm scintillator layers. The outer radius of each module increases at increasing $|z|$, that gives the characteristic "plug" shape to this calorimetric system. Each module is segmented into 12 azimuthal sectors, each sub-tending 30°. Within each sampling layer, the scintillator is arranged in tiles similar to those used in the electromagnetic compartment.

For the large η region the total thickness of the electromagnetic section correspond to approximately $21\,X_0$ or $1\,\lambda_{int}$, for an energy resolution of $\sigma_E/E = 16\%/\sqrt{E\sin(\theta)} \oplus 1\%$. The total thickness of the hadronic section corresponds to approximately $7\,\lambda_{int}$, for an energy resolution of $\sigma_E/E = 74\%/\sqrt{E\sin(\theta)} \oplus 4\%$

Muon detectors

The long-lived particle produced by the interaction and subsequent decays are with a very high probability absorbed by the system described above, the most common particle that escapes the calorimetric system is the muons. The muon detectors are multiple layer of drift chambers placed in outermost shell of the detector. In between the chambers and the calorimeters some additional steel shielding layers reduce the probability for other particles to escape the calorimetric system. Four independent systems detect penetrating charged particles in the $|\eta| \lesssim 1.5$ pseudo-rapidity range, employing similar combinations of drift tubes, scintillation counters, and absorbers with differential azimuthal coverage [39, 40]. All type of muon detectors use a single wire, rectangular drift chambers, arranged in arrays with various azimuthal segmentation and coupled with scintillator counters. The chambers use a 50:50 gas admixture of Argon and Ethane, and operates in proportional regime. The four sub-detector systems are:

Central MUon detector: the CMU detector is located around the central hadron calorimeter at a radius of 347 cm and covers the region $0.03 \lesssim |\eta| \lesssim 0.63$. Each array covers 12.6° in ϕ, with a gap of 2.4°, that results in a global coverage to 84%.

Central Muon uPgrade: CMP is placed after an additional 60 cm-thick of steel. Its function is to cover the ϕ gaps of the CMU, more the additional absorber thick helps to reject penetrating high energy hadrons. The η coverage is the same of the CMU detector.

Central Muon eXtension and Intermediate MUon system: CMX and IMU detectors extends the muon coverage to the plug region, have a design similar to the other detectors. The CMX covers the pseudo-rapidity region $0.6 \lesssim |\eta| \lesssim 1$, IMU the region $1.0 \lesssim |\eta| \lesssim 1.5$.

In each azimuthal sector, stacks of up to eight layers of chambers are overlaid along the radial direction to allow coincidences among hits. The chambers are staggered in various patterns of alternating layers, for azimuthal ambiguity resolution. The difference of the drift electrons arrival-time between neighboring cells provides up to 250 μm hit-position resolution in the (r, ϕ) view. Division of the charge collected at the opposite ends of sense wire allows a measurement of the z coordinate of the hit with up to 1.2 mm resolution. Resolutions were measured using cosmic rays. The charge from each of the 7,316 channels is preamplified, shaped, discriminated, and digitized. The arrival time is digitized also. Scintillators provide timing information to suppress backgrounds due to secondary interactions on the beam-pipe and to cosmic rays.

Cherenkov Luminosity Counters

The main purpose of this detector is to measure the instantaneous luminosity ($\mathcal{L}$) in the B0 interaction point. The relation used is $\bar{N} \times f_{b.c.} = \sigma_{p\bar{p}} \times \epsilon \times \mathcal{L}$, where $\bar{N}$ is the number of interaction for bunch-cross, $f_{b.c.}$ the BC frequency, $\sigma_{p\bar{p}}$ is the inelastic cross-section, and ϵ is the detector efficiency. The inelastic cross-section come from CDF and E811 luminosity-independent measurement done during Run I at $\sqrt{s} = 1.8$ TeV[41], and extrapolated at the Run II energy. The global uncertainty on the luminosity is $\approx 5.6\%$.

This detector covers the $3.7 \lesssim |\eta| \lesssim 4.7$ range, with two symmetrical detector placed in the forward and in the backward regions. It is composed by long Cherenkov detectors, 100-108 cm, with a conical shape, filled with Isobutane. The light emitted are collected in a PMT shielded by the solenoidal magnetic field.

The performances of this detector are not crucial for the CDF measurement reported in this thesis, this because the measurement don't involve an absolute branching-ratio measurement. However this detector is used in the trigger criteria that select interesting events. As example of the use of the CLC information at Level-1 trigger, see Sec. 2.6.1.

2.4 CDF Tracking system

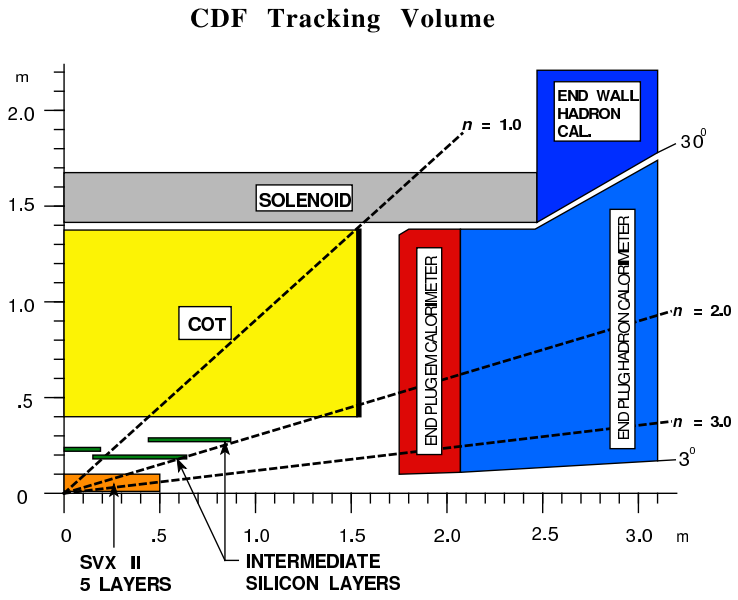

Figure 2.5: Elevation view of one quadrant of the inner portion of the CDF II detector showing the tracking volume surrounded be the solenoid and the forward calorimeters

Three-dimensional charged particle tracking is achieved through an integrated system consisting of three silicon inner sub-detectors and a large outer drift-chamber, all contained in a super-conducting solenoid.

In the central region ($|\eta| \lesssim 1$) we have: 7 silicon samplings, one in the (r,ϕ) view plus six in the (r,ϕ,z) view; 96 chamber samplings, 58 (r,ϕ) plus 48 (r,z). The samplings are available between 1.6 and 132 cm radial distance from the beam. In the forward and backward regions ($1 \lesssim |\eta| \lesssim 2$)), 8 silicon points are available between 1.6 and 29 cm, along with partial information from the chamber.

The high number of samplings over the 88 cm lever-arm of the drift chamber ensure a precise determination of the curvature, the azimuth and the pseudo-rapidity of the tracks in the central region. The chamber provides also track seeds for pattern-recognition in the silicon detector. The various silicon sub-systems will complete the track reconstruction improving the quality of the track parameters connected with the production vertex.

The inner extension, called Layer 00 (L00), is a light-weight silicon layer. It is placed on the beam pipe and is important to improve the secondary vertex identification. The nearness with the collision point reduces the effect of the multiple scattering, its single hit measurements are more precise than other sub-detectors.

In the L00 construction many efforts spent to use state-of-the-art radiation-tolerant sensors, able to extend the lifetime of the whole system. This feature is important due to the radiation environment existing around the collision point, that will degrade the performance of the inner SVXII layers. During the design of the tracking system was chosen components sharing chips with similar architecture among sub-detectors (read-out chip, support structures, etc.) thus simplified the construction and the operations.

All 722,432 channels from the $\approx 7.0\,\mathrm{m}^2$ silicon active-surface employ 5644 radiation-tolerant integrated read-out chips of the same type. This custom chip allows independent cycles of analog processing and of subsequent digitization of the data. It optimizes charge collection using sparsification, neighbor logic, and common-mode noise suppression. The discriminated differential pulse from each channel is preamplified, digitized and propagated to the downstream data-acquisition. The ISL and SVXII, whose mass is approximately 138 kg, share also the carbon-fiber supporting structure.

The total amount of material in the silicon system, averaged over ϕ and z, varies roughly as $0.1\ \mathrm{X}_0/\sin(\theta)$ in the $|\eta| \lesssim 1$ region, and roughly doubles in $1 \lesssim |\eta| \lesssim 2$ because of the presence of cables, cooling bulk-heads, and portions of the support frame. The average amount of energy loss for a charged particle is about 9 MeV. The total heat load of the silicon system is approximately 4 kW. To prevent thermal expansion, relative detector movements, increased leakage-current, and chip failure due to thermal heating, the silicon detectors and the associated front-end electronics are held at a constant temperature ranging from $-6\,\mathrm{C}^\circ$ to $-10\ \mathrm{C}^\circ$ for L00 and SVXII, and around $10\,\mathrm{C}^\circ$ for ISL, by an under-pressurized water and ethylene-glycol coolant flowing in aluminum pipes integrated in the support structures.

2.4.1 Magnet

All the tracking detectors are within a solenoidal magnetic field of ~ 1.41 T. The region covered by the magnet is $r \lesssim 150$ cm and $|z| \lesssim 250$ cm. The magnet is made using aluminum-stabilized NTi/Cu super-conducting coil in 1164 turns, with a current of 4650 T The solenoid has a global size of 4.8 m in length and 1.5 m in radius, with a radial thickness of 0.85 X_0 for a normal incident particle. The cooling system uses a forced flow of two-phase helium. The field is oriented along positive z direction, the proton direction, and is uniform within 0.1% in the tracking volume. The non-uniformities are taken into account by the tracking algorithm .

The magnet current and in general the magnetic field map are continuously monitored. In particular the magnetic field map is measured using nuclear magnetic resonance probes, with a relative accuracy of 0.01%. Any deviation from

the mapped values is stored to be applied as off-line correction to the measured track parameters. The momentum threshold for a particle to radially escape is $p_T \geq 0.3$ GeV/c.

Outside the coil, the return of the field flux is a box-shaped steel yoke, 9.4 m high by 7.6 m wide by 7.3 m long.

2.4.2 Layer 00

These radiation-tolerant sensors are biased to about 500 V, which allows full depletion after about 5 Mrad integrated radiation doses. The strips are parallel to the beam axis allowing sampling of track in the (r,ϕ) plane. The inter-strip implant pitch 25 μm with floating alternate strips results in 50 μm read-out pitch. The analog signals of the 13,824 channels are fed via fine-pitch cables, up $\approx$ 50 cm long, to the front-end electronics outside the tracking volume. These cables pick-up ambient noise, causing a significant fraction of channels to have non-uniform and event-by-event changing pedestals that can not be controlled with dynamic pedestal subtraction. As a consequence, all channels have to be read-out, and pedestals are fit to 6th-order Chebyshev polynomial functions and subtracted off-line on an event-by-event basis. The fit procedure is iterative and excludes channels with isolated, positive signals (hits).

2.4.3 Silicon VerteX detector

The SVXII has a cylindrical geometry coaxial with the beam and its mechanical layout is segmented in three 32 cm axial section, each containing two "barrels". Each barrel is composed by a radial slice replicated in twelve 30° azimuthal sectors ("wedges"). Each wedge is a sequence of five equally spaced radii layers that contains the active sensors. A small overlap between to adjacent wedges, or barrels, helps the alignment and optimizes the coverage (Fig. 2.6).

The sensors in a single layer are arranged into independent longitudinal read-out units, called "ladders". Each ladder comprises two, double-sided, sensors and a multi-layer electronic board, all glued on a carbon-fiber support to ensure a light structure. Front-end electronics, biasing circuits and fan-out are located on the board that serves the pair of sensors whose strips are wire-bounded together resulting in a 15 cm active length. At a given radial layer and azimuth, each barrel contains pairs of ladders stacked length-wise head-to-head to keep the read-out electronic at the two outside extremities of the barrel (Fig. 2.6(a)).

The active surface consists of double-sided, AC-coupled, silicon sensors, arranged in micro-strips resistors of dimension 7.5 cm x 1.5-5.8 cm, the sensors have micro-strips implanted on a 300 μm thick, high resistivity bulk. Bias is applied through integrated poly-silicon resistors. On one side all sensors have axial strips,

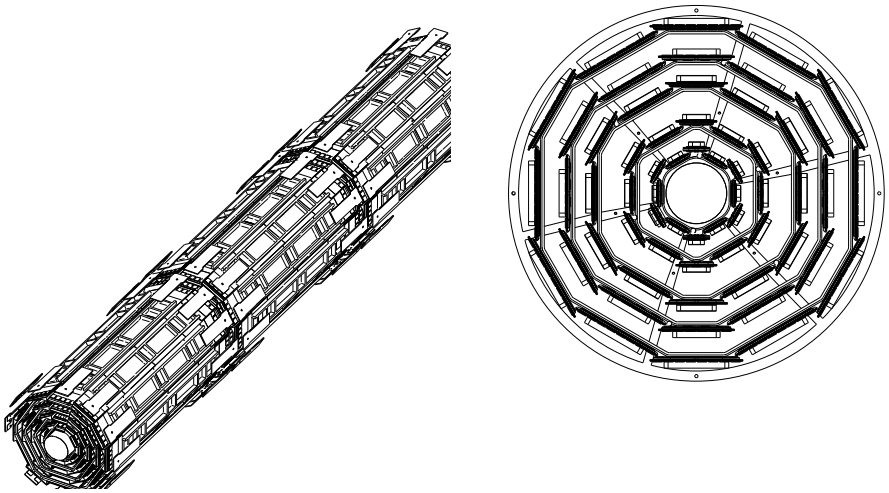

(a) Three-dimensional view (b) Transverse plane section

Figure 2.6: The figures show the SVXII silicon detector. The left plot(a) is a three-dimensional view of the detector, is possible to see the barrel structure along the beam axes. The right plot(b) shows in detail the layers sequence.

parallel to the beam axis, spaced by approximately $60 - 65$ μm, for a precise reconstruction of the ϕ coordinate. On the reverse side the following combination of read-out pitch (strip orientations with respect to the beam) is used: 141 μm (90°), 125.5 μm (90°), 60 μm (1.2°), 141 μm (90°), and 60 μm (1.1°) from the innermost to the outermost layer for reconstructing the z coordinate. A total of 405,504 electronics channels are used for SVXII.

2.4.4 Intermediate Silicon Layers

The internal segmentation follows the azimuthal segmentation seen for the L00 and SVXII into 30° sectors. The basic read-out unit consists of an electronic board and three sensors ganged together resulting in a total active length of 25 cm. ISL employs 888 5.7 cm x 7.5 (or 6.7) cm double-sided, AC-coupled, 300 μm thick sensors. Each sensor has axial strips spaced by 112 μm on one side and 1.2°-angled strips, spaced 112-146 μm on the reverse, for 303,140 total channels.

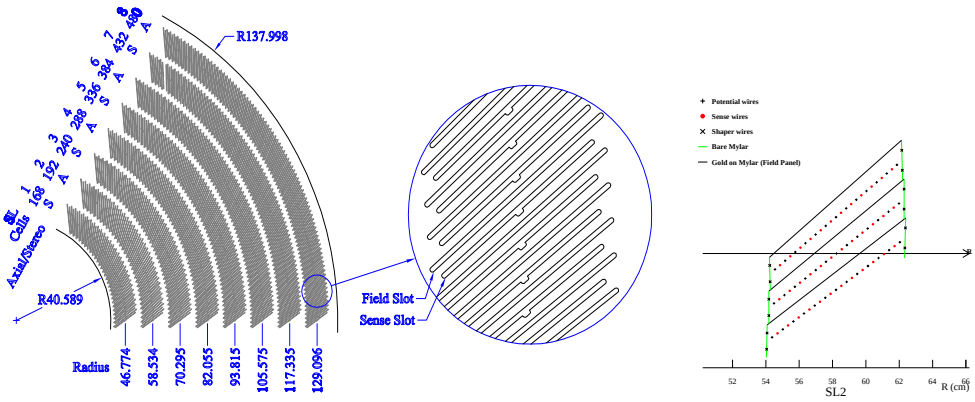

(a) COT sector (b) COT Cell

Figure 2.7: A 1/6 section of the COT end-plate(a). For each super-layer is given the total number of cells, the wire orientation (axial or stereo), and the average radius in cm. The enlargement shows in details the slot where the wire planes (sense and field) are installed. (b) shows a sketch of an axial cross-section of three cells in the super-layer 2, the arrow shows the radial direction.

2.4.5 Central Outer Tracker

It is arranged radially into eight "super-layers", for a total of 96 planes of wires that run the length of the chamber between the two end-plates (see Fig. 2.7(a)). Each super-layer is divided into ϕ cells; within a cell the trajectory of a charged particle is sampled at 12 radii, spaced 0.583 cm apart where sense wires (anodes) are strung. Four super-layers employ sense-wires parallel to the beam axis, for the measurement of the hit coordinates in the (r,ϕ) plane. These are radially interleaved with four stereo super-layers whose wires are alternately canted at angles of $+2°$ and $-2°$ with respect to the beam-line. Combined read-out of stereo and axial super-layers allows the measurement of the (r,z) hit coordinates.

Each super-layer is azimuthally segmented into open drift-cells. The drift cell layout (see Fig. 2.7(b)) consists of a wire plane closed azimuthally by cathode sheets spaced approximately 2 cm apart. The wire plane contains sense wires alternating with field-shaping wires, which control the gain on the wires optimizing the electric field intensity. The cathode is a 6.35 μm-thick Mylar sheet with vapor-deposited gold shared with the neighboring cell. Innermost and outermost radial extremities of a cell (i.e. the boundaries between the super-layers) are closed both mechanically and electrostatically by Milar strips with an additional field-shaping wire attached, the shaper wire.

Both field sheet and wire plane in correspondence of $z \approx 0$ cm have a support rod, this reduce the wire deformations due to the electrostatic forces. Each wire

plane contains 12 sense, 13 field-shaping and 4 shaper wires, with a diameter of 40 μm, made with gold-plated tungsten. Wire planes are not aligned with the chamber radius: a $\zeta = 35^\circ$ azimuthal tilt (see fig. 2.7(b)) partially compensates for the Lorentz angle of the drifting electrons in the magnetic field. The tilted-cell geometry helps in the drift-velocity calibration, since every high-pt (radial) track samples the full range of drift distances within each super-layer. Further benefit of the tilt is that the left-right ambiguity is resolved for particles coming from the z-axis since the ghost track in each super-layer appears azimuthally rotated by $\arctan\big(\tan(\zeta)\big) \approx 54^\circ$, simplifying the pattern recognition problem.

A mixture composed of 50% of argon and 50% of ethane bubbled through Isopropyl alcohol (1.7%) flows at 9.45 l/min in the active volume of the chamber with its pressure being continuously monitored by four probes.

High voltage is applied to the sense and field-shaping wires to generate a 1.9 kV/cm drift electric-field. This value, combined with the drift gas properties, results in a maximum drift-time of about 177 ns along a maximum drift-distance of 0.88 cm, allowing for read-out ad processing of the COT data between two consecutive bunch-crossing. The average 180 kV/cm field present at the surface of the sense wire produces typical gains of $2 \cdot 10^4$. The 30,240 sense wires are read-out by the front-end chip, which provides input protection, amplification, shaping, baseline restoration, discrimination, and charge measurement. The input-charge information is encoded (logarithmically) in the signal width for dE/dx sampling, and is passed to a time-to-digital converter that records leading and trailing-edge times of the signal in 1 ns bins. Hit times are later processed by the pattern recognition software to reconstruct trajectories. The dE/dx information is important for many analysis to recognize the identity of the particle associated to the reconstructed track. In particular in the analysis that I will describe later, Chap. 3, how this information is used. The material amounts of the COT corresponds to an average 0.017 radiation length for tracks at normal incidence.

2.4.6 Tracking performance

In the analysis presented in this thesis the only detector information used are related to the charged tracks. The good CDF tracking performance is crucial for the analysis described after. The good track resolution permits, as I will show in next chapter, a mass resolution of $25\,\mathrm{MeV/c}$ for a B-meson and $11\,\mathrm{MeV/c^2}$ for a D-meson.

Within an uniform axial magnetic field, the trajectory of a charged particle produced with non-zero initial velocity in the bending plane of the magnet is described by an helix. The arc of an helix described by a charged particle in tracking system of CDF is parameterized using three transverse (see fig. 2.8), and two longitudinal parameters:

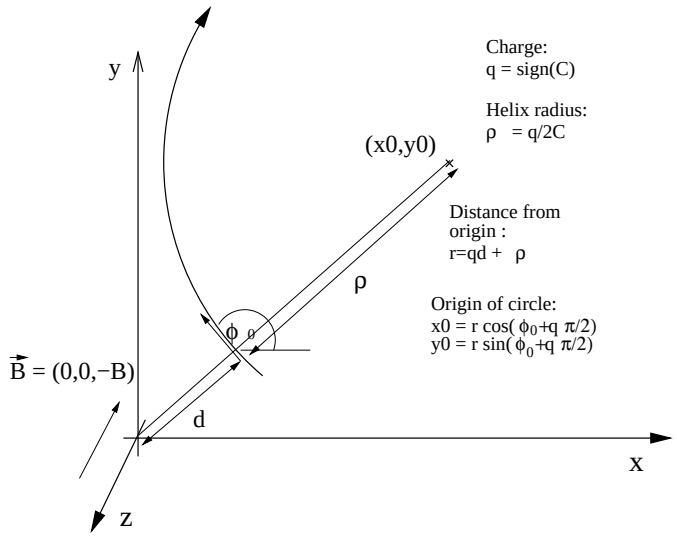

Figure 2.8: The figure shows an helix projected x-y plane of the CDF II cartesian coordinate system.

c: the signed half-curvature of the helix, defined as $c = q/2R$, where R is the radius of the helix and q is the charge, defining if the helix contains (or not) the collision point. The magnitude of this quantity is directly connected to the transverse momentum: $p_T = 0.3eBR$.

φ_0**:** is the direction of the particle at the point of closest approach to the to z-axis.

d_0**:** the signed impact parameter, is the distance of the closest point of the helix to the z-axis, defined as $d_0 = |q| \cdot \left(\sqrt{x_0^2 + y_0^2} - R\right)$.

λ**:** the helix pitch, i.e., $\cot(\theta)$, where θ is the polar angle of the particle at the point of its closest approach to the z-axis. This is directly related to the longitudinal component of the momentum: $p_z = p_T \cot(\theta)$.

z_0**:** the z coordinate of the point of the closest approach to the z-axis.

The reconstruction of a charged-particle trajectory consists in determining the above parameters trough an helix fit of a set of spatial measurements ("hits") reconstructed in the tracking sub-detectors with two basic steps: clustering multiple close measurements coming from the same track, and pattern-recognition algorithm to joint the hits along the whole track arc. The helix fit takes into account field non-uniformities and the multiple-scattering effects in the material.

In CDF is possible to use different tracking algorithms, with different tuning performances. For this analysis, only COT-seeded silicon tracks were used, because

the pattern recognition algorithms that use stand-alone silicon information would have given marginal contribution because the trigger is not optimized in this region.

All tracks were first reconstructed in the COT and then extrapolated inward to the silicon. This approach guarantees fast and efficient tracking with high purity. The grater radial distance of the COT with respect to the silicon tracker results in a lower track density and consequent fewer accidental combination of hits in the track reconstruction. A concise overview of the tracking algorithm is given in [42, 43].

2.5 Trigger and Data Acquisition System

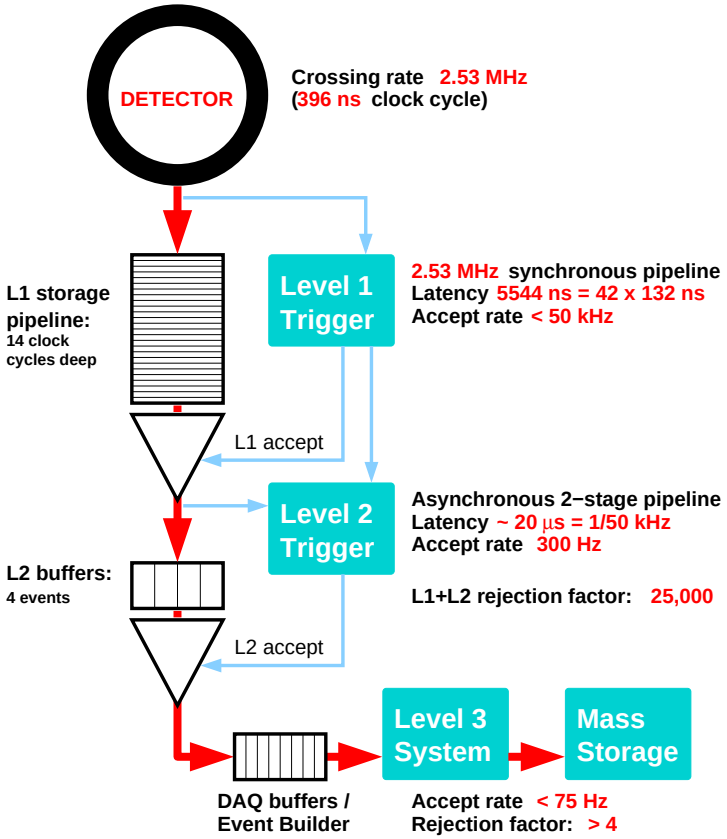

Figure 2.9: Functional block diagram of the CDF II trigger and data acquisition system.

At the typical Tevatron instantaneous luminosity $\mathcal{L} \approx 100 \cdot 10^{30}\,\mathrm{cm}^{-2}\mathrm{s}^{-1}$, and with an inelastic $p\bar{p}$ cross-section of $\sigma_{p\bar{p}} \approx 60\,\mathrm{mb}$, approximately $2.6 \cdot 10^6$ inelastic collisions per second occur, corresponding to one interaction per bunch-crossing

on average. Since the read-out of the entire detector needs about 2 ms on average, after the acquisition of one event, another approximately 5,000 interactions would remain unrecorded. When an event recording is prevented because the system is busy with a different event or a different task, this is called dead-time.

Expressing the same concept in term of information units, the average size of information associated to each event is 140 Kbytes. Even in case of deadtime-less read-out of the detector, in order to record all events, an approximate throughput and storage rate of 350 Gbyte/s would be needed, largely beyond the possibility of currently available technology[1].

The read-out system has to reduce the 2.3 MHz interaction-rate to the 100 Hz storage rate attainable at CDF. The challenge for the whole system is be smart enough to cut-off events that don't have the minimal requirements to be reconstructed or seem to contain well-known processes, that don't need further study, focusing the acquisition system on the interesting processes. The Fig. 2.9 shows a scheme to explain how the information flows trough the different parts.

To suppress unwanted events, the CDF Data Acquisition System (DAQ) is segmented in three levels, each level receiving the accepted event from the previous one, and, provided with detector information with increasing complexity and with more time for processing, determines if one of a set of existing criteria is verified by the event.

Prior to any trigger level, the bunched structure of the beam is exploited to reject cosmic-ray events by gating the front-end electronics of all sub-detectors in correspondence of the bunch crossing. The front-end electronics of each sub-detector, packaged in Vesa Module Eurocard (VME) modules hosted in about 120 crates, has a 42-cells deep pipeline synchronized with the Tevatron clock-cycle set to 132 ns. The Tevatron clock picks up a timing marker from the synchrotron RF and forwards this bunch-crossing signal to the trigger and to the front-end electronics. Since the inter-bunch time is 396 ns, three times the Tevatron clock-cycle, the pipeline can collect data corresponding to a maximum of 14 bunch crossings. The pipeline depth gives the amount of time that Level-1 trigger has to decide to accept or reject an event otherwise the buffer content is overwritten: $396\,\text{ns} \cdot 14 = 5.5\,\mu\text{s}$. An event accepted by the Level is passed to the Level 2 buffer, where the number of buffers in the pipeline is 4, that gives $5.5\,\mu\text{s} \cdot 4 = 22\,\mu\text{s}$. This means that if an event is accepted by the Level 1 and the Level 2 doesn't have a free buffer deadtime will incur. Level 3 is composed by a computer farm, the Level 2 output rate is low enough to avoid in general deadtime problem in the connection between Level 2 and Level 3.

The following description will emphasize the aspect of the CDF trigger that are related with the selection of rare events including b-hadrons with high purity.

[1] The maximum current storage rate is approximately 250 Kb/s

2.5.1 Level-1

At Level-1 a synchronous system of custom-designed hardware process a simplified subset of data in three parallel streams to reconstruct coarse information from the calorimeters (total energy and presence of single towers over threshold), the COT (two-dimensional tracks in the transverse plane), and the muon system (muon segments in the CMU, CMX, and CMP chambers). The information extracted from the sub-detectors usually doesn't have the maximum resolution, to fit within the tight Level-1 time requirements only fast and approximate quantities can be extracted from the raw data. A decision stage combines the information from these low-resolution physic objects, called "primitives", into more sophisticated objects, e.g., track primitives are matched with muon stubs or tower primitives, to from muon, electron, or jet object, which are subject to basic selection.

2.5.2 Level-2

At Level-2, as asynchronous system of custom-designed hardware processes the time-ordered events accepted by the Level-1. Additional information from the shower-maximum strip chambers in the central calorimeter and the axial hits in the SVXII is combined with the Level-1 primitives to produce Level-2 primitives. A simplified energy-clustering is done in the calorimeters, merging the energies in adjacent towers to the energy of a seed tower above threshold. Level-1 track primitives matched with consistent shower-maximum clusters provided refined electron candidates whose azimuthal position is known with 2°. Information from the (r, ϕ) sides of the SVXII is combined with Level-1 tracks primitives to form two-dimensional tracks with resolution similar to the off-line one: SVT, see Sec. 2.6.2. Finally, an array of programmable processors makes the trigger decision, while the Level-2 objects relative to the following event accepted at Level-1 are already being reconstructed.

2.5.3 Level-3

The digitized output relative to the Level-2-accepted event arrives fragmented from all sub-detectors via optical fibers. It is collected by a custom hardware switch that arranges it in the proper order and transfers it to 300 commercial CPUs, organized in a modular and paralleled structure of 16 sub-systems[44]. The ordered fragments are assembled in the *event record*, a block of data that uniquely identifies a bunch crossing and is ready for the analysis of the Level-3 software.

The event reconstruction at Level-3 benefits from full detector information and improved resolution with respect to the preceding trigger levels,including three-dimensional track reconstruction, tight matching between tracks and calorimeters

or muon information, and more precise calibrations. If an event satisfies the Level-3 requirements, the corresponding event record is transferred to mass storage at a maximum rate of 20 Mbyte/s.

The Level-3 decision is made after the full reconstruction of the event is completed and the integrity of its data is checked, a process that takes a few milliseconds. A fraction of the output is monitored in real time to search for detector malfunctions, to derive calibrations constants and to graphically display events.

2.5.4 Other trigger consideration

The trigger algorithm at each level has greater information, discriminating variables, and resolution on variables used in the event selection. As a consequence the number of trigger algorithms increases at each level: in a standard trigger table used in winter 2006-2007 at Level-1 there were 54 triggers, 143 at Level-2, and 207 at Level-3.

Triggers are grouped in the so called *trigger paths*. A trigger path is sequence of triggers, one per trigger level, designed to select a particular kind of physical events. The selection of interesting events starts from the choice of the trigger paths best suited to collect events with the interesting processes.

2.6 The Track Trigger of CDF

The collection of b-hadron decays an hadronic collider, like the Tevatron, is difficult not because the production of these states is uncommon, on the contrary it's challenging due to the richness of the production. The goal of a trigger that want to collect a large number of rare hadronic decay in this case is to implement the most sophisticated selection, in order to have a reasonable amount of bandwidth used by these triggers. The important quantities taken into account to have the optimal selection are: signal efficiency, the background rejection, and the final rate of the trigger.

In the CDF experiment the implementation of the strategies that have a good rejection on the background, with a reasonable efficiency on the interesting signal, had great advantage from the use of custom hardware devoted to the reconstruction of the track parameters in real-time. In the next sub-sections will be described the two processor that are doing this task at Level-1 and Level-2: XFT and SVT.

2.6.1 Drift chamber track-processor

The COT is connected to a custom processor that identifies two-dimensional tracks, in the (r, ϕ) plane, in time with the Level-1 decision. This processor is called eX-

tremely Fast Tracker (XFT), and uses pattern matching to first identify short segments of tracks, within each super-layer, and then links them into full-length tracks[45]. After classifying the hits of the four axial COT super-layers in "prompt" (0-66 ns) or "delayed" hits (67-220 ns), depending upon the observed drift-time within the cell, track segments reconstructed in each axial super-layer – a minimum of 11 (out of 12) hits required – and a set of predetermined patterns. If a coincidence between segments crossing four super-layers is found, two-dimensional XFT-tracks are reconstructed by linking the segments. The segments are compared with a set of about 2,400 predetermined patterns corresponding to all possible tracks with $p_T \geq 1.5\,\mathrm{GeV/c}$ originating from the beam line. The comparison proceeds in parallel each of the 288 azimuthal 1.25°-sectors in which XFT logically divides the chamber. If no track is found using all four super-layers, then the best track found in the innermost three super-layers is output.

The track-finding efficiency and the fake rate with respect to the off-line tracks depends of the instantaneous luminosity, and were measured to be $\varepsilon \approx 96\%$, and 3% respectively, for tracks with $P_T \geq 1.5 GeV/c$ at $\mathcal{L} \simeq 10^{31}\,\mathrm{cm^{-2}s^{-1}}$. The observed momentum resolution is $\sigma_{p_T}/p_T^2 = 0.017\,(\mathrm{GeV/c})^{-1}$, and the azimuthal resolution is $\sigma_{\phi_6} = 0.3°$, where ϕ_6 is the azimuthal position at the sixth COT super-layer, located at 106 cm radius from the beam line.

The fake rate needs a particular treatment when the instantaneous luminosity exceeds $10^{32}\,\mathrm{cm^{-2}s^{-1}}$. In [46] is shown as in this range the presence of multiple interactions increases the XFT fake rate, with a correlated increase of the Level-1 rate occupied by the so called Two-Track Trigger, TTT. To limit the bandwidth requested by the TTT in the high-luminosity scenario was studied the effect on it of the use of the CLC information at Level-1 [47]. A threshold on the maximum number of the CLC hits on an events selects the bunch-crossing discarding multiple collisions. This criteria is more effective on the background with respect to the signal, keeping the trigger alive also at high luminosity with good purity.

2.6.2 Silicon Vertex Trigger at CDF

The CDF trigger system uses tracks from the Level-1 (Sec. 2.6.1). The XFT track information at Level-2 time can be merged with the silicon information to have an high quality track reconstruction. The Silicon Vertex Trigger (SVT)[48] fully reconstruct the tracks in (r, ϕ) plane, giving information about: impact parameter, curvature, and ϕ track angle, following the convention in Sec. 2.4.6.

The use of the full spatial resolution of silicon detector permits to reconstruct track parameters with almost the same quality of the off-line reconstruction, in particular the high quality impact parameter reconstruction (see Fig. 2.11) give the possibility to implement cuts that select displaced vertex decays from hadrons with quarks b and c with high purity. The SVT processor requires the coincidence

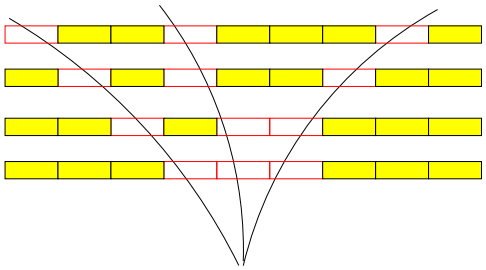

Figure 2.10: The schematic illustration of combinations of super-bins corresponding to the passage of charged particles in four radial silicon layers.

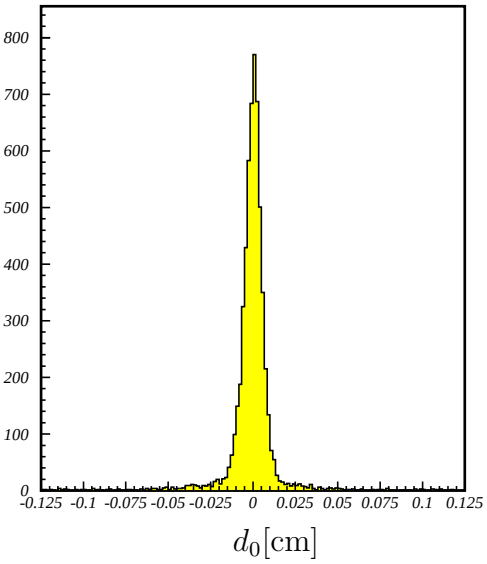

Figure 2.11: The plot shows the distribution of the impact parameter measured by SVT processor.

of hits in four axial SVXII layers with a XFT track. Since the silicon signals are digitized only after the Level-1 accept decision, the hits are send to the SVT hardware that within the $20\,\mu$m budget of the Level-2 returns the tracks parameter, a task that using offline CPU needs a time of about one second. SVT speed is largely due to a highly-paralleled structure whose segmentation matches the SVXII 12-fold azimuthal symmetry: each 30° azimuthal sector of each six longitudinal half-barrels is processed by its own asynchronous, data-driven pipeline.

2.6.3 Pattern recognition with Associative Memory

As input quantity SVT uses XFT track list and digitized pulse-height from SVXII layers. In a first stage the list of silicon hits, after clustering and ordering are read using a smaller silicon segmentation. This low resolution segmentation is done grouping together adjacent channels into "super-strip" (SS). The SS width is programmable, with $250 - 700\,\mu$m typical values. The possible SS combinations, called "patterns", generated by tracks with $p_T \geq 2\,\mathrm{GeV/c}$ and impact parameter $|d| \leq 1\,\mathrm{mm}$ are calculated using the simulation and stored in a large Associative Memory (AM) board. The pattern-bank is not large enough to contain all possible combinations, for each azimuthal sectors only the 32,768 most probable patterns

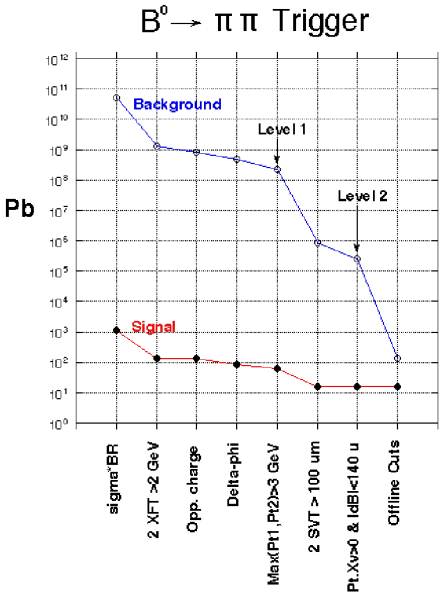

Figure 2.12: The plot shows how effective is the SVT trigger to select two-body decays of a B-meson. It's visible how the selection criteria reject a large background fraction while the effect over the signal is small.

are stored in the AM. Using the pre-calculated pattern banks the first SVT stage uses silicon and XFT data, searching the fired roads in the pattern banks in parallel to speed-up the process. Fig. 2.10 shows a schematic illustration of this stage. For a limit in the board, a maximum of 4 roads per event, each one having a maximum of 8 hits per super-bin, can be stored to be processed at the next stage.

Track fitting with linear constraints

After the step described before, within a road found by the AM board the hit combinations are calculated and used to reconstruct the helix parameters (d_0, ϕ, and the curvature) in the transverse plane. The base of the SVT ability to fit tracks in a very short time is challenging and discussed in its TDR[48].

The fit step uses a technique derived by the Principal Analysis Component (PAC)[49]. The main idea is that dividing the detector in sufficient small sectors it is possible to verify a linear correlation between the hits coordinates, then a linear relation between the hit coordinates and the track parameters. The covariance matrix will then identified as

$$\hat{S}_{ij} = \frac{\langle (x_i - \langle x_i \rangle)(x_j - \langle x_j \rangle) \rangle}{\sqrt{\sigma_i \sigma_j}} \tag{2.7}$$

where $x_{i(j)}$ is the hit coordinate on the $i(j)$ layer, $\sigma_{i(j)}$ is the standard deviation for the hit position. The collection of hit position is then represented by the vector $\vec{x}$.

Introducing now the track parameters vector $\vec{p}$, under the condition described

before it's possible to evaluate each parameter using the formula:

$$p_i = \vec{c}_i \cdot \vec{x} + q_i \tag{2.8}$$

the $\vec{c}_i$ and q_i coefficients are evaluated minimizing a χ^2 where the weights are extracted by the $\hat{S}$ matrix, see [48] for further details.

For each fitted tracks, using the evaluation of the $\hat{S}$, it is possible to evaluate the evaluation quality

$$\chi^2 = \left| \hat{S}^{-1} \left(\vec{x} - \langle \vec{x} \rangle \right) \right|^2 \tag{2.9}$$

where $\langle \vec{x} \rangle$ represents average hit vector.

For each combination a linear fit is performed, the fitting-board spends less than 250 ns for each fit. The global time used for the fit stage depends to the number of combination and is a function of the instantaneous luminosity. The average latency is 24 μs, 9 μs spent waiting for the start of the read-out of silicon data. The final resolution is $\sigma_{d_0,SVT} = 35\,\mu$m, in Fig. 2.11. This resolution is close to the offline resolution obtained without using L00 hits; to the previous value has to be added the uncertainty on the beam position, with a resolution on prompt tracks $\sigma_{d_0} = 47\,\mu$m.

After the fit stage the list of SVT tracks are matched with the XFT track list. This is done because the fit procedure can duplicate the real tracks, producing "ghost" tracks, or can try to fit a fake track, that can be easily removed using further information by other detectors. The SVT track list is cleaned by all tracks not matching the ϕ angle of one XFT track, if more than one SVT track matches with a XFT track the track with the best χ^2 is keep. The SVT efficiency is about 85%, this efficiency is defined as the ratio between the number of tracks reconstructed by SVT and all XFT-matched off-line silicon tracks that are of physics analysis quality.

2.7 CDF Monte Carlo simulation

In a modern high energy physics experiment is important to have a precise simulation of the detector response and ability to reconstruct energy and momentum of the particle. The geometry of a detector is quite complex, to reduce the uncertainties over the detector capabilities, the use of detailed Monte Carlo is mandatory. Some examples of this kind of information are: the efficiency in reconstruction a decay channel, geometrical acceptances, and other similar tasks. In this document the use of Monte Carlo technique is alternated, or mixed, to the use of data-driven approach, in general preferred where was possible, but in some case was unavoidable.

In the standard CDF simulation, the detector geometry and material are modeled using the version 3 of the GEANT package[50] tuned using data from the test-beams and collision data. GEANT receives in input the positions, the four-momenta, and the identities of all particles produced by the simulated collisions that have long enough lifetimes to exit the beam pipe. It simulates their passage in the detector, modeling their interactions (*bremmstrhalung*, multiple scattering, nuclear interactions, photon conversions, etc.) and the consequent generation of signals on a channel by channel basis.

Specific packages replace GEANT for some sub-detectors: the calorimeter response is simulated with GFLASH, a faster parametric shower-simulator[51] tuned from single-particle response and shower-shape using test-beam data (8-230 GeV/c electrons and charged pions) and collision data (0.5-40 GeV/c single isolated tracks); the drift-time within the COT is simulated using GARFIELD standard package[52, 53] further tuned on data; the charge-deposition model in the silicon uses a parametric model, tuned on data, which accounts for restricted Landau distribution, production of δ-rays, capacitive charge-sharing between neighboring strips, and noise. Furthermore, the actual trigger logic is simulated for all digital parts of the trigger. The output of the simulated data has the same format of the collision data, allowing their analysis with the same reconstruction programs used for collision data.

The detector and trigger configuration underwent several changes during data-taking. Minor variations may occur between runs, while larger variations occur, for instance, after major hardware improvements, or Tevatron shut-down periods. For a more detailed simulation of the actual experimental conditions, the simulation has been interfaced with the off-line database that reports, on a run-by-run basis, all known changes in configuration (position and slope of the beam line, relative mis-alignments between sub-detectors, trigger-table used, set of SVT parameters) and local or temporary inefficiencies of the silicon tracker (active coverage, noisy channels, etc.). This allows simulating the detailed configuration of any set of real runs, to match the distribution of real data in any given sample.

Chapter 3

Reconstruction of Charmless decay signals at CDF

In this chapter I describe the techniques used to extract the b-hadron charmless decays: here eight different decay channels are each one very close to the others. The signal separation needs to use a very refined statistical analysis. I will describe the trigger selection (Sec. 3.1), the analysis strategy used to extract the signals (Sec. 3.6), and various checks done to validate some preliminary assumptions (Sec. 3.8.2).

The analysis described in this thesis is based on about $1\,\mathrm{fb}^{-1}$ of data collected by the CDF II detector. The observation of the $\Lambda_b^0 \to ph^-$ decays is done in a signal region compatible with the charmless decays of the b-mesons[54, 55]. With respect to the $B_{(s)}^0$ charmless analysis the Λ_b^0 analysis needs some specific changes to take into account issues related to a baryon that has a different production mechanisms and different kind of systematic.

3.1 Trigger selection

The data used for the analysis was collected between February 2002 and March 2006. The data are divided into three data acquisition periods, for a total of $1\,\mathrm{fb}^{-1}$. The trigger paths used are `B_PIPI` and `B_PIPIHIGHPT`. These two paths take advantage from the use of the XFT (Sec. 2.6.1) and SVT processors (Sec. 2.6.2). The possibility to select the events according the track parameters, as already pointed out in the Sec. 2.6, is of great importance for this analysis.

At Level-1 the handles that XFT processor permits are: the p_T, ϕ, and the charge q for each track. An event is selected if there are two opposite-charged tracks, both with $p_T > 2\mathrm{GeV/c}$, or $p_T > 2.5\mathrm{GeV/c}$ for HIGHPT, with a scalar sum of the $\sum p_T > 5.5\mathrm{GeV/c}$ or $\sum p_T > 6.5\mathrm{GeV/c}$. To increase the purity also a cut on

Quantity	Units	B_PIPI	B_PIPIHIGHPT
$p_T(1),\ p_T(2)$	$^{\mathrm{GeV}}/_{\mathrm{c}}$	> 2.0	> 2.5
$\Delta\varphi_0$		$\in [20°, 135°]$	$\in [20°, 135°]$
$p_T(1) + p_T(2)$	$^{\mathrm{GeV}}/_{\mathrm{c}}$	> 5.5	> 6.5
$\lvert d_0(1)\rvert,\ \lvert d_0(2)\rvert$	μm	$\in [100, 1000]$	$\in [100,\ 1000]$
$\lvert d_0(B)\rvert$	μm	< 140	< 140
$\lvert L_{xy}(B)\rvert$	μm	> 200	> 200
$\lvert\eta(1)\rvert,\ \lvert\eta(2)\rvert$		< 1.2	< 1.2
$M_{\pi\pi}$	$^{\mathrm{GeV}}/_{\mathrm{c}^2}$	$\in [4.0, 7.0]$	$\in [4.0, 7.0]$

Table 3.1: Summary of the most relevant trigger requirements. The two used selection are compared, the differences are in the p_T thresholds. The tight requirements in the B_PIPIHIGHTPT permit to limit the trigger rate at high luminosity.

the opening angle between the two-tracks is applied: $0° \leq \Delta\phi \leq 135°$ between the two-tracks. This cuts result in a Level-1 rate of $\approx 25\,\mathrm{KHz}$ at $\mathcal{L} \approx 60 \cdot 10^{30}\,\mathrm{cm}^{-2}\mathrm{s}^{-1}$, $\approx 14\,\mathrm{KHz}$ at $\mathcal{L} = 100 \cdot 10^{30}\,\mathrm{cm}^{-2}\mathrm{s}^{-1}$ for the high luminosity scenario.

At Level-2 the p_T thresholds are verified, using the better accuracy, while the opening angle cut is tightened to $\Delta\phi \in [20°, 135°]$. This cut on the angle is more effective and specific for a two-body decay, this was not requested before because the same Level-1 trigger is shared with other b-physics trigger paths, not specific for a two-body decay. At Level-2 SVT gives information on the impact parameter, therefore is possible looks for: two displaced-track with impact parameter $100\mu\mathrm{m} \leq |d_0| \leq 1\,\mathrm{mm}$, from a common vertex with $L_{xy} > 200\ \mu\mathrm{m}$. These cuts have an efficiency on the signal $\approx 50\%$ but reduce the background of a factor ≈ 100.

At Level-3 all the criteria listed above are reproduced, using the further improvement to the resolution at this trigger-level. Using the full three-dimensional reconstruction is also asked that the $|\Delta z_0| < 5\,\mathrm{cm}$ for the two-tracks. Where z_0 is z-coordinate at the point of minimum distance from the beams. This helps to reject pairs produced by different interactions. At this stage there are no more differences between B_PIPI or B_PIPIHIGHPT.

In Tab. 3.1 are summarized the principal selection criteria based on the Level-2 quantities, for the two luminosity scenarios. The different rates, and shapes, as function of the Tevatron instantaneous luminosity are shown in Fig. 3.1. The B_PIPIHIGHPT rate is in general lower because the p_T thresholds are higher. The use in this trigger of the CLC detector, (Sec. 2.3.2), helps also to select very clean events, with a lower pile-up, cutting away the event with large pile-up. This effect can be seen because the rate decreases at high luminosity.

Other strategies are also used to keep low the b-trigger bandwidth: as the dynamic prescales, luminosity enable trigger, and more. The quality of the trigger

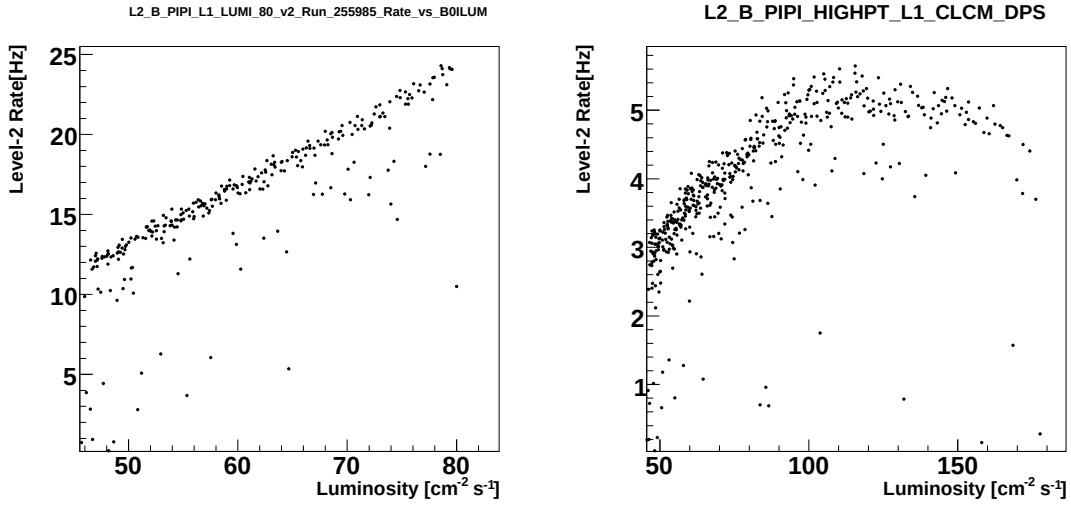

Figure 3.1: The plots show the Level-2 rates, as function of the Tevatron instantaneous luminosity, for the two used triggers. The left plot shows the B_PIPI rate while the right plot shows the B_PIPIHIGHPT rate. The left plot in this range increase linearly as function of the luminosity, due the increasing amount of fakes in XFT. The right plot as a more complex shape, this because the use the CLC detectors. The CLC monitor the number of interactions per bunch-crossing (see Sec. 2.3.2) and used as "veto" they permit to keep low the rate at high luminosity.

selection is shown in figure 3.2; here is shown the mass distribution of the track candidates just after the trigger selection. A narrow peak at the between B^0 and B_s^0 masses is visible.

3.2 Offline selection

In the off-line track reconstruction the used detectors are SVXII, ISL, and COT. The L00 micro-vertex was not used because the tracking resolution enhancement for the used quantity was negligible, while its use introduces some complications in the analysis, because this sub-detector was not correctly simulated the CDF Monte Carlo. We re-fit offline tracks using the KALMAN algorithm and we applied corrections for the energy loss in the detector[1]. We explicitly required that the offline tracks assigned to the $B^0_{(s)} \to h^+h'^-$ candidates are matched to two SVT-tracks passing the Level 2 trigger cuts ("SVT-matching"), in order to reject non-triggered offline candidates (*"volunteers"*). The trigger confirmation removes about 3% of the data, but improves the knowledge on the data quality. I re-applied

[1]The use of these correction needs of to take care of possible biases treated in Sec. 4.1.

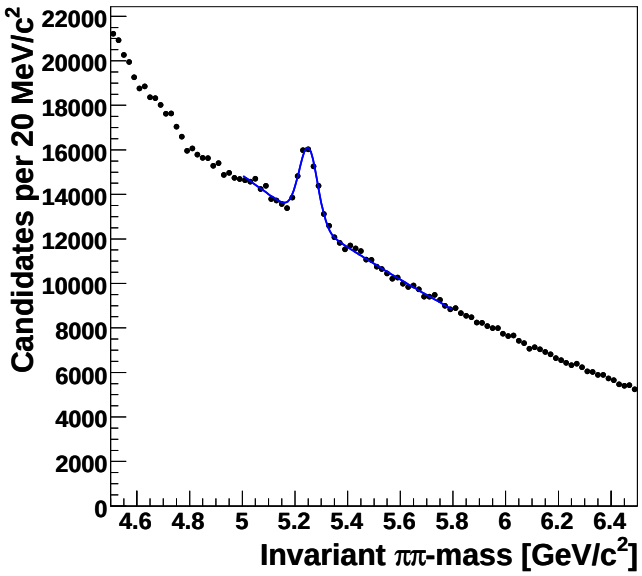

Figure 3.2: The plot shows the candidate's mass distribution after the trigger cuts.

all the Level 2 trigger selection cuts using the offline-quality track parameters.

Other standard track-quality requirements are applied to permit the use of the detector calibrations and other standard algorithms. The quality requirements for each track are: hits on at least two axial COT Super Layers (SL), two stereo SL, with at least five hits in each SL. After the use of the refit the tracks as to have at least three axial silicon hits.

3.3 Disentangle the signals

The CDF II tracking mass resolution for this kind of events using CDF MC is expected to be $\sigma_{Mass} \approx 25\text{MeV/c}^2$. Even if we add other information on the decay kinematics, this will be not sufficient to separate the signal produced by different $B^0_{(s)}$ and Λ^0_b decays, each very close to the other (see Fig. 3.3). Another information that can be used is the amount of energy deposit in the COT chamber, giving information on the particle identification, see the following section 3.5. This information can be added to the kinematic information and can help to disentangle signals with similar kinematic but with different particles in the final state.

The strategy, refined during the last years, combined both the kinematic and the PID informations in an unbinned maximum likelihood fit[16, 56]. This technique was showed to separate the individual contribution in the signal regions,

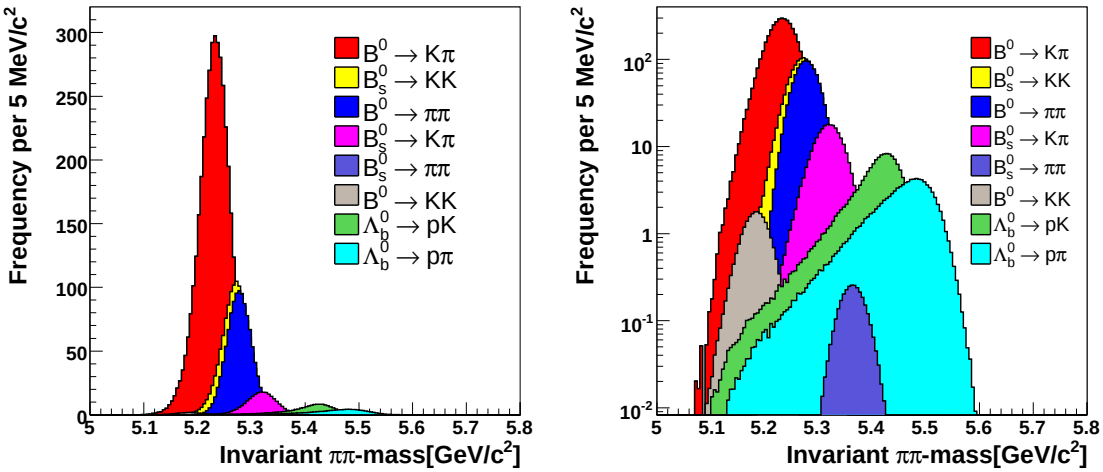

Figure 3.3: The plots show the invariant mass distribution in $\pi\pi$-hypothesis for the different expected signals, in linear scale on the left and logarithmic scale on the right. The signal fractions are set to the predicted values.

disentangling all the sources. The fit is based on Probability Distribution Function (p.d.f.) describing the kinematic and the PID part of each signal or background source. Will follow a part describing in more detail the variable used in the p.d.f. functions.

3.4 Kinematic separation

The first kinematic variable used to describe a two body decay is the invariant mass of the pair of tracks. Using only the information given by the tracking system the 2-track mass is evaluated with an arbitrary mass assumption for the final state involved particles. The formula for the two-track invariant mass is:

$$\begin{aligned} M^2 = (E_1 + E_2)^2 - (\vec{p}_1 + \vec{p}_2)^2 = \\ = \left(\sqrt{m_1^2 + p_1^2} + \sqrt{m_2^2 + p_2^2}\right)^2 - \left(\vec{p}_1 + \vec{p}_2\right)^2 \end{aligned} \tag{3.1}$$

where M is the invariant mass of the pair, $m_{1(2)}$ is the real mass of the particle 1(2), $p_{1(2)}$ is the measured momentum. In this analysis we have a mix of states, so we don't know the identity of each particle. We therefore assign a chosen nominal mass (we use the pion mass) to all particles, and separately account for the shifts caused by this arbitrary choice. The effect is shown in Fig. 3.3, where many final states have a spectrum not centered in the original meson (baryon) mass.

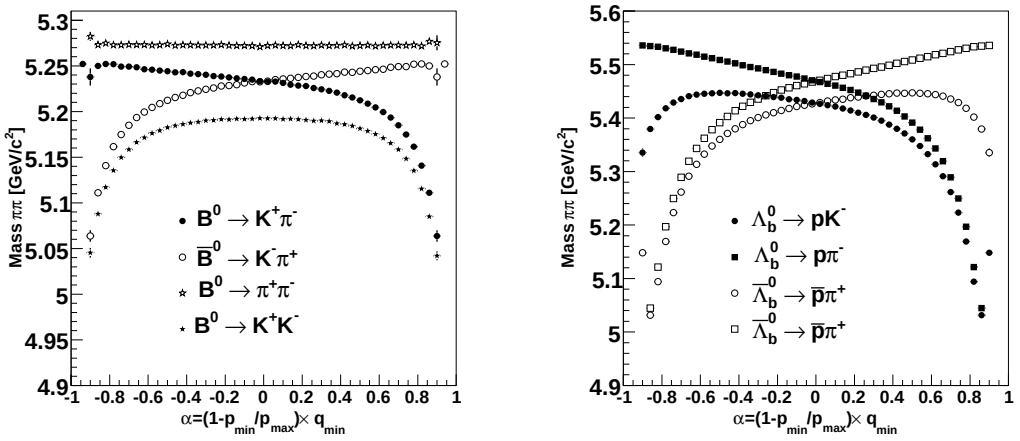

(a) $B^0 \to h^+h'^-$ and $\bar{B}^0 \to h^+h'^-$ (b) $\Lambda_b^0 \to ph^-$ and $\bar{\Lambda}_b^0 \to \bar{p}h^+$

Figure 3.4: The plots show the distribution of the central value of the invariant mass distribution, in $\pi\pi$ hypothesis, as function of the charged momentum unbalance, α, defined in (3.3). (a) shows the function for the B^0 decay modes, (b) shows the functions for the Λ_b^0. It's possible to see how this helps to separate two charge-conjugate channels because they have an opposite trend.

The shift due to pion mass assignment is function of the tracks momenta according to the equation:

$$\begin{aligned} \Delta M = M_{\pi\pi}^2 - M^2 = 2m_\pi^2 - \left(m_1^2 + m_2^2\right) + \\ +2\left(\sqrt{p_1^2 + m_\pi^2}\sqrt{p_2^2 + m_\pi^2} - \sqrt{p_1^2 + m_1^2}\sqrt{p_2^2 + m_2^2}\right) \end{aligned} \tag{3.2}$$

A different variable used to separate the different signals is the charged momentum imbalance of the tracks, defined as:

$$\alpha = \left(1 - \frac{p_{min}}{p_{max}}\right) \cdot q_{min} \tag{3.3}$$

where $p_{min(max)}$ is the track with minimum (maximum) momentum, q_{min} is the charge of the track with the minimum momentum. Using α in conjunction with:

$$p_{tot} = p_{min} + p_{max} \tag{3.4}$$

it is possible to change variables in eq. (3.2) from (p_1, p_2) to (p_{min}, p_{max}), obtaining

mode	$\Delta M\,(p_1, p_2)$, $\alpha < 0$
$B^0 \to \pi^- K^+$	$(m_\pi^2 - m_K^2) + 2 \cdot \sqrt{p_1^2 + m_\pi^2} \cdot \left(\sqrt{p_2^2 + m_\pi^2} - \sqrt{p_2^2 + m_K^2} \right)$
$\bar{B}^0 \to K^- \pi^+$	$(m_\pi^2 - m_K^2) + 2 \cdot \sqrt{p_2^2 + m_\pi^2} \cdot \left(\sqrt{p_1^2 + m_\pi^2} - \sqrt{p_1^2 + m_K^2} \right)$
$B^0/\bar{B}^0 \to K^- K^+$	$2 \cdot (m_\pi^2 - m_K^2) + 2 \cdot \left(\sqrt{p_1^2 + m_\pi^2} \cdot \sqrt{p_2^2 + m_\pi^2} - \sqrt{p_1^2 + m_K^2} \cdot \sqrt{p_2^2 + m_K^2} \right)$
$B^0/\bar{B}^0 \to \pi^- \pi^+$	0
$\bar{B}_s^0 \to \pi^- K^+$	$(m_\pi^2 - m_K^2) + 2 \cdot \sqrt{p_1^2 + m_\pi^2} \cdot \left(\sqrt{p_2^2 + m_\pi^2} - \sqrt{p_2^2 + m_K^2} \right)$
$B_s^0 \to K^- \pi^+$	$(m_\pi^2 - m_K^2) + 2 \cdot \sqrt{p_2^2 + m_\pi^2} \cdot \left(\sqrt{p_1^2 + m_\pi^2} - \sqrt{p_1^2 + m_K^2} \right)$
$B_s^0/\bar{B}_s^0 \to K^- K^+$	$2 \cdot (m_\pi^2 - m_K^2) + 2 \cdot \left(\sqrt{p_1^2 + m_\pi^2} \cdot \sqrt{p_2^2 + m_\pi^2} - \sqrt{p_1^2 + m_K^2} \cdot \sqrt{p_2^2 + m_K^2} \right)$
$B_s^0/\bar{B}_s^0 \to \pi^- \pi^+$	0
$\Lambda_b^0 \to \pi^- p$	$(m_\pi^2 - m_p^2) + 2 \cdot \sqrt{p_1^2 + m_\pi^2} \cdot \left(\sqrt{p_2^2 + m_\pi^2} - \sqrt{p_2^2 + m_p^2} \right)$
$\bar{\Lambda}_b^0 \to \bar{p} \pi^+$	$(m_\pi^2 - m_p^2) + 2 \cdot \sqrt{p_2^2 + m_\pi^2} \cdot \left(\sqrt{p_1^2 + m_\pi^2} - \sqrt{p_1^2 + m_p^2} \right)$
$\Lambda_b^0 \to K^- p$	$2m_\pi^2 - (m_K^2 + m_p^2) + 2 \cdot \left(\sqrt{p_1^2 + m_\pi^2} \cdot \sqrt{p_2^2 + m_\pi^2} - \sqrt{p_1^2 + m_K^2} \cdot \sqrt{p_2^2 + m_p^2} \right)$
$\bar{\Lambda}_b^0 \to \bar{p} K^+$	$2m_\pi^2 - (m_p^2 + m_K^2) + 2 \cdot \left(\sqrt{p_1^2 + m_\pi^2} \cdot \sqrt{p_2^2 + m_\pi^2} - \sqrt{p_1^2 + m_p^2} \cdot \sqrt{p_2^2 + m_K^2} \right)$

Table 3.2: The table lists the mass differences between measured $M_{\pi\pi}$ and the real mass, computed with the correct mass hypothesis for the two tracks. The relations are function of the momenta and are computed for $\alpha < 0$. The case $\alpha > 0$ has the same formulas for the cases with two equal particles in the final state, while hadron and anti-hadron are exchanged in the other cases.

this formula:

$$\begin{aligned} \Delta M = 2m_\pi^2 - \left(m_1^2 + m_2^2\right) + \\ +2 \left(\sqrt{\left(\frac{1-|\alpha|}{2-|\alpha|} \right)^2 p_{tot} + m_\pi^2} \sqrt{\left(\frac{1}{2-|\alpha|} \right)^2 p_{tot} + m_\pi^2} - \right. \\ \left. - \sqrt{\left(\frac{1-|\alpha|}{2-|\alpha|} \right)^2 p_{tot} + m_{min}^2} \sqrt{\left(\frac{1}{2-|\alpha|} \right)^2 p_{tot} + m_{max}^2} \right) \end{aligned} \tag{3.5}$$

In Tab. 3.2 the mass shift computation is showed for different decays. In Fig. 3.4 is shown as the opposite dependence of the mass shift for two charge conjugated decays helps to separate them: i.e. $B^0 \to K^+\pi^-$ against $\bar{B^0} \to K^-\pi^+$ in Fig. 3.4(a), or $\Lambda_b^0 \to p\pi^-$ with respect to $\bar{\Lambda}_b^0 \to p\pi^-$ in Fig. 3.4(b).

3.5 Particle identification

The mass trend helps to separate charge-conjugated decay channels of a neutral mesons. This alas doesn't help to separate two decays, with similar kinematic but

different particle in the final states. For this reason we use also track PID.

Hadron identification is difficult at CDF II, since the detector was designed for high-p_T physics measurements [57, 58]. The TOF is the only detector entirely devoted to this function, but its performance is marginal for particles with momenta greater than 2.0 GeV/c. Similarly, specific ionization from the silicon tracker is of little help for this analysis, because its identification power is only effective for particles with $p_T \leq 800$ MeV/c. For charged particles with $p_T \geq 2$ GeV/c a reasonable particle identification can be obtained from the rate of energy loss through ionization (dE/dx) in the gas that fills the active volume of the drift chamber.

The average total energy-loss per unit length of a particle (heavier than the electron) of charge q traversing a gas volume with velocity $c\beta$ is approximated by the Bethe-Bloch formula [59, 60]

$$\left\langle \frac{\mathrm{dE}}{\mathrm{dx}} \right\rangle = \frac{4\pi N e^4}{m_e c^2 \beta^2} q^2 \left[\ln\left(\frac{2 m_e c^2 \beta^2 \gamma^2}{I} \right) - \beta^2 - \frac{\delta(\beta)}{2} \right], \tag{3.6}$$

where N is the electron density in the medium, m_e (e) is the electron mass (charge), I is the mean excitation energy of the medium atoms, and $\delta(\beta)$ is the correction that accounts for the density effect at high velocities. To a good approximation, the most probable dE/dx value of a charged particle is a function of its velocity. If the momentum of the particle is measured, the mass can also be determined. In the COT, the signal induced on each sense-wire depends on the amount of ionization charge produced by the passage of the charged particle near the wire. It is measured in nanoseconds because it is encoded as the digital pulse-width between the leading and the trailing-edge time of the hit. Multiple samplings along the trajectory of the charged particle allow a more reliable estimation of dE/dx, which has usually a broad distribution. The COT samples a maximum of 96 dE/dx measurements per track, from which a 80% truncated mean is calculated to avoid the adverse effect of long positive tails in the estimation of the average dE/dx.

The empirical equation that better models the COT average energy-loss observed at CDF as a function of velocity is the following variant of the Bethe-Bloch curve:

$$\left\langle \frac{\mathrm{dE}}{\mathrm{dx}} \right\rangle = \frac{1}{\beta^2} \left[c_1 \ln\left(\frac{\beta\gamma}{b + \beta\gamma} \right) + c_0 \right] + a_1(\beta - 1) + a_2(\beta - 1)^2 + C, \tag{3.7}$$

with a_i, b, c_j, and C parameters extracted from data. The above function has all the features that are present in the Bethe-Bloch curve (3.6). The parameters c_0 and c_1 represent the intensities of the $1/\beta^2$ fall and of the relativistic rise. The parameter b is associated with the COT gas properties, i.e. mean excitation energy of the gas atoms, etc. The parameters a_1 and a_2 provide a further adjustment, especially in the low $\beta\gamma$ region.

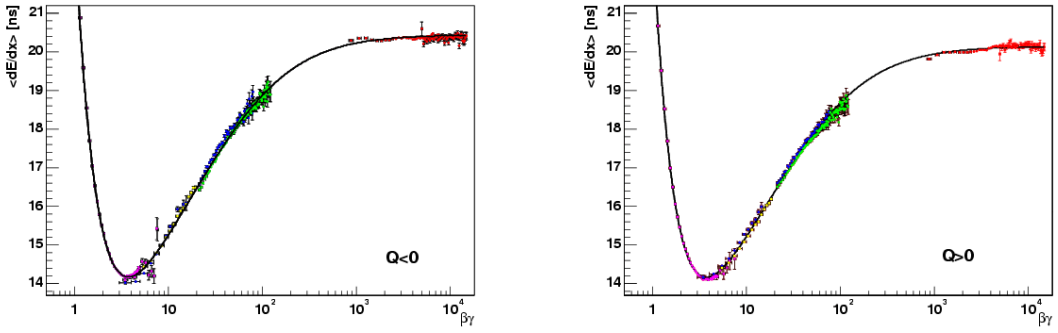

(a) Negative charge (b) Positive charge

Figure 3.5: Experimental dE/dx as a function of $\beta\gamma$. The fit function (3.7) is overlaid (continuous line). Negative particles (a), positive particles (b). The electrons are in red, the muons are in green, the kaons in yellow, the pions in blue and the protons in magenta.

The individual charge collections output by the COT are subject to several corrections (*hit-level* corrections), applied in the off-line production, to eliminate a number of detector related conditions: hit merging, electronic pedestal subtraction, path-length correction, high-voltage correction, z correction, angle and drift distance corrections, wire correction, super-layer correction, and pressure correction. An exhaustive description of these corrections can be found in [54, 61] In addition to the hit-level corrections [61] an accurate calibration of the uniformity of the dE/dx response in time and over the chamber volume was required. These were determined using track-oriented parameters (like ϕ_0, η, hit multiplicity and time) which allowed complementary corrections accounting for some "macroscopic" effects (i.e. the track length dependence). This improved the PID performance in terms of *separation power* to distinguish different classes of particles and reduced the effects due to the *correlations* between the dE/dx response of tracks. Understanding the dE/dx correlations is crucial to avoid bias in the estimate of physical observables.

The details of the calibration procedure are reported in [54], in the next sections we will describe only the relevant results: the dE/dx performance and the templates used to model the dE/dx response [62], and what we needed to change for the purpose of the present analysis.

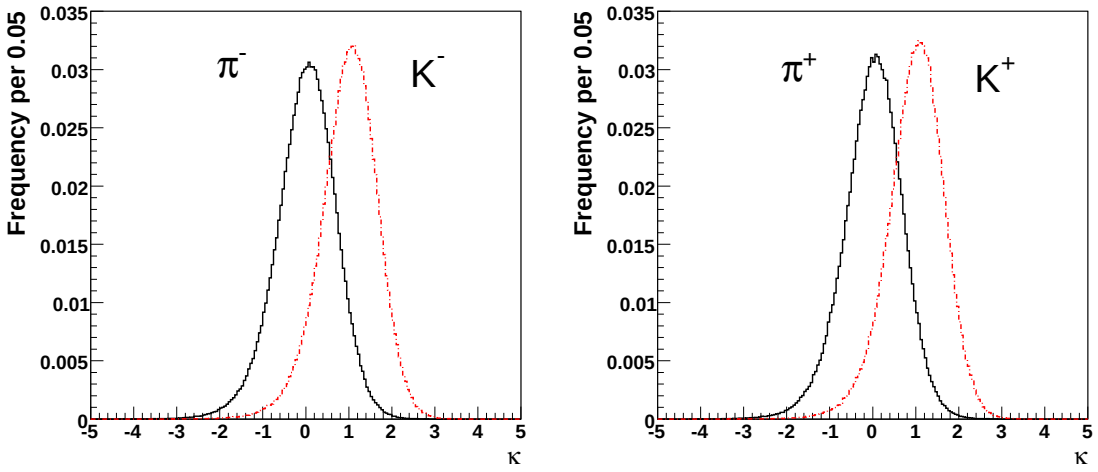

(a) (b)

Figure 3.6: Distribution of the dE/dx around the average pion response for negatively (a) and positively(b) charged particles. Pions and Kaons are identified by the $D^{*\pm}$ decays.

3.5.1 PID calibration and use

The PID calibration at CDF is made using data samples collected by the same trigger used for the $B^0_{(s)} \to h^+h'^-$ analysis, or others with very similar cuts. In particular the calibration for pions and kaons is made using $D^{*+} \to D^0[K^-\pi^+]\pi^+$ decays, or the conjugated D^{*-} decay, while the protons and anti-protons calibration is performed using $\Lambda^0 \to p\pi^-$, $\bar{\Lambda}^0 \to \bar{p}\pi^+$ decays. Other kind of particles that can be found in the $B^0_{(s)} \to h^+h'^-$ sample are electrons, calibrated using γ conversions, and muons, that in this range of momenta are indistinguishable from the pions.

The π-K separation power achievable in CDF is shown in Fig. 3.6: this separation is equal to $1.5\,\sigma$ for negatively charged particles, and $1.53\,\sigma$ for positively charged. That values are almost constant in the range $2 \lesssim p \lesssim 20$ GeV/c.

In particular the variable used in this analysis is the so called *kaon-ness*, defined as:

$$\kappa = \frac{\frac{dE}{dx}\Big|_{meas} - \frac{dE}{dx}\Big|_{exp-\pi}}{\frac{dE}{dx}\Big|_{exp-K} - \frac{dE}{dx}\Big|_{exp-\pi}} \tag{3.8}$$

where $\frac{dE}{dx}|_{meas}$ is the measured value of specific ionization energy loss for the given particle in the event, $\frac{dE}{dx}|_{exp-K}$ ($\frac{dE}{dx}|_{exp-\pi}$) are the expected values of the specific ionization energy loss for the given particle assuming it is a kaon (pion).

Another variable often used is the dE/dx residual:

$$\delta = \left.\frac{dE}{dx}\right|_{meas} - \left.\frac{dE}{dx}\right|_{exp-\pi} \tag{3.9}$$

These quantities are determined using the ionization curve, which relates the Lorentz-boost of a charged particle to an expected dE/dx value. The Lorentz-boost is a function of the measured momentum of the particle, p, and of a desired mass (m) hypothesis as $\beta\gamma = p/m$.

A second order effect related with the particle identification response is the existence of a correlation between the two tracks emerging from the decay. This effect needs to be evaluated in the parameterization of the κ response to avoid possible effect or degradation of the separation power. These correction are taken into account in this analysis, that will be shown in Sec. 3.5.1, later in this chapter.

3.6 The likelihood function

Since this point some quantity are described to help to extract a partial information from the signal. To use their different abilities the Maximum-Likelihood method is used. The likelihood function uses the five discriminating observables discussed before:

- $M_{\pi\pi}$: the invariant mass of the track pair, computed by assigning the pion mass to both tracks;
- $\alpha = \left(1 - \frac{p_{\min}}{p_{\max}}\right) q_{\min}$: the signed momentum imbalance where $p_{\min}$ ($p_{\max}$) is the magnitude of the momentum of the softer (stiffer) track of the pair. $q_{\min}$ is the charge of the track with the lowest momentum;
- $p_{tot} = p_{\min} + p_{\max}$: the scalar sum of the 3-D momenta;
- $\kappa_{\min}$ and $\kappa_{\max}$: functions of the dE/dx for the two tracks, as defined in eq. (3.8).

The likelihood function is:

$$\mathcal{L} = \prod_{i=1}^{Nev} \mathcal{L}_i \qquad\qquad \mathcal{L}_i = b \cdot \mathcal{L}^{bkg} + (1-b) \cdot \mathcal{L}^{sig} \tag{3.10}$$

the index sig (bkg) labels the part relative to the signal (background); b is the fraction of background events. In terms of p.d.f., the likelihood of the signal is

factorized as follows:

$$\mathcal{L}^{sig} = \sum_j f_j \cdot pdf_j^M(M_{\pi\pi}|\alpha, p_{tot}; \vec{\theta}) \cdot pdf_j^{PID}(\kappa_{\min}, \kappa_{\max}|\alpha, p_{tot}; \vec{\theta}) \cdot \cdot pdf_j^P(\alpha, p_{tot}; \vec{\theta}) \quad (3.11)$$

The index j labels the contributions of each signal decay: $B^0 \to \pi^+\pi^-$, $B^0 \to K^+\pi^-$, $\overline{B}^0 \to K^-\pi^+$, $B^0 \to K^+K^-$, $B_s^0 \to K^+K^-$, $B_s^0 \to K^-\pi^+$, $\overline{B}_s^0 \to K^+\pi^-$, $B_s^0 \to \pi^+\pi^-$, $\Lambda_b^0 \to p\pi^-$, $\overline{\Lambda}_b^0 \to \overline{p}\pi^+$, $\Lambda_b^0 \to pK^-$, and $\overline{\Lambda}_b^0 \to \overline{p}K^+$; f_j are the corresponding fractions, which are determined by the fit.

For the background the likelihood is:

$$\mathcal{L}^{bkg} = pdf^M(M_{\pi\pi}|\alpha, p_{tot}; \vec{\theta}) \cdot pdf^{PID}(\kappa_{\min}, \kappa_{\max}|\alpha, p_{tot}; \vec{\theta}) \cdot pdf^P(\alpha, p_{tot}; \vec{\theta}) \quad (3.12)$$

the form of the *pdf* in this equation are extracted using both CDF Monte Carlo or Data, their forms will be discussed in depth later in this chapter.

The validity of the above factorization of the likelihood has been carefully studied in the previous iterations of the analysis. A more detailed description can be found in [56, 63, 64].

3.7 Optimized offline cuts

Quantity	Loose	Tight	Λ_b^0
# axial COT SL	$\geq$ 2(5 hits)	$\geq$ 2(5 hits)	$\geq$ 2(5 hits)
# stereo COT SL	$\geq$ 2(5 hits)	$\geq$ 2(5 hits)	$\geq$ 2(5 hits)
# $r-\phi$ SVXII hits	≥ 3	≥ 3	≥ 3
tracking algorithm	sil. r-ϕ and 90°z hits (OIZ)		
$\mid \eta \mid$	$\leq$1	$\leq$1	$\leq$1
$p_T(1) + p_T(2)$	$\geq$ 5.5 GeV/c	$\geq$ 5.5 GeV/c	$\geq$ 5.5 GeV/c
$q(1) \cdot q(2)$	< 0	< 0	< 0
$\Delta\phi$	$\geq$20°	$\geq$20°	$\geq$20°
$\Delta\phi$	$\leq$135°	$\leq$135°	$\leq$135°
$\mid d_0 \mid$	$\geq$100 μm	$\geq$120 μm	$\geq$120 μm
$\mid d_0 \mid$	$\leq$ 1 mm	$\leq$ 1 mm	$\leq$ 1 mm
$d_0(1) \cdot d_0(2)$	$<$0 cm^2	$<$0 cm^2	$<$0 cm^2

Table 3.3: Offline track cuts, optimized for the search for rare modes.

variable	Loose	Tight	Λ_b^0
$p_T(B)$	-	-	≥ 6 GeV/c
$\mid \eta(B) \mid$	≤ 1	≤ 1	≤ 1
$\mid d_0(B) \mid$	≤ 80 μm	≤ 60 μm	≤ 60 μm
$L_{xy}(B)$	≥ 300 μm	≥ 350 μm	≥ 350 μm
$\chi^2_{3D}(B)$	≤ 7	≤ 5	≤ 5
isolation $I_{R=1}$	≥ 0.5	≥ 0.525	≥ 0.525

Table 3.4: Offline candidate cuts, optimized for the search of rare modes.

The data extracted following the prescription described in Sec. 3.2 are chosen to have the best performance on the trigger side: good signal efficiency and high background rejection, using variable and algorithms fast enough to be used in time with the data-acquisition system.

It's intuitive that at the analysis stage the candidates can be selected using more refined quantities: applying all the calibrations, not crucial at the on-line, or quantities the are too time-consuming to be calculated in an on-line algorithm.

The procedure followed to obtain the best selection criteria is described in [65, 18]. The general idea is to choose the set of cuts that have the best resolution on the parameter that is the goal of the measurement. In this case the quantity to measure is the ratio $f(B_s^0 \to K^-\pi^+)/f(B^0 \to K^+\pi^-)$. This criteria was found be good also for the measurement of the Λ_b^0 related quantity because the $\Lambda_b^0 \to ph$ decay are in a very near kinematic region and we want to refer at the same abundant channel.

The most important observed variables to have a good separation of the signal from the background are: the transverse momentum, the impact parameter for each track, the opening angle, the 3D vertex quality for the pair, the transverse momentum, the decay length, and the isolation for the B-meson candidate. The candidate isolation variable was introduced in b-quark fragmentation usually the particle containing the b carries a large fraction of the momentum. Looking in a cone of $\Delta R = \sqrt{\Delta\eta^2 + \Delta\phi^2} \leq 1$ around the B-candidate is indeed possible to define:

$$I(B) = \frac{p_T(B)}{\sum\limits_{track \in \Delta R \leq 1} p_T(track)} \tag{3.13}$$

this quantity peaks to 1 for a B-candidate.

The list of cuts used to select tracks is in Tab. 3.3, while in Tab. 3.4 are listed the cuts to select the candidates. Tracks compatible with the trigger selection, as p_T and number of hits requested, are selected. Other track cuts ensure the track

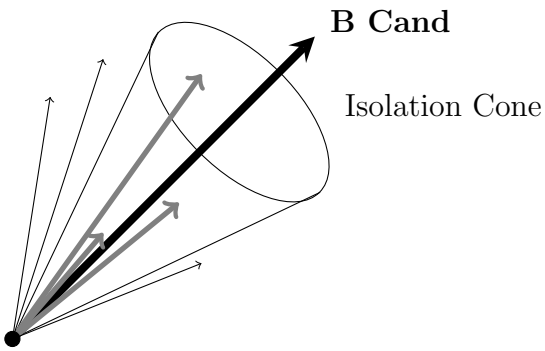

Figure 3.7: The sketch shows how the isolation for a B-meson is calculated: a cone around the the momentum of the candidate is created, all the tracks within the cone are counted.

quality. The candidate related cuts were imposed to have an optimal signal to background ratio.

The cut over the candidate transverse momentum, the third column in 3.4, was explicitly required to restrict the transverse momentum domain to a region in which Λ_b^0 has been studied in exclusive channels [66] allowing proper simulation of kinematic distributions. In addition, the baryonic fragmentation fraction is known only for Λ_b^0 produced with $p_{\rm T} > 6$ GeV/c, thus the choice of this momentum domain allows a measurement of the $\Lambda_b^0 \to ph$ decay-rate relative to $B_{(s)}^0 \to h^+h'^-$ decays.

The final sample obtained through this selection contains just one $B_{(s)}^0 \to h^+h'^-$ meson candidate per event. The invariant mass distribution of the candidates (with pion mass assignment for both tracks) is shown in Fig. 3.8. A simple binned fit, assuming a Gaussian shape for the signal, and an exponential (combinatorial background) plus an *"Argus function"*[67] for the physics background coming from the multi-body B-decays. The binned fit estimates a yield of 3966 ± 70 $B_{(s)}^0 \to h^+h'^-$ events in the peak with a standard deviation $\sigma = 41.0 \pm 0.7$ MeV/c^2, and a purity $S/B \approx 15$ at the peak.

3.8 Signal composition

The maximum-likelihood fit technique needs to know model of the distributions for the discriminating variables. This means that it's necessary have the some knowledge about the detector response for the various variables. Several informations are extracted, as for the PID, using calibration samples, while other information related to the kinematic come from the detailed MC and from a custom Monte Carlo, that will be described in Cap. 4.

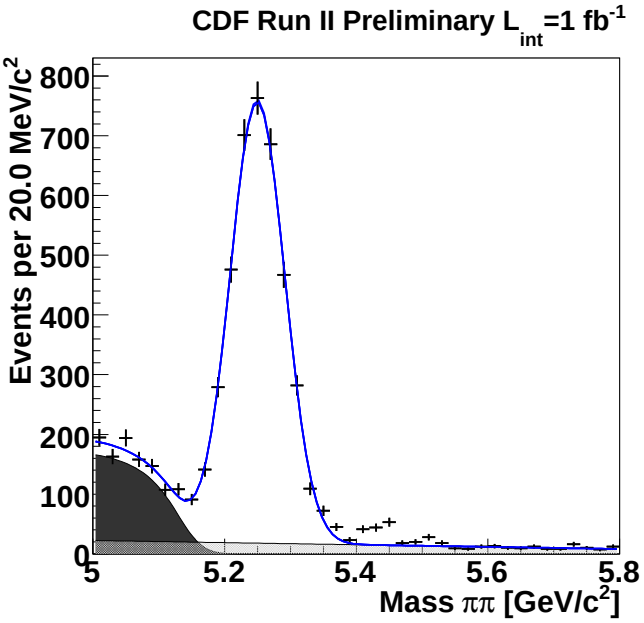

Figure 3.8: Invariant $\pi\pi$-mass distribution after the analysis cuts of Tab. 3.3 and 3.4. A Gaussian (signal), plus a straight line (combinatoric background) and a smeared Argus function (physics background) fit is overlaid. The region of mass between 5.35 and 5.55 GeV/c^2, in which $B_s^0 \to K^-\pi^+$and $\Lambda_b^0 \to ph^-$ signals are expected, is excluded from the fit range.

This section explains how the data samples, real or from Monte Carlo simulation, are processed and validated before being used in the analysis.

3.8.1 Simulated samples

Simulated samples for each mode are generated using the official CDF Monte Carlo (Sec. 2.7) and a custom, fast, parametric, Monte Carlo (FMC), necessary to model the effect of final state radiation (FSR), see Cap 4 and [68].

To generate the B-hadron decay sample in the CDF Monte Carlo there are three different steps: the first step is the B-hadron generation, then the hadron is forced to decay in a particular final state, and finally the decay products are propagated within the CDF detector. The hadron generation and the decay were generated using BGenerator[69] algorithm. In this step the algorithm as input information the joint distribution of transverse momentum and pseudo-rapidity for the different b-hadrons. The rapidity distribution was in particular assumed flat in the range $|y(B)| < 1.3$, this assumption is standard in the CDF simulation and is valid

for the detector range covered by the tracking system. The p_T distribution was taken from the published measurements [23]. The $B^0_{(s)}$ oscillations were inhibited ($\Delta m_d = \Delta m_s = 0$) and the lifetime differences was set to zero ($\Delta\Gamma_s/\Gamma_s = 0$) to ensure the decay mode.

I generated 10 million of events for each signal sample. To reproduce the experimental conditions I used the condition database prepared during the on-line operations. This permits to simulate: the alignment, dead channels, etc. The simulation output uses the same format off the real data samples. This technical aspect allows to reconstruct real and simulated data samples with the same software, thus limiting biases and errors.

We also simulated a sample of $B^+ \to \rho^0\pi^+$ decays. This decay channel is used as a template for the partially-reconstructed B decays on lower mass sideband of the peak. This channel was chosen because is the most abundant.

$p_T(B)$ re-weight of the Monte Carlo sample

The simulated data produced by the CDF Monte Carlo show some small discrepancies with respect to the real data in some distributions. An in-depth study was performed on this regard in [70]. The main differences are related to the p_T distribution. In particular the $p_{\rm T}$-distribution of simulated Λ^0_b can be different from the one observed in data for two reasons:

1. the $p_{\rm T}$-spectrum of Λ^0_b at production is different from the $B^0_{(s)}$ spectrum. Since our simulated Λ^0_b samples are generated from the inclusive $p_{\rm T}$-spectrum measured by CDF, which is dominated by the $B^0_{(s)}$ component, some discrepancies may occur.

2. the second effect that contributes on the measured $p_{\rm T}$ spectrum is the isolation cut described before. This because the efficiency as function of the candidate $p_{\rm T}$ is not uniform. This effect can be measured using a control sample, that unfortunately was not usable for the Λ^0_b case. For this reason we applied a correction extracted from the $B^0_{(s)}$ case[70], that in approximation could be not very different from the Λ^0_b. After in this chapter this assumption will be proved.

A comparison between the generation spectrum used for B-mesons and the measured spectrum of the Λ^0_b is shown if Fig. 3.9. For the range $p_T > 6\,\mathrm{GeV/c}$ we extracted the re-weight function that has to be applied to the Λ^0_b decay samples to correct the effect of the p_T distribution used at the generation level. The other re-weight function applied to the b-mesons channels for the isolation cut effect is applied also to these channels. So the final re-weight function for the Λ^0_b channels

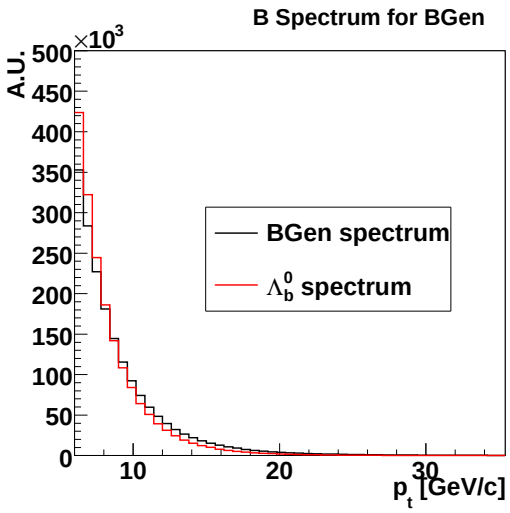

Figure 3.9: Comparison of the spectrum for B-meson generation used in BGen and the spectrum measured for Λ_b^0 production (obtained from the CDF measurement [66])

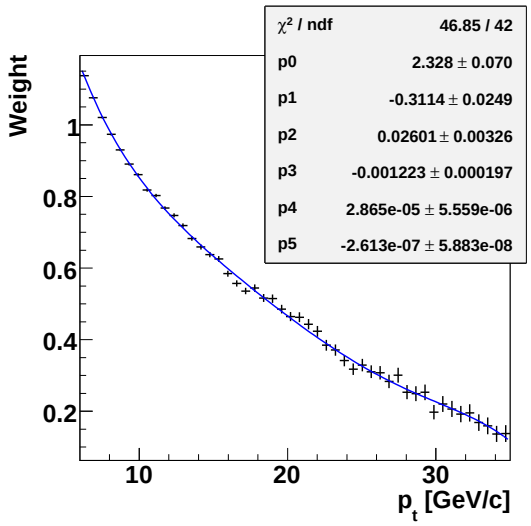

Figure 3.10: Weight function for the Λ_b^0 Monte Carlo samples. The points represent the ratio between generation spectra of B meson and Λ_b^0. The line is a polynomial fit.

applied to the MC samples is written as:

$$f_w(p_T) = F_{Gen}(p_T) \cdot F_I(p_T) \tag{3.14}$$

the function F_{Gen} represents the conditional re-weight function and is shown in Fig. 3.10, together with a polynomial fit. The last factor in (3.14) is the effect of the isolation cut. As announced before we used here the same weight function used in B-mesons, in section 3.8.2, this assumption will be validated on data.

Fast Monte Carlo sample

The CDF Monte Carlo can include the effects of FSR only by enabling the PHOTOS generator [71] . However, PHOTOS (at least in the version included in the CDF simulation) is known to be inaccurate in modeling radiation in heavy-flavor decays at low p_{T}. Therefore, we developed an alternative method based on a Fast Monte Carlo (FMC) [68] that uses recent QED calculation to accurately simulate the FSR effect [72] extensively described in the next chapter (see Cap. 4). The input p_T and η distributions are the same used for the CDF detailed MC.

The samples produced using the parametric simulation in this analysis are mainly used for the mass line shapes and to perform some preliminary checks. The mesons channels ($B^0 \to \pi^+\pi^-$, $B^0 \to K^+\pi^-$, ...) are simulated including the

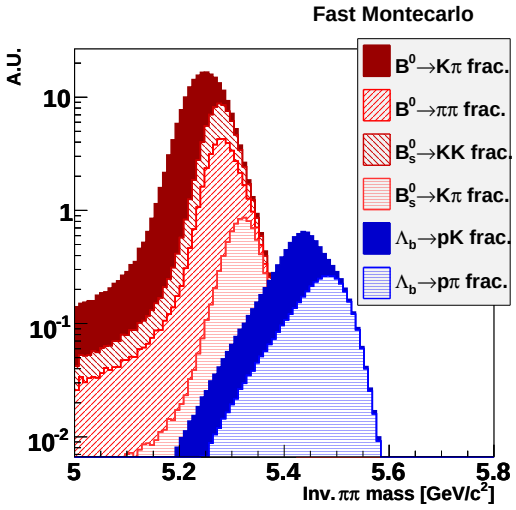

Figure 3.11: Templates for the mass-only fit. Histograms stacks are divided in components according to the fractions of Tab. 3.5.

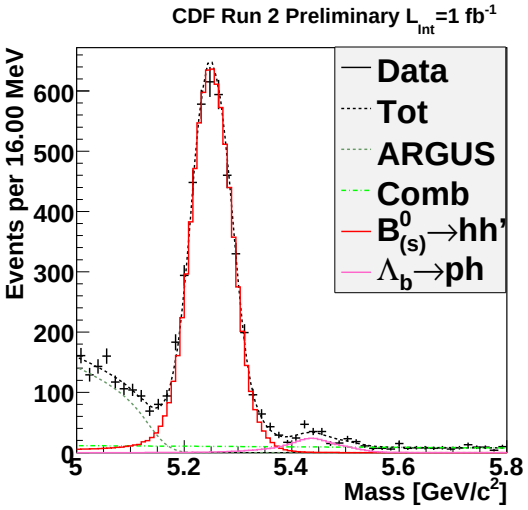

Figure 3.12: Invariant $\pi\pi$-mass distribution with projections resulting from the mass-only fit overlaid (see Tab. 3.6).

FSR effect. The Λ_b^0 decays are instead generated without the radiation effect, this because the formula used in the FMC is not suitable for a decay involving $1/2$ spin particles but also because the effect in this case is expected to be negligible.

3.8.2 Check of the re-weighting

The re-weight for the Λ_b^0 transverse-momentum in (3.14) and the re-weight shown in Fig.3.10 to correct the difference in the generation spectrum were validated on real data.

To extract all the information from the data to check these quantities we used the $_s$Plot technique [73]. To extract the p_T distribution of the different channels, we did a one-dimensional, invariant $\pi\pi$-mass fit; due to the limited power of mode separation available in a mass-only fit, we imposed some extra constraints on relative signal fractions, allowing only the following free parameters:

- the number of $B^0 \to K^+\pi^-$ decays, $N(B^0 \to K^+\pi^-)$;
- the number of $\Lambda_b^0 \to pK^-$ decays, $N(\Lambda_b^0 \to pK^-)$
- the number of mis-reconstructed multi-body decays $N(\text{Argus})$, and the shape parameters for these decays.

Quantity	Input
$\frac{\mathcal{B}(B_s^0 \to K^+K^-)}{\mathcal{B}(B^0 \to K^+\pi^-)}$	0.323
$\frac{\mathcal{B}(B^0 \to \pi^+\pi^-)}{\mathcal{B}(B^0 \to K^+\pi^-)}$	0.277
$\frac{\mathcal{B}(B_s^0 \to K^-\pi^+)}{\mathcal{B}(B^0 \to K^+\pi^-)}$	0.061
$\frac{\mathcal{B}(\Lambda_b^0 \to p\pi^-)}{\mathcal{B}(\Lambda_b^0 \to pK^-)}$	0.69

Table 3.5: Relative fractions used for the mass-only fit.

Quantity	Estimate
Argus yield	938 ± 49
cutoff $[\mathrm{GeV/c^2}]$	5.158 ± 0.001
slope	0.7 ± 3
Combinat. yield	478 ± 86
slope	-0.136 ± 0.036
$B^0 \to K^+\pi^-$ yield	2389 ± 43
$\Lambda_b^0 \to pK^-$ yield	108 ± 15

Table 3.6: Composition of the sample as determined by the mass-only fit.

- the number of combinatoric background events and a parameter for the shape.

The remaining $B^0_{(s)}$ fractions were fixed relatively to the $B^0 \to K^+\pi^-$ using the results of the $B^0_{(s)} \to h^+h'^-$ analysis [70], as well as the fraction of $\Lambda_b^0 \to p\pi^-$ decays relatively to the $\Lambda_b^0 \to pK^-$. The rarest decay channels $B^0 \to K^+K^-$ and $B_s^0 \to \pi^+\pi^-$ were assumed to give negligible contribution. The mass shapes in $\pi\pi$ mass hypothesis were extracted from the Fast MC simulation [68]. Fig. 3.11 shows the pdfs used for the two signal channels: B and Λ_b^0. Each pdf shows relative composition in terms of the single channels. The relative fractions used to constrain the fit parameters are shown in Tab. 3.5.

The fit results are listed in table 3.6 and the projections are shown in Fig. 3.12. The comparison between the p_T distribution extracted from the data using the ${}_s$Plot and the same distributions for a MC sample of a chosen signal are in Fig. 3.13(a) in the B meson case and in 3.13(b) for the Λ_b^0 case.

Fig. 3.13(b) shows that the agreement between data and MC for the Λ_b^0 is good within uncertainties. This indicates that the applied re-weighting (eq.(3.14)) is accurate enough for our purpose.

3.9 Backgrounds

In order to properly include the backgrounds in the fit we treated separately the two main sources: combinatorial and physics backgrounds. The combinatorial background is composed of pairs of independent tracks that randomly satisfy the selection requirement. Its distribution is expected to be nearly constant in invariant mass and its contribution is more visible in the higher-mass sideband of the signal where is the only background component. For an accurate modeling of the kinematic distribution of the combinatorial background, we used the sample of real data

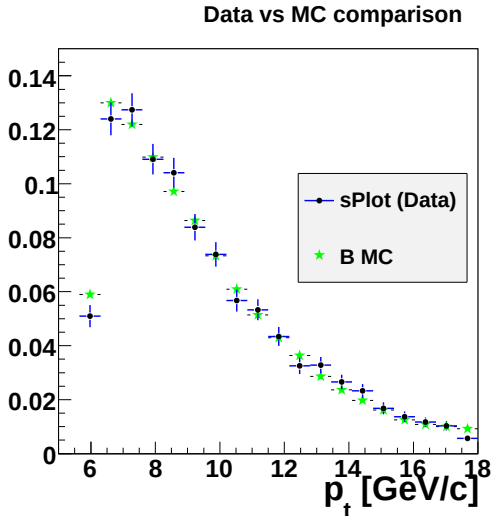

(a) Data-simulation comparison of $p_{\mathrm{T}}(B)$ distributions.

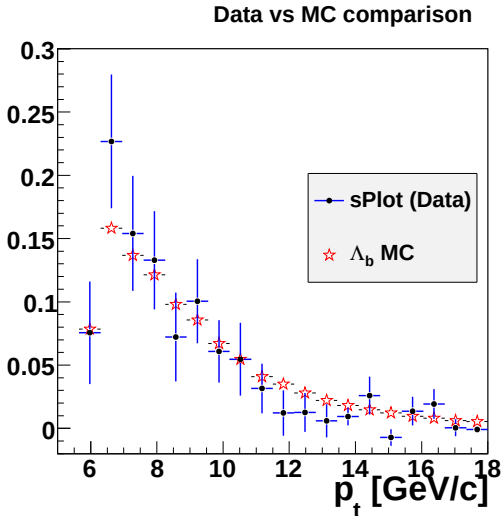

(b) Data-simulation comparison of $p_{\mathrm{T}}(\Lambda_b^0)$ distributions.

Figure 3.13: Comparison of the p_T distribution of B mesons (a) and Λ_b^0 (b) between the standard CDF simulation and data. The data distributions are extracted using the $_s$Plot technique.

selected using the cuts of Tab. 3.3 and 3.4, and adding a $M_{\pi\pi} > 5.6$ requirement, that ensures the selected events being out of the signal region. In addition, the χ^2_{3D} was also removed to increase the statistics, after verifying that this choice does not bias the kinematics distributions: Fig. 3.14, shows the Kolmogorov-Smirnov compatibility between the kinematic distributions of background events selected in different slices of χ^2_{3D}. As already mentioned, the other background source are mis-reconstructed multi-body B decays. Their contribution lies at masses lower than the main $B^0_{(s)} \to h^+h'^-$ peak, forming a shoulder near 5.05 MeV/c^2, probably dominated by partially reconstructed $B \to \rho\pi$ decays. This physical background is modeled using a floating "Argus" function in the fit of composition, as detailed in the following section [67]. The accuracy of this parameterization was verified on simulated $B \to \rho\pi$ decays, in which the $\pi\pi$-assignments was chosen for a pair of the final state tracks.

3.10 Fit templates

The final step to prepare the maximum-likelihood fit is the extraction of the parameterizations of some of p.d.f. functions to be used within the likelihood function. The next sub-sections will describe the extraction of the templates for the mass

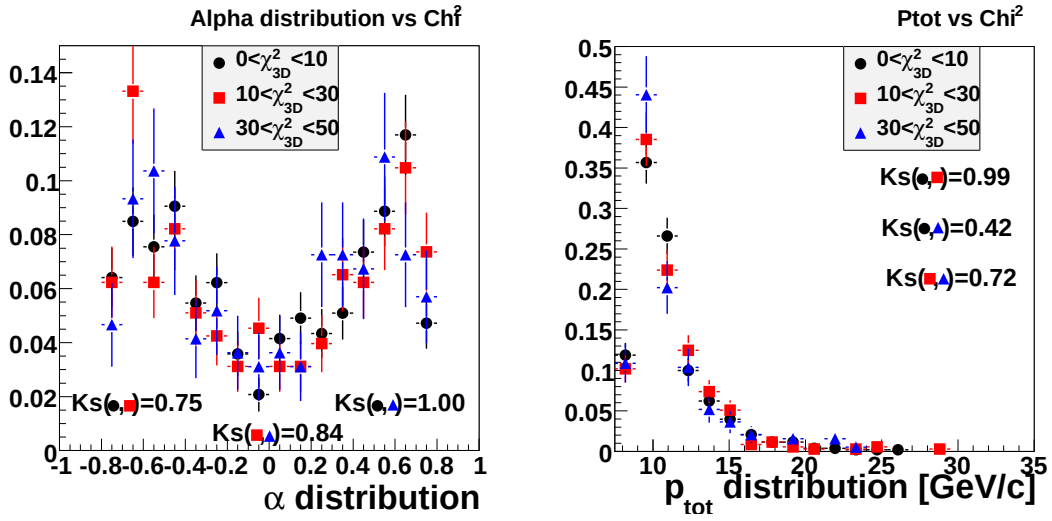

Figure 3.14: Distributions of the momentum imbalance (left) and of the scalar sum of momenta (right) suing background events selected in different χ^2_{3D} slices. The results of a Kolmogorov-Smirnov tests are superimposed.

shapes and momenta distributions, for the signal and the background. Where is not explicit the described CDF Monte Carlo are used, otherwise real, for the signal mass line-shape are instead used a different tool the will be described in next chapter.

3.10.1 Signal kinematics

Mass

The parameterization of the mass line shape requires a particular attention. The main reason is because the signals are so close one to the others, that an uncertainty on a shape can result in a significant uncertainty in the extraction of the relative fraction. So a reliable mass line-shape is very important.

As already noticed before we found instead the CDF Monte Carlo prediction for the mass distribution not in agreement with the data. To solve this, in order to have the p.d.f. for the invariant mass of the signals, I performed a detailed work described in the next chapter. The mass templates will be described at the end of this chapter in Sec. 4.10.

Momentum

The fitter uses the observables α and p_{tot}, for which we need the appropriate templates for each channel.

Note that the α domain is limited by the cuts on p_T. In particular:

$$|\alpha| < \frac{p_{tot} - 2 \cdot p_{T,\min}}{p_{tot} - p_{T,\min}} \tag{3.15}$$

where $p_{T,\min} = 2$ GeV/c is the trigger threshold. So it is convenient to define the variable:

$$\alpha' = \alpha \cdot \frac{p_{tot} - p_{T,\min}}{p_{tot} - 2 \cdot p_{T,\min}} \qquad \alpha' \in [-1, 1] \tag{3.16}$$

whose domain is independent of the value of $p_{\rm tot}$. The model used for the α' distribution is a sum of orthogonal Chebyshev polynomial of type U [74] defined by:

$$T_i(\alpha') = \cos\big(i \arccos(\alpha')\big) \qquad i = 0, 1, \ldots, N \tag{3.17}$$

The α' distribution are thus written as

$$f(\alpha') = N \cdot \left(\frac{\sum_{i=0}^{n} c_i T_i(\alpha')}{I} \right) \tag{3.18}$$

where I is the integral of the sum in the interval $\alpha' \in [-1, 1]$ and is a function only of the c_i coefficients. As a further constrain, we add the condition that the function vanishes at the boundaries:

$$\int_{-1}^{1} f(\alpha') d\alpha' = N, \tag{3.19a}$$

$$f(-1) = f(1) = 0. \tag{3.19b}$$

The α' distribution depends on p_{tot}. Thus the values of N and the c_i coefficients must be function of p_{tot}. We therefore parameterize the shape using a two-dimensional function:

$$\begin{aligned} F(\alpha', p_{tot}) &= N(p_{tot}) \cdot \left(\frac{\sum_{i=0}^{n} c_i(p_{tot}) T_i(\alpha')}{I(p_{tot})} \right) \\ N(p_{tot}) &= \frac{\exp(p_{tot} - a) \cdot \left(\sum_{j=0}^{N_p} p_i \, (p_{tot} - a)^j \right)}{I_p} \\ c_i(p_{tot}) &= \sum_{i=0}^{m} q_i p_{tot}^i \end{aligned} \tag{3.20}$$

I_P is the integral of the polynomial in the appropriate p_{tot} range. The order m is different for each channel, but is between 3 and 5.

The last step of the procedure is to re-transform (α', p_{tot}) to (α, p_{tot}) using the equation:

$$\begin{aligned} pdf(\alpha, p_{tot}) =& k \cdot F(\alpha' \cdot k, p_{tot}) \\ k =& \frac{p_{tot} - p_{T,\min}}{p_{tot} - 2 \cdot p_{T,\min}} \end{aligned} \tag{3.21}$$

To extract the above parameterization we used signal samples generated by the CDF Monte Carlo. The number of parameters needed to model the templates depends on the channel. Typically, a symmetric (i.e. KK or $\pi\pi$) mode needs 8 parameters for $N(p_{tot})$ part and 8 terms in the Chebyshev polynomial for a total of about 24 parameters. Parameterizations of other B or Λ_b^0 decays need more than 30 parameters each.

3.10.2 Background kinematics

For the combinatoric background we used the sample described in Sec. 3.9 while for the multi-prong decays we use a sample of $B^+ \to \rho^0\pi^+$ decays simulated by the CDF Monte Carlo, as described in Sec. 3.8.1.

Mass

The mass shape of background is modeled using a simple straight-line function for the combinatoric background and an Argus function [67] for the physics background resulting from partially- (and mis-)reconstructed B meson decays. The floating parameters are the slope of the line, the fraction of the physics-component with respect to the whole background, the mass cut-off value of the Argus function.

Momenta

We used six parameters for the $N(p_{tot})$ model and six terms for the series. The polynomial to parametrize the $c_i(p_{tot})$ coefficient in this case needs a polynomial of order 8.

The parameterizations results are shown in Figs. 3.15-3.24.

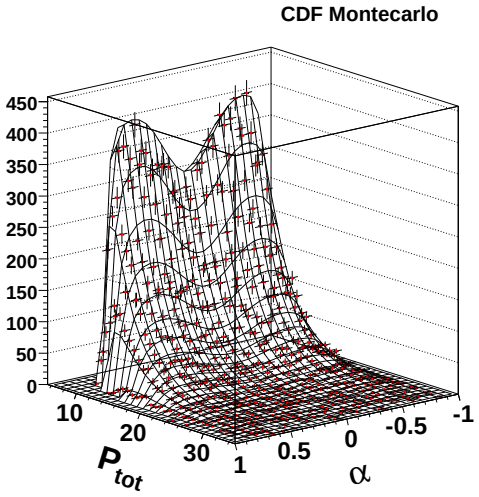

(a) Two-dimensional momentum parameterization. The points are extracted from the CDF Monte Carlo while the surface shows the fit result.

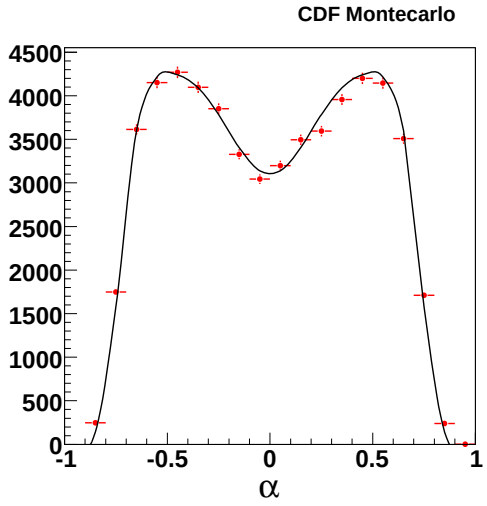

(b) α projection. The points represent CDF Monte Carlo, the line shows the fit result.

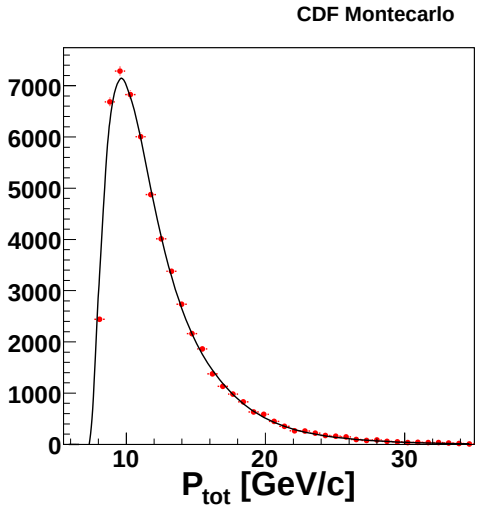

(c) p_{tot} projection. The points represent CDF Monte Carlo, the line shows the fit result.

Figure 3.15: Joint (α, p_{tot}) density for the mode $B^0 \to \pi^+\pi^-$. (a) shows the two-dimensional fit overlaid to the distribution of Monte Carlo data. The bottom plots show the projections of the parameterization in the α axis ((b)), and p_{tot} axis ((c)).

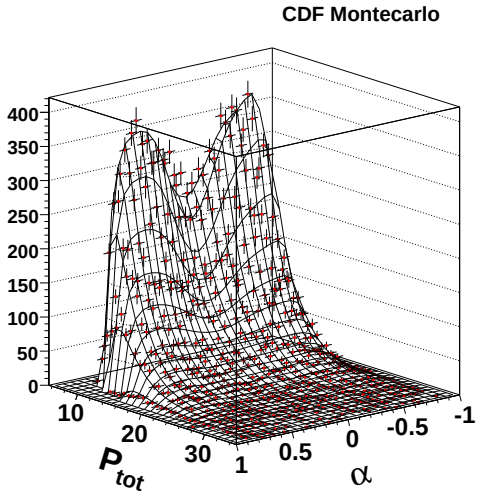

(a) Two-dimensional momentum parameterization. The points are extracted from the CDF Monte Carlo while the surface shows the fit result.

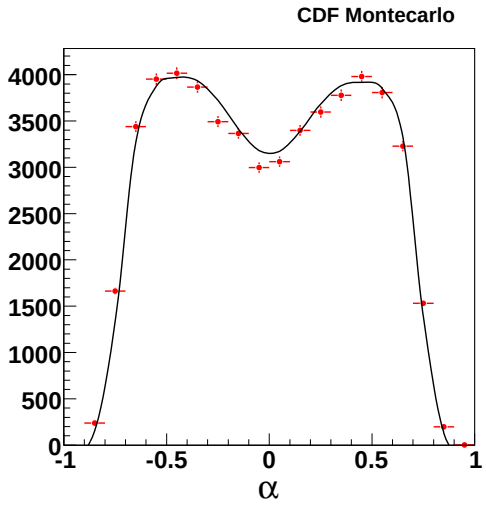

(b) α projection. The points represent CDF Monte Carlo, the line shows the fit result.

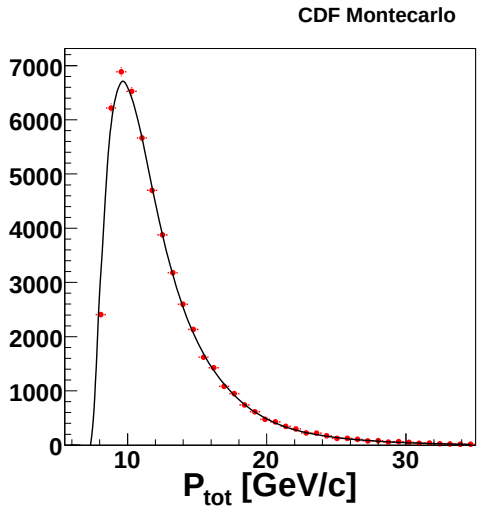

(c) p_{tot} projection. The points represent CDF Monte Carlo, the line shows the fit result.

Figure 3.16: Joint (α, p_{tot}) density for the mode $B^0 \to K^+\pi^-$. (a) shows the two-dimensional fit overlaid to the distribution of Monte Carlo data. The bottom plots show the projections of the parameterization in the α axis ((b)), and p_{tot} axis ((c)).

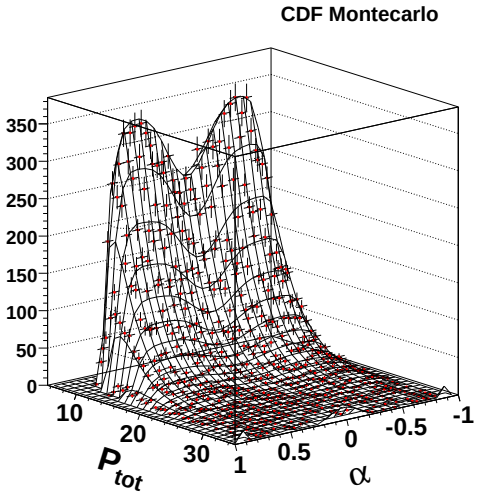

(a) Two-dimensional momentum parameterization. The points are extracted from the CDF Monte Carlo while the surface shows the fit result.

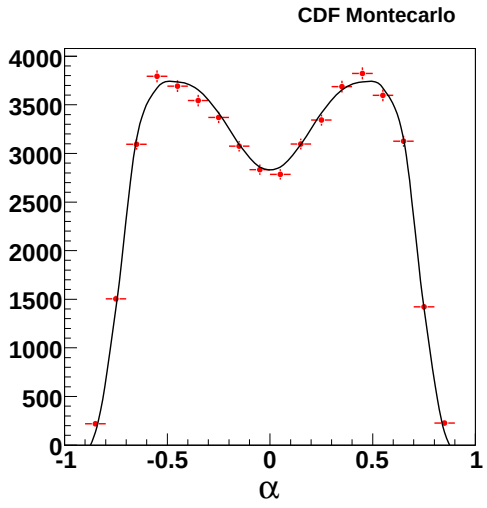

(b) α projection. The points represent CDF Monte Carlo, the line shows the fit result.

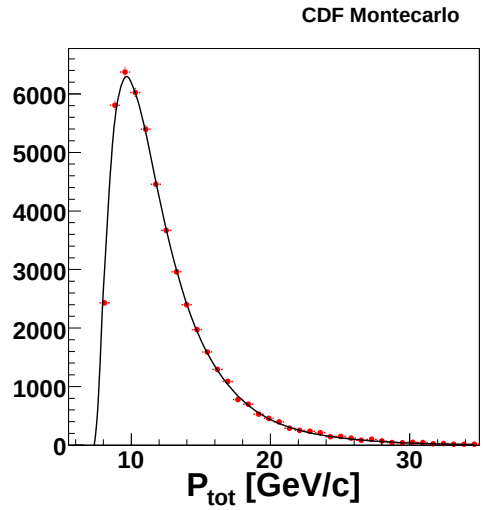

(c) p_{tot} projection. The points represent CDF Monte Carlo, the line shows the fit result.

Figure 3.17: Joint (α, p_{tot}) density for the mode $B^0 \to K^+K^-$. (a) shows the two-dimensional fit overlaid to the distribution of Monte Carlo data. The bottom plots show the projections of the parameterization in the α axis ((b)), and p_{tot} axis ((c)).

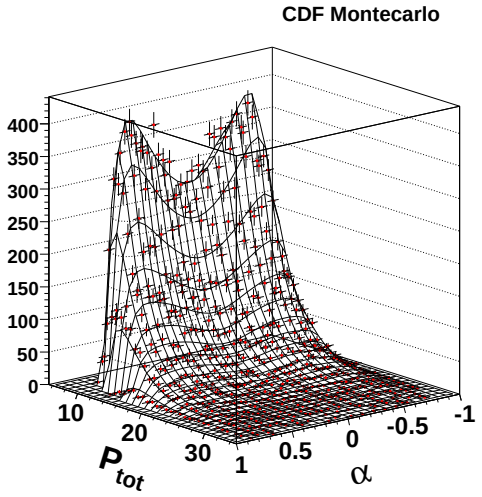

(a) Two-dimensional momentum parameterization. The points are extracted from the CDF Monte Carlo while the surface shows the fit result.

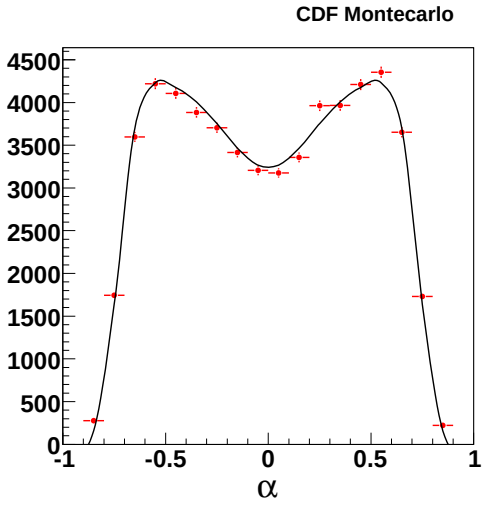

(b) α projection. Points represent CDF Monte Carlo, line the fit result.

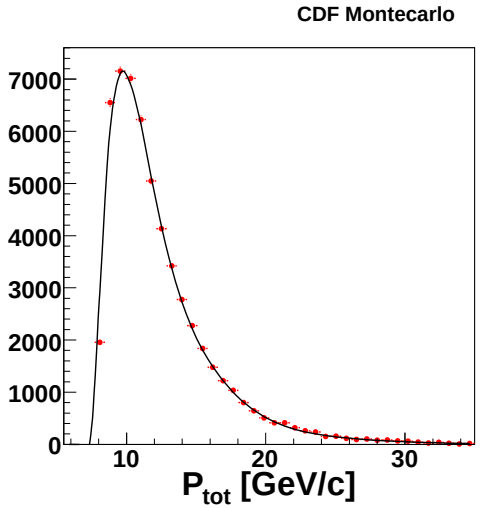

(c) p_{tot} projection. The points represent CDF Monte Carlo, the line shows the fit result.

Figure 3.18: Joint (α, p_{tot}) density for the mode $B_s^0 \to \pi^+\pi^-$. (a) shows the two-dimensional fit overlaid to the distribution of Monte Carlo data. The bottom plots show the projections of the parameterization in the α axis ((b)), and p_{tot} axis ((c)).

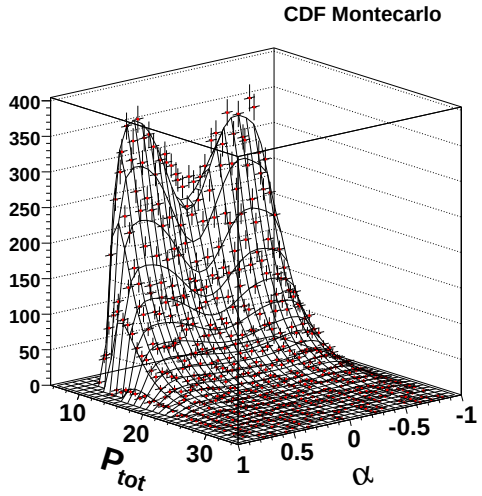

(a) Two-dimensional momentum parameterization. The points are extracted from the CDF Monte Carlo while the surface shows the fit result.

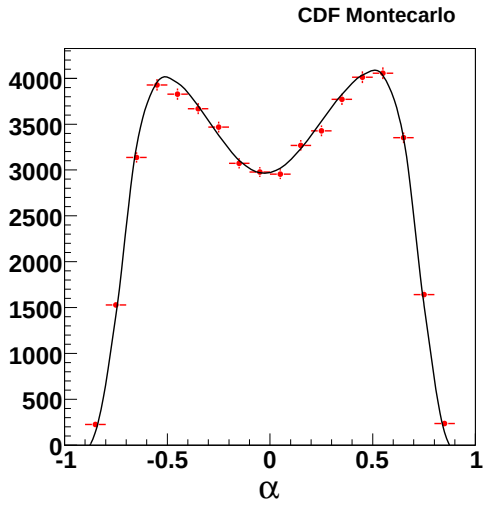

(b) α projection. The points represent CDF Monte Carlo, the line shows the fit result.

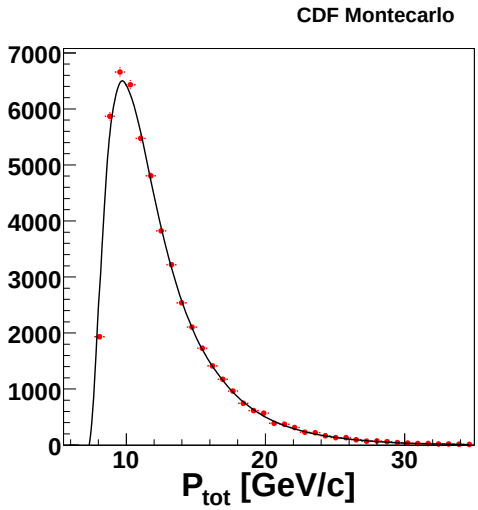

(c) p_{tot} projection. The points represent CDF Monte Carlo, the line shows the fit result.

Figure 3.19: Joint (α, p_{tot}) density for the mode $B_s^0 \to K^-\pi^+$. (a) shows the two-dimensional fit overlaid to the distribution of Monte Carlo data. The bottom plots show the projections of the parameterization in the α axis ((b)), and p_{tot} axis ((c)).

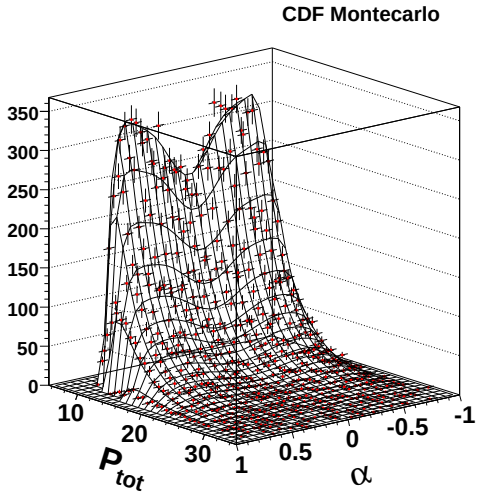

(a) Two-dimensional momentum parameterization. The points are extracted from the CDF Monte Carlo while the surface shows the fit result.

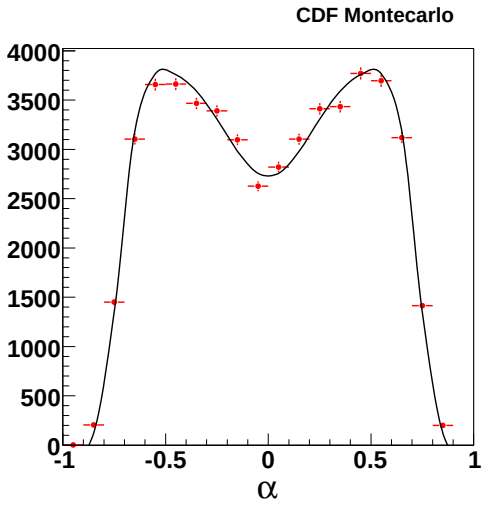

(b) α projection. The points represent CDF Monte Carlo, the line shows the fit result.

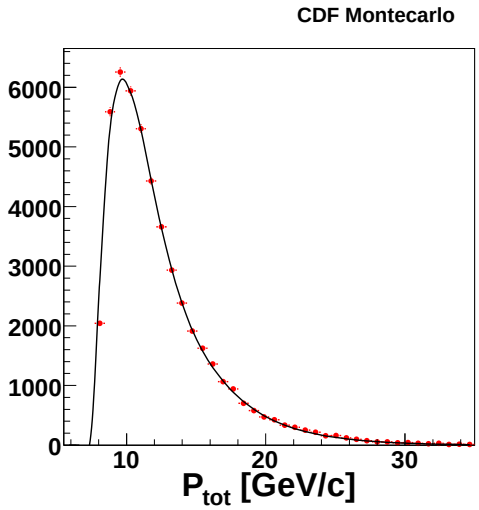

(c) p_{tot} projection. The points represent CDF Monte Carlo, the line shows the fit result.

Figure 3.20: Joint (α, p_{tot}) density for the mode $B_s^0 \to K^+K^-$. Fig. (a) shows the two-dimensional fit overlaid to the distribution of Monte Carlo data. The other two plots show the projections of the parameterization in the α axis (Fig. (b)), and p_{tot} axis (Fig. (c)).

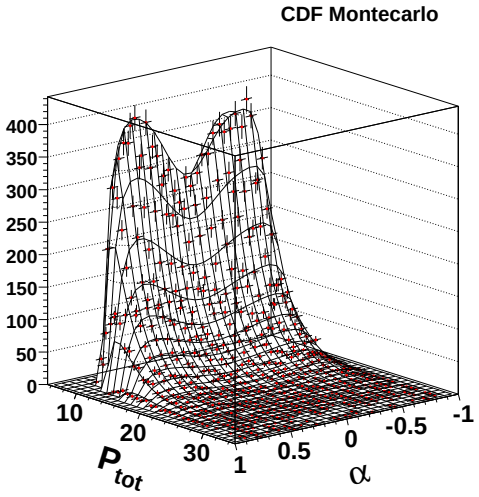

(a) Two-dimensional momentum parameterization. The points are extracted from the CDF Monte Carlo while the surface shows the fit result.

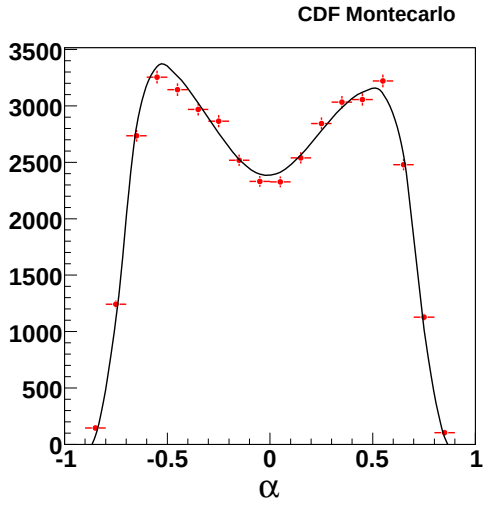

(b) α projection. The points represent CDF Monte Carlo, the line shows the fit result.

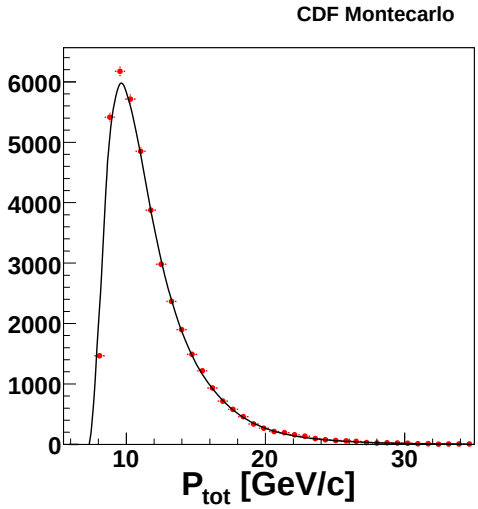

(c) p_{tot} projection. The points represent CDF Monte Carlo, the line shows the fit result.

Figure 3.21: Joint (α, p_{tot}) density for the mode $\Lambda_b^0 \to p\pi^-$. (a) shows the two-dimensional fit overlaid to the distribution of Monte Carlo data. The bottom plots show the projections of the parameterization in the α axis ((b)), and p_{tot} axis ((c)).

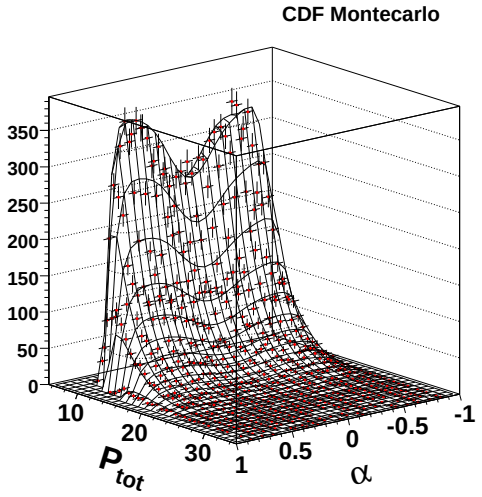

(a) Two-dimensional momentum parameterization. The points are extracted from the CDF Monte Carlo while the surface shows the fit result.

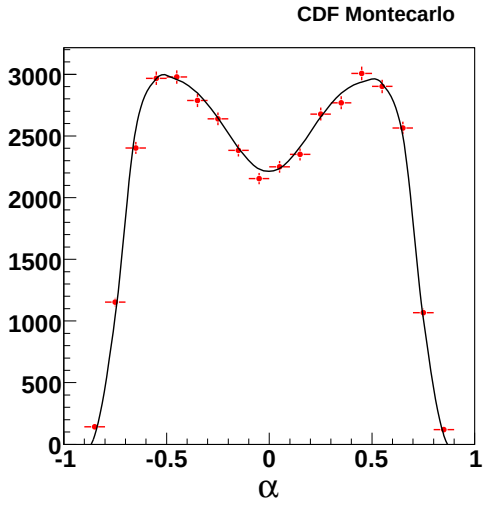

(b) α projection. The points represent CDF Monte Carlo, the line shows the fit result.

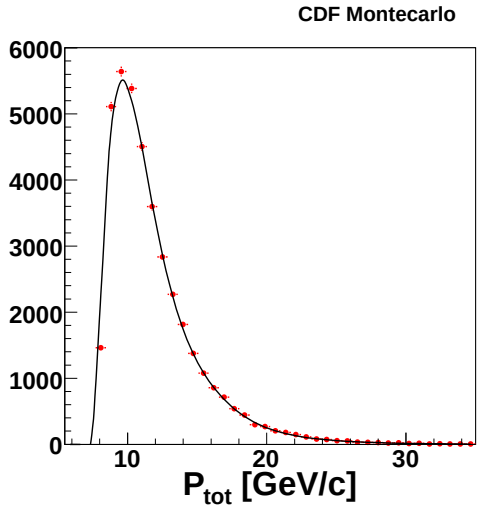

(c) p_{tot} projection. The points represent CDF Monte Carlo, the line shows the fit result.

Figure 3.22: Joint (α, p_{tot}) density for the mode $\Lambda_b^0 \to pK^-$. (a) shows the two-dimensional fit overlaid to the distribution of Monte Carlo data. The bottom plots show the projections of the parameterization in the α axis ((b)), and p_{tot} axis ((c)).

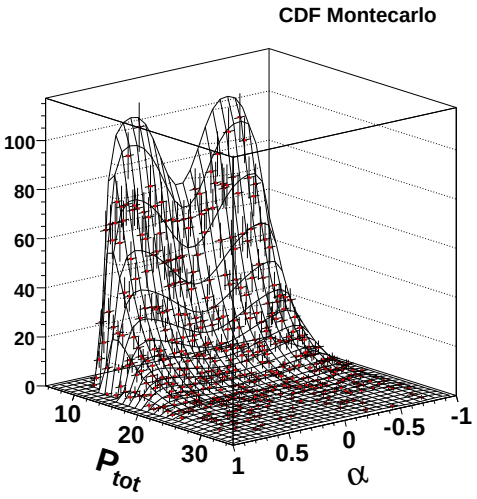

(a) Two-dimensional momentum parameterization. The points are extracted from the CDF Monte Carlo while the surface shows the fit result.

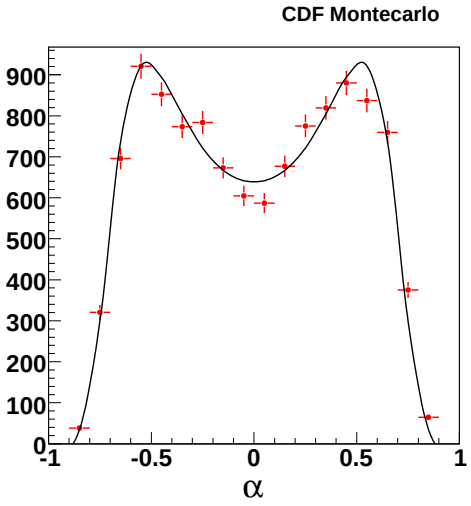

(b) α projection. The points represent CDF Monte Carlo, the line shows the fit result.

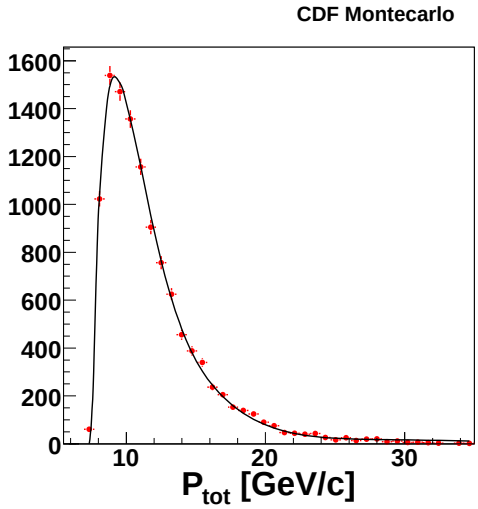

(c) p_{tot} projection. The points represent CDF Monte Carlo, the line shows the fit result.

Figure 3.23: Joint (α, p_{tot}) density for the mode multi-body decays. (a) shows the two-dimensional fit overlaid to the distribution of Monte Carlo data. The bottom plots show the projections of the parameterization in the α axis ((b)), and p_{tot} axis ((c)).

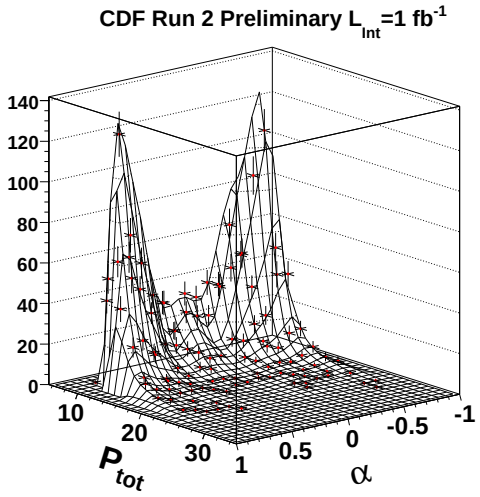

(a) Two-dimensional momentum parameterization. The points are extracted from data with $m_{\pi\pi} > 5.6$ MeV/c^2 while the surface shows the fit result.

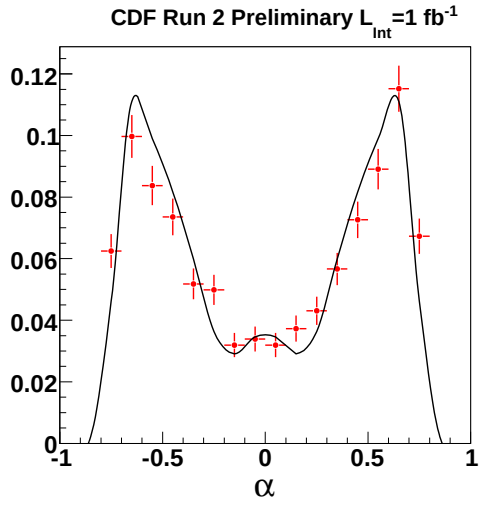

(b) α projection. The points represent data with $m_{\pi\pi} > 5.6$ MeV/c^2, the line shows the fit result.

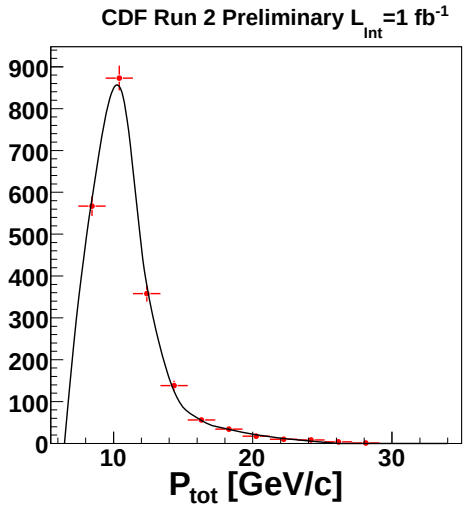

(c) p_{tot} projection. The points represent data with $m_{\pi\pi} > 5.6$ MeV/c^2, the line shows the fit result.

Figure 3.24: Joint (α, p_{tot}) density for the combinatoric background. (a) shows the two-dimensional fit overlaid to the distribution of real data with $m_{\pi\pi} > 5.6$ MeV/c^2. The bottom plots show the projections of the parameterization in the α axis ((b)), and p_{tot} axis ((c)).

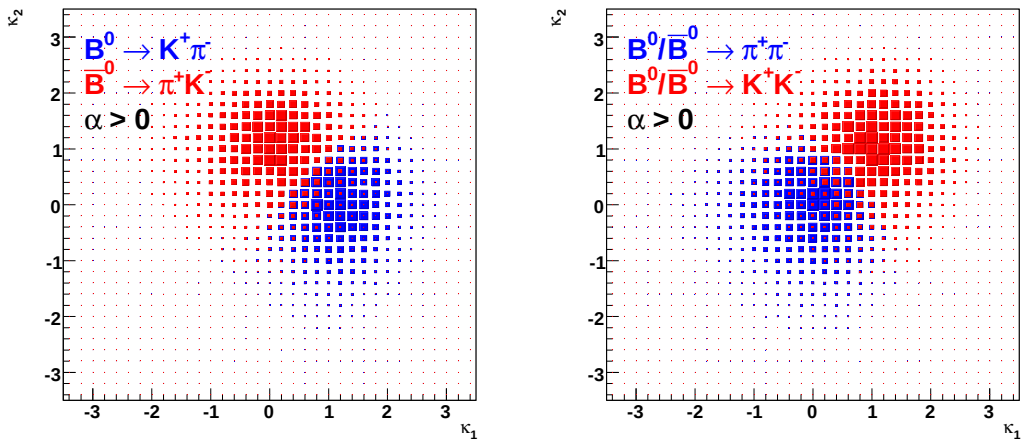

(a) $K\pi$ separation

(b) KK and $\pi\pi$ separation

Figure 3.25: The plots show the bi-dimensional separation for two cases: (a) shows the separation of the K^+-π^- pair with respecte to a π^+-K^- pair, (b) show π^+-π^- and K^+-K^-.

3.10.3 Particle identification templates

The only remaining parameterizations to introduce are the ones related with the particle identification. These functions are the same for the signals and the background and were extracted using calibration samples (Sec. 3.5.1). In the Sec. 3.5.1 was introduced the use of the κ variable defined in (3.8), was also discussed how it is possible to use in the best manner its information to identify the couple of tracks. In particular in (3.11) and (3.12) is exploited the use of a template for the p.d.f. describing the joint probability of both tracks in the decay.

The parameterization for the residual δ (eq. (3.9)) looks for a p.d.f. that is the convolution of a distribution for the single track residual, while a second function represents the distribution of the correlation.

$$\wp(\delta^{\text{obs}}) = \wp(\delta + c) = \wp(\delta) \otimes \wp(c). \tag{3.22}$$

The form used to parameterize the two intrinsic functions is a sum of gaussians, because the convolution calculus is easier than in other cases: for the residuals we needed three Gaussians, while for the correlations two was enough.

We can explicitly calculate the pion-kaon case:

$$\wp\left(\delta_K^{\text{obs}} = \delta_K + c\right) = (gauss_{K'}(\delta_K) + gauss_{K''}(\delta_K) + gauss_{K'''}(\delta_K)) \otimes (gauss_{C'}(c) + gauss_{C''}(c)) \tag{3.23a}$$

$$\wp\left(\delta_\pi^{\text{obs}}\right) = \delta_\pi + c) = (gauss_{\pi'}(\delta_\pi) + gauss_{\pi''}(\delta_\pi) + gauss_{\pi'''}(\delta_\pi)) \otimes (gauss_{C'}(x) + gauss_{C''}(x)) \tag{3.23b}$$

$$\wp\left(\delta_K^{\text{obs}} + \delta_\pi^{\text{obs}}\right) = (gauss_{K'}(\delta_K) + gauss_{K''}(\delta_K) + gauss_{K'''}(\delta_K)) \otimes (gauss_{\pi'}(\delta_\pi) + gauss_{\pi''}(\delta_\pi) + gauss_{\pi'''}(\delta_\pi)) \otimes (gauss_{C'}(2c) + gauss_{C''}(2c)) \tag{3.23c}$$

$$\wp\left(\delta_K^{\text{obs}} - \delta_\pi^{\text{obs}}\right) = (gauss_{K'}(\delta_K) + gauss_{K''}(\delta_K) + gauss_{K'''}(\delta_K)) \otimes (gauss_{\pi'}(-\delta_\pi) + gauss_{\pi''}(-\delta_\pi) + gauss_{\pi'''}(-\delta_\pi)) \tag{3.23d}$$

the sums of Gaussian distributions are through normalized to 1, the normalization parameter for each one is omitted. Using a sample of decays with the final state having kaons and pions is indeed possible to solve all the equations in (3.23).

The plots in 3.26 show the parameterizations used for intrinsic residual for protons, kaons, and pions.

It's also important to note as these parameterization are used to identify the single track but are joined to have the identification of the pairs. Fig 3.25 shows the p.d.f density distributions for the $K^+\pi^-$ pairs with respect the $K^-\pi^+$ and K^+K^- with respect to $\pi^+\pi^-$, these plots can be compared with the single track separation in Fig. 3.6.

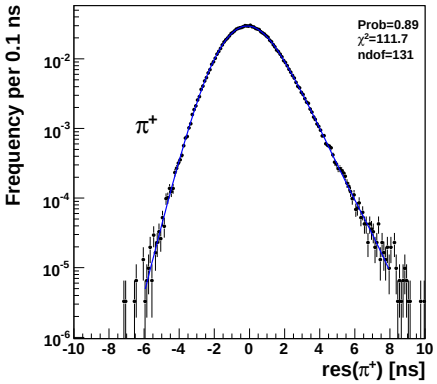

(a) π^+

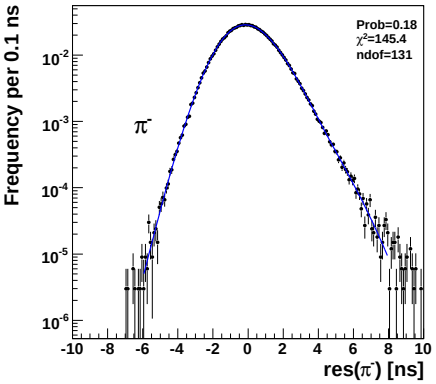

(b) π^-

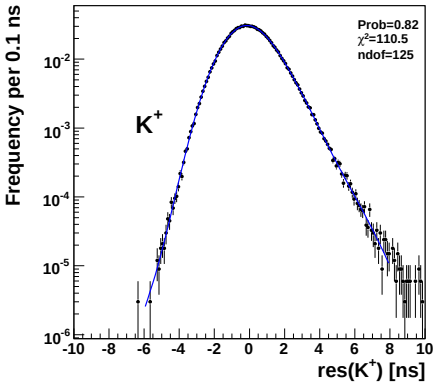

(c) K^+

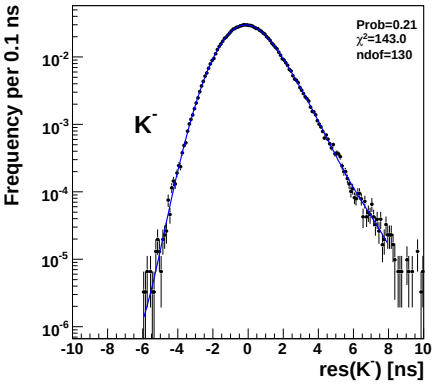

(d) K^-

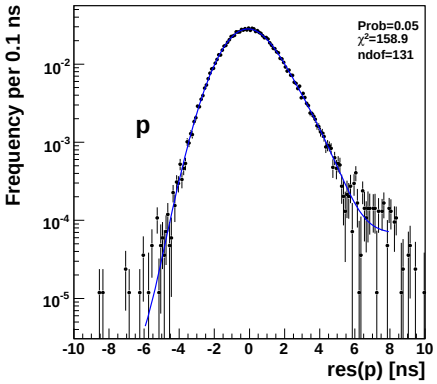

(e) Proton

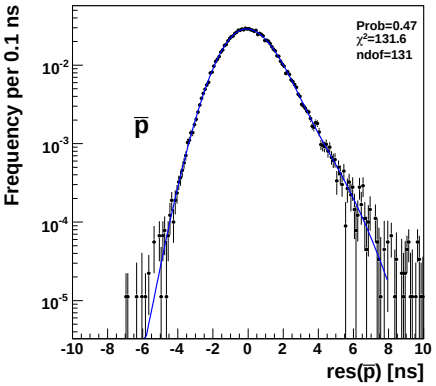

(f) anti-Proton

Figure 3.26: the plots show the observed distribution fitted from the calibration data sample. The fit procedure use the equation in (3.23).

Chapter 4

Detailed mass-shape reconstruction

In the previous chapter I described the issues related with the b-charmless decays extraction. An important aspect is the prediction of the mass shape for each signal. Fig. 3.3 showed plots produced with the CDF II Monte Carlo.

Past studies comparing the CDF Monte Carlo mass resolution to real data found only approximate agreement, with data showing somewhat worse resolution and larger tails [17, 75]. For that reasons some kind of tuning of the simulation was required to reproduce the data. Fig. 4.1 is an example of a fit on a D^0 mass peak, the signal shape is fixed and extracted using the CDF MC, it is possible to see a significant discrepancy between the fit and the data in the low-mass tail. The CDF MC doesn't describe the emission of low-energy photons from the charged particle in the final state, effect called Final State Radiation (FSR). This effect has an additional contribution that distorts the mass distribution at low masses.

The general problem is to have a method to predict, in a satisfactory and reliable way, the mass-shape for a particular decay. The use of this kind of tool is general and can help the most simple analysis and the more complex. For the b-hadron charmless decay analysis the problem has a greater importance because the different decays channels overlaps. A partial knowledge on the mass shape reduces the precision on the relative fraction measurement.

In this chapter I describe the software tool developed to obtain reliable line shapes of invariant mass peaks at least in the simplest and commonest cases. The first ingredient is a simple Monte Carlo describing the kinematics of the decay; the second a detailed parameterization of the resolution functions of individual track parameters; the third ingredient is the simulation of FSR based on accurate formulas from recent QED calculations [76, 72, 77]. These QED formulas are claimed to be more accurate [72, 78], for the applicable decays, of currently available simulations packages like Photos [71] and have been adopted in this work. The idea

is to use this Monte Carlo program to generate distributions of mass and other kinematic variables for resonances that profit of a large data samples collected by the CDF displaced track trigger. The original goal was to have the simplest Monte Carlo, depending on very few parameters; these parameters should then be adjusted to reproduce observed line-shapes in data.

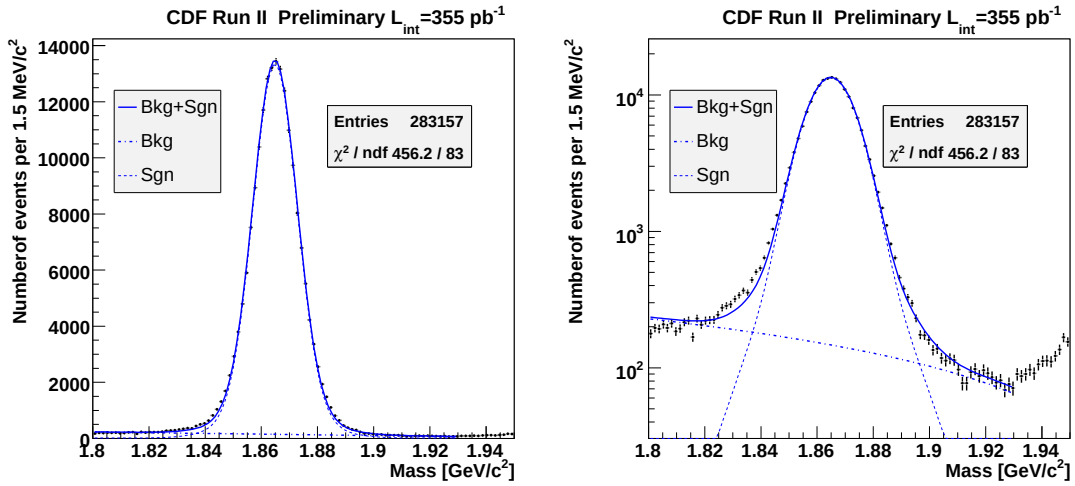

Figure 4.1: The plots show an attempt to the $D^0 \to K^-\pi^+$ fixing the mass template to the CDF MC prediction, that doesn't include the FSR.

This approach is expected to be more reliable than the methods used in the past [17, 55, 54], based on tuning the mass distribution itself on some reference signal, and then trying to extrapolate the results to a different signal. The present approach, instead, is based on tuning the resolution track quantities (e.g. track curvature) and it is independent from the chosen reference signal. This approach guarantees a reliable extrapolation to the mass line shape of interest, since the invariant mass resolution depends on these quantities in the same way for each decay mode, given the momentum distribution and the mass of mother particle.

A secondary but not negligible advantage of the use of this fully parametric simulation is the much lower CPU time needed to generate the necessary high-statistics, compared to the standard CDF Monte Carlo.

4.1 Invariant mass distribution from CDF II simulation

The invariant mass distribution returned from CDF II simulation, despite the small discrepancies in the tails of the hadronic modes was proved precise in other

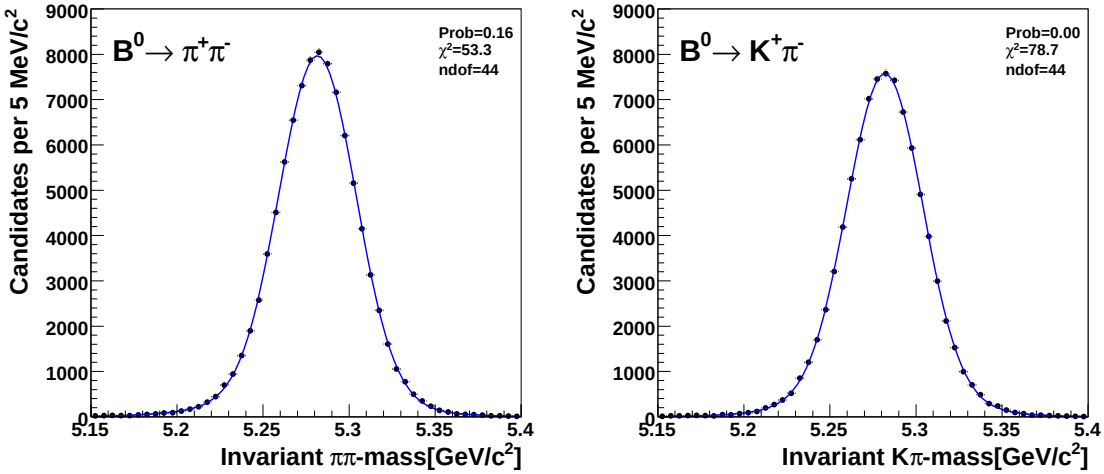

Figure 4.2: The plots show the invariant mass distribution extracted from the CDF II detailed MC. The left plot shows the distribution fro the $B^0 \to \pi\pi$ while the $B^0 \to K\pi$ signal is in the right plot. The points represent the MC results and don't contain the FSR effect, the function overlaid is in the form of (4.1), the parameters are extracted using a fit.

decays. For this the CDF MC is considered enough to preliminary understand how to parameterize the mass resolution and bias independent from the radiative effect. For these reasons we started the mass line-shape using for simulated $B^0_{(s)} \to h^+h'^-$ decays that are also out final goal. The FSR has not been introduced in the CDF II simulation, since in the current version this task can be performed only using Photos[71], that was found not to be accurate B and D hadronic decays.

Fig. 4.2 shows two examples of simulated invariant mass distributions of single signal modes. The distributions are computed assigning the correct mass hypothesis and are fitted using a sum of two Gaussians:

$$f(m; N, f_1, \mu_1, \sigma_1, \mu_2, \sigma_2) = N \cdot \left[f_1 \frac{1}{\sqrt{2\pi}\sigma_1} e^{-\frac{1}{2}\left(\frac{m-\mu_1}{\sigma_1}\right)^2} + (1-f_1) \frac{1}{\sqrt{2\pi}\sigma_2} e^{-\frac{1}{2}\left(\frac{m-\mu_2}{\sigma_2}\right)^2} \right] \tag{4.1}$$

where the means of the two Gaussians, μ_1 and μ_2, the standard deviations, σ_1 and σ_2, the relative fraction of the first Gaussian with respect to the second one, f_1, and the absolute normalization N, are determined by the fit. A similar shape was found for all the charmless decay modes generated with the CDF II Monte Carlo, the result for the fits of each mode are summarized in Tab .4.1. The non-Gaussian model for the signal peak, also without the inclusion of the radiative

mode	f_1 [%]	$\hat{\mu}$ $[GeV/c^2]$ μ_1 $[GeV/c^2]$ μ_2 $[GeV/c^2]$	 σ_1 $[GeV/c^2]$ σ_2 $[GeV/c^2]$
$B^0 \to \pi\pi$	89.3 ± 0.8	5280.9 ± 0.1	
		5281.7 ± 0.1	21.8 ± 0.1
		5274.5 ± 0.7	44.6 ± 1.1
$B^0 \to K\pi$	89.3 ± 1.2	5281.5 ± 0.1	
		5281.9 ± 0.1	21.6 ± 0.2
		5277.8 ± 0.8	41.7 ± 1.3
$B^0 \to KK$	89.6 ± 1.2	5282.2 ± 0.1	
		5282.1 ± 0.1	21.1 ± 0.2
		5282.8 ± 0.7	39.3 ± 1.2
$B_s^0 \to \pi\pi$	89.1 ± 0.9	5371.1 ± 0.1	
		5371.9 ± 0.1	22.2 ± 0.1
		5364.9 ± 0.8	44.8 ± 1.2
$B_s^0 \to K\pi$	88.0 ± 1.2	5372.0 ± 0.1	
		5372.3 ± 0.1	21.8 ± 0.2
		5369.4 ± 0.7	40.6 ± 1.1
$B_s^0 \to KK$	89.8 ± 1.2	5372.3 ± 0.1	
		5372.3 ± 0.1	21.6 ± 0.2
		5372.6 ± 0.7	40.7 ± 1.3
$\Lambda_b^0 \to p\pi^-$	90.4 ± 0.9	5626.2 ± 0.1	
		5624.9 ± 0.1	22.1 ± 0.1
		5623.4 ± 0.7	44.9 ± 1.4
$\Lambda_b^0 \to pK^-$	89.3 ± 1.3	5626.8 ± 0.1	
		5626.8 ± 0.1	21.7 ± 0.2
		5627.6 ± 0.7	40.2 ± 1.3

Table 4.1: Fit results on the invariant mass distribution for the simulated modes computed with the correct mass assignment for both particles. Every loss correction was performed using the pion hypothesis for both tracks.

corrections, is expected also from data analysis. In all the modes a dominant Gaussian component of about 89% and with a width of about 22 MeV/c^2 was found.

4.1.1 Re-fitting bias

In the two-Gaussians model described in 4.1 μ_1 and μ_2 are not constrained and are in general different; for this reasons we also quoted $\hat{\mu} = f_1\mu_1 + (1 - f_2)\mu_2$,

mode	m [MeV/c^2]
B^+	5279.0
B^0	5279.4
$B_s^0 \to \pi\pi$	5369.6
$B_s^0 \to K\pi$	5369.6
$B_s^0 \to KK$	5369.6
Λ_b^0	5624.0

Table 4.2: Summary of the input masses in the simulation.

mode	$\pi\pi$ (a)	correct (b)	δ_{Kal} (c)
$B^0 \to \pi\pi$	5280.9 ± 0.1	5280.9 ± 0.1	–
$B^0 \to K\pi$	5281.5 ± 0.1	5280.4 ± 0.1	1.1
$B^0 \to KK$	5282.2 ± 0.1	5280.1 ± 0.1	2.1
$B_s^0 \to \pi\pi$	5371.1 ± 0.1	5371.1 ± 0.1	–
$B_s^0 \to K\pi$	5372.0 ± 0.1	5370.9 ± 0.1	1.1
$B_s^0 \to KK$	5372.3 ± 0.1	5370.2 ± 0.1	2.1
$\Lambda_b^0 \to p\pi^-$	5626.2 ± 0.1	5624.5 ± 0.1	1.7
$\Lambda_b^0 \to pK^-$	5626.8 ± 0.1	5624.2 ± 0.1	2.6

Table 4.3: Mean value $\hat{\mu}$ of invariant mass in simulated events. All masses in the table are computed using the correct mass hypothesis for both tracks. Both tracks are processed with pion mass assignment (a), with correct mass assignment to compensate the energy losses in the material (b). Invariant mass shift δ_{Kal} due to the uncorrected mass assignment in the refitting (c)=(a)-(b). The unit is MeV/c^2.

reported in the last column of Tab 4.1, to estimate the average of the invariant mass distribution for each signal mode. By the comparison between $\hat{\mu}$ and the input mass values reported in Tab. 4.2 of the simulation we observed a slight (but non negligible) discrepancy. Such a discrepancy, $\mathcal{O}(2-3$ MeV/$c^2)$, can be explained with a wrong correction applied in some cases.

To better understand the reason for this bias we can look how the Monte Carlo simulation performs the track propagation and the following reconstruction, this can be divided into two logical steps: in the first the events are generated and the final state tracks are processed to simulate the propagation of the particles in the detector material. All silicon layers, all wires in the drift chamber and every part of the detector are simulated accurately. In the second step, the simulated events are reconstructed, like real data, by the off-line reconstruction code. This off-line code applies a track by track correction for the energy lost in the material and other constraints suggested by the decay topology (e.g. vertex constraints).

The energy corrections, in particular, to be applied needs of mass hypothesis,

and in the real and MC samples each tracks is treated as a pion. This assumption is arbitrary; in the modes in which not both tracks are pions this assumption produce a bias in curvature fit that become a systematic bias in the mass peak position. The bias value can be measured by reprocessing the simulated events with the correct mass hypothesis for both tracks (see Tab 4.3), as, in this case, we know events by events the correct particle assignment. From the difference between the simulated events processed, first with the pion mass hypothesis for both tracks (like the real data), and second with the exact mass hypothesis for both tracks we obtain the mass shift due to this effect. This information will be used in the fit of composition (Sec. 3.3) to cancel out the bias on the mass difference between signals.

Even, when tracks are refitted using the correct mass hypothesis and the energy losses are compensated correctly (see column (c) of Tab. 4.3) an additional residual shift from the input values still remains. This residual shift depends on several factors. This appears only in the simulated samples but not when we process real data. The compensation of energy losses in the material was tuned accurately using large sample of real data $K^0_s \to \pi^+\pi^-$, $B^\pm \to J/\psi K^\pm$, $J/\psi \to \mu^+\mu^-$ and $\Upsilon(4S) \to \mu^+\mu^-$ decays [79, 80], so that the absolute mass scale in the data is reproduced accurately. When, instead, we process the simulated events, using the off-line code tuned on real data, we put in evidence that the energy losses in the material are not reproduced by the CDF Monte Carlo within the precision level obtained with real data. This discrepancy depends on particle mass and it is large about ≈ 2 MeV/c^2 for $B^0 \to \pi\pi$ mode and it becomes ≈ 0.2 MeV/c^2 for $\Lambda^0_b \to pK^-$ mode.

This residual discrepancy does not affect the fit of composition of real data (see Sec. 4.10) and we will not apply any correction, we will use as input masses the masses measured by CDF in run II [79]. Using the masses measured with the same apparatus and reconstruction code as for $B^0_{(s)} \to h^+h'^-$ data allows the cancellation of common systematic uncertainties due to a possible overall shift of the CDF II mass scale.

4.2 Fast Monte Carlo Simulation (FMC)

The parametric Monte Carlo took the name of *Fast Monte Carlo Simulation* (FMC). It is developed as a C++ library integrated with the ROOT framework[81].

The code has two main nodes:

MassResToy: this is the main class, the core of the FMC: it collects the tracks generated in the simulated events, parametrizes the detector measurements and stores the simulated data in an external file;

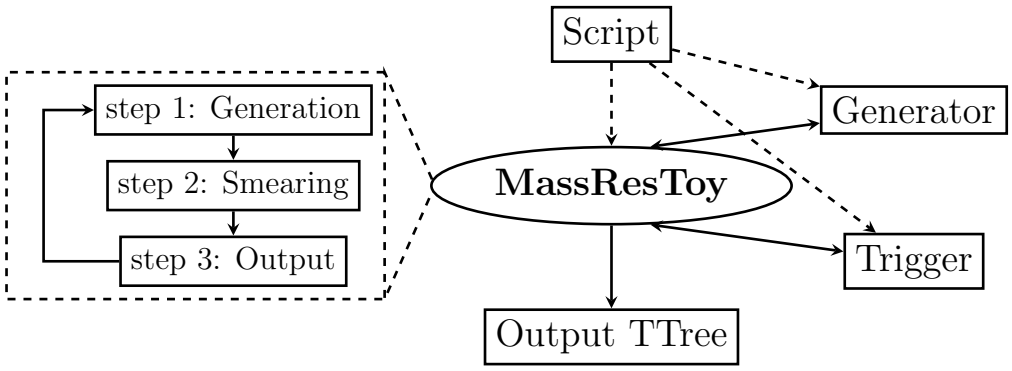

Figure 4.3: Fast Monte Carlo working scheme. It shows the interconnection between the main classes. The "Script" will choose and setup the "Trigger" and "Generator" classes, connecting them to the "MassResToy". The "MassResToy" node calls at any iteration the object to to generate and filter the events. A more detailed scheme for the internal loop of the "MassResToy" is also shown.

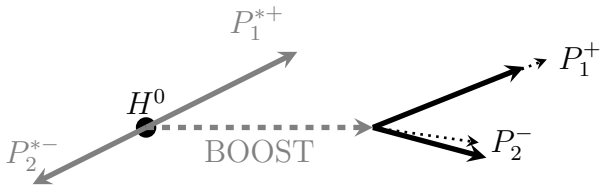

Figure 4.4: Scheme of the generation of a two body decay in the FMC. The cartoon shows how the decay is generated in the center-of-mass system, propagated according the initial energy. Then the stable tracks, the dotted lines, are smeared in the principal parameters by the FMC.

Generator: this kind of object generates a particular decay and provides the tracks to the MassResToy;

the objects are controlled within a ROOT session. The default parameters can be modified to generate many kind of decays.

The Fig. 4.4 shows an example of a two body decay generation . The scheme is common to the other decay generators: the particle H^0 is decayed in its rest frame. Then the three-dimensional momenta of decay products $\vec{P}_1^*$ and $\vec{P}_2^*$ are boosted to obtain the corresponding quantities in the laboratory frame ($\vec{P}_1$ and $\vec{P}_2$) according to the two-dimensional distribution of the particle H in rapidity and transverse momentum in the laboratory frame. In the case of the b-meson we used a flat rapidity distribution in the range $|y(B)| < 1.3$, as I did for the CDF Monte Carlo samples (see Sec. 3.8.1 at pag. 61); the $p_{\mathrm{T}}(B)$ input distribution was taken from an the data published in CDF Run II measurement [23]. This is the same

procedure adopted by the the official CDF Monte Carlo.

The track parameters in the laboratory frame are smeared according the appropriate resolution. The resolution functions are crucial tunable parameters of the FMC. Our strategy consists in:

1. tuning the resolution functions of the FMC using the information from the CDF Monte Carlo;

2. implementing the FSR into the FMC;

3. comparing the FMC with some reference signal from real data (i.e. $D^0 \to K^-\pi^+$ decays);

4. in case of discrepancy between FMC and this reference signal, performing a finer tuning of resolution functions to reproduce the real data.

5. generate the $B^0_{(s)} \to h^+h'^-$ templates are need from the tuned Monte Carlo.

the 4th step was not necessary, as I will show next in this chapter, Sec. 4.8.

4.3 Resolution function for curvature (k)

The trajectory of a particle with momentum p and charge Ze in a constant magnetic field $\vec{B}$ is a helix, with radius of curvature R and pitch angle θ ($\lambda = \cot\theta$)[1]. The radius of curvature and momentum component perpendicular to $\vec{B}$ are related by:

$$p\sin(\theta) = 0.3ZBR, \tag{4.2}$$

where p is GeV/c, B is in Tesla and R in meters. If the distribution of the measurements of the curvature $k \equiv 1/R$ is approximately Gaussian, the curvature error for a large number of uniformly spaced measurements on the trajectory of a charged particle in a uniform magnetic field can be approximately by

$$(\delta k)^2 = (\delta k_{\rm res})^2 + (\delta k_{\rm ms})^2, \tag{4.3}$$

where δk is the total curvature uncertainty, $\delta k_{\rm res}$ is the curvature uncertainty due to finite measurement resolution and $\delta k_{\rm ms}$ is the curvature uncertainty due to the multiple scattering.

[1] $\lambda = \cot(\theta)$ is the helix pitch, where θ is the polar direction of the particle at the point of its closest approach to the z-axis. This is directly related to the longitudinal component of the momentum: $p_z = p_{\rm T}\cot(\theta)$

If many ($\geq$ 10) uniformly spaced position measurements are made along a trajectory in a uniform medium [10]

$$\delta k_{\rm res} = \frac{\epsilon}{L'^2}\sqrt{\frac{720}{N+4}} \simeq \text{constant}, \tag{4.4}$$

where N is the number of points measured along the track, L' is the projected length of the track into the bending plane and ϵ is the measurement error for each point, perpendicular to the trajectory. If a vertex constraint is applied at the origin of the track, the coefficient under the square root becomes 320. $\delta k_{\rm res}$ is independent of the curvature.

The contribution due to the multiple Coulomb scattering is approximately [10]

$$\delta k_{\rm ms} \approx \frac{(0.16)(\text{GeV}/c)Z}{Lp\beta\ \sin^2\theta}\sqrt{\frac{L}{X_0}} \propto \frac{k}{\beta\sin\theta}, \tag{4.5}$$

where p is the momentum in GeV/c, Z is the charge of the incident particle in units of e, L is the total track length, X_0 is the radiation length of the scattering medium (in units of length) and β is the kinematic variable v/c. $\delta k_{\rm ms}$ can be considered approximately proportional to the curvature k, since for pions and kaons with transverse momentum greater than 2 GeV/c $\beta \approx 1$, and for protons $\beta > .9$, the pseudo-rapidity of both tracks is $|\eta| < 1$, namely $\sin\theta > 0.648$ with $< \sin\theta >= 0.91$. Then the contribution due to the multiple Coulomb scattering is approximated as:

$$\delta k_{\rm ms} \approx \text{constant} \cdot k. \tag{4.6}$$

Therefore, in our sample, the curvature uncertainty can be parameterized by the approximate formula:

$$\delta k \approx A \cdot \sqrt{1 + B \cdot k^2}. \tag{4.7}$$

where A and B are parameters to be determined.

Using the MC we can access simultaneously the distributions of the smeared quantities after the full simulation chain of the detector and the "true" quantities before the experimental smearing. We used a sample of 10M generated events of $B^0 \to \pi\pi$, $B^0 \to K\pi$ and $B^0 \to KK$ modes (see Sec. 3.8.1), yielding about 80,000 events of each mode after the selections (trigger and off-line reconstruction). The specific decay or mode has no particular relevance in this context, and we used the whole sample of tracks as a single sample. The Fig. 4.5 shows the curvature residual $r = k - k_t$, where k is the smeared curvature and k_t is the true curvature, as a function of k_t, for both negative and positive tracks. The curvature resolution depends on the curvature value, and we fitted the distribution of the variable r in 10 k_t slices using a single Gaussian distribution:

$$N_k \cdot G(r;\mu_k,\sigma_k) = N_k \cdot \frac{1}{\sqrt{2\pi}\sigma_k}\ e^{-\frac{1}{2}\left(\frac{r-\mu_k}{\sigma_k}\right)^2}, \tag{4.8}$$

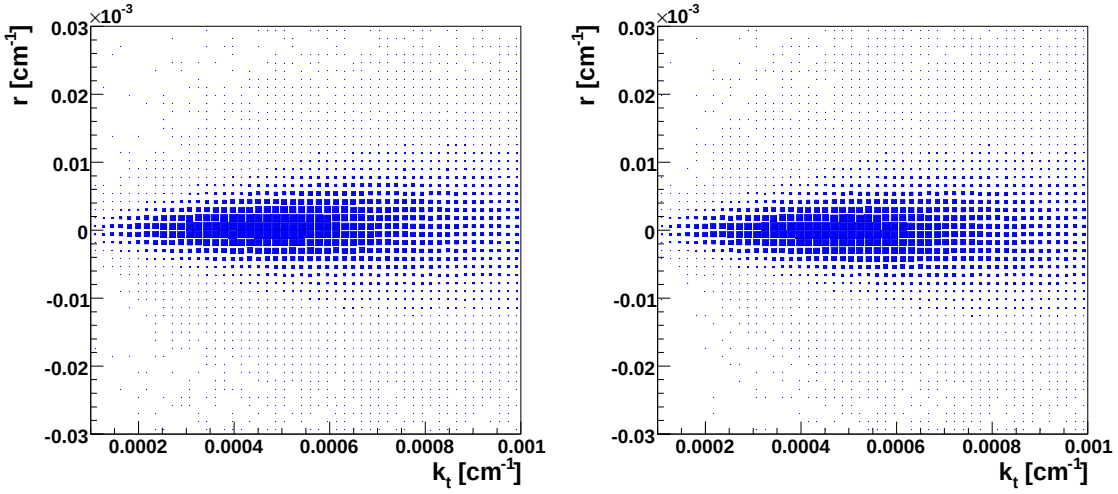

(a) Negative curvature

(b) Positive curvature

Figure 4.5: Curvature residual as a function of the true curvature of the simulated events for $B^0 \to \pi\pi$, $B^0 \to K\pi$ and $B^0 \to KK$ modes. Negative tracks (a), positive tracks (b).

where N_k is the absolute normalization, μ_k and σ_k are respectively the mean and the standard deviation of the Gaussian. The resulting values of σ_k are reported in Fig. 4.6 and are fitted with the function described in (4.7) as a function of k_t. A and B are extracted from these fits separately for negative and positive tracks. $\chi^2/\text{ndof} = 12.4/8$ and $\chi^2/\text{ndof} = 8.2/8$ demonstrate the goodness of the model in (4.7).

The model with a single Gaussian is sufficient to reproduce the relationship between the δk and k but it is not sensitive to possible non-Gaussian deviations of the curvature resolution function. We know from Tab. 4.1 that we expect deviations of order 10%. To parameterize the non-Gaussian tails of the curvature resolution, we chose to extract the distribution of the variable r':

$$r' = \frac{k - k_t}{\sigma_k(k_t)} = \frac{r}{\sigma_k(k_t)}. \tag{4.9}$$

this variable is independent from the true curvature k_t and it allows to parameterize the non-Gaussian effects in a single fit. Fig. 4.7 reports the distribution of the r' variable. Three Gaussians are necessary to achieve a good parameterization of

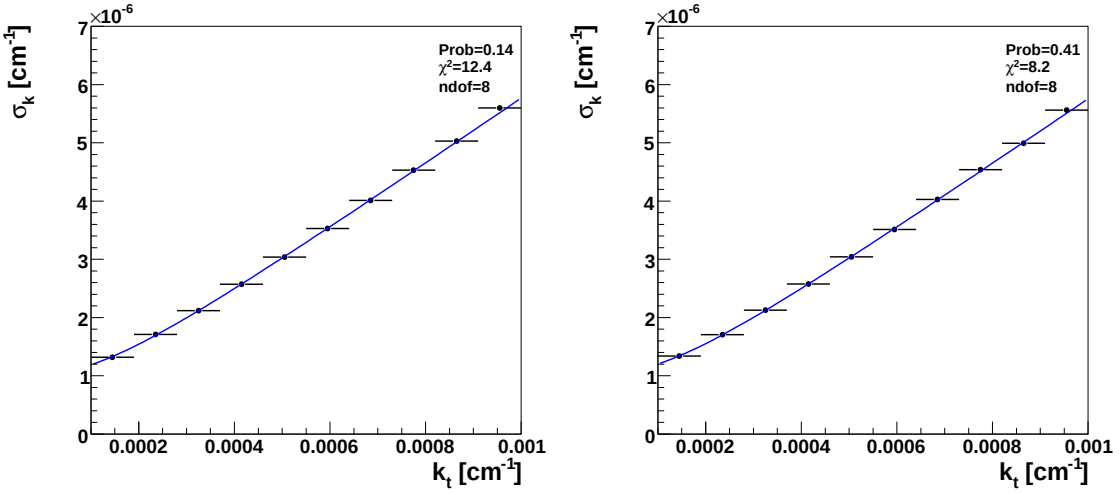

(a) (b)

Figure 4.6: Curvature uncertainty as a function of the true curvature for simulated events of $B^0 \to \pi\pi$, $B^0 \to K\pi$ and $B^0 \to KK$ modes. (a) Negative tracks, (b)positive tracks.

these functions:

$$N'_k \cdot \Big[f_1 \; gauss(r'; \mu'_{k1}, \sigma'_{k1}) + f_2 \; gauss(r'; \mu'_{k2}, \sigma'_{k2}) + (1 - f_1 - f_2) \; gauss(r'; \mu'_{k3}, \sigma'_{k3}) \Big]. \tag{4.10}$$

where N'_k is the absolute normalization, $f_{1(2)}$ is the relative fraction of the first (second) Gaussian and μ'_{ki} and σ'_{ki} are respectively the mean and the standard deviation of the i^{th} Gaussian.

In our FMC simulation, we first smeared the r' variable according to the parameters f_i, μ_{ki} and σ_{ki} of the triple Gaussian extracted, and then changed variable $r' \to r$ to obtain the smeared curvature k. We performed two independent smearings for negative and positive tracks.

We verified that the curvature resolution depends mainly on the curvature k and the effect of λ and ϕ_0 dependences are much smaller. They have a negligible influence on the invariant mass distribution, thus their effect on the curvature resolution was neglected.

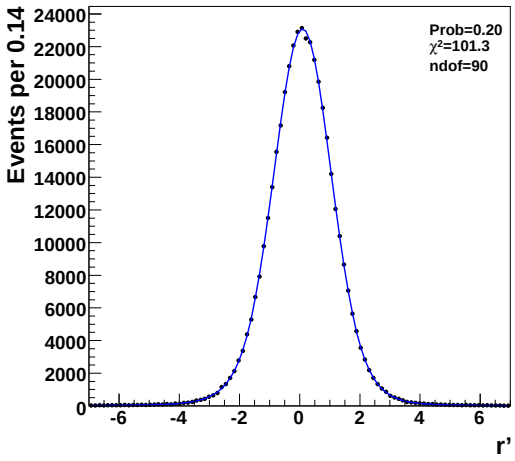

(a) Negative charge

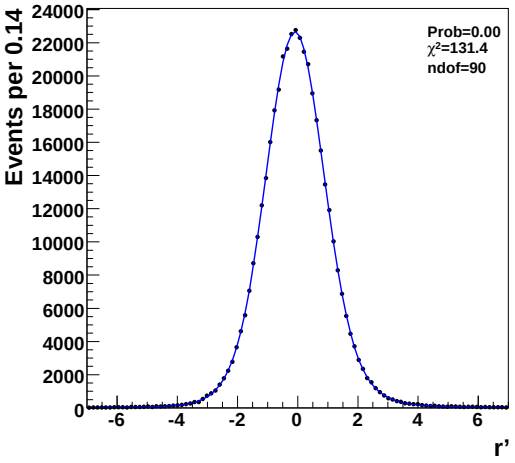

(b) Positive charge

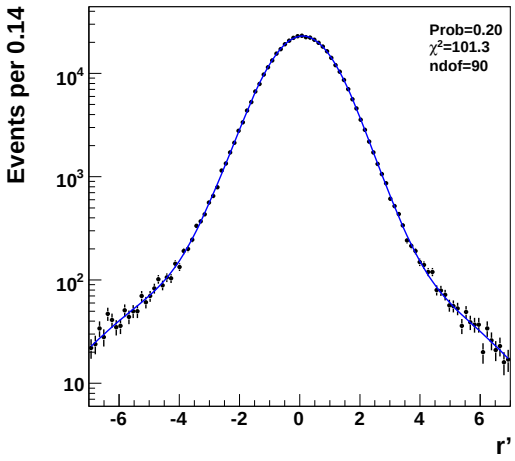

(c) Negative charge, log-scale

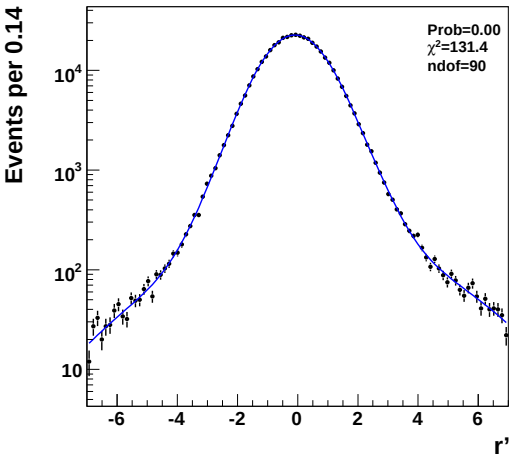

(d) Positive charge, log-scale

Figure 4.7: Resolution function of the rescaled curvature residual $r' = (k - k_t)/\sigma_k(k_t)$ of simulated samples.

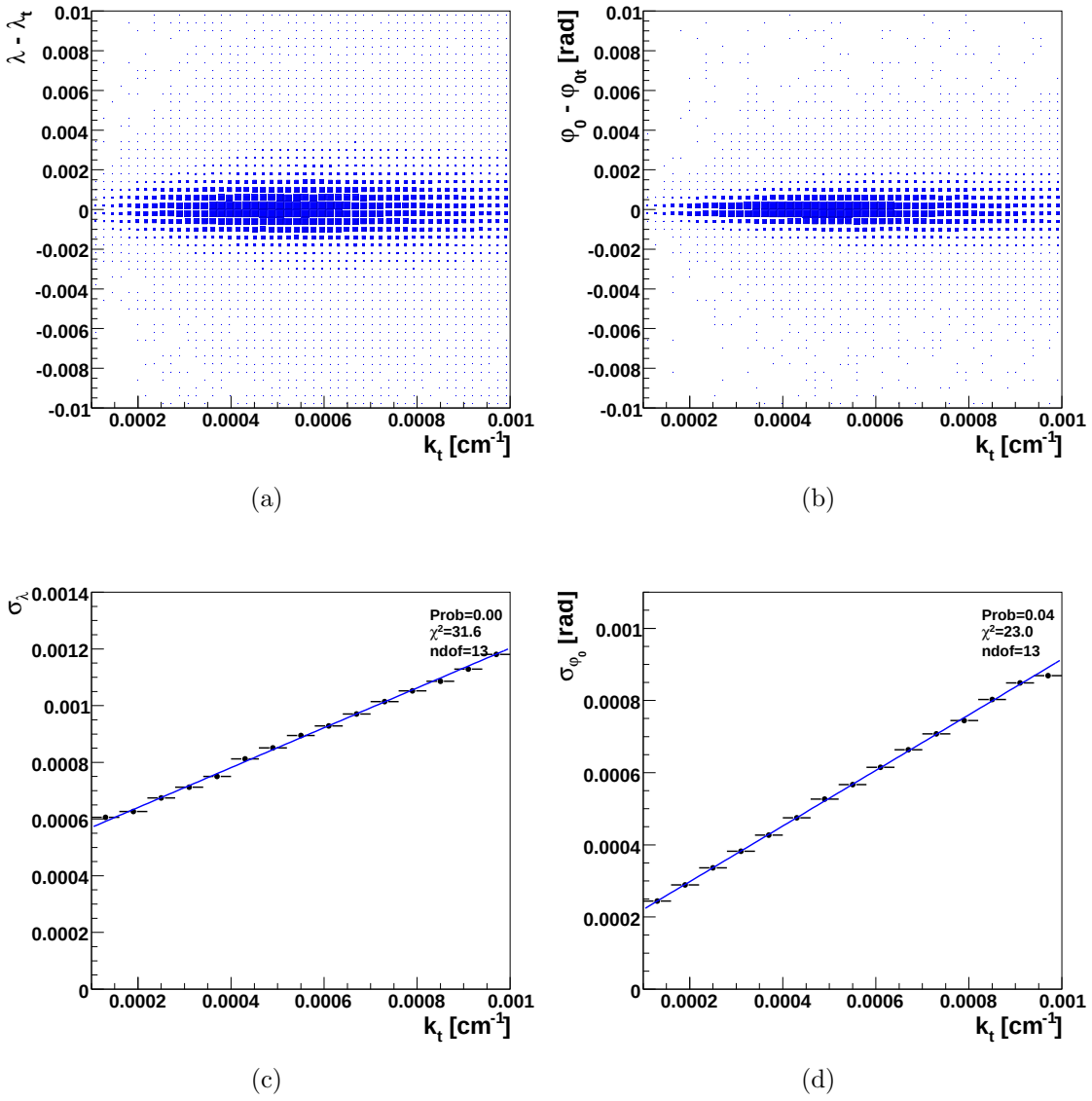

(a) (b)

(c) (d)

Figure 4.8: λ (a) and ϕ_0(b) residual as a function of the true curvature of the simulated events. λ (c) and phi_0 (d) resolution as a function of the true curvature of the simulated events, the fit function is overlaid.

4.4 Resolution function of λ and ϕ_0

In order to simulate the measurement of helix pitch $\lambda \equiv \cot\theta$, and azimuthal angle ϕ_0 we parameterized the resolution σ_λ and σ_{ϕ_0} as a function of curvature using the same technique described in previous section. The resolution function,

as for the curvature, was expressed as function of the curvature. This because we don't expected any dependence from the angular, because the cylindrical symmetry of the detector, and found no evidence of a dependence due the $\cot\theta$, probably because the η range of tracks is limited.

In the case of λ and ϕ_0 smearing we have not found any dependence of the residual from the charge of the track, therefore negative and positive tracks were treated together.

The figures 4.8(a) and 4.8(b) show the residuals $\lambda - \lambda_t$ and $\phi_0 - \phi_{0t}$, where λ and ϕ_0 are the smeared quantities and λ_t and ϕ_{0t} are the true quantities in the MC, as a function of the true curvature k_t. We fitted the residual distributions in 15 slices of the k_t variable using a single Gaussian distribution. The fitted values of σ_λ and σ_{ϕ_0} are reported in 4.8(c) and 4.8(d) respectively, and we empirically parameterized them with linear functions:

$$\sigma_\lambda(k_t) = a_0 + a_1 k_t \tag{4.11}$$

$$\sigma_{\phi_0}(k_t) = b_0 + b_1 k_t \tag{4.12}$$

$a_0(b_0)$, $a_1(b_1)$ are free parameters in the fit. The quality of the fit is slightly worse than in the curvature case that was derived from a physical model but still good considering the large statistics involved. I also verified as the effect of the experimental smearing on these variable is marginal on mass resolution with respect to the curvature resolution.

4.5 Resolution function of impact parameter, d_0

In addition to smearing the tracks parameters k, λ and ϕ_0, we also needed to smear the impact parameter d_0. While d_0 is not of direct interest in a model of mass resolution, it is important because of its correlation with kinematic variables. Our samples are selected using cuts on d_0 or related quantities, so it is necessary to have at least an approximate simulation of d_0 distributions because the cuts will affect the distribution of kinematic quantities.

For the impact parameter we followed the same procedure used for λ and ϕ_0. The plots in Fig. 4.9 show the residual distribution of $d_0 - d_{0t}$ as a function of the true curvature k_t and the parameterization of σ_{d_0} in curvature slices with a linear function. Again, the only significant resolution dependence is from the curvature.

4.6 Comparison FMC vs MC

The preliminary test for the FMC is to reproduce the distribution of the main kinematic distribution of the CDF II Monte Carlo. The distribution of interest in

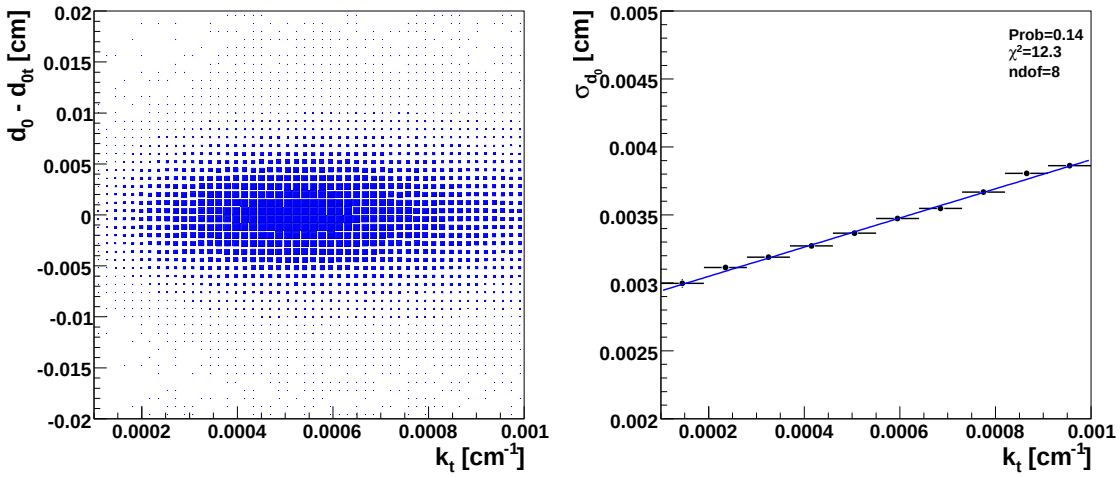

Figure 4.9: d_0 residual as a function of the true curvature of the simulated events in the left plot. d_0 resolution as a function of the true curvature of the simulated events, in right plot, the fit function is overlaid.

this analysis, that is expected to reproduce the FMC are: mass, $p_{\rm T}(B)$, $p_T(1) + p_T(2)$, L_{xy}, $\Delta\varphi_0$, $d_0(B)$, $d_0(1)$, $d_0(2)$, $p_{\rm T}(1)$, $p_{\rm T}(2)$. In the plot showed in this section only decay mode is compared, the $B^0 \to \pi\pi$ mode, but based on the structure of the Monte Carlo the same results are expected in the other modes.

Our FMC tries to model resolution accurately but makes no attempt at reproducing detector geometrical and trigger acceptance. For this reason the p_T distribution of the FMC and CDF MC data are not the same applying the same set of cuts. Since the mass line-shape is sensitive to this difference the following comparison plots will be re-weighted to correct this difference.

Fig. 4.10 shows this comparison for the invariant mass distribution and $\chi^2/\text{ndof} = 87.5/49$ indicates a satisfactory agreement between the two distributions. This confirms that the invariant mass resolution shape is determined by the tracks parameters uncertainty, and that possible correlations between two tracks can be neglected. This is important for our purpose, because we want to calibrate on a mass peak ($D^0 \to K^-\pi^+$) and export the calibration to the $B^0_{(s)} \to h^+h'^-$ via the single track resolutions. The results show that the source of the observed 10% non–Gaussian tails of the invariant mass distribution are the tails in the curvature resolution function. Fig. 4.11 shows how mass resolution is mainly caused by the curvature resolution.

The comparison of other kinematics variables (see Fig. 4.12) also shows a satisfactory agreement.

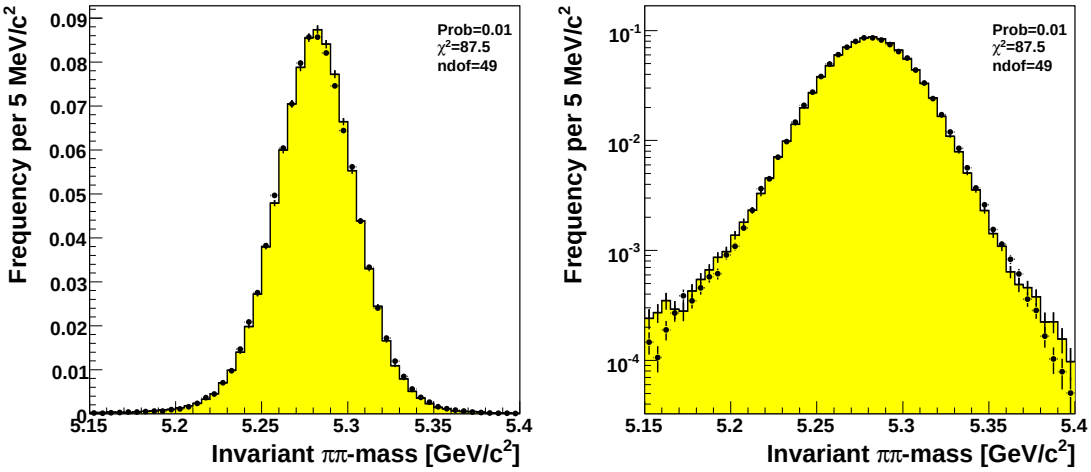

(a) (b)

Figure 4.10: Comparison of the invariant mass distribution of the $B^0 \to \pi\pi$ events simulated with the the official CDF Monte Carlo (filled yellow histogram) and with the Fast Monte Carlo simulation (points with error bars). Both simulations don't include the radiation effects. (a) linear scale, (b) logarithmic scale.

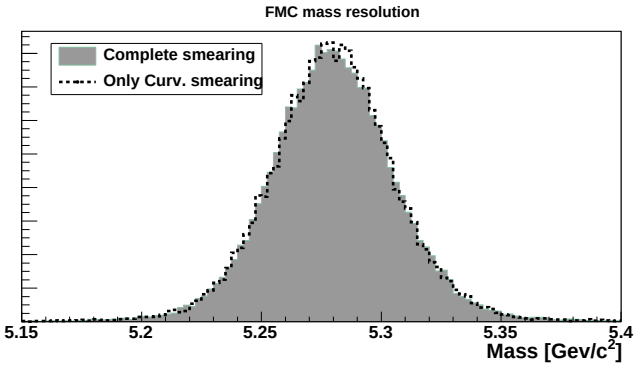

Figure 4.11: The plot shows the comparison between the mass line-shape obtained applying all the resolution functions, the filled area, with the respect the distribution obtained applying the curvature resolution only, the dashed line. This demonstrates how the mass resolution is mainly due to the curvature resolution.

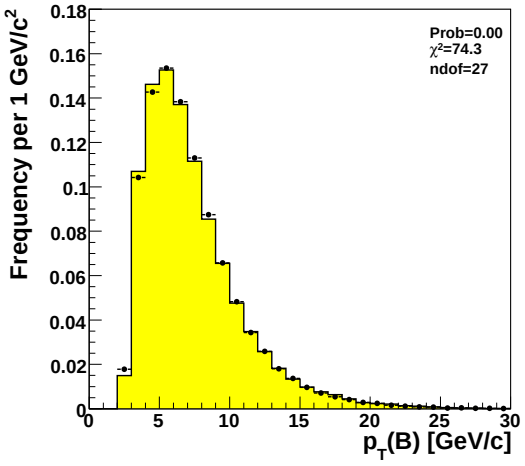
Frequency per 1 GeV/c^2
Prob=0.00
χ^2=74.3
ndof=27
p_T(B) [GeV/c]

(a)

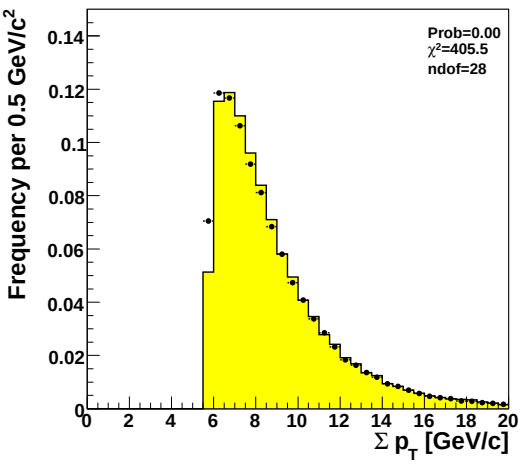
Frequency per 0.5 GeV/c^2
Prob=0.00
χ^2=405.5
ndof=28
Σ p_T [GeV/c]

(b)

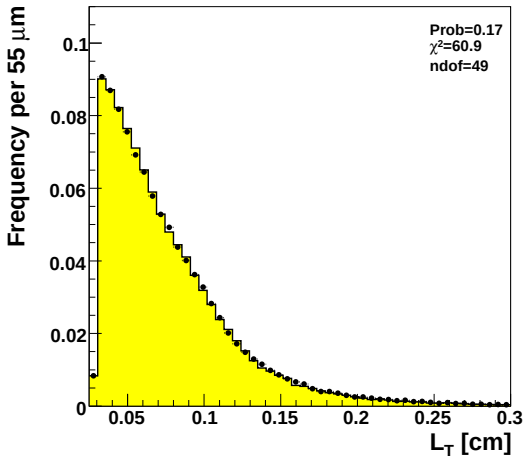
Frequency per 55 μm
Prob=0.17
χ^2=60.9
ndof=49
L_T [cm]

(c)

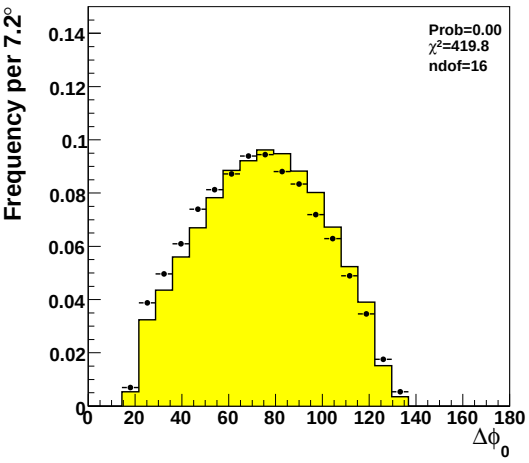
Frequency per 7.2°
Prob=0.00
χ^2=419.8
ndof=16
$\Delta\phi_0$

(d)

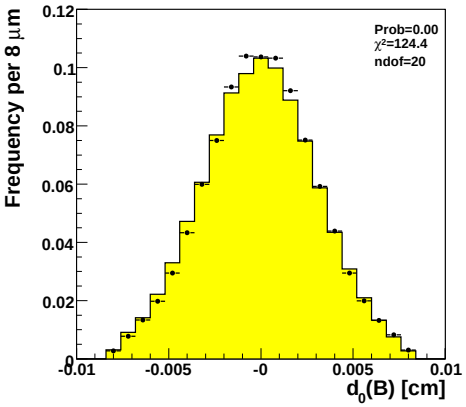

(e)

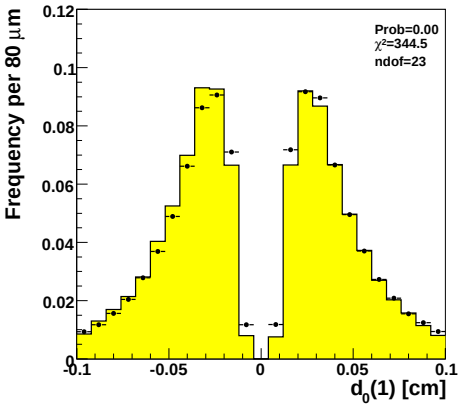

(f)

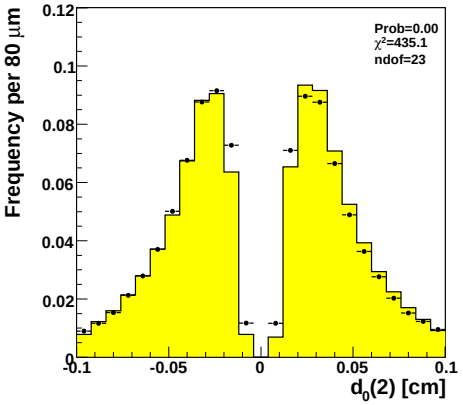

(g)

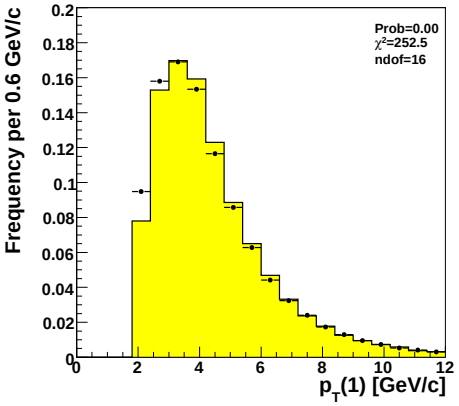

(h)

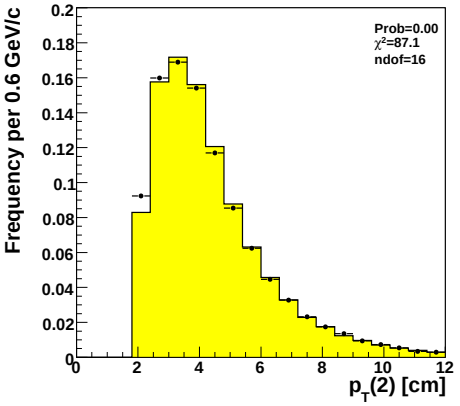

(i)

Figure 4.12: Comparison of the distributions of the single mode $B^0 \to \pi\pi$ simulated with the Fast Monte Carlo Simulation (points with error bars) and the official CDF Monte Carlo simulation (filled histogram). $p_{\mathrm{T}}(B)$ (a) $p_T(1) + p_T(2)$ (b), L_{xy} (c), $\Delta\varphi_0$ (d), $d_0(B)$ (e), $d_0(1)$ (f), $d_0(2)$ (g), $p_{\mathrm{T}}(1)$ (h), $p_{\mathrm{T}}(2)$ (i).

4.7 Final State Radiation

Before, in this and the previous chapter, was announced that the FMC will be also able to simulate, using a reliable way, the radiation effect. The final state radiation (FSR) happens because the calculation of the decay amplitude of a process with N charged stable particle in the final state, at the next orders, is corrected by a similar process with an arbitrary number of photons. The correction are finite and the energy distribution, as will be better explained later, peaks to low energy. Therefore the emission of photons is not revealable in the detector, causing a distortion some distributions. We simulated soft photon emission in our FMC, based on QED calculations described in [72]. We summarize here the main formulas used.

4.7.1 QED calculations

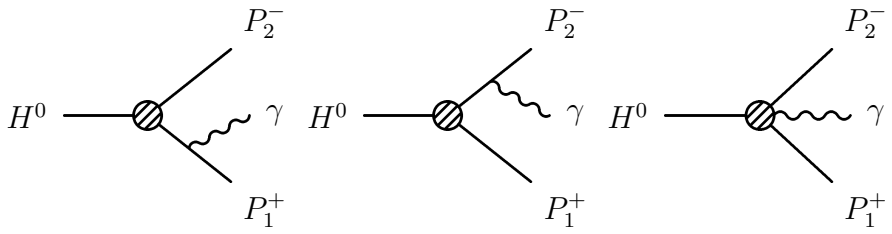

Figure 4.13: Electromagnetic contributions to the $H^0 \to P_1^+ P_2^-$ process with a real photon in the final state: *bremsstrahlung*.

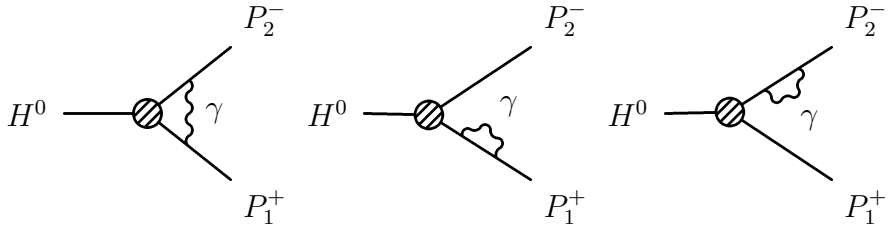

Figure 4.14: Electromagnetic contributions to the $H^0 \to P_1^+ P_2^-$ process with a virtual photon: one-loop vertex correction and $P_{1(2)}$ self-energy.

The most convenient infrared-safe observable related to the process $H^0 \to P_1^+ P_2^-$, where H^0 is a pseudo-scalar meson (B^0 or D^0) and $P_{1(2)}^{+(-)}$ are scalar or pseudo-scalar particles, is the photon-inclusive decay width

$$\Gamma_{12}^{\text{incl}}(E^{\max}) = \Gamma(H^0 \to P_1^+ P_2^- + n\gamma)\,\big|_{\sum E_\gamma < E^{\max}} \tag{4.13}$$

namely the width for the process $H^0 \to P_1^+ P_2^-$ accompanied by any number of (undetected) photons, with total energy $\sum E_\gamma \leq E^{\max}$ in the H^0 meson rest frame.

At any order in perturbation theory $\Gamma_{12}^{\rm incl}$ can be factorized into two theoretical quantities: the so-called non-radiative width, Γ_{12}^0, and the corresponding energy-dependent e.m. correction factor $G_{12}(E^{\rm max})$,

$$\Gamma_{12}^{\rm incl}(E^{\rm max}) = \Gamma_{12}^0\, G_{12}(E^{\rm max}) \tag{4.14}$$

The energy dependence of $G_{12}(E)$ is unambiguous and universal (i.e. independent on the short-distance dynamics which generate the decay) up to terms which vanish in the limit $E \to 0$. On the contrary, the normalization of $G_{12}(E)$ is arbitrary: it is always possible to move part of the finite (energy-independent) electromagnetic corrections from Γ_{12}^0 to $G_{12}(E)$. Only the product in (4.14) corresponds to an observable quantity.

From the purely experimental point of view, the only relevant aspect of the $G_{12}(E)$ factors is their energy dependence. This allows to evaluate the missing-energy distribution, or the soft-photon spectrum, $d\Gamma_{12}^{\rm incl}(E)/dE$. The $E \to 0$ singularity of this distribution is not integrable if evaluated at any fixed order in perturbation theory; however, the all–order resummation of the leading infrared singularities leads to an integrable distribution [72]. In our case, the differential decay rate of the process $H^0 \to P_1^+ P_2^- + n\gamma$ with respect to the total photons energy E can be written as:

$$\frac{d\Gamma_{12}^{\rm incl}(E)}{dE} = \frac{2\alpha}{\pi}\,\frac{|b_{12}|\Gamma_{12}^0}{E}\left(\frac{2E}{m_{H^0}}\right)^{\frac{2\alpha}{\pi}|b_{12}|}\left[1+\mathcal{O}\left(\frac{E}{m_{H^0}},\frac{\alpha}{\pi}\right)\right] \tag{4.15}$$

where α is fine structure constant and β and b_{12} are the coefficients defined as:

$$\beta^2 = \left[1-(r_1+r_2)^2\right]\left[1-(r_1-r_2)^2\right] \qquad r_i = \frac{m_i}{m_{H^0}} \tag{4.16}$$

$$b_{12} = \frac{1}{2} - \frac{4-\Delta_1^2-\Delta_2^2+2\beta^2}{8\beta}\,\ln\left(\frac{\Delta_1+\beta}{\Delta_1-\beta}\right) + (1\to 2) \tag{4.17}$$

where $\Delta_{1(2)} = 1 + r_{1(2)}^2 - r_{2(1)}^2$, and m_{H^0}, m_1, m_2 are respectively the masses of H^0, P_1^+ and P_2^-.

Concerning, instead, the angular distribution of the *bremsstrahlung* photons (see Fig. 4.13), the differential decay rate up to $\mathcal{O}(\alpha)$ terms can be written:

$$\frac{d^2\Gamma(H^0\to P_1^+P_2^-\gamma)}{dE_\gamma\, d\cos\theta_\gamma} = \frac{\alpha}{2\pi}\,\frac{1}{\beta}\,\frac{\Gamma_{12}^0}{E_\gamma}\,R_{12} \tag{4.18}$$

where E_γ and θ_γ denote, respectively, photon energy and angle between photon and P_1^+ momenta in the H^0 meson rest frame, and in this case β has a different definition:

$$\beta^2 = \left[1-\frac{(r_1+r_2)^2}{1-2z}\right]\left[1-\frac{(r_1-r_2)^2}{1-2z}\right] \qquad z = \frac{E_\gamma}{m_{H^0}} \tag{4.19}$$

The R_{12} coefficients assume the following explicit form

$$R_{12} = \frac{1 - r_1^2 - r_2^2 - 2z}{t_1 t_2} - \frac{r_1^2}{t_1^2} - \frac{r_2^2}{t_2^2} \tag{4.20}$$

in terms of the kinematic variables

$$t_{1,2} = \frac{1}{2}\left[1 + \frac{r_{1,2}^2}{1 - 2z} \mp \cos\theta_\gamma\right] \tag{4.21}$$

The Fig. 4.15(a), 4.15(b), 4.15(c), and 4.15(d) show the distribution of (4.18) for the emission of a real photon respectively for $B^0 \to \pi\pi$, $B^0 \to K\pi$, and $B^0 \to KK$ modes. The photon direction is, mostly, nearly collinear or anti-collinear to the direction of P_1^+ momentum in H^0 rest frame. The differential decay rate is invariant under the transformation $\cos\theta_\gamma \to -\cos\theta_\gamma$ for symmetrical final states like $\pi^+\pi^-$ or K^+K^-. This implies that the probability of a photon to be emitted in the same direction of P_1^+ (namely $\cos\theta_\gamma > 0$) is equal to of being emitted in opposite direction (namely $\cos\theta_\gamma < 0$). Instead, in final states with different kind of particles, like $B^0 \to K\pi$, the photon has a larger probability to be emitted in the direction of the lighter particle (in our case the pion) as the Fig. 4.15b shows. The size of this asymmetry is related to the mass difference $m_1 - m_2$ relative to the mass m_{H^0} through the coefficients R_{12}.

Expression (4.18) is divergent for $E_\gamma \to 0$ and for $\cos\theta_\gamma \to \pm 1$, and its integral is also divergent and cannot be integrated in both energy and angular domains. The first singularity is due to the infrared divergence, since the (4.18) was calculated only for real contributions (*bremsstrahlung* photons, see Fig. 4.13), while the second divergence is due to the relativistic conservation of four-momentum. The photon has zero mass and therefore it cannot be emitted exactly collinear or anti-collinear to the direction of the emitting particle.

The (4.15) is the soft-photon spectrum $d\Gamma_{12}^{\text{incl}}(E)/dE$, and although it has a singularity for $E \to 0$ it is integrable, since it was evaluated by all-order resummation of the leading infrared singularities (*bremsstrahlung* plus virtual photons , see Fig. 4.13 and 4.14).

From the phenomenological point of view both equations ((4.18) and (4.15)) only make sense if the information on detection threshold for photons (or maximum missing energy) $E_{\max}$ is available. Without this information, an unambiguous comparison between theory and experiments, and also the combination of different experimental results, cannot be performed. For this reason (4.15) is well defined only in a given integration domain $[0, E_{\max}]$. In practice, in our case of relative branching fractions measurements in a fixed mass window, it is sufficient to make sure that the cut–off $E_{\max}$ is set large enough to have effects only outside of the mass window being considered in the analysis.

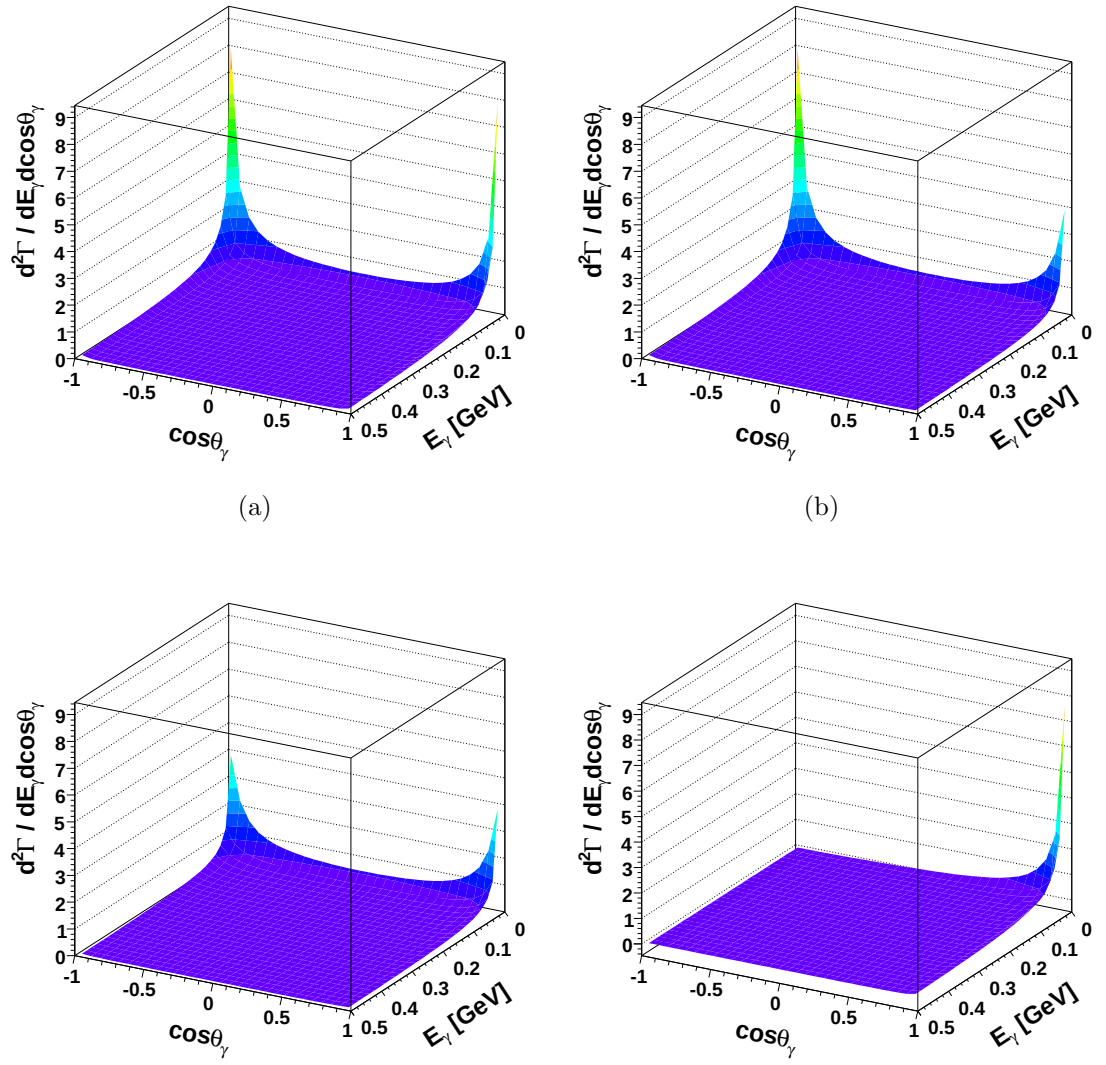

(a) (b)

(c) (d)

Figure 4.15: Differential decay rate for *bremsstrahlung* process $H^0 \to P_1^+ P_2^- \gamma$ with respect to photon energy E_γ and the cosine of angle between photon and P_1^+ momenta in the H^0 meson rest frame. (a) $B^0 \to \pi\pi$, (b) $B^0 \to K\pi$, (c)$B^0 \to KK$, (d) $B^+ \to \pi^+ \overline{D}^0$.

4.7.2 $H^\pm \to P_1^\pm P_2^0 + n\gamma$ case

The case of soft photon emission in the process $H^\pm \to P_1^\pm P_2^0 + n\gamma$ is very similar and we describe it briefly. This is not used directly in our analysis, but we use

it as a control on $D^{\star+} \to D^0\pi^+$ decays, and that relevant code has been used in other CDF analysis [62]. The calculations described in Sec. 4.7.1 and extracted from [72] can be applied also in this case. Only the definition of some coefficients in this case is different. The coefficient $b_{12} = b_{+-}$ of (4.17) becomes $b_{\pm 0}$:

$$b_{\pm 0} = 1 - \frac{\Delta_1}{2\beta} \ln\left(\frac{\Delta_1 + \beta}{\Delta_1 - \beta}\right) \ , \tag{4.22}$$

and the coefficient $R_{12} = R_{+-}$ of (4.20) becomes $R_{\pm 0}$:

$$R_{\pm 0} = \frac{1 + r_1^2 - r_2^2 - 2z(1 - t_1)}{t_1} - \frac{r_1^2}{t_1^2} - 1 \ . \tag{4.23}$$

All other quantities are unchanged. Fig. 4.15c shows the distribution of (4.18) for the emission of a real photon for $B^+ \to \pi^+\overline{D}^0$ mode. From this two-dimensional distributions we notice that the photon is emitted in most cases nearly collinear to the direction of P_1^+ (in this specific case $P_1^+ = \pi^+$) in the H^0.

4.7.3 Putting everything together

Our FMC simulates a generic $H^0 \to P_1^+ P_2^-$ ($H^+ \to P_1^+ P_2^0$) decays in the rest frame of the H^0 meson, and then after boosts to the laboratory frame the momentum of the $P_{1(2)}^{+(-)}$ particle (see Sec. 4.2). For simplicity we used the same notation of Sec. 4.7.1. We indicate with $(E^*_{1(2)}, \vec{p}^{\,*}_{1(2)})$ the four-momentum of decay product $P_{1(2)}^{+(-)}$ in the rest frame of meson H^0 while the same quantities in the laboratory frame will be indicated by $(E_{1(2)}, \vec{p}_{1(2)})$. Regarding the photon, we used only the quantities in the rest frame of H^0 meson and they are indicated without the star: E is the total missing energy of undetected photons defined in (4.15), E_γ and $\cos\theta_\gamma$ are respectively the energy of the *bremsstrahlung* photon and the cosine of angle between himself and P_1^+ momentum defined in (4.18).

To include the FSR in our FMC we made the following approximations.

- We used the eq. (4.15) to generate the energy spectrum of the soft photon, integrating the distribution between $E_\gamma \to 0$ and $E_\gamma = E_{\max}$. The cut-off $E_{\max}$ depends on the decay mode we want to analyze and its choice is motivated by the acceptance fit interval in the invariant mass distribution.

  The fit of composition to disentangle individual $B^0_{(s)} \to h^+h'^-$ modes (described Sec. 3.3) is performed in the invariant mass region $5.0 < M_{\pi\pi} < 5.8\, GeV/c$. The inclusion of soft photon emission a long lower-mass tail produces in the invariant mass distribution and this must be well–defined within this range. We chose a cut-off $E_{\max} = 0.5$ GeV, which is large enough so

that the radiative tail is well defined in the mass interval, but still smaller than the kinematic energy cut-off $m_{B^0_{(s)}} - m_{h^+} - m_{h'^-}$.

In this thesis we quote only ratios of branching fractions, like $\mathcal{B}(B^0 \to \pi^+\pi^-)/\mathcal{B}(B^0 \to K^+\pi^-)$, and we are therefore interested only in the line shape of the distribution and not to the absolute normalization of the soft photon emission. The main concern in a reliable description of the tails of the larger peaks, in order to have confidence in the smaller signals from rare B and Λ_b^0 modes.

A cut $E_{\max} = 0.5$ GeV is also a valid choice for $D^0 \to K^-\pi^+$ and $B^+ \to \bar{D}^0\pi^+$ decay modes if we choose an invariant mass window where the tail is well defined: $1.800 < M_{K\pi} < 1.950$ GeV/c^2 for the D^0 and $5.170 < m_{B^+} < 5.600$ GeV/c^2 for the B^+, but it is not valid for example in the case of $D^{*+} \to D^0\pi^+$ decays, where the available energy in the rest frame of D^{*+} is small ($m_{D^{*+}} - m_{D^0} - m_{\pi^+} \simeq 5.83$ MeV/c^2) and E_γ cannot exceed $E_{\max} = 5.83$ MeV.

- We approximated the direction of the photon as collinear with the positive (50% of cases) or the negative (50% of cases) track in H^0 rest frame (see Sec. 4.7.1). This violates conservation of the total momentum, but it works fine for the purpose of evaluating the effect of the reconstructed 2-body invariant mass. The 50% probability to be collinear/anti-collinear is accurate in the decay modes with same particles in the final state, but it is very good approximation also in cases, like $B^0 \to K\pi$ and $B^0_s \to K\pi$. In cases like $D^{*+} \to D^0\pi^+$ or $B^+ \to \bar{D}^0\pi^+$, the emitted photon is collinear to the direction of $P_1^+ = \pi^+$ momentum in H^0 rest frame in the majority of cases, and we assumed the probability to be 100%.

- We ensured conservation of the total energy. If $(E'^*_{1(2)}, \vec{p}\,'^*_{1(2)})$ is the particle four-momentum after the photon emission in the rest frame of H^0, and the particle 1 is emitting, we can write:

  - $E'^*_1 = E^*_1 - E_\gamma$;
  - $p'^*_1 = \sqrt{(E'^*_1)^2 - m_1^2}$;
  - $\hat{p}'^*_1 = \hat{p}^*_1$;
  - $E'^*_2 = E^*_2$ and $\vec{p}\,'^*_2 = \vec{p}^*_2$

  where $\hat{p} = \vec{p}/|\vec{p}|$ and $p = |\vec{p}|$.

Using the above to obtain all kinematic distributions of the generic $H^0 \to P_1^+P_2^-$ decay with the soft photon emission, it is sufficient to boost in the laboratory

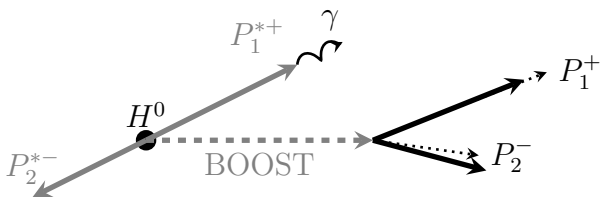

Figure 4.16: The sketch shows how the generation of a two-body decay, Fig. 4.4, is modified when the FSR is added.

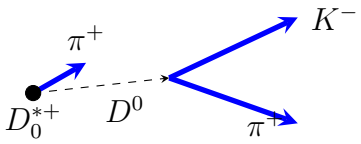

Figure 4.17: Sketch of the $D^{*\pm}$ decay topology in the plane transverse to the proton beam direction.

frame the four-momenta of the particles $(E'^*_{1(2)}, \vec{p}'^*_{1(2)}) \rightarrow (E'_{1(2)}, \vec{p}'_{1(2)})$ with the same prescription described in Sec. 4.2. The scheme that shows the modified two-body decays generator is in Fig. 4.16.

4.8 Testing of the model with real data

Having included in our FMC simulation a detailed model of the CDF II detector resolution, and an accurate description of the soft photon emission effects, we are ready to compare it to data. To this purpose, we used a real data sample of $D^0 \rightarrow K^-\pi^+$ decays, reconstructed from $D^{*\pm}$.

The sample was collected by the `B_CHARM` trigger, a path that belongs, along with the `B_PIPI` path, to the Displaced-Tracks Trigger(Sec. 2.5). Most trigger requirements are common to both paths. Thus, most trigger-dependent effects are automatically accounted in the checks. The sample contains the same physics-quality runs used for the $B^0_{(s)} \rightarrow h^+h'^-$ analysis.

Following [75], the reconstruction of signal (see Fig. 4.17) was based solely on tracking, the flavor of the D^0 is guessed by the charge of the third soft track. One $D^0 \rightarrow K^-\pi^+$ and one $\overline{D}^0 \rightarrow K^+\pi^-$ candidate were formed for each pair of oppositely-curved tracks found in the XFT fiducial region ($|\eta| < 1$). Further requirements, in Tab. 4.4, on the product of impact parameters of tracks ($d_0(K) \times d_0(\pi) < 0$ cm^2), on candidate transverse momentum ($p_{\rm T}(D^0) > 5.5$ GeV/c), on its transverse decay-length ($L_{xy}(D^0) > 300$ μm), and on its impact parameter ($|d_0(D^0)| < 140$ μm) were applied to suppress a 10% contribution [82] from

non-prompt D^{*+} decays. Candidates with reconstructed invariant mass within 200 MeV/c^2 of the world–average D^0 mass [10] were combined with a third charged particle with $p_{\rm T} > 0.4$ GeV/c (soft pion) to form a $D^{*+} \to D^0[K\pi]\pi^+$ candidate. The charged pion mass is assigned to the like-sign pair of particles. The difference between the reconstructed D^{*+} and D^0 masses was required to be within $[0.1435, 0.1472]$ GeV/c^2 corresponding to an interval of $\pm 3\sigma$ from the nominal value of 0.1454 GeV/c^2 to reduce backgrounds (combinations of true D^0 decays with random tracks, random three-track combinations that satisfy the selection requirements, etc.).

Quantity of the track	Units	Requirement
$p_{\rm T}(\pi)$, $p_{\rm T}(K)$	GeV/c	> 2.0
$p_{\rm T}(\pi_s)$	GeV/c	> 0.4
$\lvert\eta(\pi)\rvert$, $\lvert\eta(K)\rvert$	–	< 1.0
$\lvert d_0(\pi)\rvert$, $\lvert d_0(K)\rvert$	μm	[120, 1000]
Quantity of the candidate		
$q(\pi) \times q(K)$	e^2	-1
$d_0(\pi) \times d_0(K)$	μm^2	< 0
$p_{\rm T}(D^0)$	GeV/c	> 6
$L_{xy}(D^0)$	μm	> 300
$p_T(1) + p_T(2)(K, \pi)$	GeV/c	> 5.5
$\lvert d_0(D^0)\rvert$	μm	< 140
$\lvert d_0(D^{*+})\rvert$	μm	< 80
$\chi^2_{r\phi}$	–	< 20
$\Delta\varphi_0(K, \pi)$	Degrees	[2°, 90°]
$m_{D^{*+}} - m_{D^0}$	GeV/c^2	[0.1435, 0.1472]

Table 4.4: The $D^{*\pm}$ selection. To distinguish the "soft" pion originated from the D^{*+} decay from the pion originated from the D^0 decay in the table they are labeled respectively as π_s and π.

The selection results in about 1.5×10^6 signal decays. The invariant mass distributions are shown in Fig. 4.19 and 4.20, in the assumption that the D^0 decays in the Cabibbo-favored mode $K^-\pi^+$.

To allow an accurate comparison between data and FMC even in the tails, we adopted tight selection cuts. We chose a tight D^0 mass window ($1.820 < m_{K\pi} < 1.900$ GeV/c^2) to avoid contamination from mis-reconstructed decays in other modes (see Fig. 4.18). At lower masses, there are $D^0 \to K^+K^-$ decays ($\mathcal{B} \simeq 3.9\times10^{-3}$) in which a kaon is mis-assigned the pion mass, and $D^0 \to K^-\pi^+\pi^0$ ($\mathcal{B} \simeq 13\%$) decays in which a π^0 is not reconstructed. At higher masses the situation is different, since the radiative tail of the $D^0 \to \pi^+\pi^-$ decays ($\mathcal{B} \simeq$

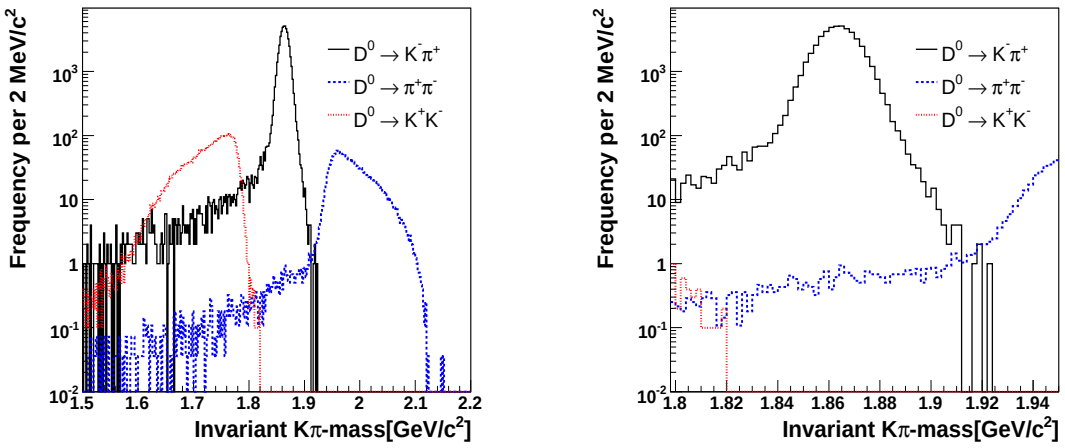

(a) (b)

Figure 4.18: Invariant $K\pi$-mass distribution of simulated $D^0 \to h^+h'^-$ modes using the FMC simulation. (a) $1.500 < m_{K\pi} < 2.100$ GeV/c^2, (b) $1.800 < M_{K\pi} < 1.950$ GeV/c^2. In the figure we assumed $\frac{\mathcal{B}(D^0\to\pi^+\pi^-)}{\mathcal{B}(D^0\to K^-\pi^+)} = 0.03594$ and $\frac{\mathcal{B}(D^0\to K^+K^-)}{\mathcal{B}(D^0\to K^-\pi^+)} = 0.0992$ from [75].

1.4×10^{-3}), in which a pion is mis-assigned the kaon mass [75], contaminates almost uniformly the mass region chosen to perform the test. For similar reasons we chose a tight mass region also for the $D^{*+} \to D^0\pi^+$ ($1.960 < m_{D^0\pi} < 2.050$ GeV/c^2).

To verify the accuracy of our mass line shape model, we used the FMC simulation to predict the invariant $K\pi$-mass distribution of the $D^0 \to K^-\pi^+$ decays and invariant $D^0\pi$-mass distribution of the $D^{*+} \to D^0\pi^+$ decays. We generated a sample of $D^{*\pm}$ events, corresponding to about 700,000 candidates after the selection described in Tab. 4.4. To ensure similar kinematics we extended the two-body FMC simulation described in Sec. 4.2, to a three-body FMC simulation, as a sequential chain of two two-body decays $D^{*+} \to D^0\pi^+$ plus $D^0 \to K^-\pi^+$, as in Fig. 4.18.

In order to compare with date, the mass line shape predicted by FMC was parameterized using the following p.d.f.:

$$\wp_s(m;\vec{\theta}) = f_{\rm bulk}[f_1 gauss(m; m_{D^0}+\delta_1, \sigma_1) + (1-f_1) gauss(m; m_{D^0}+ \\ + \delta_2, \sigma_2)] + (1-f_{\rm bulk})\mathscr{T}(m; b, c, m_{D^0}+\delta_1), \tag{4.24}$$

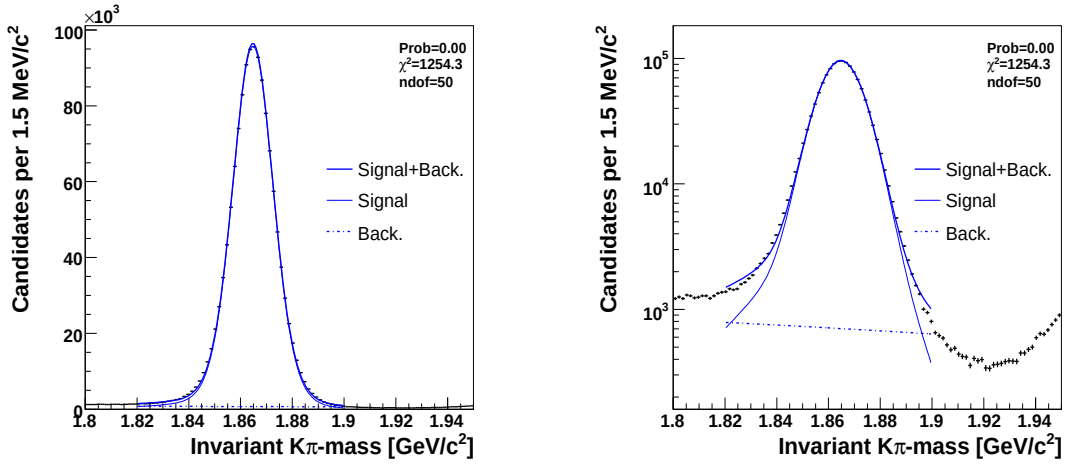

(a) (b)

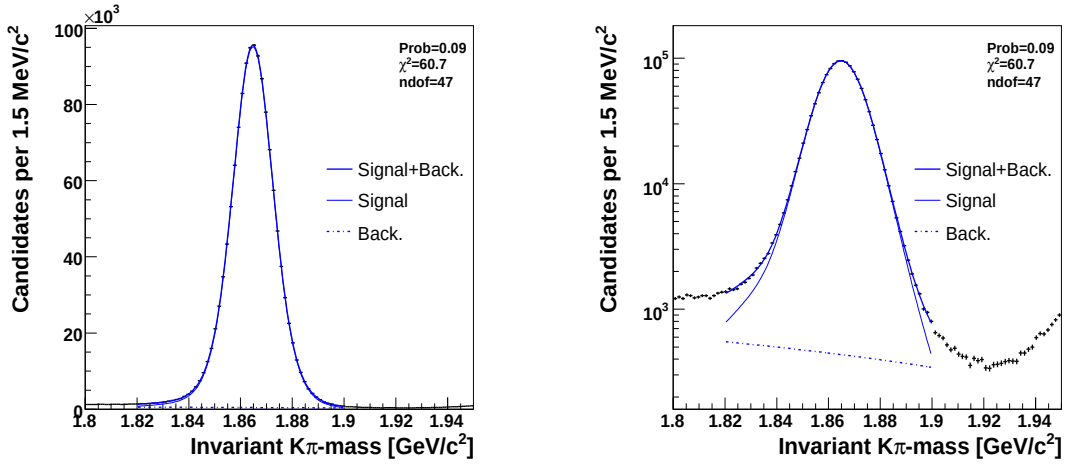

(c) (d)

Figure 4.19: Check of the mass line shape template using a data sample of $D^0 \to K^-\pi^+$ decays from reconstructed $D^{*\pm}$. Invariant $K\pi$-mass distribution. The signal p.d.f. $\wp_s(m_{K\pi};\vec{\theta})$ is completely fixed from FMC in (a,b), the parameters σ_1, σ_2, f_{bulk} of $\wp_s(m_{K\pi};\vec{\theta})$ are free to vary in the fit in (c,d). (a)(c) linear scale on y-axis, (b)(d) logarithmic scale on y-axis.

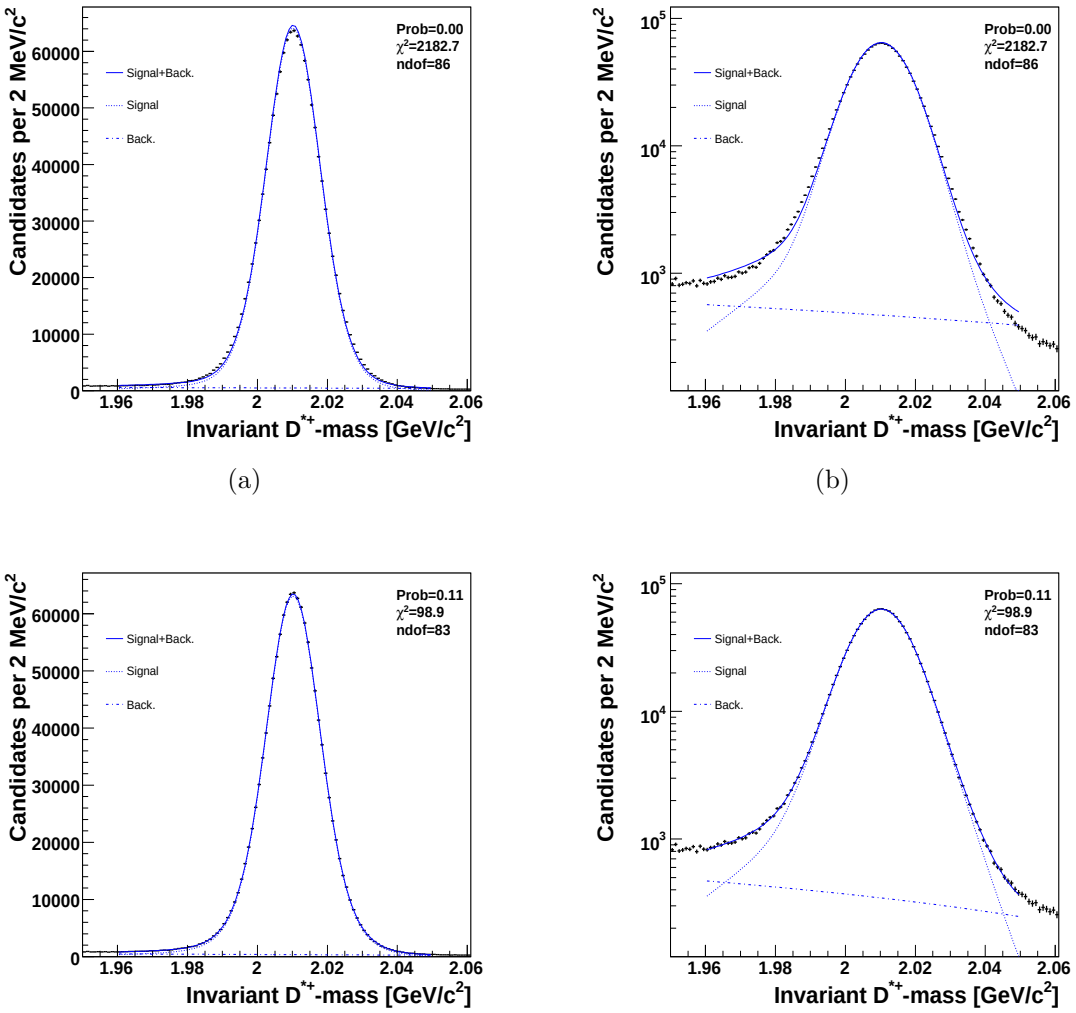

Figure 4.20: Check of the mass line shape template using a data sample $D^{*+} \to D^0\pi^+$ decays from reconstructed $D^{*\pm}$. Invariant $D^0\pi$-mass distribution. The top plots show the result using a signal p.d.f. $\wp_s(m_{D^0\pi};\vec{\theta})$ fixed from FMC, the parameters σ_1, σ_2, in the bottom plots $f_{\rm bulk}$ of $\wp_s(m_{D^0\pi};\vec{\theta})$ are free to vary in the fit. (a)(c) linear scale on y-axis, (b)(d) logarithmic scale on y-axis.

where:

$$gauss(m;\mu,\sigma) = \frac{1}{\sqrt{2\pi}\sigma} e^{-\frac{1}{2}\left(\frac{m-\mu}{\sigma}\right)^2}, \tag{4.25}$$

$$\mathscr{T}(m;b,c,\mu) = \frac{1}{K} e^{b(m-\mu)} \cdot \mathrm{Erfc}(c(m-\mu)), \tag{4.26}$$

$$K = \int_{m_1}^{m_2} e^{b(m-\mu)} \cdot \mathrm{Erfc}(c(m-\mu))dm, \tag{4.27}$$

$$\mathrm{Erfc}(x) = 1 - \mathrm{Erf}(x) = \frac{2}{\sqrt{\pi}} \int_x^{+\infty} e^{-t^2} dt. \tag{4.28}$$

We used a sum of two Gaussians to parameterize the bulk of the distribution, while the long lower-mass tail due to the soft photon emission was parameterized with the function $\mathscr{T}(m;b,c,\mu)$. f_{bulk} is the relative fraction of the double Gaussian bulk with respect the total (bulk plus tail), while $1 - f_{\mathrm{bulk}}$ is the fraction of the tail term. f_1 is the relative fraction of the more abundant Gaussian, labeled with the index 1, with respect to the sum of two Gaussians, while $\sigma_{1(2)}$ is the the width of the Gaussian 1(2). $\delta_{1(2)}$ is the mass shift from the input mass value of the D^0 ($m_{D^0} = 1.8646$ GeV/c^2) in the FMC simulation. The soft photon emission makes the mass distribution asymmetric, and the means of the Gaussians are not necessary equal. For this reasons m_{D^0} was fixed in the parameterization while $\delta_{1(2)}$ is free to vary. In practice the parameterization returned similar values for δ_1 and δ_2, so we used a single parameter $\delta = \delta_1 = \delta_2$. The parameters vector is defined as $\vec{\theta} \equiv \{f_{\mathrm{bulk}}, f_1, \sigma_1, \sigma_2, \delta_1, \delta_2, b, c\}$ and it is extracted by fitting the FMC simulated invariant mass distribution. Fig. 4.21 shows the parameterization of the invariant mass distribution simulated using the FMC; the corresponding parameters are reported in Tab. 4.5.

Parameter	Units	Value
f_{bulk}	$-$	0.918 ± 0.005
f_1	$-$	0.490 ± 0.051
σ_1	$\mathrm{MeV/c^2}$	6.88 ± 0.10
σ_2	$\mathrm{MeV/c^2}$	9.02 ± 0.15
$\delta = \delta_1 = \delta_2$	$\mathrm{MeV/c^2}$	-0.61 ± 0.13
b	$\left[\mathrm{GeV/c^2}\right]^{-1}$	52.8 ± 2.1
c	$\left[\mathrm{GeV/c^2}\right]^{-1}$	49.9 ± 1.1

Table 4.5: Parameterization of the invariant $K\pi$-mass for $D^0 \to K^-\pi^+$ simulated events. See Fig. 4.21.

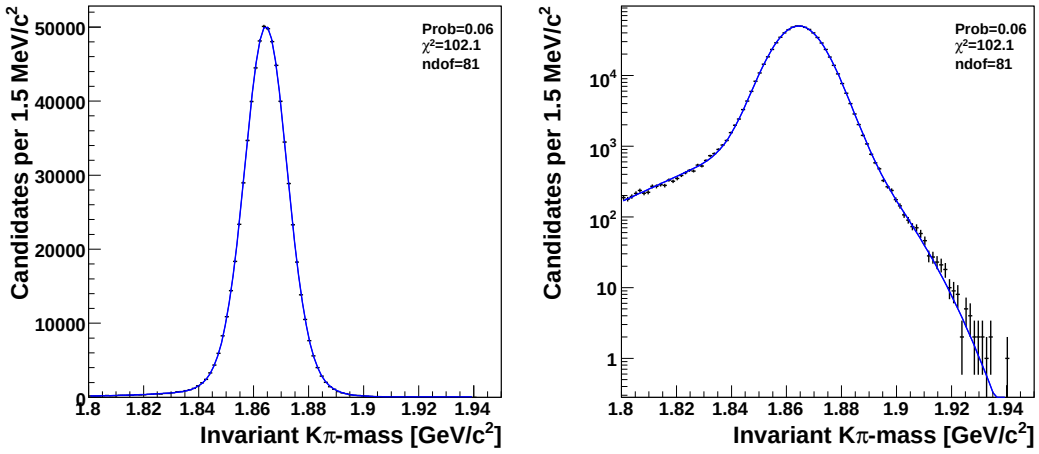

(a) (b)

Figure 4.21: Mass template of $D^0 \to K^-\pi^+$ decays. Parameterization of the invariant $K\pi$-mass distribution for the $D^0 \to K^-\pi^+$ decays using the Fast Monte Carlo. (a) linear scale on y-axis, (b) logarithmic scale on y-axis.

Parameter	Units	(I)	(II)	Δ [%]
f_{bulk}	–	0.918	0.910 ± 0.032	0.87
f_1	–	0.490	0.490	
σ_1	MeV/c^2	6.88	6.71 ± 0.02	2.47
σ_2	MeV/c^2	9.02	9.63 ± 0.02	6.76
$\delta = \delta_1 = \delta_2$	MeV/c^2	-0.61	-0.61	
b	$[\text{GeV}/c^2]^{-1}$	52.8	52.8	
c	$[\text{GeV}/c^2]^{-1}$	49.9	49.9	
f_s	–	0.9719 ± 0.0003	0.9824 ± 0.0004	1.08
a_0	–	-2.4 ± 0.3	-4.7 ± 0.4	48
Δ_m	MeV/c^2	0.798 ± 0.008	0.804 ± 0.008	0.74
χ^2/ndof	–	1254.3/50	60.7/47	

Table 4.6: Fit on $D^0 \to K^-\pi^+$ data. (I) Signal shape is completely fixed from the FMC, we fitted only parameters f_s, a_0, δ_m. (II) Some parameters of the signal shape are free to vary: f_s, a_0, δ_m plus f_{bulk}, σ_1, σ_2 (II). $\Delta = \frac{\text{(I)}-\text{(II)}}{\text{(I)}}$. See Fig. 4.19.

4.8.1 D^0 test

After extracting the parameterization of the $D^0 \to K^-\pi^+$ signal from the FMC we performed a binned-χ^2 fit of the real data in invariant $K\pi$-mass with the following

p.d.f.:

$$N \cdot \wp(m_{K\pi}; N, f_s, a_0) = N \cdot \Big(f_s \wp_s(m_{K\pi}; \vec{\theta}) + f_d \wp_d(m_{K\pi}; \mu_d, \sigma_d) + \\ + (1 - f_s - f_d)\ \wp_b(m_{K\pi}; a_0) \Big) \tag{4.29}$$

where the absolute normalization N, the relative signal fraction f_s, the background shape a_0 were determined by the fit. $\wp_s(m_{K\pi}; \vec{\theta})$ is the signal p.d.f. correctly normalized in the mass fit domain $[1.820, 1.900]$ GeV/c^2 and it was completely determined from the FMC (see above (4.24)). The functions $\wp_d$ and $\wp_b$ are:

- $\wp_d(m_{K\pi}; \mu_d, \sigma_d) = \dfrac{1}{\displaystyle\int_{1.820}^{1.900} \frac{1}{\sqrt{2\pi}\sigma_d} e^{-\frac{1}{2}(\frac{m_{K\pi}-\mu_d}{\sigma_d})^2} dm_{K\pi}} \left(\frac{1}{\sqrt{2\pi}\sigma_d} e^{-\frac{1}{2}\left(\frac{m_{K\pi}-\mu_d}{\sigma_d}\right)^2} \right)$,
- $\wp_b(m_{K\pi}; a_0) = \dfrac{1}{\displaystyle\int_{1.820}^{1.900} (1 + a_0 m_{K\pi}) dm_{K\pi}} (1 + a_0 m_{K\pi})$.

where $\wp_d(m_{K\pi}; \mu, \sigma)$ parametrizes the $\mathcal{O}(10^{-3})$ contamination of the doubly-Cabibbo-suppressed mode $D^0 \to K^+\pi^-$ [83]. The uncorrected mass assignment to the decay products inflates the width of the mass distribution by about a factor ten, with respect to the Cabibbo-favored mode $D^0 \to K^-\pi^+$ reconstructed with the correct mass assignment. μ_d and σ_d were extracted from the simulation and are fixed in the fit. f_d is defined as

$$f_d = f_s R_d \int_{1.820}^{1.900} \frac{1}{\sqrt{2\pi}\sigma_d} e^{-\frac{1}{2}(\frac{m_{K\pi}-\mu_d}{\sigma_d})^2} dm_{K\pi}, \tag{4.30}$$

where $R_d = \mathcal{B}(D^0 \to K^+\pi^-)/\mathcal{B}(D^0 \to K^-\pi^+) = 4.05 \cdot 10^{-3}$ was measured by CDF [83]. $\wp_b(m_{K\pi}|a_0)$ is the background parameterization (linear function), correctly normalized in the mass fit domain. To allow for a global mass scale shift, we fitted an additional parameter Δ_m by substituting $m_{K\pi} \to m_{K\pi} + \Delta_m$.

We first fitted the invariant $K\pi$-mass distribution of the $D^0 \to K^-\pi^+$ decays, by using a signal shape completely fixed by the parameterization extracted from the FMC (Tab. 4.5). Only the parameters N,f_s, a_0 and the global mass scale Δ_m were allowed to vary. The results of this fit are reported in column (I) of Tab. 4.6 while in Fig. 4.19ab the fit function is superimposed on data. The χ^2/ndof = 1254.3/50 of this fit is poor, but the curve describes the data with a precision unprecedented in previous CDF comparison of data vs MC: the large statistics in this sample makes the χ^2 sensitive to very small deviations. There is no evidence for the presence of an additional tail in the data, a long standing discrepancy

between CDF data and MC. These observations seem to suggest that previously observed mismatches were due to the lack of a good model of soft photon radiation. We performed a second fit, in which we left free to vary three additional parameters related to the signal shape $f_{\rm bulk}$, σ_1, σ_2. The results are reported in column (II) of Tab. 4.6 while in Fig. 4.19cd the fit function is superimposed on fitted data. The χ^2/ndof = 60.7/47 of this fit is now very good and the agreement between the FMC and the data is satisfactory. The parameters of the signal shape $f_{\rm bulk}$, σ_1, σ_2 differ from those extracted from FMC by just a few percents (see column Δ of Tab. 4.6).

When we allow the additional parameters of the signal shape to vary the background level changes. It is difficult to extract better parameters without a greater knowledge of the background. However the discrepancies of the nominal FMC parameters are so small that it does not appear worthwhile to attempt any tuning unless one needs to model samples containing order $10^5 - 10^6$ signal events, while the samples we are interested in are just order 10^3.

4.8.2 $D^{\star\pm}$ test

We repeated for $D^{*+} \to D^0\pi^+$ the same checks performed for $D^0 \to K^-\pi^+$ mode. It is sufficient to replace in the equations m_{D^0} with $m_{D^{*+}}$ and to drop the contribution of the double Cabibbo suppressed decays in the p.d.f. in (4.29) by fixing $f_d = 0$. Also in this case we first do a fit (I) where all parameters of the signal mass shape are extracted by FMC, and left free to vary only N, f_s, a_0 and Δ_m. In the fit named (II) we fitted also $f_{\rm bulk}$, σ_1, σ_2. The signal parameterization for the invariant $D^0\pi$-mass distribution extracted from the FMC is reported in Tab. 4.7 (see Fig. 4.22). The results of fit (I) and (II) are reported in Tab. 4.7 and projections of these fits are in Fig. 4.20. Also in this case the fit quality improves drastically from χ^2/ndof = 2182.7/86 to χ^2/ndof = 98.9/83 when moving from (I) to (II), but the changes in the parameters $f_{\rm bulk}$, σ_1, σ_2 are very small, and amount to an impressive confirmation of the accuracy of the model parameters.

4.9 Summary

We built a fast stand-alone Monte Carlo program in C++ (FMC) to simulate the invariant mass distribution of generic $B(D)$ meson decays into two scalar or pseudo-scalar mesons P_1P_2 ($H \to P_1P_2$). The FMC includes a detailed description of non–Gaussian tails from both resolution and soft photon radiation. Tests performed against real data samples of $\mathcal{O}(10^6)$ show that this FMC is reliable model of invariant mass distribution for our $B^0_{(s)} \to h^+h'^-$ signals.

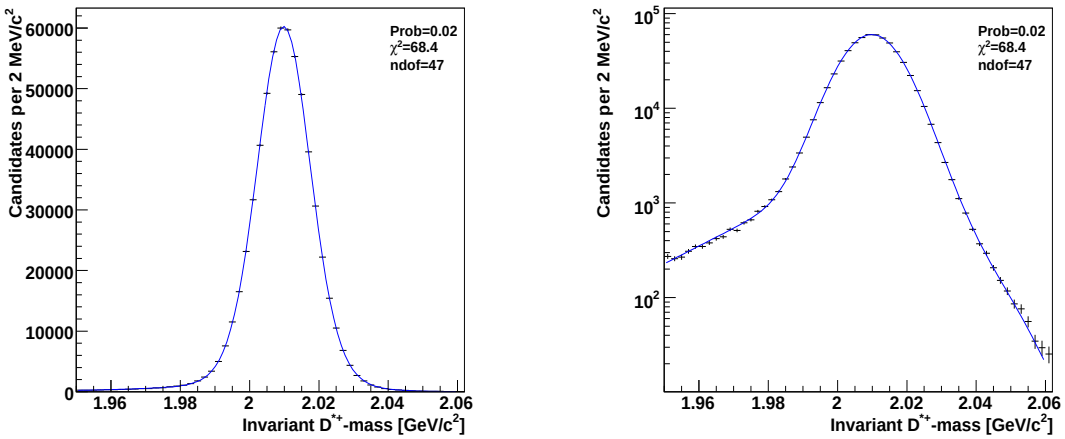

(a) (b)

Figure 4.22: Mass template of $D^{*+} \to D^0\pi^+$ decays. Parameterization of the invariant D^{*+}-mass distribution for the $D^{*+} \to D^0\pi^+$ decays using the Fast Monte Carlo. (a) Linear scale on y-axis, (b) logarithmic scale on y-axis.

Parameter	Units	Value
f_{bulk}	$-$	0.926 ± 0.004
f_1	$-$	0.606 ± 0.001
σ_1	MeV/c^2	7.049 ± 0.026
σ_2	MeV/c^2	9.420 ± 0.091
$\delta = \delta_1 = \delta_2$	MeV/c^2	-0.120 ± 0.012
b	$[\text{GeV}/c^2]^{-1}$	48.5 ± 2.1
c	$[\text{GeV}/c^2]^{-1}$	47.9 ± 1.1

Table 4.7: Parameterization of the invariant $D^0\pi$-mass for $D^{*+} \to D^0\pi^+$ simulated events. See Fig. 4.22.

The tests justify the use of the FMC simulation to extract the invariant mass templates for all $B^0_{(s)} \to h^+h'^-$ signal modes.

4.10 Fit mass templates

In the previous chapter, in Sec. 3.10, the only templates the I weren't shown the mass templates. After the description of the developed fast parametric Monte Carlo and the checks, I used it to generate the needed distributions. The formula

Parameter	Units	(I)	(II)	Δ [%]
f_{bulk}	–	0.926	0.925 ± 0.003	0.1
f_1	–	0.606	0.606	
σ_1	MeV/c^2	7.049	7.02 ± 0.01	0.4
σ_2	MeV/c^2	9.420	10.35 ± 0.05	9.9
$\delta = \delta_1 = \delta_2$	MeV/c^2	-0.120	-0.120	
b	$[\text{GeV}/c^2]^{-1}$	48.5	48.5	
c	$[\text{GeV}/c^2]^{-1}$	47.9	47.9	
f_s	–	0.9683 ± 0.0003	0.976 ± 0.001	0.8
a_0	–	-0.444 ± 0.003	-0.465 ± 0.002	4.7
Δ_m	MeV/c^2	0.373 ± 0.008	0.367 ± 0.008	1.6
χ^2/ndof	–	2218.7/86	98.9/83	

Table 4.8: Fit on $D^{*+} \to D^0\pi^+$ data.(I) The signal shape is completely fixed from the FMC, we fitted only parameters f_s, a_0, δ_m. (II) Some parameters of the signal shape are left free to vary: f_s, a_0, δ_m plus f_{bulk}, σ_1, σ_2. $\Delta = \frac{\text{(I)}-\text{(II)}}{\text{(I)}}$. See Fig. 4.20.

used for each mass shape is in the form

$$pdf(m;\vec{\theta}) = f_{\text{FSR}} \cdot \left(\frac{\exp(b \cdot (m - M_B)) \cdot \text{erf}\,(c \cdot (m - M_B))}{\text{Norm}} \right) + \\ +(1 - f_{\text{FSR}}) \cdot \left(f_1 \cdot \frac{e^{\frac{-(m-M_B)^2}{2\sigma_1^2}}}{\sqrt{2\pi\sigma_1^2}} + (1 - f_1) \cdot \frac{e^{\frac{-(m-M_B)^2}{2\sigma_2^2}}}{\sqrt{2\pi\sigma_2^2}} \right) \tag{4.31}$$

where f_{FSR} is the fraction of the tail in the low-mass region, mainly due to the radiation, b and c are parameters for the tail shape; f_1 is the fraction between the first and second Gaussian used to model the bulk of each mass peaks. The mass templates are shown in Fig. 4.23 (a, b, c) for B^0 decays, in Fig. 4.23 (d) and Fig. 4.24 (a, b) for B_s^0 decays and in Fig. 4.24 (c, d) for Λ_b^0 decays. In Λ_b^0 decays, the effects of final state radiation are neglected, because the contribution of this effect in these modes is expected to be marginal in this context.

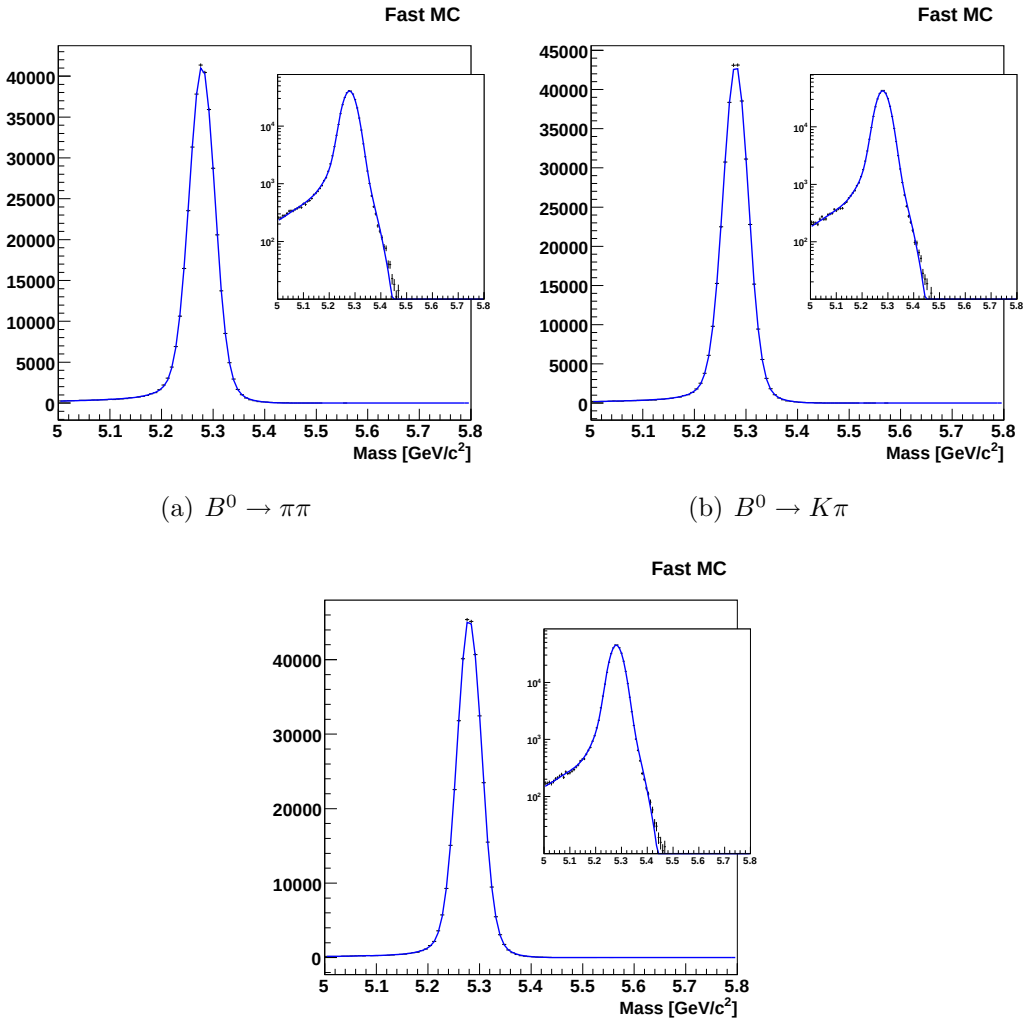

(a) $B^0 \to \pi\pi$

(b) $B^0 \to K\pi$

(c) $B^0 \to KK$

Figure 4.23: Mass templates extracted by the FMC for the B^0 decay modes. The line is the fit result using the function of (4.31).

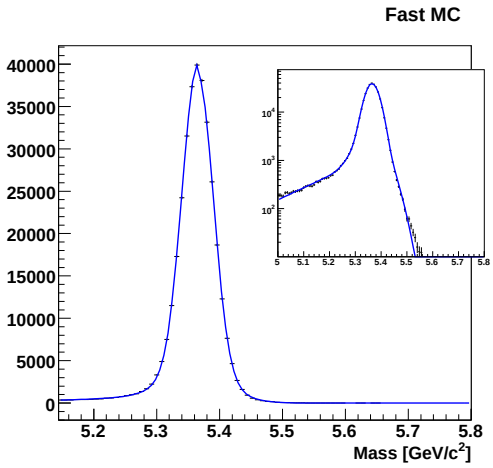

(a) $B_s^0 \to \pi\pi$

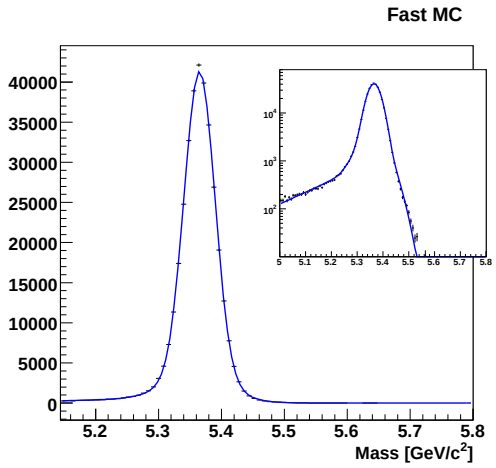

(b) $B_s^0 \to K\pi$

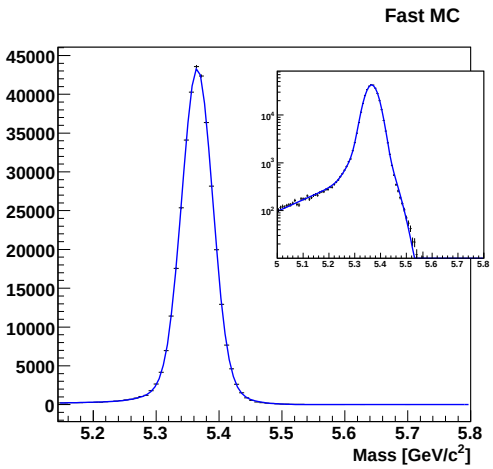

(c) $B_s^0 \to KK$

Figure 4.24: Mass templates extracted by the FMC for B_s^0 decay modes. The line is the fit result using (4.31).

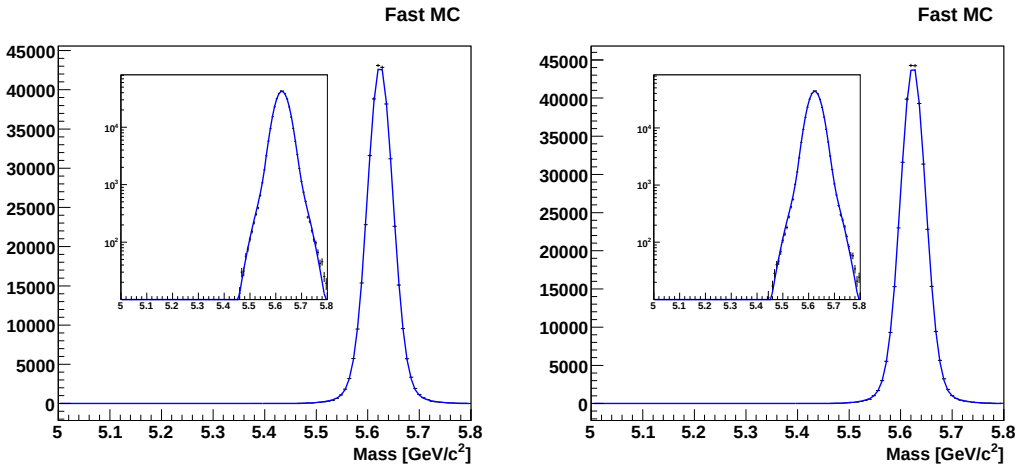

(a) $\Lambda_b^0 \to p\pi$ (b) $\Lambda_b^0 \to pK$

Figure 4.25: Mass templates for the Λ_B^0 decay modes. Note that the final state radiation was not included here. The line overlaid to the points follows the (4.31) with $f_{FSR} = 0$

Chapter 5

Final results

After describing the detailed study done for the b-charmless and other CDF analysis, here I show the results of the likelihood fit (Chap. 3) and the measurement of the relative branching ratios and direct A_{CP}. The total number of events used in the fit was 5563. The results of the fit are shown below. The subscript "raw" indicates that the fit output is not yet corrected for relative efficiencies.

$$A_{\mathsf{CP}}\Big|_{\text{raw}} = \frac{N_{\text{raw}}(\Lambda_b^0 \to p\pi^-) - N_{\text{raw}}(\overline{\Lambda}_b^0 \to \bar{p}\pi^+)}{N_{\text{raw}}(\Lambda_b^0 \to p\pi^-) + N_{\text{raw}}(\overline{\Lambda}_b^0 \to \bar{p}\pi^+)} = 0.02 \pm 0.17 \tag{5.1}$$

$$A_{\mathsf{CP}}\Big|_{\text{raw}} = \frac{N_{\text{raw}}(\Lambda_b^0 \to pK^-) - N_{\text{raw}}(\overline{\Lambda}_b^0 \to \bar{p}K^+)}{N_{\text{raw}}(\Lambda_b^0 \to pK^-) + N_{\text{raw}}(\overline{\Lambda}_b^0 \to \bar{p}K^+)} = 0.37 \pm 0.17 \tag{5.2}$$

$$\frac{N_{raw}(\Lambda_b^0 \to pK)}{N_{raw}(B^0 \to K\pi)} = 0.0486 \pm 0.0065 \tag{5.3}$$

$$\frac{N_{raw}(\Lambda_b^0 \to p\pi)}{N_{raw}(B^0 \to K\pi)} = 0.0325 \pm 0.0058 \tag{5.4}$$

parameter	fraction	yield	MINUIT code
$B^0 \to \pi^+\pi^-$ + c.c.	(0.149 ± 0.010)	625± 40	1
$B^0 \to K^+\pi^-$ + c.c.	(0.574 ± 0.013)	2398 ± 56	2
$A_{\mathsf{CP}}(B^0 \to K^+\pi^-)$	(-0.077 ± 0.028)	–	3
$B_s^0 \to K^-\pi^+$ + c.c.	(0.034 ± 0.006)	142 ± 27	4
$A_{\mathsf{CP}}(B_s^0 \to K^-\pi^+)$	(0.22 ± 0.19)	–	5
$B_s^0 \to K^+K^-$ + c.c.	(0.182 ± 0.010)	760 ± 41	–
$B_s^0 \to \pi^+\pi^-$ + c.c.	(0.004 ± 0.003)	17 ± 13	6
$B^0 \to K^+K^-$ + c.c.	(0.011 ± 0.005)	45 ± 20	7
$\Lambda_b^0 \to pK^-$ + c.c.	(0.028 ± 0.004)	116 ± 15	8
$A_{\mathsf{CP}}(\Lambda_b^0 \to pK^-)$	(0.37 ± 0.17)	–	9
$\Lambda_b^0 \to p\pi^-$ + c.c.	(0.019 ± 0.003)	78 ± 14	10
$A_{\mathsf{CP}}(\Lambda_b^0 \to p\pi^-)$	(0.01 ± 0.17)	–	11

Table 5.1: Raw physics results from the fit. By 'raw" we mean that the numbers have not been corrected for the relative efficiency factors.

Correlation matrix

The correlation matrix of the fit is shown at pag. 124. The legend for the fit parameters is in third column of Tab. 5.1 and Tab. 5.2.

parameter	value	MINUIT code
f_{π^+} (combinatorial)	0.536 ± 0.066	–
f_{e^+} (combinatorial)	0.085 ± 0.028	–
f_p (combinatorial)	0.079 ± 0.087	16
f_{K^+} (combinatorial)	0.299 ± 0.119	–
f_{π^-} (combinatorial)	0.583 ± 0.064	–
f_{e^-} (combinatorial)	0.056 ± 0.026	–
$f_{\bar{p}}$ (combinatorial)	0.173 ± 0.102	17
f_{K^-} (combinatorial)	0.188 ± 0.127	–
fraction of physics bckg (ARGUS norm.)	0.673 ± 0.034	22
ARGUS cut-off [GeV/c^2]	5.149 ± 0.001	23
ARGUS shape	4.528 ± 2.76	24
background fraction	0.249 ± 0.008	12
c_1 (background shape)	-0.130 ± 0.043	14

Table 5.2: Results for other fit parameters.

PARAMETER CORRELATION COEFFICIENTS

NO.	GLOBAL	1	2	3	4	5	6	7	8	9	10	11	12	14	16	17	18	19	20	21	22	23	24	27
1	0.65566	1.000																						
2	0.69963	-0.498	1.000																					
3	0.12497	-0.020	0.019	1.000																				
4	0.52757	-0.252	-0.042	0.004	1.000																			
5	0.21999	0.040	0.000	0.053	-0.128	1.000																		
6	0.51298	-0.059	-0.047	0.007	-0.299	0.026	1.000																	
7	0.48352	0.040	-0.397	-0.013	0.020	-0.008	0.002	1.000																
8	0.43234	-0.027	-0.116	0.004	-0.055	0.000	-0.028	0.020	1.000															
9	0.22143	-0.002	-0.016	0.007	-0.008	-0.014	0.001	0.015	0.112	1.000														
10	0.43842	-0.047	-0.122	0.005	0.007	-0.009	-0.014	0.019	-0.245	0.008	1.000													
11	0.29915	-0.001	0.002	0.023	0.003	-0.022	0.011	-0.001	0.054	-0.146	-0.075	1.000												
12	0.57841	0.021	0.113	-0.018	-0.069	0.030	-0.179	-0.142	-0.091	-0.057	-0.161	-0.003	1.000											
14	0.78407	-0.014	-0.113	0.020	0.081	-0.034	0.194	0.124	0.090	0.057	0.112	0.007	-0.492	1.000										
16	0.82659	0.001	0.004	0.009	0.008	0.011	0.018	0.004	-0.009	0.054	-0.020	0.033	-0.016	0.017	1.000									
17	0.87568	0.023	0.024	-0.036	-0.026	0.049	-0.015	-0.021	-0.041	-0.048	-0.065	-0.094	0.098	-0.112	-0.035	1.000								
18	0.82497	-0.027	-0.004	-0.033	0.027	0.077	-0.087	0.035	0.031	0.038	-0.023	-0.076	0.018	-0.046	0.734	0.038	1.000							
19	0.55636	-0.021	-0.038	-0.001	0.040	-0.018	0.050	0.040	0.040	0.051	0.052	0.012	-0.147	0.178	0.221	-0.069	-0.148	1.000						
20	0.86963	-0.014	0.008	-0.002	0.005	-0.016	-0.090	0.016	0.018	-0.018	-0.043	-0.006	0.069	-0.095	-0.042	0.808	0.025	-0.043	1.000					
21	0.52011	0.001	-0.020	0.006	0.003	-0.005	0.033	0.020	0.020	-0.003	0.001	-0.002	-0.055	0.064	0.034	0.174	0.024	0.031	-0.127	1.000				
22	0.81782	-0.023	-0.142	0.021	0.092	-0.040	0.234	0.115	0.119	0.071	0.193	0.006	-0.540	0.776	0.011	-0.135	-0.051	0.200	-0.107	0.070	1.000			
23	0.07697	-0.001	0.001	0.001	-0.001	0.000	-0.003	0.012	-0.002	-0.001	-0.003	-0.000	-0.005	-0.010	-0.001	0.002	0.001	-0.000	0.003	-0.002	-0.015	1.000		
24	0.23882	0.000	0.016	-0.001	-0.017	0.005	-0.043	0.064	-0.020	-0.009	-0.032	0.001	0.008	-0.141	0.002	0.009	0.018	-0.022	0.020	-0.012	-0.182	-0.065	1.000	
27	0.28394	0.000	0.016	-0.004	-0.027	0.011	0.006	0.024	-0.051	-0.020	-0.036	-0.004	0.069	-0.138	0.040	0.083	-0.039	-0.045	-0.011	-0.002	-0.157	0.003	0.032	1.000

5.1 Fitter checks

5.1.1 Mass scale

The central fit is performed by assuming a known global mass scale, in which we assigned to the B^0, B_s^0 and Λ_b^0 masses the values measured by CDF in Run II [79]. Since the mass is one of the information used in separating the different contributions, it is good to check how the fit behaves when the mass scale is allowed to float. An additional free parameter Δ was therefore added to the fit in the parameterization of the input masses: $m^{\rm fit}_{B_s^0} = m^{\rm CDFII}_{B_s^0} + \Delta$, $m^{\rm fit}_{B^0} = m^{\rm CDFII}_{B^0} + \Delta$ and $m^{\rm fit}_{\Lambda_b^0} = m^{\rm CDFII}_{\Lambda_b^0} + \Delta$ and the global scale of masses is determined to be: 1.6 ± 0.8 MeV/c^2. The difference $-2\Delta logL$ between the our central fit and the fit with the free mass scale is $= -4$, while the fitted value of the shift is just 2σ off the chosen nominal value. This confirms the assumption on mass values.

5.1.2 Fit projections

In order to visualize the agreement between the fit and the data, we reported the plots of the fit *projections*. In figures 5.1 and 5.2 projections for variable: $M_{\pi\pi}$, α, p_{tot}, κ_1, κ_2, $\kappa_1 + \kappa_2$, and $\kappa_1 - \kappa_2$ are shown in the whole mass range; in 5.3 and 5.4 there are the same kind of plots but for the Λ_b^0 signal region only, with $M_{\pi\pi} \in [5.35, 5.6]$ GeV/c^2. The agreement between data and fit function appears to be completely satisfactory.

5.1.3 Relative Likelihood

To better visualize the capability of the fit to separate Λ_b^0 decay samples from background and Λ_b^0 from $\bar{\Lambda}_b^0$ we also used the *relative likelihood* variable, defined as:

$$RL = \frac{P_s}{P_s + P_b} \tag{5.5}$$

where P_s is the total p.d.f. for the signal, function of the discriminating observables, and P_b is the p.d.f. for the background, where background in this case is identified as any another signal in the p.d.f. excluding the chosen one. Evaluating this quantity in a true Λ_b^0 event would yield likely a number close to one, while for a background event it would yield a number close to zero. Figures 5.5, 5.6, and 5.7 show that the fitter has indeed strong capability of separating Λ_b^0 from $\bar{\Lambda}_b^0$ and from background.

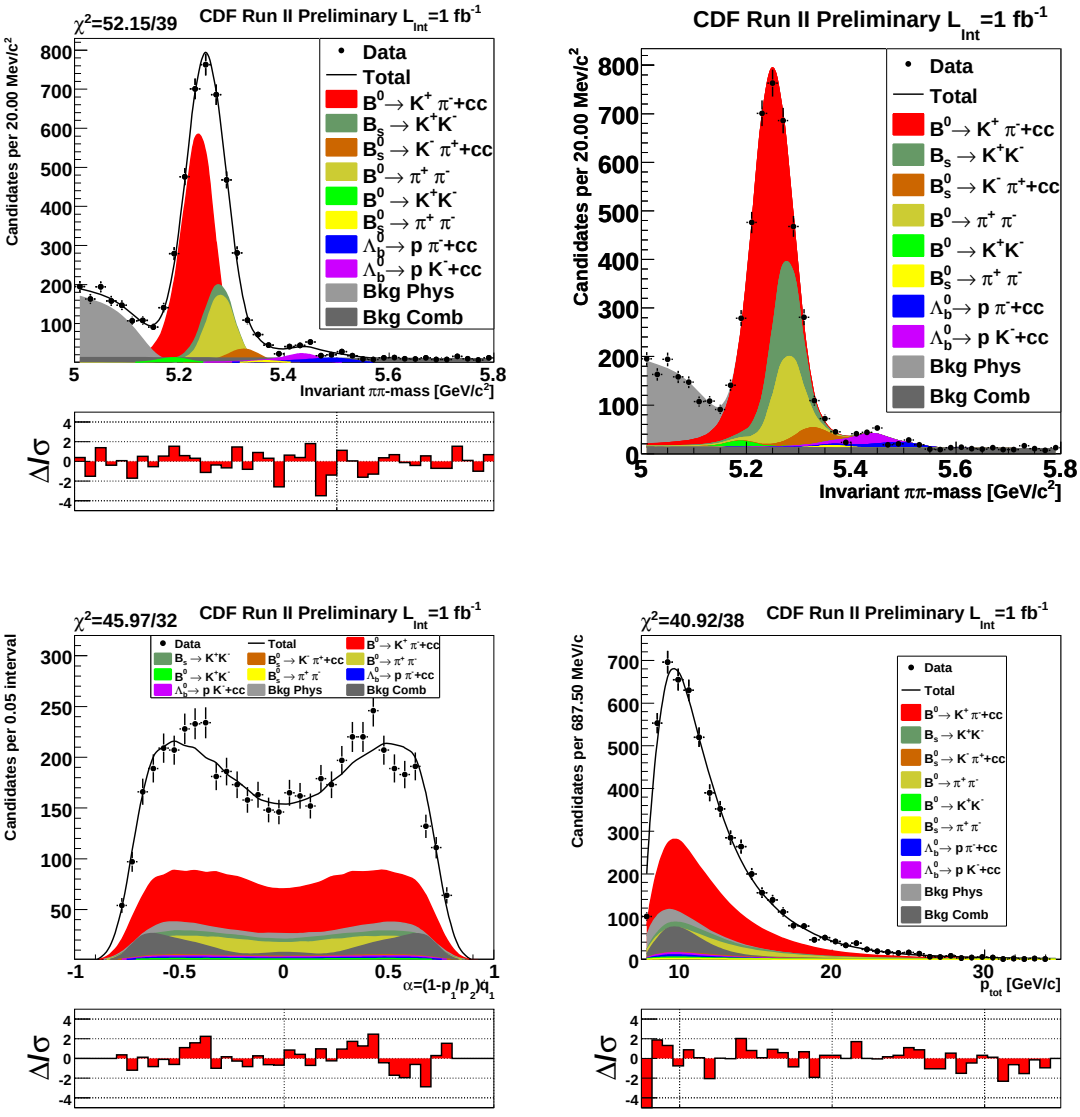

Figure 5.1: Fit projections in all mass range onto $m_{\pi\pi}$, α, p_{tot} variables.

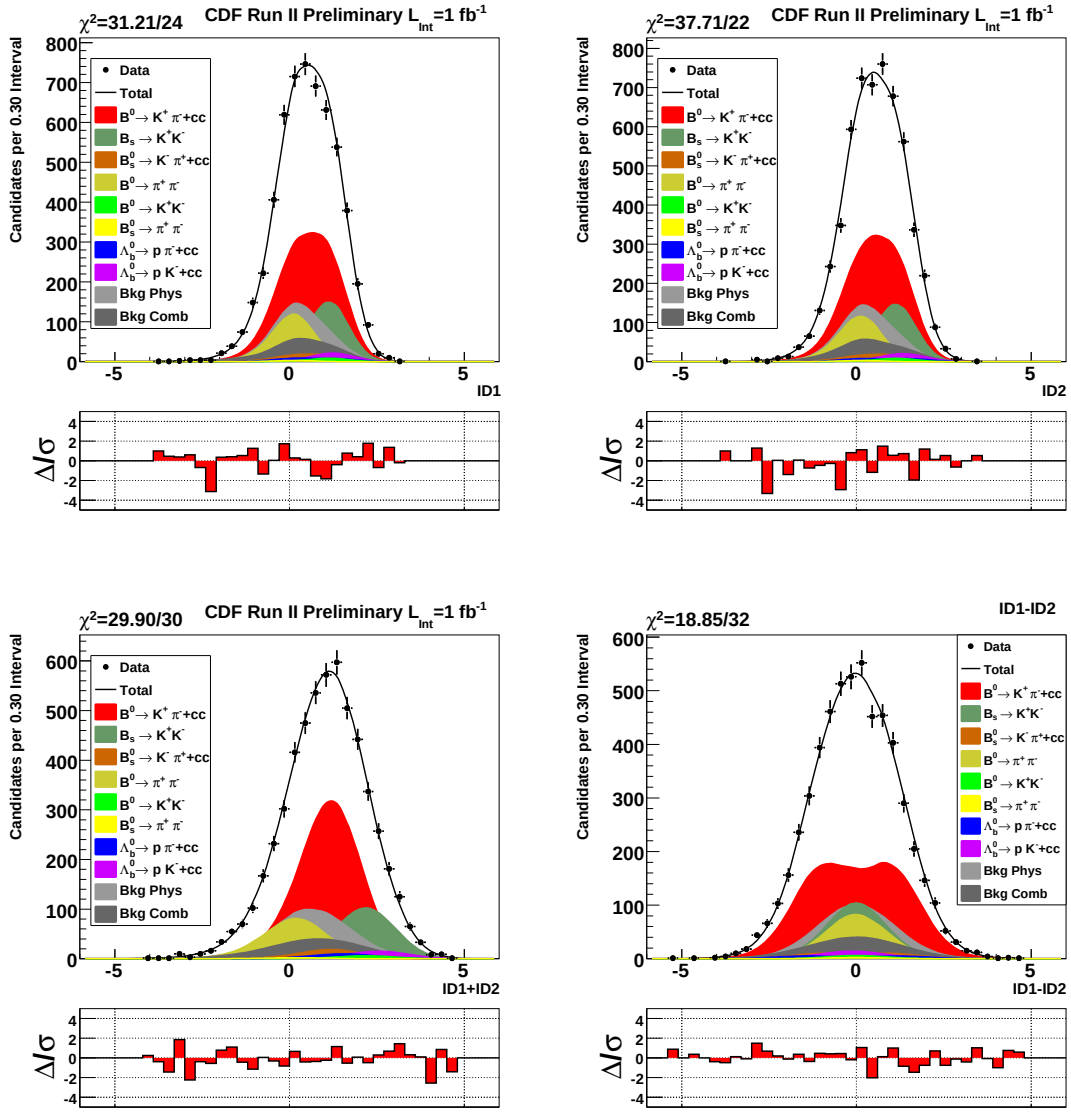

Figure 5.2: Fit projections in all mass range onto the $\kappa_{\min}$, $\kappa_{\max}$, $\kappa_{\min} + \kappa_{\max}$, $\kappa_{\min} - \kappa_{\max}$ variables.

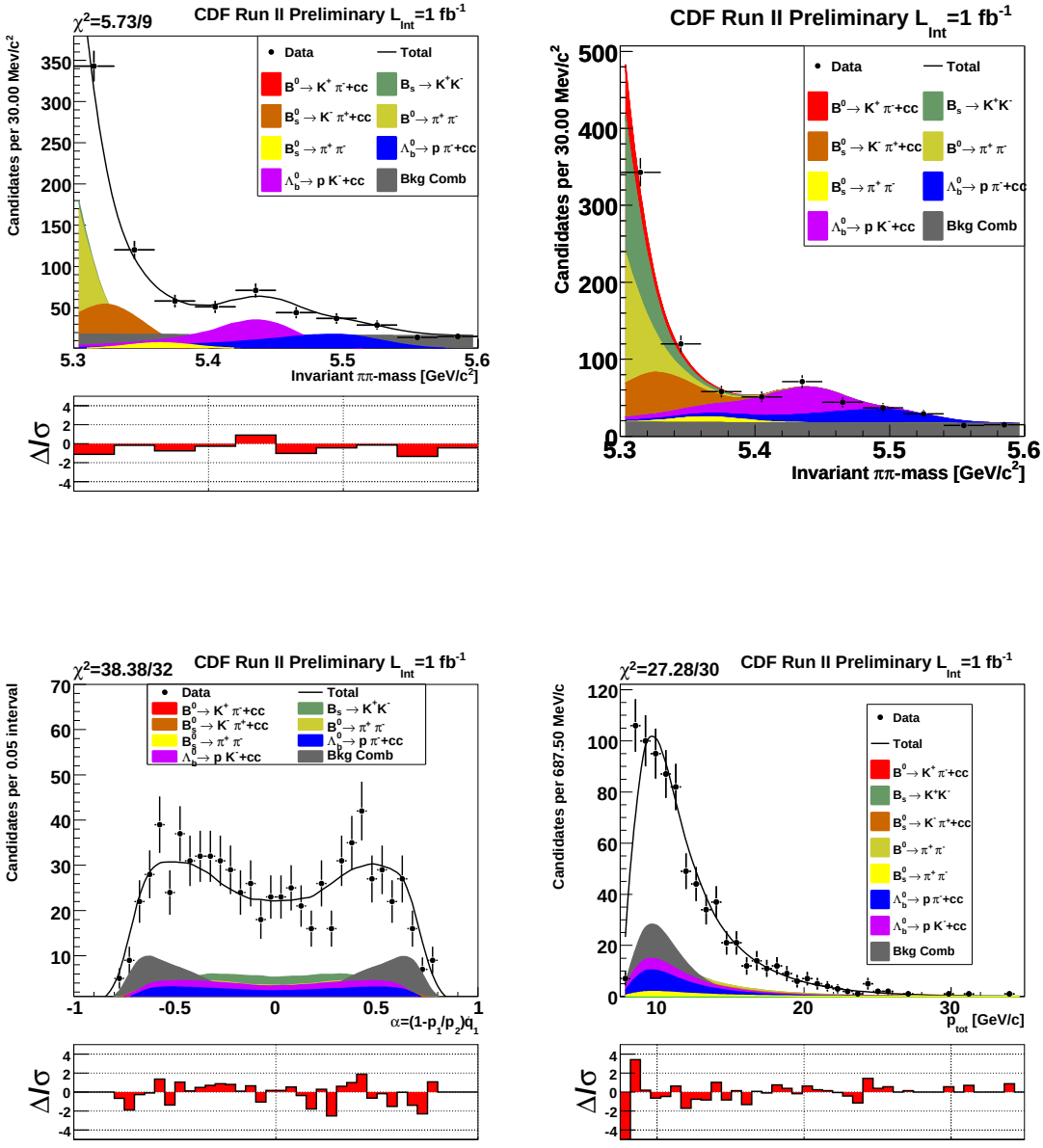

Figure 5.3: Fit projections in the Λ_b^0 mass range ($5.35 < m_{\pi\pi} < 5.6$ GeV/c^2) onto the $m_{\pi\pi}$, α, p_{tot} variables.

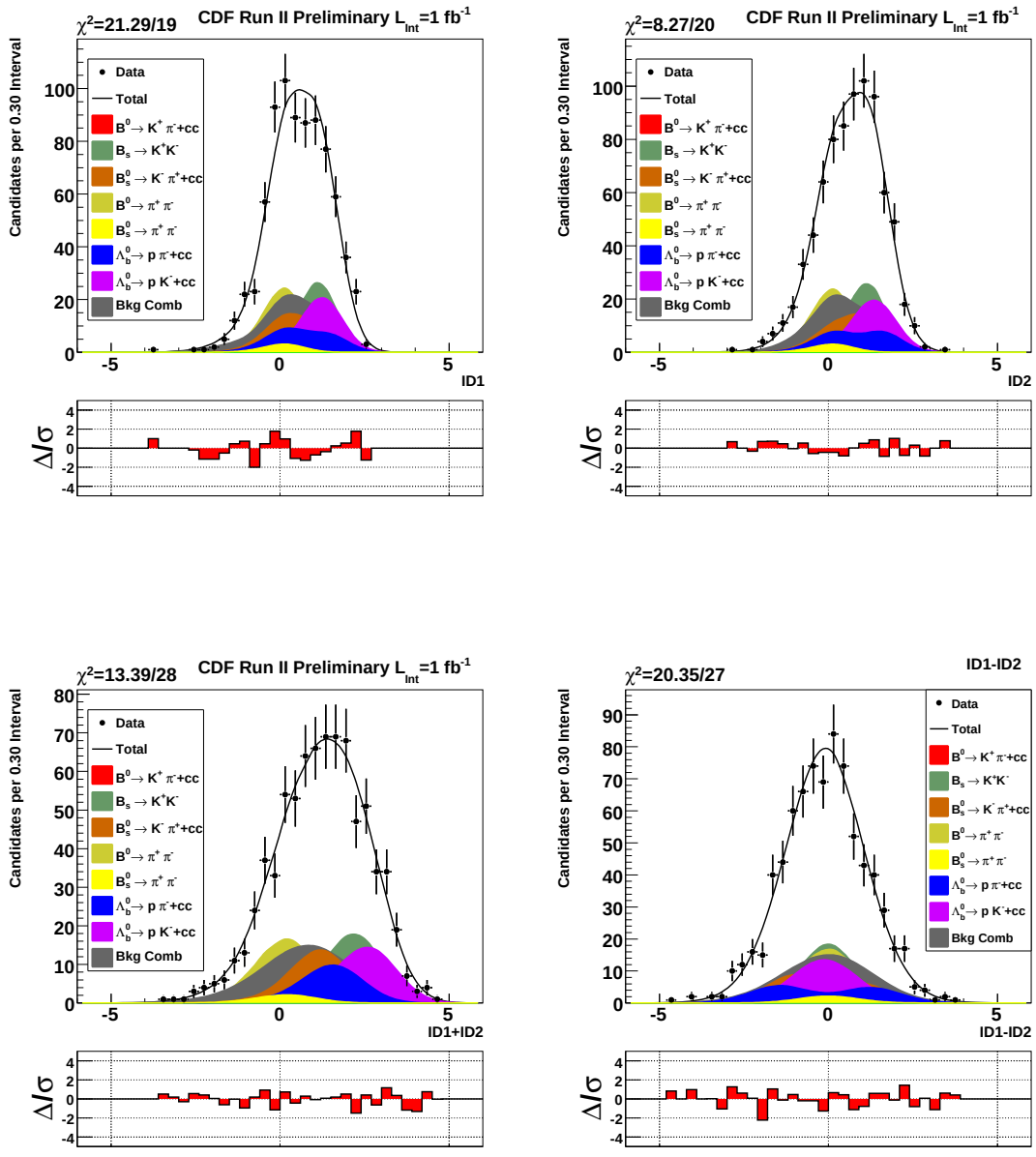

Figure 5.4: Fit projections in the Λ_b^0 mass range ($5.35 < m_{\pi\pi} < 5.6$ GeV/c^2) onto the $\kappa_{\min}$, $\kappa_{\max}$, $\kappa_{\min} + \kappa_{\max}$, $\kappa_{\min} - \kappa_{\max}$ variables.

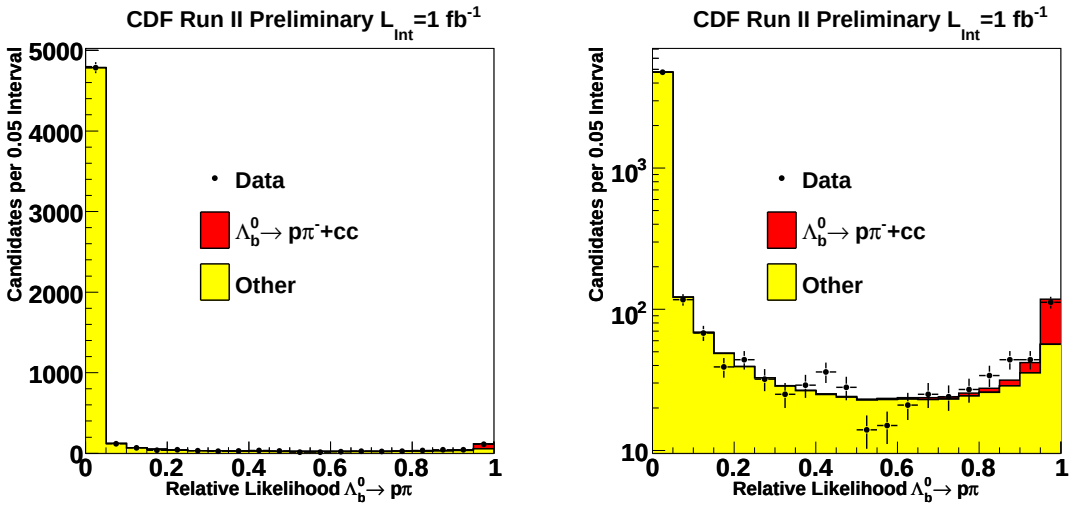

Figure 5.5: Relative Likelihood for $\Lambda_b^0 \to p\pi^-$vs background in the signal mass region ($5.1 < m_{\pi\pi} < 5.6$ GeV/c^2).

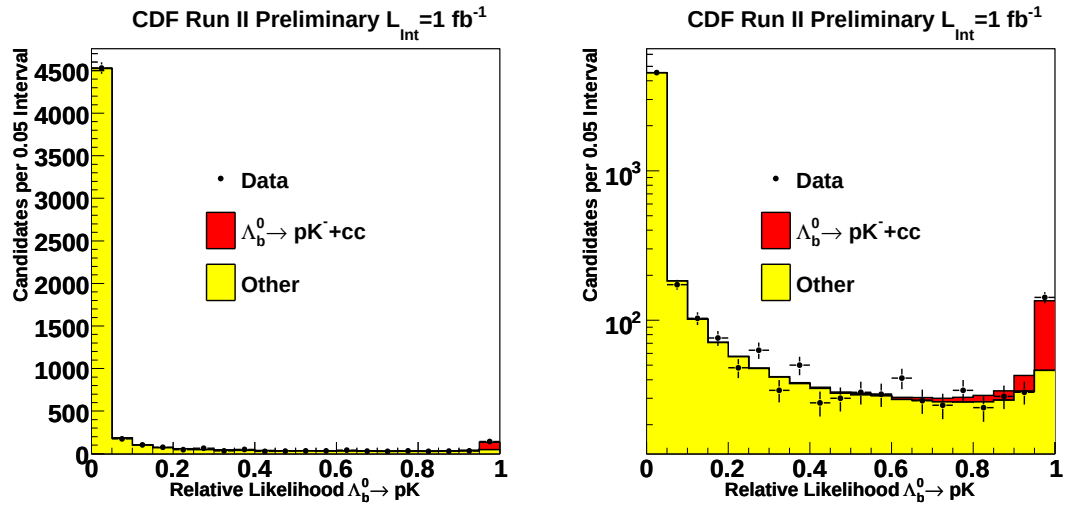

Figure 5.6: Relative Likelihood for $\Lambda_b^0 \to pK^-$vs background in the signal mass region ($5.1 < m_{\pi\pi} < 5.6$ GeV/c^2).

5.1.4 Pulls and likelihood scans

We applied the fitting procedure to about 500 pseudo-experiments generated according our global p.d.f., and fluctuating the true values around those found by the fit on data. All fit pulls have Gaussian distributions centered in zero and unit variance, as shown in Fig. 5.8 and 5.9, thus giving confidence on the correctness and unbiasedness of our results.

The only detectable bias in the pulls of physics parameter affects the $B_s^0 \to \pi^+\pi^-$ fraction, which seems to be biased by -0.3. We further investigated this effect with higher statistics pseudo-experiments, and we found that the effect is an artifact of the $B_s^0 \to \pi^+\pi^-$ fraction being constrained to be positive, combined with the negligible fraction $B_s^0 \to \pi^+\pi^-$ in our sample: the fitter tends to estimate zero $B_s^0 \to \pi^+\pi^-$ events, but since the fraction is constrained to be positive the numerical minimization is prevented from exploring values of the $B_s^0 \to \pi^+\pi^-$ fraction around zero. With an higher statistics sample and a $B_s^0 \to \pi^+\pi^-$ fraction free-to float, the bias was found to disappear. In either case, no influence on the Λ_b^0-related fit parameters was observed.

We also monitored the profile of the likelihood nearby the minimum as a function of the fit parameters of interests (likelihood scans). The corresponding plots are shown in fig. 5.10. The plots show smooth profiles without no pathologies are visible.

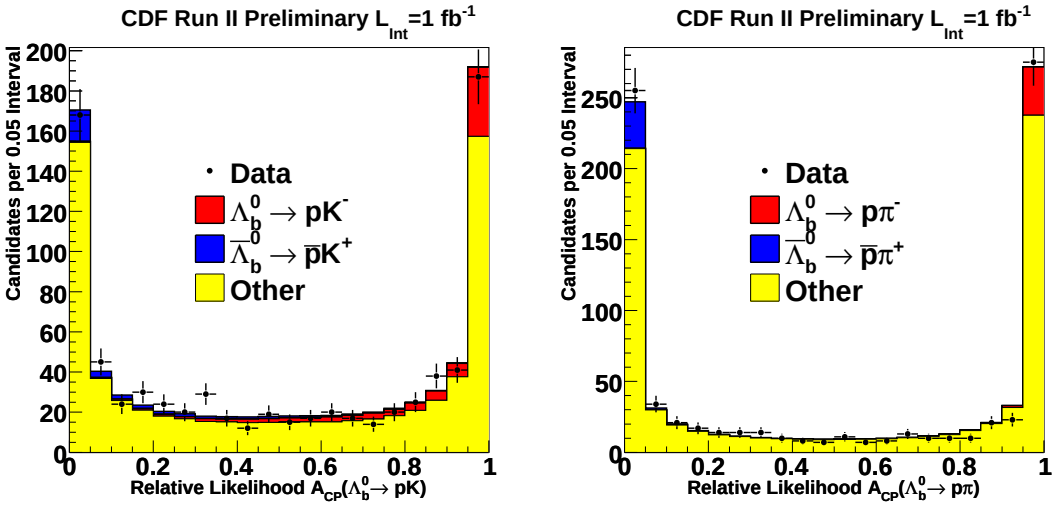

Figure 5.7: Relative Likelihood for the CP-violating asymmetries in the signal mass region ($5.1 < m_{\pi\pi} < 5.6$ GeV/c^2).

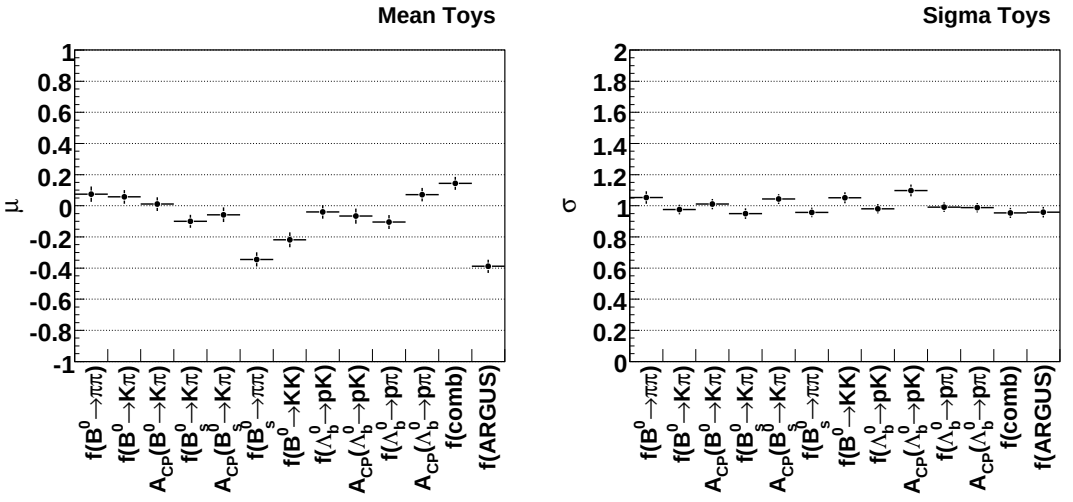

Figure 5.8: Summary of fit results of pulls to Gaussian distributions

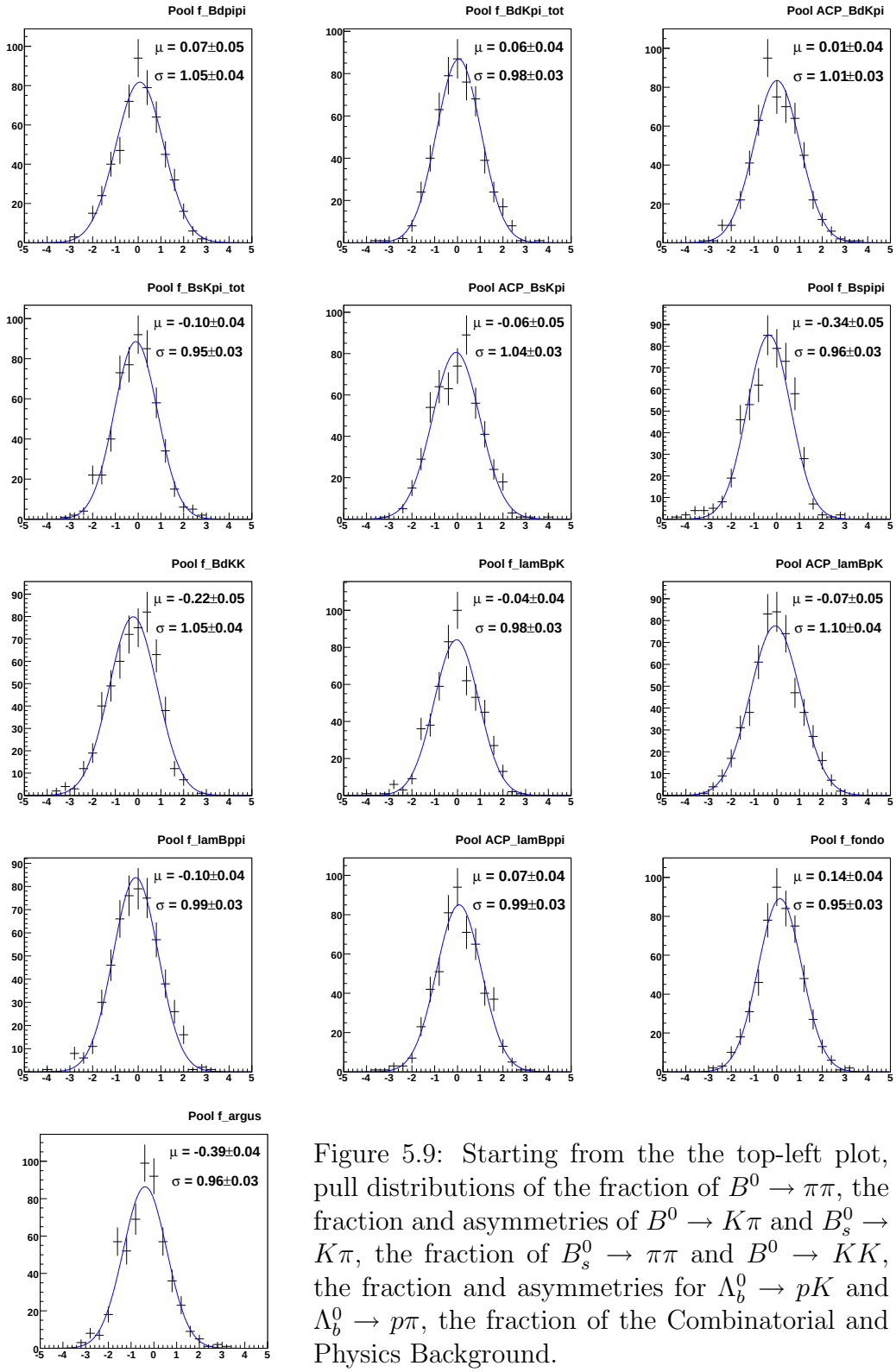

Figure 5.9: Starting from the the top-left plot, pull distributions of the fraction of $B^0 \to \pi\pi$, the fraction and asymmetries of $B^0 \to K\pi$ and $B_s^0 \to K\pi$, the fraction of $B_s^0 \to \pi\pi$ and $B^0 \to KK$, the fraction and asymmetries for $\Lambda_b^0 \to pK$ and $\Lambda_b^0 \to p\pi$, the fraction of the Combinatorial and Physics Background.

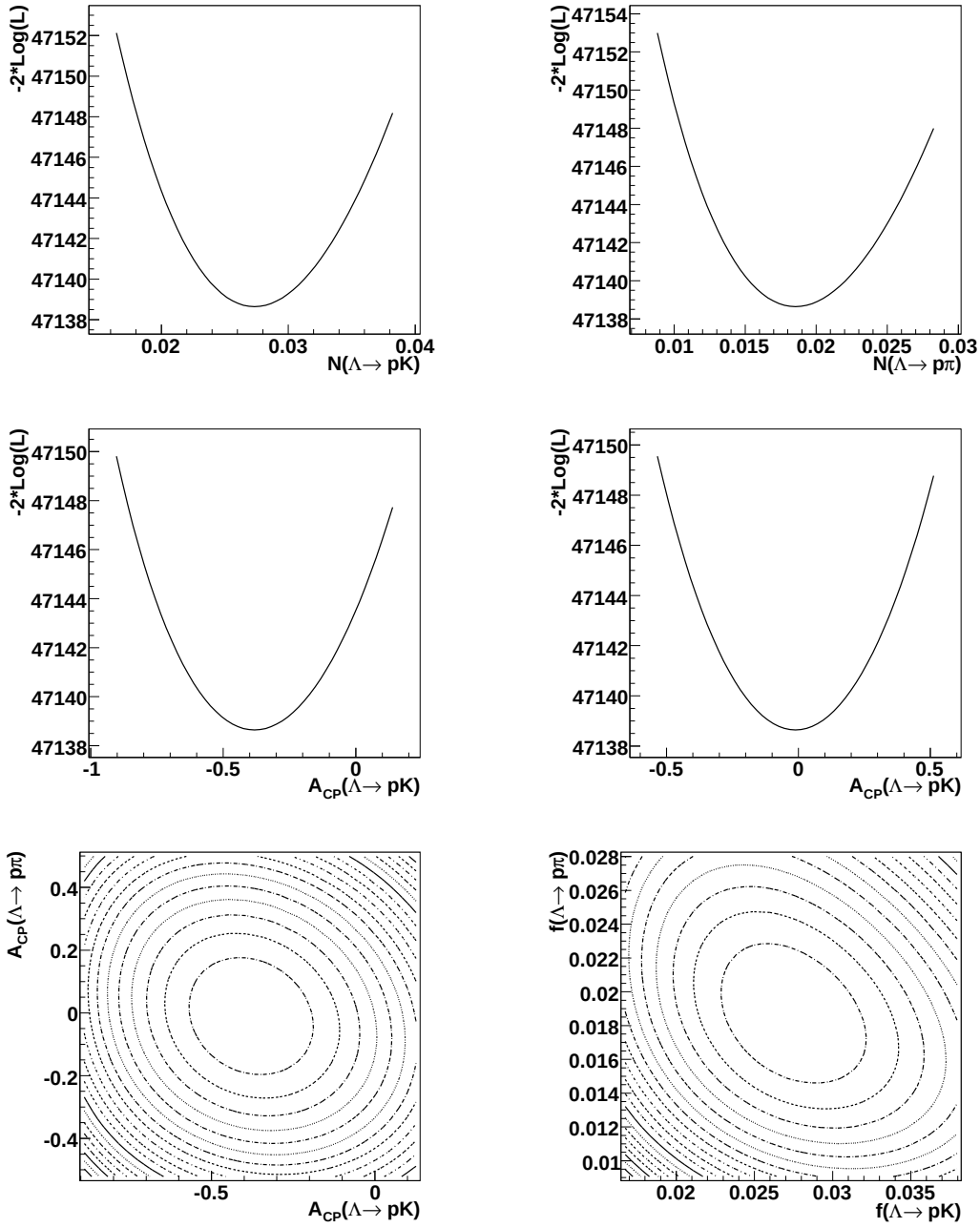

Figure 5.10: Likelihood scans for the main variables.

5.2 Efficiency corrections

In order to convert into measurement of CP-violating asymmetries and relative branching fractions the raw fit results must be corrected for all relevant differences in acceptance and efficiency.

5.2.1 Efficiency correction for the measurement of the direct CP-violating asymmetry

The differential decay rate between particles and antiparticles needs to be corrected for the effect of different hadronic interaction with matter of positively- and negatively-charged protons, kaons, and pions as follows:

$$A_{\mathsf{CP}}(\Lambda_b^0 \to ph) = \frac{N_{\rm raw}(\Lambda_b^0 \to ph^-) \cdot \frac{\varepsilon(ph^+)}{\varepsilon(\bar{p}h^-)} - N_{\rm raw}(\bar{\Lambda}_b^0 \to \bar{p}h^+)}{N_{\rm raw}(\Lambda_b^0 \to ph^-) \cdot \frac{\varepsilon(ph^+)}{\varepsilon(\bar{p}h^-)} + N_{\rm raw}(\bar{\Lambda}_b^0 \to \bar{p}h^+)} \tag{5.6}$$

We used a sample of $1\,\mathrm{fb}^{-1}$ $\Lambda \to p\pi$ decays to determine from data the efficiency ratios $\varepsilon(p\pi^-)/\varepsilon(\overline{p}\pi^+)$ and $\varepsilon(pK^-)/\varepsilon(\overline{p}K^+)$. The Λ^0 in this decay channel is not expected to show charge asymmetry, so if an asymmetry is found in the number of the Λ^0 with respect to the $\bar{\Lambda}^0$ this is due to the detection asymmetry.

Quantity	Requirement
$p_T(sum)$	$> 1.1\,\mathrm{GeV}/c$
χ^2_{xy}	< 10
$\lvert z0_1 - z0_2\rvert$	$< 2\,\mathrm{cm}$
L_{xy}	$\geq 5\,mm$
$M_{\pi\pi}$	$\in [.5, 1.5]\,\mathrm{GeV/c^2}$
$Q_1 \cdot Q_2$	< 0
$alg_{1,2}$	11
$\lvert d0_{1,2}\rvert$	$\leq 1\,\mathrm{mm}$
$p_T(p)$	$> 2\,\mathrm{GeV}/c$

Table 5.3: Selection requirements for reconstructing the Λ^0 signal.

We reconstructed $\Lambda^0 \to p\pi^-$ decays, which enter the two-track trigger sample as volunteers, the cuts to reconstruct the signal are listed in Tab. 5.3. The kinematic features of this sample make it possible to unambiguously distinguish Λ^0 from $\bar{\Lambda}^0$ decays, simply by evaluating the invariant mass under the hypothesis that the momentum of the proton is always greater than the pion's (kaon's) one. In fact,

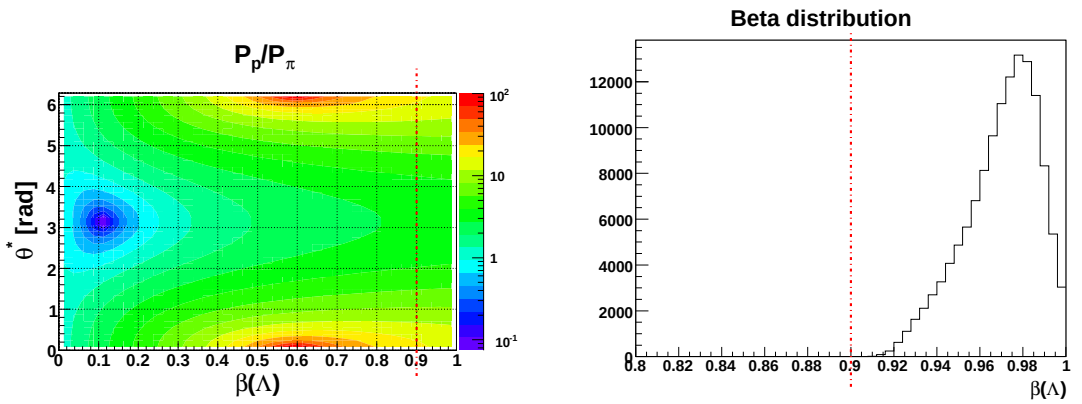

Figure 5.11: Values of the p_p/p_π ratio as a function of θ^* and β (left plot). Distribution of β for the Λ^0 in our sample.

the ratio of those momenta is given by the following expression:

$$\frac{p_p}{p_\pi} = \sqrt{\frac{(\beta\gamma E_p^* + \gamma p_p^* \cos(\theta^*))^2 + \left(p_p^* \sin(\theta^*)\right)^2}{(\beta\gamma E_\pi^* - \gamma p_\pi^* \cos(\theta^*))^2 + (p_\pi^* \sin(\theta^*))^2}} \tag{5.7}$$

which is function of the angle (in the plane of the decay) between decay-products in the center-of-mass frame (θ^*) and of their velocity (β). The values of the ratio of momenta based on the above formula are plotted in left plot of the figure 5.11. Clearly, the only cases in which the momentum of the pion (or kaon) is larger than the proton momentum occur in a very non-relativistic limit in which $\beta \approx 0.1$. Since our sample contains only relativistic Λ^0, i.e. their velocity is $0.9 < \beta < 1$ (see fig. 5.11, right plot), our choice of mass assignment is always correct and we obtain a perfect kinematic separation between Λ^0 and $\bar{\Lambda}^0$.

Assuming the production rate of Λ^0 and $\bar{\Lambda}^0$ to be equal, any residual asymmetry in the relative yield of Λ^0 and $\bar{\Lambda}^0$ is caused by asymmetries of the tracking system in the reconstruction of the $p\pi^-$ and $\bar{p}\pi^+$ pairs. The tracking system has an asymmetry in the reconstruction of π^+ and π^- with low momentum [84]; this asymmetry varies with the p_T, but reaches a plateau for a p_T of the pion greater than 0.7 GeV/c. In Fig. 5.13 shows the asymmetry we observe in the Λ^0 and $\bar{\Lambda}^0$ candidate yields, as function of the pion transverse momentum. This plot is in very good agreement with Fig. 5.14 and indicates that for decays in which the pion momentum exceeds 0.7 GeV/c any residual momentum dependence becomes negligible. So we added this cut to avoid this effect.

Fig. 5.12 shows some enhancements in the $\Lambda^0/\bar{\Lambda}^0$ yield for L_{xy} values corresponding to the average radii of the inner silicon layers. To also avoid possible effects of the material extracting the charge asymmetry, we require that the can-

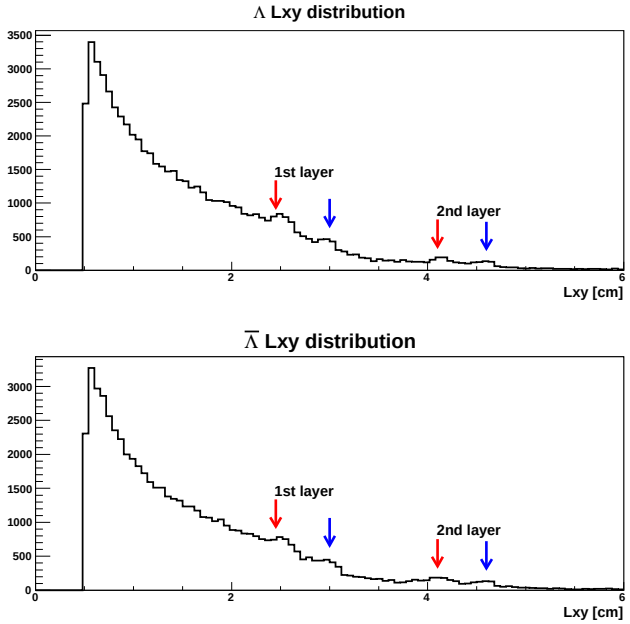

Figure 5.12: Number of reconstructed Λ^0 or $\bar{\Lambda}^0$ as function of L_{xy}.

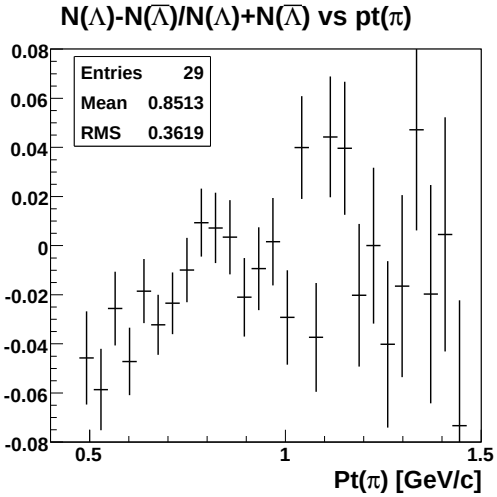

Figure 5.13: Asymmetry in the Λ^0 and $\bar{\Lambda}^0$ yields as a function of the pion transverse momentum

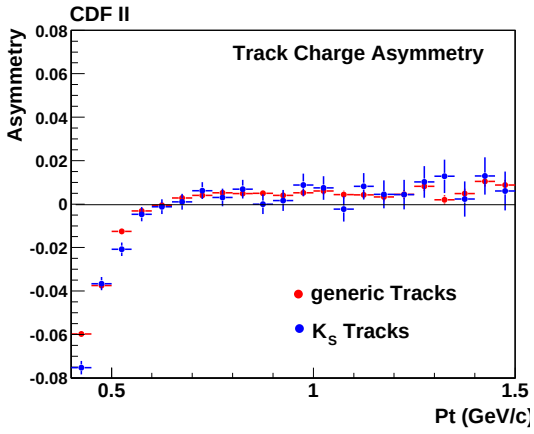

Figure 5.14: Asymmetry in the number of reconstructed charged pion tracks, plot from [84].

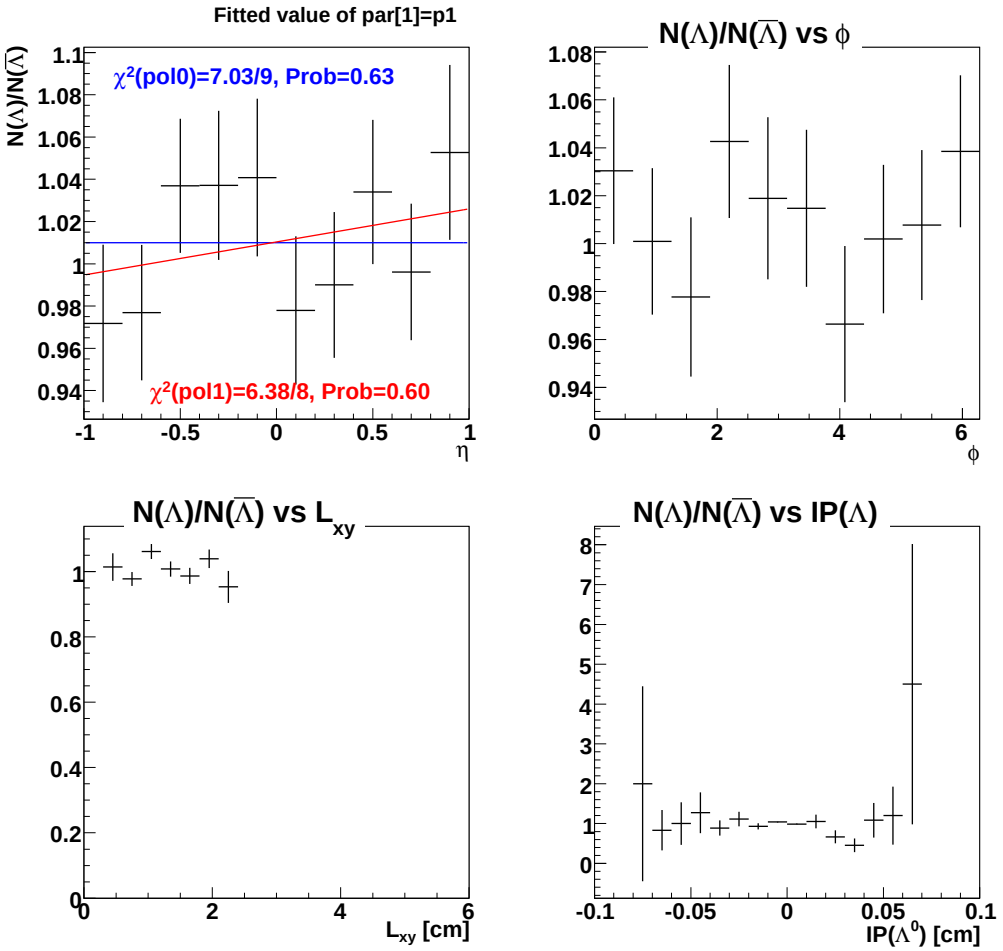

Figure 5.15: Dependence of the $\Lambda^0/\bar{\Lambda}^0$ ratio of yields as a function of η, ϕ, $L_{xy}(\Lambda^0)$, and $d_0(\Lambda^0)$.

didates satisfy: $L_{xy} < 2.2$ cm and $p_T(\pi) > 0.7$ GeV/c, in addition to the cuts of Table 5.3. Fig. 5.16(a) shows the ratio of Λ^0 and $\bar{\Lambda}^0$ as function of $1/p_T$ of the tracks. No dependence on the momenta is seen in these plots.

As a further check, we searched for possible variations of the Λ^0 asymmetry within the detector volume and as a function of displacement of the (anti)-baryon from the primary vertex. No dependencies are found, as shown in fig. 5.15.

Therefore using the above selection we reconstructed the mass peaks for the $\Lambda^0 \to p\pi^-$ and $\bar{\Lambda}^0 \to \bar{p}\pi^+$ signals. The detector-induced asymmetry in $\Lambda^0 \to p\pi$ decays is determined through a simple likelihood fit. The likelihood is:

$$\mathcal{L} = \frac{(N_\Lambda + N_{\bar{\Lambda}})^{N_{evt}}\, e^{-N_\Lambda - N_{\bar{\Lambda}}}}{N_{evt}} \prod_{i=1}^{N_{evt}} pdf(M) \tag{5.8}$$

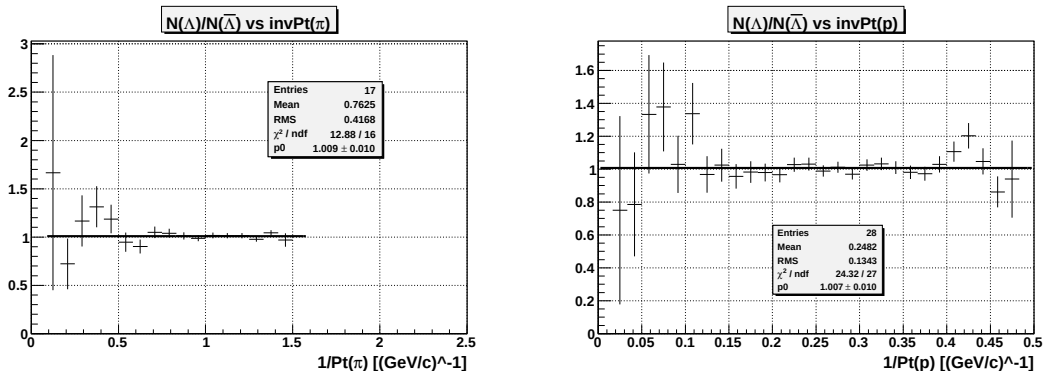

(a) Ratio as function of the inverse p_T of π (b) Ratio as function of the inverse p_T of p

Figure 5.16: $N(\Lambda)/N(\bar{\Lambda})$ ratio as function pion and proton inverse transverse momentum.

in which N_{evt} is the total number of event, $N_l = N_l(sgn)+N_l(bkg)$, with $l = \Lambda^0, \bar{\Lambda}^0$, is the total number of signal and background candidates, and M is the mass. The *pdf* for the mass distribution was the same for both channel, expressed as:

$$pdf(M) = f_s\big(f_1 G_1(M;\mu,\sigma_1) + (1-f_1)G_2(M;\mu,\sigma_2)\big) + \\ +(1-f_s)\frac{1+a\cdot M}{\int(1+a\cdot M)dM} \tag{5.9}$$

the free parameters are: $f_s = N_l(sgn)/(N_l(sgn)+N_l(bkg))$, the signal ratio, f_1 the fraction for the first Gaussian, μ the central mass and the two Gaussians, $\sigma_{1,2}$ the standard deviation of the 1st and the 2nd Gaussian, a the background shapes; fitting together Λ^0 and $\bar{\Lambda}^0$ the fit gives also the A_{CP} asymmetry for the signal and the backgrounds.

The fit results are shown in Fig. 5.17 and Table 5.4. From these results we obtained the needed correction factor:

$$\frac{\epsilon(p\pi^-)}{\epsilon(\bar{p}\pi^+)} = 1.0145 \pm 0.0075\ (stat.) \qquad \frac{\epsilon(\bar{p}\pi^+)}{\epsilon(p\pi^-)} = 0.9857 \pm 0.0074\ (stat.) \tag{5.10}$$

To extract the correction for the pK^- and $\bar{p}K^+$ asymmetry, we exploit the very reasonable assumption: $\epsilon(p\pi^-)/\epsilon(\bar{p}\pi^+) = \epsilon(p)\cdot\epsilon(\pi^-)/\epsilon(\bar{p})\cdot\epsilon(\pi^-)$. Then, from [85] we can use:

$$\frac{\epsilon(K^-\pi^+)}{\epsilon(K^+\pi^-)} = 0.9837 \pm 0.0027$$

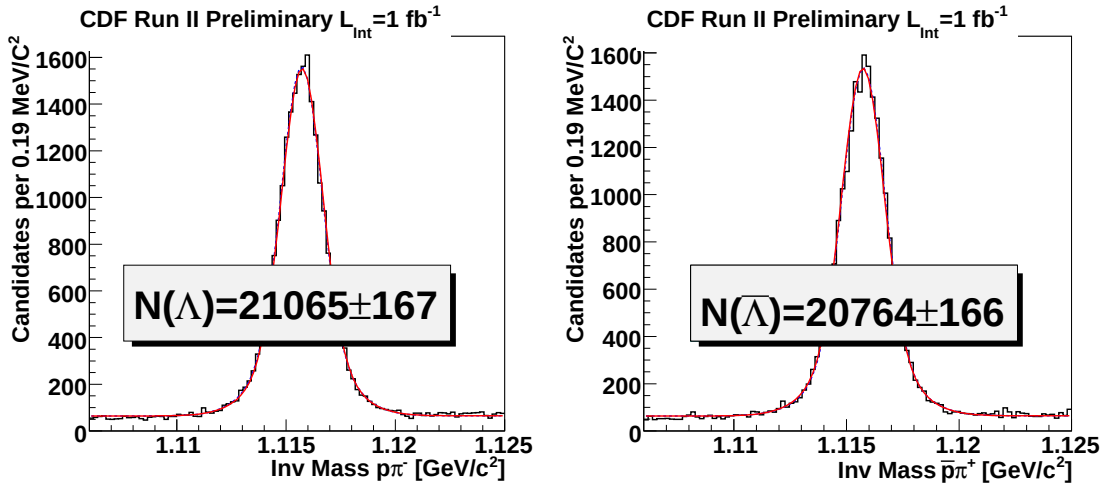

(a) Λ^0 (b) $\bar{\Lambda}^0$

Figure 5.17: Λ^0(a) and $\bar{\Lambda}^0$(b) mass peaks. Overlaid is the result of a simultaneous fit that measures the mass shape parameters and the charge asymmetry for the signals and the background.

Quantity	Estimate
Λ^0 yield	$(209140 \pm 13) \times 10^3$
f_1	0.700 ± 0.033
μ [MeV/c²]	$1115.740 \pm 6 \cdot 10^{-03}$
σ_1 [MeV/c²]	0.91 ± 0.02
σ_2 [MeV/c²]	1.8 ± 0.08
background yield	6447 ± 90
a	42.2 ± 3.0
$A_{CP}(\Lambda^0)$ [%]	0.72 ± 0.53
A_{CP}(bckg) [%]	0.89 ± 1.1

Table 5.4: Results of the fit that determines the detector-induced asymmetries in the Λ^0 sample.

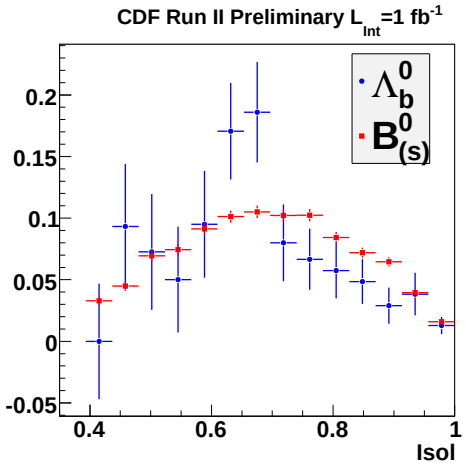

Figure 5.18: Comparison between isolation distributions of B mesons and Λ_b^0 baryons in our sample, obtained through the ${}_s$Plot technique. To obtain this plot we select a sample satisfying all the requirements but removing the isolation cut.

which in combination with (5.10) gives the result

$$\frac{\epsilon(pK^-)}{\epsilon(\bar{p}K^+)} = 0.9979 \pm 0.0079\ (stat.) \qquad \frac{\epsilon(\bar{p}K^+)}{\epsilon(pK^-)} = 1.0020 \pm 0.0079\ (stat.) \tag{5.11}$$

5.2.2 Efficiency corrections for the measurement of the relative branching fraction

The relative efficiencies for charmless Λ_b^0 decays with respect to the $B^0 \to K\pi$ decay are factorized into kinematic efficiencies and isolation efficiency.

The kinematic efficiency accounts for detector acceptances and for trigger (including XFT) and selection efficiency. This is determined using our simulated samples, by simply counting how many of initial events survive the trigger and detector simulation and the subsequent selection. The result is then re-weighted for the different probability that a kaon, a proton, or a pion have to trigger the XFT track processor, due to the differences in ionization between these particles since this effect is not accounted for by the CDF simulation. The momentum-dependent re-weight factor used is the official one as determined from real data[70]. The re-

sults are the following:

$$\frac{\epsilon_{\rm kin}(B^0 \to K^+\pi^-)}{\epsilon_{\rm kin}(\Lambda_b^0 \to p\pi^-)} = 1.28 \pm 0.01(stat.) \pm 0.05(XFT) \quad (5.12)$$

$$\frac{\epsilon_{\rm kin}(B^0 \to K^+\pi^-)}{\epsilon_{\rm kin}(\Lambda_b^0 \to pK^-)} = 1.36 \pm 0.01(stat.) \pm 0.05(XFT) \quad (5.13)$$

The above efficiency does not include the effect coming from a possible difference between isolation spectra of B^0 and Λ_b^0 hadrons, which would cause a difference in relative efficiency due to the isolation cut used in our selection. In order to check for this possibility we made an $_s$Plot as I showed in Sec. 3.8.1 to compare between the isolation of the $B^0_{(s)}$ candidates with respect to the Λ_b^0 candidates, Fig 5.18 shows the comparison of isolation distribution for the two candidates. Based on this agreement shown by this plot, we apply no correction for the isolation cut, but conservatively assign a 10% uncertainty to the relative efficiency, to account for the possibility of small differences not visible with the current statistics.

$$\frac{\epsilon_{\rm iso}(B^0)}{\epsilon_{\rm iso(\Lambda_b^0)}} = 1.0 \pm 0.1(stat.) \quad (5.14)$$

5.3 Corrected results

After applying the correction factors we obtain the following results for the asymmetries:

$$A_{\mathsf{CP}}(\Lambda_b^0 \to p\pi^-) = 0.03 \pm 0.17\ (stat.)$$

$$A_{\mathsf{CP}}(\Lambda_b^0 \to pK^-) = 0.37 \pm 0.17\ (stat.)$$

and for the relative branching fractions

$$\frac{\sigma(p\bar{p} \to \Lambda_b^0 X, p_T > 6\ \text{GeV}/c)}{\sigma(p\bar{p} \to B^0 X, p_T > 6\ \text{GeV}/c)} \frac{\mathcal{B}(\Lambda_b^0 \to p\pi^-)}{\mathcal{B}(B^0 \to K^+\pi^-)} = 0.0415 \pm 0.0074\ (stat.)$$

$$\frac{\sigma(p\bar{p} \to \Lambda_b^0 X, p_T > 6\ \text{GeV}/c)}{\sigma(p\bar{p} \to B^0 X, p_T > 6\ \text{GeV}/c)} \frac{\mathcal{B}(\Lambda_b^0 \to pK^-)}{\mathcal{B}(B^0 \to K^+\pi^-)} = 0.0663 \pm 0.0089\ (stat.)$$

.

5.4 Systematic uncertainties

In this section we describe the main sources of systematic uncertainties. In all cases in which pseudo-experiments were used, the number of toy-MC is 100, if not otherwise specified.

5.4.1 Input masses

Particle	Mass $\pm$ σ $[\mathrm{GeV/c^2}]$
B^0	5.27963±0.00053 $[\mathrm{GeV/c^2}]$
B_s^0	5.36601±0.00073 $[\mathrm{GeV/c^2}]$
Λ_b^0	5.6197 ± 0.0012 $[\mathrm{GeV/c^2}]$

Table 5.5: The table list the mean values and the uncertainties for masses of the B-hadrons, from ref. [79]. In the composition fit the mass of each state was fixed to the nominal value, the systematic uncertainties were evaluated doing a 100 toys for each mass combination.

The B masses are an input parameter to the fit through the analytic expressions of $\mathcal{M}(\alpha, p_{tot})$. We generated distinct ensembles of pseudo-experiments in which we independently varied the B^0, B_s^0 and Λ_b^0 input masses within $\pm 1\sigma$ statistical uncertainty of the published CDF II mass measurement, in Tab. 5.5. The results of fits of these simulated samples are used to evaluate the systematics due to the uncertainty on the input masses.

5.4.2 dE/dx induced systematics

The systematics related to the dE/dx were assessed by repeating the fits in which the dE/dx parameters of the likelihood function are randomly varied in a 1σ-radius multidimensional sphere in the space of the parameters of the dE/dx calibrations, according to the general method documented in [86].

5.4.3 Combinatorial-background model

Our central fit assumes a mass-shape of the combinatorial background events distributed as a linear. We repeated the fit over the data, changing the shape for the background model into an exponential and higher order polynomials. The results were used to produce pseudo-experiments that were then fitted with the default model. The difference with respect to the central fit has been used as systematic uncertainty.

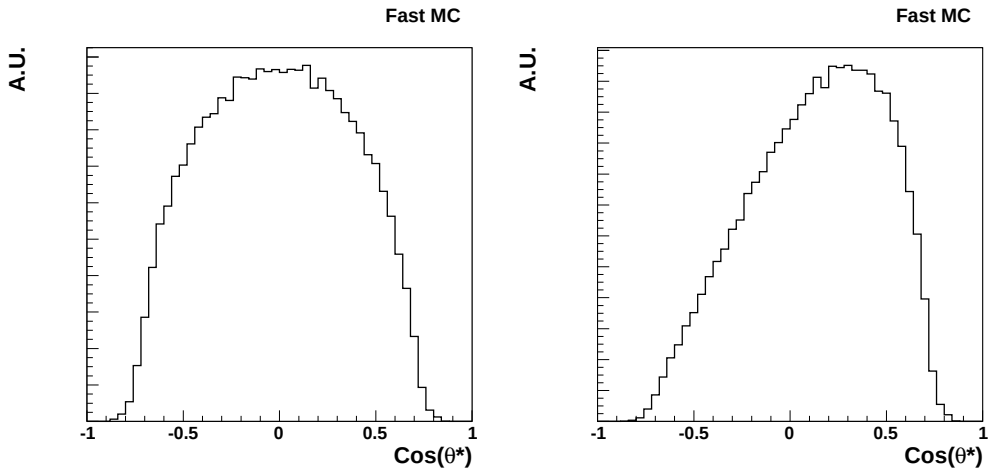

Figure 5.19: Distribution of the cosine of the polar angle in the SCM frame for protons decaying from unpolarized Λ_b^0 (left) and from fully positively polarized Λ_b^0 (right).

5.4.4 Effect of Λ_b^0 polarization

In the central fit we assumed no polarization for the Λ_b^0. However, in case that hadroproduced Λ_b^0 have non-zero polarization, the kinematics of the decay would change. In this case, the inaccurate parameterization of the momentum p.d.f. would induce some change in efficiency and in our fit results. Assuming the (non-relativistic) worst-case, the angular distribution of a final state particle from decays of fully polarized Λ_b^0 is the following: $dN/d\cos(\theta^*) \propto f_{\pm}(\theta^*) = 1 \pm \cos(\theta^*)$, as a function of the polar angle in the center-of-mass reference frame. The $\pm$ choice depends on whether the baryons are positively or negatively polarized. In such a case, the global efficiency of reconstructing $\Lambda_b^0 \to p\pi^-$ and $\Lambda_b^0 \to pK^-$ decays will be affected by approximately 1%. Fig. 5.19 shows the difference in $\cos(\theta^*)$ distribution between decays of unpolarized Λ_b^0 (left) and polarized Λ_b^0 (right). However, the effect on fit results might be larger since the kinematic variable α is a direct function of θ^* and its distribution gets strongly distorted in case of Λ_b^0 polarization (Fig 5.20 and 5.21).

It is therefore necessary to assess a systematic uncertainty for the possible effects of polarization. We modified our main fit, to describe two components for each Λ_b^0 state: with positive and negative polarization. Using the modified version of the fit we repeated the fit with a floating polarization parameter $\mathcal{P}$. In this fit we used the momentum templates of Fig. 5.20 and 5.21. The fit results (see Tab. 5.6) show that no evidence for polarization within our uncertainty: $\mathcal{P} =$

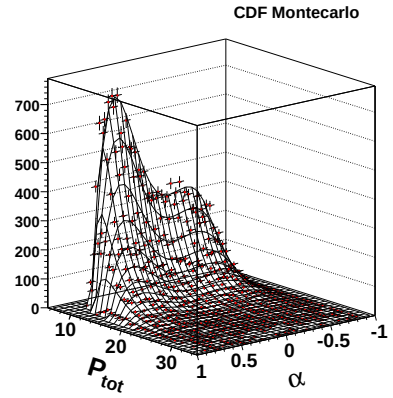

(a) (α, p_{tot}) distribution from CDF Monte Carlo.

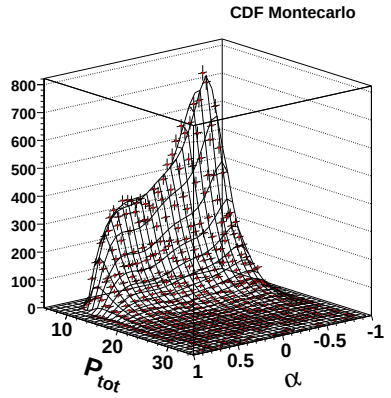

(d) (α, p_{tot}) distribution from CDF Monte Carlo.

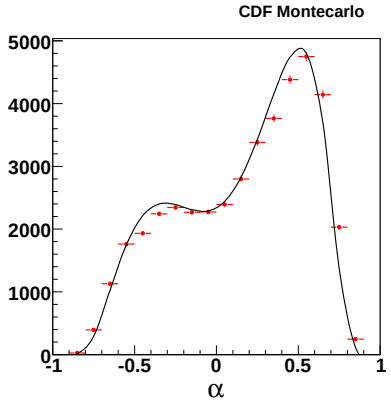

(b) α distribution.

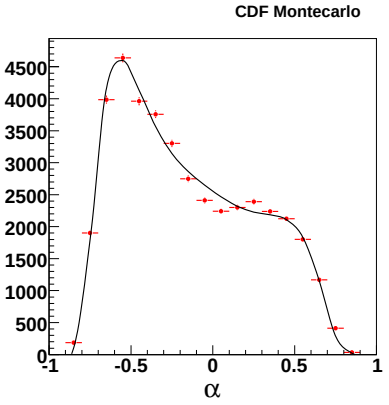

(e) α distribution.

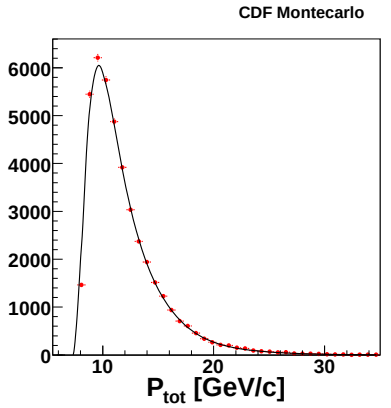

(c) p_{tot} distribution.

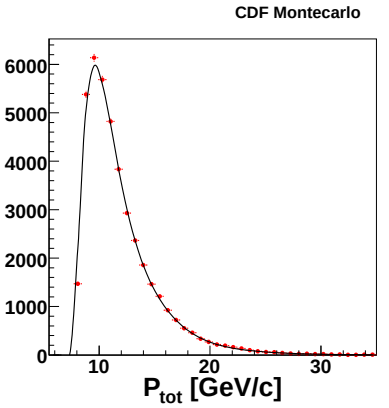

(f) p_{tot} distribution.

Figure 5.20: Momentum templates for the $\Lambda_b^0 \to p\pi^-$ decays for negative polarization, the left series, and for positive polarization, on the right.

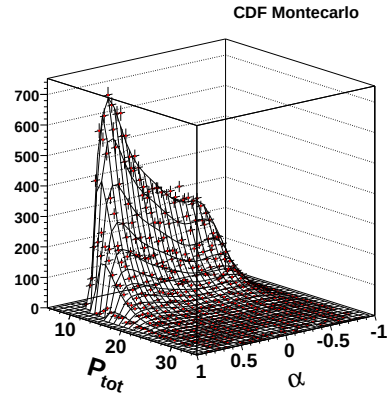

(a) (α, p_{tot}) distribution from CDF Monte Carlo.

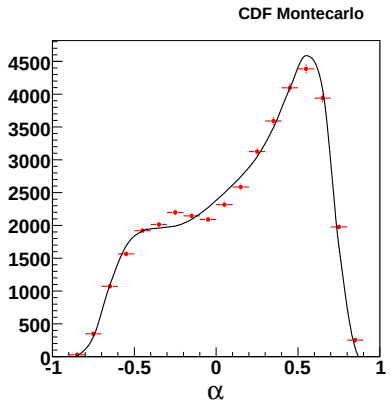

(b) α distribution.

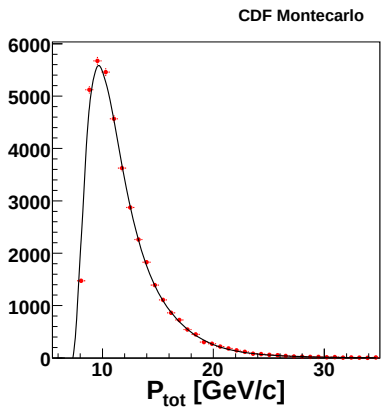

(c) p_{tot} distribution.

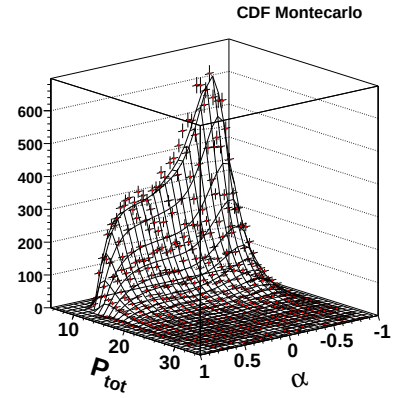

(d) (α, p_{tot}) distribution from CDF Monte Carlo.

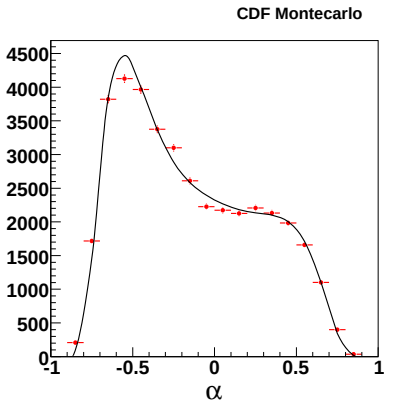

(e) α distribution.

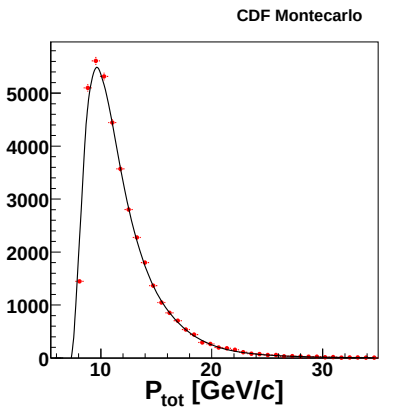

(f) p_{tot} distribution.

Figure 5.21: Momentum templates for the $\Lambda_b^0 \to pK^-$ decays for negative polarization, the left series, and for positive polarization, on the right.

Parameter	Floating polarization	central fit
$N(\Lambda_b^0 \to pK^-)$	116 ± 15	116 ± 15
$A_{\mathsf{CP}}(\Lambda_b^0 \to pK^-)$	0.37 ± 0.17	0.37 ± 0.17
$N(\Lambda_b^0 \to p\pi^-)$	74 ± 14	78 ± 14
$A_{\mathsf{CP}}(\Lambda_b^0 \to p\pi^-)$	0.00 ± 0.17	0.02 ± 0.17
$\frac{N(\Lambda_b^0 \to pK^-)}{N(B^0 \to K^+\pi^-)}$	0.0486 ± 0.0066	0.0486 ± 0.0065
$\frac{N(\Lambda_b^0 \to p\pi^-)}{N(B^0 \to K^+\pi^-)}$	0.0312 ± 0.0057	0.0324 ± 0.0058
$\mathcal{P}$	0.55 ± 0.18	0.50 ± 0.00
$\frac{\mathcal{P}(\bar{\Lambda}_b^0) - \mathcal{P}(\Lambda_b^0)}{\mathcal{P}(\bar{\Lambda}_b^0) + \mathcal{P}(\Lambda_b^0)}$	0.02 ± 0.16	–

Table 5.6: Comparison between the results on data of a fit that allows for Λ_b^0 polarization and the central fit.

0.55 ± 0.18 to be compared to $\mathcal{P} = 0.5$ in case of unpolarized baryons. The measured asymmetries and relative branching ratios vary very little with respect to the central fit. We used the results of this fit to produce 200 pseudo-experiments in which Λ_b^0 (and $\bar{\Lambda}_b^0$) were generated with polarizations ranging from $\mathcal{P}_+ = 0.55 + 0.18 = 0.73$ to $\mathcal{P}_- = 0.55 - 0.18 = 0.37$. These pseudo-experiments were fit using the likelihood of our central fit (that assumes $\mathcal{P} = 0.5$) and the difference in fit results were quoted as systematic uncertainty.

5.4.5 Detector-induced charge-asymmetries

The statistical uncertainty on the determination of the detector-induced charge asymmetries propagates as a systematic uncertainty on the measurement of the CP asymmetries so, in principal, we don't need to introduce further uncertainties. However, as a cross-check, we compared the charge-asymmetries extracted from data (see Sec. 5.2.1) with the same quantities extracted from the simulated samples:

$$\frac{\epsilon(p\pi^-)}{\epsilon(\bar{p}\pi^+)} = 1.0567 \pm 0.0017 \ (stat.) \tag{5.15}$$

$$\frac{\epsilon(pK^-)}{\epsilon(\bar{p}K^+)} = 1.0264 \pm 0.0012 \ (stat.) \tag{5.16}$$

$$\tag{5.17}$$

The comparison is not fully satisfactory. There are several possible explanations for such a discrepancy. For instance the fact that Λ^0 have spin and their production is polarized. If their polarization is different from zero the correction extracted from data may be inaccurate. Due to this not completely understood discrepancy,

we conservatively added the difference between central values from data-based correction and from simulation-based correction as a systematics, while still using the value obtained on real data as central value.

5.4.6 Λ_b^0 lifetime

The Λ_b^0 lifetime is known with $\approx 6\%$ uncertainty. This propagates as an uncertainty in acceptance and in the shape of kinematic templates in our measurement of the relative branching fractions. We repeated the analysis on toys in which we fluctuated the lifetime of the generated Λ_b^0 by one standard deviation in either side of the central value and compared with the central fit. The maximum difference was quoted as a systematic uncertainty.

5.4.7 Λ_b^0 momentum distributions

Although the agreement between data and simulation in the comparison of the Λ_b^0 spectra is visually rather good (see Fig. 3.13(b)), one might think that possible discrepancies are hidden by the currently low statistics of Λ_b^0 in data. We therefore estimated a systematic uncertainty on the poor knowledge of the Λ_b^0 spectrum by conservatively assuming that the $b-$hadron spectrum measured by Mary Bishai et al., is entirely dominated by Λ_b^0 and repeating the measurement under this assumption. The (tiny) difference between the obtained fit results and those of the central fit (in which the Λ_b^0 spectrum is reweighted according to the spectrum measured in the $\Lambda_b^0 \to \Lambda_c^0\pi$ analysis) is taken as systematics uncertainty.

An additional cross-check was done by increasing the degrees of freedom in fitting the momentum templates ($p(\alpha, p_{\rm tot})$), to allowing asymmetric α-distributions also for modes with kinematically symmetric (i.e. two particles with equal mass) final states. No difference was observed in the fit results.

5.4.8 Summary of systematic uncertainties

A summary of all systematics uncertainties is reported in Tab. 5.7. The total systematic uncertainty on each measurement has been determined as the sum in quadrature of the single systematics uncertainties. When the systematic uncertainty is asymmetric, the largest value has been used in the squared sum.

5.5 Final results and Conclusions

It's now possible complete the results showed in Sec. 5.3 adding the systematic uncertainties in the previous section. We can declare that using 1 fb^{-1} of two-track

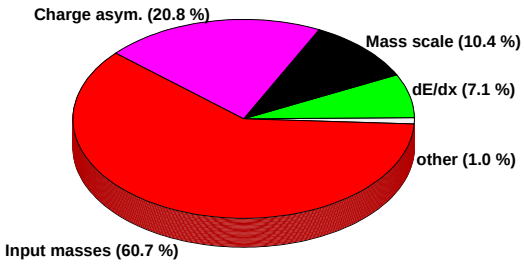

(a) A_{CP} asymmetry $\Lambda_b^0 \to pK^-$.

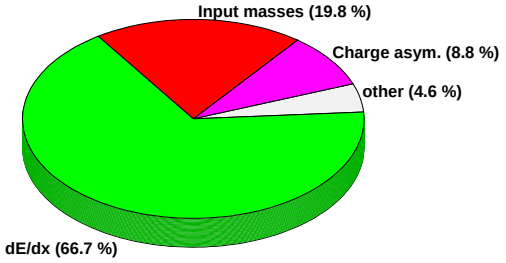

(b) A_{CP} asymmetry $\Lambda_b^0 \to p\pi^-$.

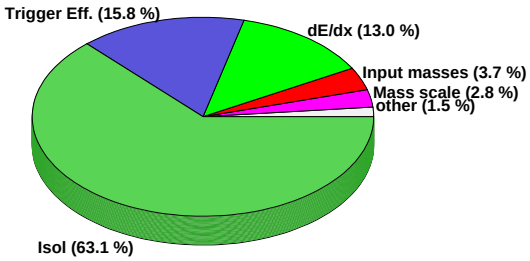

(c) Production ratio of $\Lambda_b^0 \to pK^- + c.c.$.

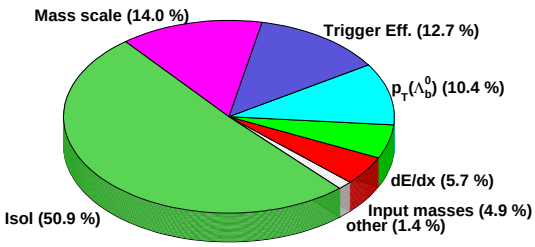

(d) Production ratio of $\Lambda_b^0 \to p\pi^- + c.c.$.

Figure 5.22: The pie-charts show the composition of the systematic errors related to the measurements.

Source	$A_{\mathsf{CP}}(\Lambda_b^0 \to pK^-)$	$A_{\mathsf{CP}}(\Lambda_b^0 \to p\pi^-)$	$\frac{N(\Lambda_b^0 \to pK^-)}{N(B^0 \to K^+\pi^-)}$	$\frac{N(\Lambda_b^0 \to p\pi^-)}{N(B^0 \to K^+\pi^-)}$
Mass scale	0.004	0.017	0.0010	0.0017
Input masses	0.011	0.041	0.0012	0.0010
dE/dx	0.022	0.014	0.0022	0.0011
Comb. bckg	0.001	0.004	0	0.0002
Polarization	0.004	0.002	0.0007	0.0004
Charge asymm.	0.008	0.024	-	-
Lifetime	-	-	0.0001	0.0003
$p_{\mathrm{T}}(\Lambda_b^0)$	< 0.001	0.003	0.0004	0.0014
Total	0.026	0.053	0.028	0.027

Table 5.7: Systematic uncertainties. The total is determined as the sum in quadrature of single contributions.

trigger data we measured the CP-violating asymmetries:

$$\begin{aligned} A_{\mathsf{CP}}(\Lambda_b^0 \to p\pi^-) =& \frac{\mathcal{B}(\Lambda_b^0 \to p\pi^-) - \mathcal{B}(\overline{\Lambda}_b^0 \to \overline{p}\pi^+)}{\mathcal{B}(\Lambda_b^0 \to p\pi^-) + \mathcal{B}(\overline{\Lambda}_b^0 \to \overline{p}\pi^+)} \\ =& 0.03 \pm 0.17\ (stat.) \pm 0.05\ (syst.) \\ A_{\mathsf{CP}}(\Lambda_b^0 \to pK^-) =& \frac{\mathcal{B}(\Lambda_b^0 \to pK^-) - \mathcal{B}(\overline{\Lambda}_b^0 \to \overline{p}K^+)}{\mathcal{B}(\Lambda_b^0 \to pK^-) + \mathcal{B}(\overline{\Lambda}_b^0 \to \overline{p}K^+)} \\ =& 0.37 \pm 0.17\ (stat.) \pm 0.03\ (syst.) \end{aligned}$$

This is the first such measurement in b-baryon decays. The statistical uncertainty dominates the resolution and prevents a conclusive statement on the presence of asymmetry.

Both asymmetries are consistent with zero within the uncertainties. $A_{\mathsf{CP}}(\Lambda_b^0 \to pK^-)$ shows a deviation of 2.2 σ from zero. The theoretical prediction [3] are of $A_{\mathsf{CP}}(\Lambda_b^0 \to p\pi^-) = \mathcal{O}(10\%)$ and $A_{\mathsf{CP}}(\Lambda_b^0 \to pK^-) = \mathcal{O}(40\%)$, in good agreement the central values of the fit.

Our measurement can be combined with another branching fraction measurement performed in CDF Run II to estimate the charmless-to-charmed ratio of branching fractions using the decay $\Lambda_b^0 \to \Lambda_c^+\pi^-$ as reference mode for the Λ_b^0 charmed branching-fraction. Thus, we quote $\frac{\mathcal{B}(\Lambda_b^0 \to p\pi^-)}{\mathcal{B}(\Lambda_b^0 \to \Lambda_c^+\pi^-)}$ and $\frac{\mathcal{B}(\Lambda_b^0 \to pK^-)}{\mathcal{B}(\Lambda_b^0 \to \Lambda_c^+\pi^-)}$ extracted

as follows:

$$\frac{\mathcal{B}(\Lambda_b^0 \to p\pi^-)}{\mathcal{B}(\Lambda_b^0 \to \Lambda_c^+\pi^-)} = \frac{f_{\rm baryon}\mathcal{B}(\Lambda_b^0 \to p\pi^-)}{f_d\mathcal{B}(B^0 \to K^+\pi^-)} \times \frac{f_d\mathcal{B}(B^0 \to D^-\pi+)}{f_{\rm baryon}\mathcal{B}(\Lambda_b^0 \to \Lambda_c^+\pi^-)} \times \frac{\mathcal{B}(B^0 \to K^+\pi-)}{\mathcal{B}(B^0 \to D^-\pi^+)}$$
$$\frac{\mathcal{B}(\Lambda_b^0 \to pK^-)}{\mathcal{B}(\Lambda_b^0 \to \Lambda_c^+\pi^-)} = \frac{f_{\rm baryon}\mathcal{B}(\Lambda_b^0 \to pK^-)}{f_d\mathcal{B}(B^0 \to K^+\pi^-)} \times \frac{f_d\mathcal{B}(B^0 \to D^-\pi+)}{f_{\rm baryon}\mathcal{B}(\Lambda_b^0 \to \Lambda_c^+\pi^-)} \times \frac{\mathcal{B}(B^0 \to K^+\pi-)}{\mathcal{B}(B^0 \to D^-\pi^+)}$$

where

- $\frac{f_{\rm baryon}\mathcal{B}(\Lambda_b^0 \to p\pi^-)}{f_d\mathcal{B}(B^0 \to K^+\pi^-)}$ = and $\frac{f_{\rm baryon}\mathcal{B}(\Lambda_b^0 \to pK^-)}{f_d\mathcal{B}(B^0 \to K^+\pi^-)}$ are the efficiency-corrected fit results;
- the ratio $\frac{f_{\rm baryon}\mathcal{B}(\Lambda_b^0 \to \Lambda_c^+\pi^-)}{f_d\mathcal{B}(B^0 \to D^-\pi+)} = 0.82 \pm 0.08(\text{stat.}) \pm 0.11(\text{syst.} \pm 0.22\ (\mathcal{B}_{\Lambda_c^+}))$ is taken from the CDF Run II measurement;
- the ratio $\frac{\mathcal{B}(B^0 \to K^+\pi-)}{\mathcal{B}(B^0 \to D^-\pi+)} = \frac{(1.88\pm0.07)\times10^{-5}}{(2.68\pm0.13)\times10^{-3}} = (7.01 \pm 0.43) \times 10^{-3}$ is taken from the PDG.

This results in:

$$\frac{\mathcal{B}(\Lambda_b^0 \to p\pi^-)}{\mathcal{B}(\Lambda_b^0 \to \Lambda_c^+\pi^-)} = (0.355 \pm 0.063\ (stat.) \pm 0.080\ (syst.) \pm 0.096\ (\mathcal{B}_{\Lambda_c^+})) \times 10^{-3}$$
$$\frac{\mathcal{B}(\Lambda_b^0 \to pK^-)}{\mathcal{B}(\Lambda_b^0 \to \Lambda_c^+\pi^-)} = (0.567 \pm 0.076\ (stat.) \pm 0.120\ (syst.) \pm 0.150\ (\mathcal{B}_{\Lambda_c^+})) \times 10^{-3}$$

.

In addition, we quote also the first branching ratio measurement of a charmless Λ_b^0 decay. Out result is quoted as relative to $B^0 \to K^+\pi^-$ decay:

$$\frac{\sigma(p\bar{p} \to \Lambda_b^0 X, p_T > 6\ \text{GeV}/c)}{\sigma(p\bar{p} \to B^0 X, p_T > 6\ \text{GeV}/c)} \frac{\mathcal{B}(\Lambda_b^0 \to p\pi^-)}{\mathcal{B}(B^0 \to K^+\pi^-)} =$$
$$= 0.0415 \pm 0.0074\ (stat.) \pm 0.0058\ (syst.)$$
$$\frac{\sigma(p\bar{p} \to \Lambda_b^0 X, p_T > 6\ \text{GeV}/c)}{\sigma(p\bar{p} \to B^0 X, p_T > 6\ \text{GeV}/c)} \frac{\mathcal{B}(\Lambda_b^0 \to pK^-)}{\mathcal{B}(B^0 \to K^+\pi^-)} =$$
$$= 0.0663 \pm 0.0089\ (stat.) \pm 0.0084\ (syst.)$$

. From the above measurement, the absolute branching fractions for charmless Λ_b^0 decays can be extracted, using the knowledge in fragmentation functions ($f_{\rm b-baryon}/f_d = 0.25 \pm 0.04$) and of the $B^0 \to K^+\pi^-$ decay rate, $\mathcal{B}(B^0 \to K^+\pi^-) = (1.82 \pm 0.08) \times 10^{-5}$[10], we obtained:

$$\mathcal{B}(\Lambda_b^0 \to p\pi^-) = (3.1 \pm 0.6\ (stat.) \pm 0.7\ (syst.)) \times 10^{-6}$$
$$\mathcal{B}(\Lambda_b^0 \to pK^-) = (5.0 \pm 0.7\ (stat.) \pm 1.0\ (syst.)) \times 10^{-6}$$

The the ratio $f_{\mathrm{b-baryon}}/f_d$ is taken from the PDG was determined from LEP measurement at the Z^0 pole. However, in this measurement we are sensitive to p_{T} of the beauty hadron much lower than those probed at LEP. For this reason we also evaluate an alternative the absolute results obtained using the value $f_{\mathrm{b-baryon}}/f_d = 0.56 \pm 0.02(stat.)^{+0.13}_{-0.12}(syst.)^{+0.26}_{-0.17}(\mathcal{B})$ extracted from a CDF analysis at Tevatron Run II[87]. They are the following:

$$\mathcal{B}(\Lambda_b^0 \to p\pi^-) = (1.4 \pm 0.3\ (stat.)^{+0.9}_{-0.5}\ (syst.)) \times 10^{-6}$$
$$\mathcal{B}(\Lambda_b^0 \to pK^-) = (2.2 \pm 0.3\ (stat.)\ ^{+1.4}_{-0.8}\ (syst.)) \times 10^{-6}$$

Comparing these values with the theoretical prediction: $\mathcal{B}(\Lambda_b^0 \to p\pi^-) = 1{\cdot}10^{-6}$ and $\mathcal{B}(\Lambda_b^0 \to pK^-) = 2 \cdot 10^{-6}$ [3], it is possible to see some excess, in particular if one uses the PDG values determined at the Z^0 pole. No conclusion can be drawn from this; in addition to the uncertainty on the production fraction, it must be kept in mind that the theoretical predictions were evaluated using a naive factorization, and probably have room for improvements. However, our measurement is much lower than the previous best limit, and we can now already safely exclude scenarios with a large contribution from RPV MSSM extension, expected to be able to increase the branching ratio up to $\approx 10^{-4}$. If there is any deviation from SM in here, it cannot be more that about a factor two from the SM itself.

A more precise measurement of the Λ_b^0 production fraction is expected from CDF soon, and this will help in interpreting these results. It would be particular interesting to be able to compare to more recent and updated predictions.

The Run II of the CDF experiment is planned to end in 2009 or 2010. According schedule, the experiment will be able to collect a final sample of 5-6 fb^{-1}; assuming no improvements in the analysis and a similar trigger efficiency, we expect to reach a $\mathcal{O}(7\%)$ statistical uncertainty on the asymmetry and $\mathcal{O}(0.003)$ statistical uncertainty on the relative branching fractions, which would be a very interesting result.

Conclusions

In conclusion, we have performed the first measurement of branching fraction and CP asymmetries of charmless modes of a b-baryon. We find results in agreement with the predictions at the current level of precision, excludig the possibility of large deviations. The measurements are not limited by systematic effects, and will keep improving with the growth of Tevatron integrated luminosity.

In addition, application to larger samples of the same analysis techniques whose reliability has been carefully demonstrated in this work, will offer the possibility of detecting for the first time the yes unseen modes $B_s^0 \to \pi^+\pi^-$ and $B^0 \to K^+K^-$, with interesting consequences for our understanding of annihilation-type decays.

This chapter concludes the part of the thesis devoted to the analysis of CDF data. The next chapter describes a first look at the future of measurements of rare decays beyond the Tevatron.

Chapter 6

A look to the future: tracking trigger at the LHC using the Fast Track Processor

6.1 Introduction

The next frontier for the HEP at a collider will be the Large Hadron Collider (LHC). The design of this accelerator[88] places it at top of both the energy of the collisions and the intensity with an energy in CM of $\sqrt{s} = 14\,\text{TeV}$ and a peak luminosity of $10^{34}\,\text{cm}^{-2}\text{s}^{-1}$, with a bunch crossing of 25 ns. These conditions are ideal to test the limit of the SM at the TeV scale, where it could be possible to observe unexpected processes, or to search for very rare decays that will benefit of the large production.

But these condition are challenging for the existing technologies used for the data acquisition and the triggers: the Level-1 trigger has to collect event at a rate of 40 MHz, while the Level-2 is expected to work to a maximum rate of 75 KHz. These requirements are very difficult for the existing hardware, with the risk to limit the ability of the experiments to collect interesting physics sample.

The Fast Track processor (FTK)[89] is a dedicated hardware processor for on-line pattern recognition of tracker detector data. FTK is an evolution of the SVT[90] that has been the crucial tool for reconstruction the channels discussed in this thesis. The FTK is a powerful processor that is designed to perform a high-quality track reconstruction, with a performance close to the offline software, for all particles of transverse momentum above about 1 GeV/c. This will be performed at the very high event rates accepted by the Level–1 trigger, i.e. up to 50-100 kHz. This processor [91] has been proposed for online track finding at very high rates for the ATLAS experiment.

The measurements that are expected to gain from the use of this processor are many. The availability of precise impact parameters at trigger level will enable online b-tagging , which is expected to help the searches of all the decay modes having b-quarks in the final state: e.g. $H \rightarrow b\bar{b}$, decay that the current limit for the Higgs mass favors [92]. Another type of decay channels that can exploit the FTK performances are those with τ leptons in the final states, that are usually tagged using a track based algorithm [93].

Given the high expected trigger rates, and the lack of a Level-1 track reconstruction at ATLAS, in this study we consider amongst the rare decays, that are the subject of this thesis, only the $B_s^0 \rightarrow \mu^+\mu^-$ channels, that can be efficiently triggered at Level-1 thanks to the presence of the muons. This study can be also useful to understand the ability of the system to reconstruct other FCNC modes such as the $B_s^0 \rightarrow l^+l^-\phi$ (Sec. 1.4.2).

I describe in this chapter my contribution to the development of algorithms needed by the FTK processor, its simulation and evaluation of performance, and first studies of its possible impact on collection of $B_s^0 \rightarrow \mu^+\mu^-$ samples.

6.2 Fast Track Processor

Fig. 6.1 shows how FTK can be integrated in the data acquisition system of a LHC experiment. Tracking data are collected at the Level–1 trigger rate in the front end (RODs)[94], then stored into large memory buffers (ROBINs). These buffers are interfaced to a large CPU farm performing higher level trigger selections. FTK looks at the tracker data flowing to the memory buffers, without interfering with the operation of the DAQ system, and reconstructs high-quality tracks. The tracks found by the processor are stored using a compact output into an additional memory buffer that can be easily accessed at high rate by the HLT Filter CPUs. This implementation scheme allows a high input bandwidth for FTK with minimal interference with the rest of the DAQ. It will be added after the baseline has been built, as an upgrade, due to the possibility of adding a bypass to spy on the events.

6.3 FTK and the ATLAS DAQ system

An optimal use of the silicon-based ATLAS tracker is crucial to obtain a good impact parameter measurement, and is therefore a necessary ingredient of an online tracker aiming at high performance. Actually the resolution obtained with silicon detectors is already very good: the impact parameter resolution found using FTK is 30 μm (see Fig. 6.10), to be compared to 20 μm with a full (Silicon and TRT) reconstruction algorithm, and we can plan, at least at the beginning, to

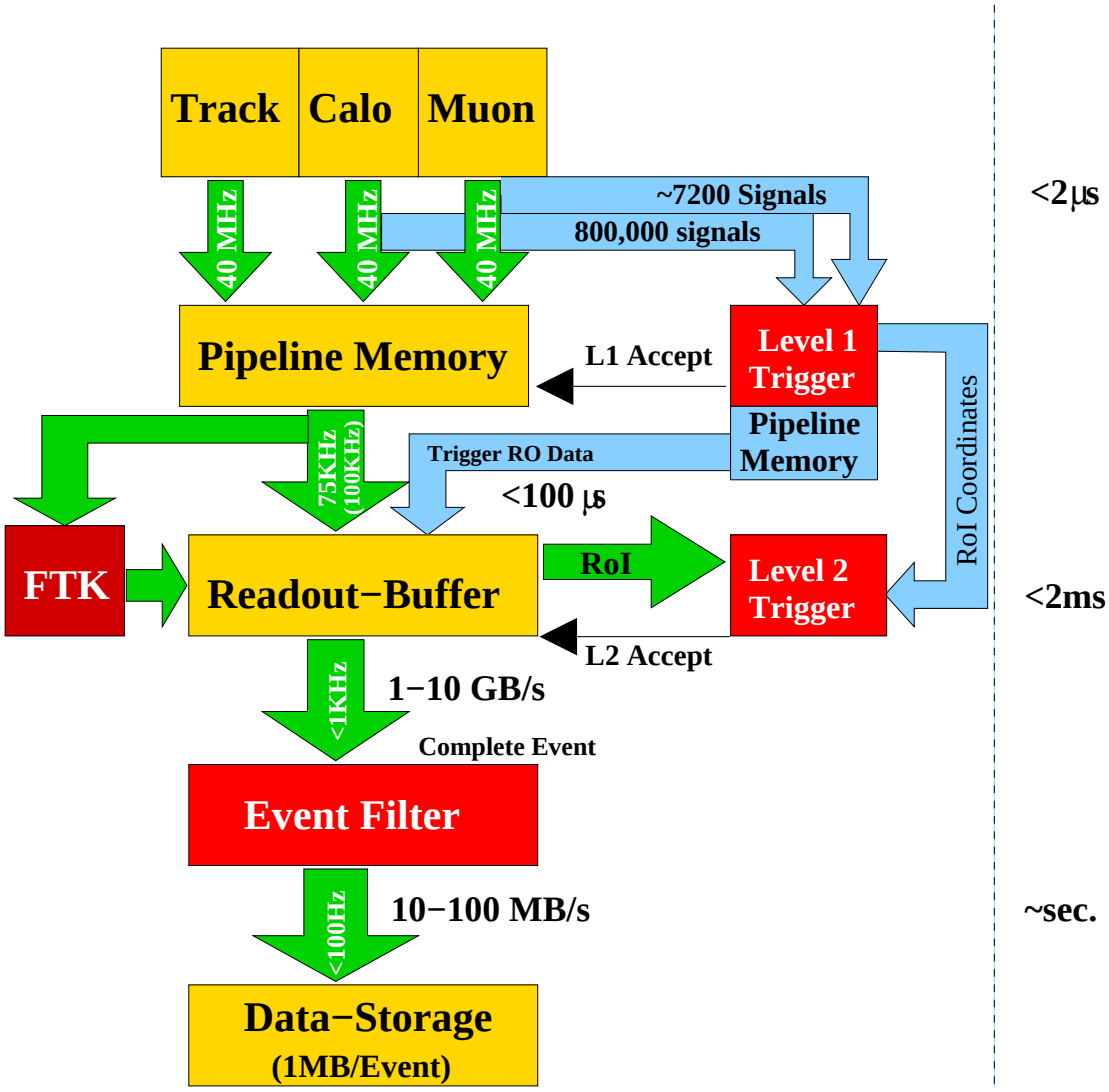

Figure 6.1: The FTK processor has access to the tracker data of Level-1 selected events flowing through the DAQ system. The FTK output is put into standard DAQ buffer memories. In the DAQ buffer FTK data are merged with the Trigger Read-out (RO) data and then sent to the Read-out Interface (RoI)

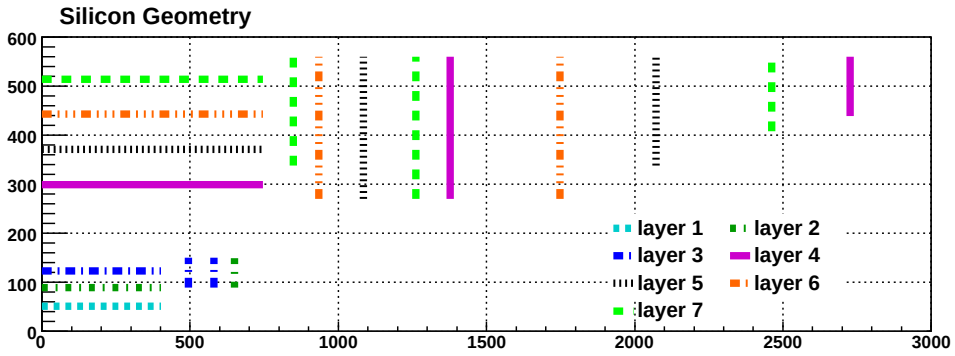

Figure 6.2: Cross-sectional view through the beam axis of one quarter of the barrel for the ATLAS SCT and pixel detectors. The figure shows the 7 inner detector layers. Each layer gives the 2D coordinates for the hits.

use only these detectors. Fig. 6.2 shows a cross-section of the layout of the silicon layers for a quarter of the detector. In this study we consider an implementation of FTK using all of the 11 silicon layers, which are of two kinds: 4 double faced SCT modules (64 mm $\times$ 128mm, arranged in 4 R-ϕ + 4 stereo layers) and Pixel modules (16.4 mm $\times$ 60.8 mm, arranged in 3 layers) The structure of the Associative Memory (AM) used by FTK allows to perform pattern recognition using up to twelve of tracking "layers". They can be easily reconfigured or extended according to the needs.

In the simplified scheme of Fig. 6.2, barrel and disk layers are linked together to guarantee full η coverage: detectors with the same patterned line are combined to build a complete layer. Each patterned line corresponds to a different layer.

An important question is how to the input bandwidth sets an upper limit both on the event rate and the size of the detector connected to it. The FTK processor increases the data flow rate with respect to SVT at the CDF by exploiting the parallel readout of the detector layers on six buses. Nevertheless, in order to sustain very high event rates, it is necessary to organize FTK as a set of independent "engines" (input bandwidth of 4 Gbit/s), each working on a different region of the silicon tracker.

A possible segmentation of the detector into azimuthal regions, Fig. 6.3. This segmentation generates some small inefficiency at sector boundaries that can be removed by allowing a small overlap zone at the boundaries.

We use the rates needed at high luminosity [91] to obtain a rough estimate for the number of the FTK processors or regions. Since each logical layer is loaded in parallel at a frequency of 40 MHz, at high luminosity, we need at least 8 phi regions. These numbers were found appropriate for a six-layer configuration and

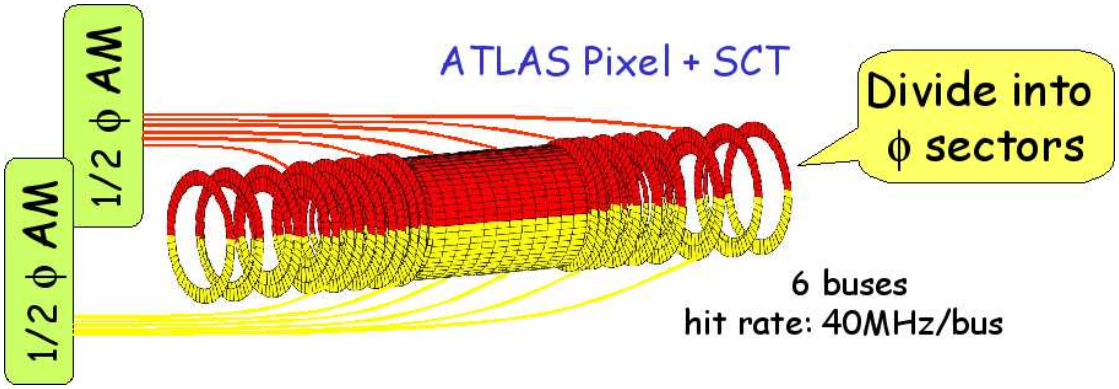

Figure 6.3: The sketch shows how the subdivision in regions helps to limit the input band-width for each of the AM board.

this work is based on this estimation. The addition of extra layers is possible but they would be received on the same six buses, so the cluster rates on each will be higher. If the this number of region will be considered too high, a feasible option is to operate FTK on only a subset of the Level-1 triggers. A single 9U VME crate would contain the engine core for a detector region, as described in [89]. The core size is dominated by the large bank of pre-calculated hit patterns (pattern bank) used to perform pattern recognition. The pattern bank size is one of the crucial parameters for the feasibility of the device. The FTK core, in conclusion, could have the dimension of 8 crates.

The FTK connection to the detector (the Data Formatters described in the next section) is excluded in this computation. In ATLAS the whole silicon tracking data are collected by roughly 180 devices, (RODs), working in parallel. Each ROD should provide an output to FTK. Design has been done of a modified S-link output mezzanine board that provides a second copy of the track data being sent from the RODs to the buffer memories, Read-Out Buffers (ROBs). If the detector is divided into 8 regions, each processor would receive 23 links, find clusters and organize them into the 24 inputs received by the processor core. In fact there are four inputs [89] for each one of the six FTK input buses. The dual-output HOLA board that drives both the usual DAQ data stream and an identical one to FTK was designed and tested, and passed an ATLAS board review. It would replace the existing HOLA on the RODs.

6.4 The FTK Architecture

Fig. 6.4 shows a sketch of the FTK internal architecture, it is FPGA based with the exception of one specially designed chip for the associative memory, that is custom

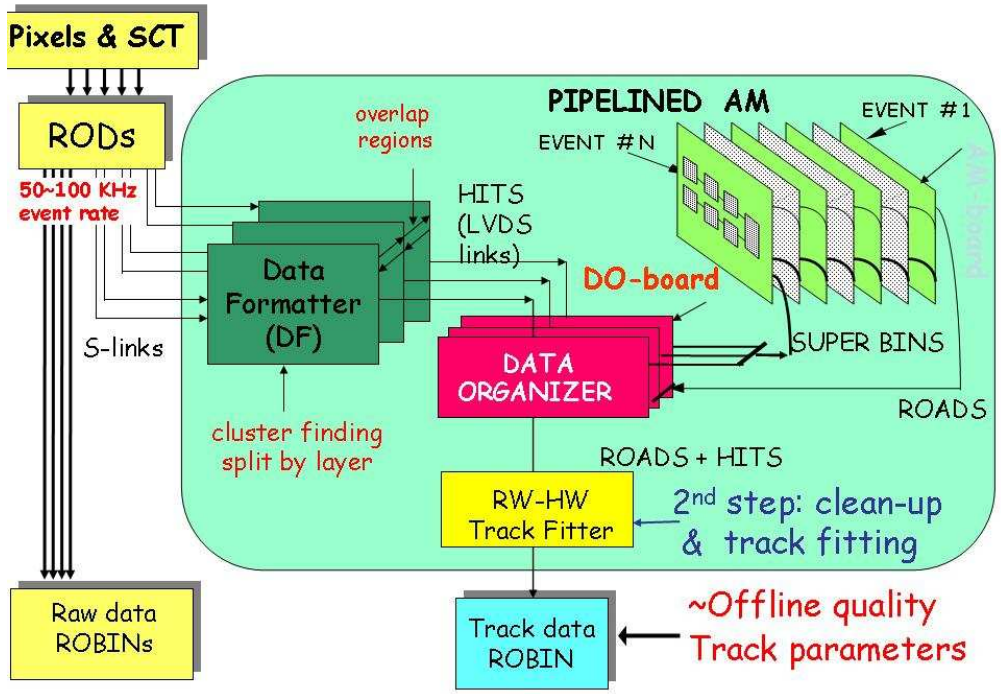

Figure 6.4: The figure shows the internal connections between the different logical part that form the FTK system.

made. An R&D program has been carried out for a number of years and prototypes have been built. Details of the design and the prototype performance are given in references [95] and [96] as well as the references in those papers. Important R&D for FTK has also been provided by the SVT upgrade. A published paper [96] describes the upgrade and its relevance to possible future applications.

The pixel and strip data are sent by a duplicated output (a spy output) in the RODs. They are received by the Data Formatters (DF), which do simple cluster finding, outputting the hits in each silicon layer to the Data Organizers (DO). The DO boards serve two functions. They store the hits at full resolution and send them to the Associative Memory (AM) at a coarser resolution (super-bins) appropriate for pattern recognition. The AM boards contain a large number of pre-loaded patterns or roads, corresponding to the possible combinations for real tracks of a super-bin at each silicon layer. These are determined in advance from full ATLAS simulation of single tracks using detector alignment extracted from real data. The AM is a massively parallel system in that all roads nearly simultaneously see each silicon hit. When a road has found the requisite number of hit layers, the AM sends that road number back to the DOs. They immediately fetch the associated full resolution hits and send them and the road number to the Track Fitter (TF).

The precalculated patterns and TF parameters are extracted using "complete" tracks, that was revealed in all the logical layers. To avoid a large efficiency loss when the TF receives an "incomplete" track that are managed using the "majority logic" in the track match criteria. For example we can require 6 fired layers among a total of 7 layers (6/7). Looser is the majority requirement larger is the track efficiency but also larger will be the number of fakes. What is the gain? It is a varying number since it is a function of the detector status which can change, even on short timescales. The gain will likely increase if the detector signal/noise will decrease causing higher thresholds and single channel inefficiencies. However, the gain will decrease if inside a wedge a full layer is broken, because in this case the 6/7 criteria will be the same as 6/6 in that wedge. The gain can be more important using raw hits from 11 layers instead of space points from 7 layers. The mathematical details are reported in Sec. 6.5.2

The use of the majority criteria 6/7 and the common presence of noise hit near a true track, combined with the pattern matching algorithm, generates duplication of real roads. In fact, for each real track it is possible to find a single 7/7 road (an hit is found on each layer) and/or a large number of 6/7 roads (an hit is missing on a layer) generated by all the patterns that differ only for a single Super-Strip. The six non-empty Super-Strips are exactly the same for all these roads. If all these roads are sent to the TF, the TF time will be wasted fitting repeatedly the same hit combinations, with small advantage. We call these ghosts "AM ghosts" since

they are generated by the AM bank. It is possible to identify and reduce them even if the track χ^2 is not available. Two more situations generate track families whose members share many hits but are not perfectly equal, since they do not share all the silicon hits: (a) very near tracks seen as a single hit in most of the layers, but not all of them and (b) a single track with contiguous noise hits in the silicon detector. We call these ghosts "detector ghosts" since they can't directly be blamed on the SVT. It is difficult to suppress part of these ghosts, without knowing the track χ^2s. The Hit Warrior algorithm is very efficient to remove all the detector ghosts, the duplicated tracks that are characterized by (1) sharing the same hits into most of the layers and (2) differing for "very near" hits in only one ore two layers. It reduces this kind of ghosts choosing the best fit. However it does not help to reduce the TF processing time.

Because each road is quite narrow, the TF can provide high resolution helix parameters using the values for the center of the road and applying corrections that are linear in the track coordinate in each layer. Fitting a track takes only 200 ns. in the CDF SVT, and will take about 1 ns. in ATLAS. FTK tracking is completed less than 100 ms after the silicon data has been sent from the ROD's. The Level-2 processors can request the track information for any Region of Interest or the entire event and then use all of its available CPU time to run sophisticated algorithms like b tagging, τ identification, and jet reconstruction. The system we are designing is intended for operation at luminosity of 10^{34} planned for 2012. The previous section explains the natural scalability of FTK. More demanding conditions can be addressed just by increasing the system parallelism (the number of associative memories working in parallel on different phi regions and their size). Moreover, the FTK system is intrinsically reconfigurable since the geometry is implicitly contained in the memory banks rather than being built into the hardware. In the SLHC era, FTK could prove even more powerful if a Level-1 track trigger is added to ATLAS within the FTK framework.

6.5 Simulation

6.5.1 General structure

A simulator program was created for the FTK (FTKSim), which is able to process complete ATLAS events and perform the FTK algorithm to produce exactly the same list of tracks that will be produced by the actual device. The purpose of this program is manifold:

- evaluation of tracking performance parameters that can then be used in fast, parametric detector simulations for high-statistic studies of physics performance;

- detailed and reliable evaluation of the physics performance of the FTK, by feeding it complete events produced by the full ATLAS detector simulation;
- evaluation of the crucial parameters needed for hardware design.
- evaluation of the large set of numeric constants needed for programming the FTK device.

These goals are attained by an intermediate–level simulation, that describes the algorithm and the FTK internal data accurately but at a high level, and avoids detailed hardware simulation, thus attaining a sufficient speed for simulation of moderately-sized samples of complete events. The core code is based on a similar simulator previously created for the SVT processor (QUICKSVT [97, 48]), inheriting its overall organization and basic algorithms, while the data structures have been recreated in accordance with the ATLAS/ATHENA data structures[98, 99].

FTKSim is a standalone program, written in C/C++ language which interfaces with ROOT [100]. It contains two main connected modules simulating the Associative Memory (AM) and the Track Fitter (TF) respectively, and two separate modules that produce the two main data banks needed for programming: the pattern bank (PB) for the AM, and the fit constants (FC) for the TF.

For this study, we grouped the 8 SCT layers in 4 pairs (r-ϕ + stereo), in order to effectively work with a total of 7 layers ("logical layers"), each providing a 2–dimensional measurement (*space point*). This is not expected to affect significantly the evaluation of performance, and allows savings in computing time. In addition, it allows a more meaningful comparison with the off-line reconstruction program (iPatRec[101]) that uses the same procedure.

6.5.2 Generation of internal FTK data banks

The internal FTK data banks encode information about the geometry and resolution of the various parts of the detector, in addition to an appropriate subdivision of the detector in regions. In order to simulate real operating conditions with unknown detector misalignments, we extracted the needed information on detector geometry and resolution from samples of simulated data rather than from a nominal geometric description of the detector. This is attained for both pattern bank and fit constants by processing a training sample of 20 million of single–muon events for fit constants and 100 million of single-muon events for the pattern banks. The events were processed by the full ATLAS detector simulation (code versions 10.0.6 and 12.0). Realistic resolution and multiple scattering effects were simulated. For the sole purpose of training, effects producing large deviations of the track from its average trajectory or multiple tracks were turned off (e.g. hard

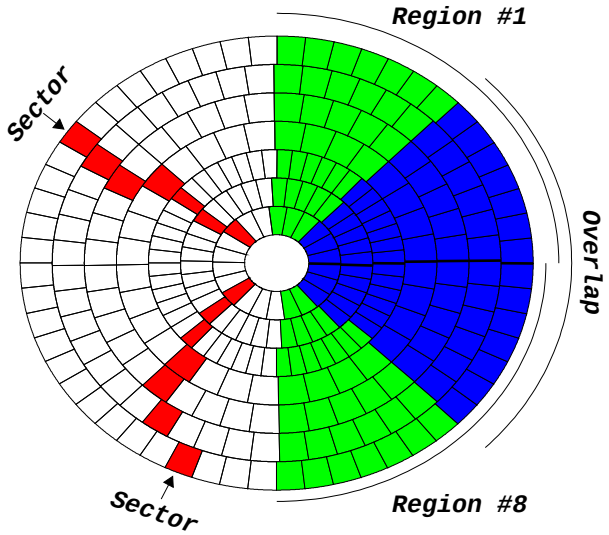

Figure 6.5: The barrel is subdivided in geometrical regions, each covering about 90°. In the figure is shown the logical subdivision of each layer, the module size is arbitrary; two regions are highlighted: the not-overlapping part is in green while the overlap is blue. The two sequences of red modules show two sectors.

interactions with detector material, delta rays, etc.) in order to optimize the performance on clean tracks. This is to avoid special cases of low probability that generating no real advantage to system efficiency.

Most tracks cross each of the 7 "logical layers" we defined (because of detector overlaps, a track can sometimes cross two modules of the same layer). We configured FTKSim to reconstruct any tracks leaving at least 6 hits on any combination of these 7 layers. A combination of 7 modules (one per layer) that can be crossed by the same track is called a "sector".

AM organization: defining sectors and regions

In the first step, it is necessary to identify all valid sectors. They were determined from the input data, set by selecting the possible sectors that are hit by tracks with a sufficient frequency. An important parameter for both sectors and patterns is the *coverage*. This is a purely geometric quantity, defined as the probability that a track (with parameters within a fiducial range) intersects the detector in a set of points that are within a sector/pattern contained in the bank. In short, it is the fraction of reconstructible tracks, when only purely geometric effects are considered. The fiducial range of track parameters is defined by their generated distribution (almost flat in the chosen range), as shown in Fig. 6.6.

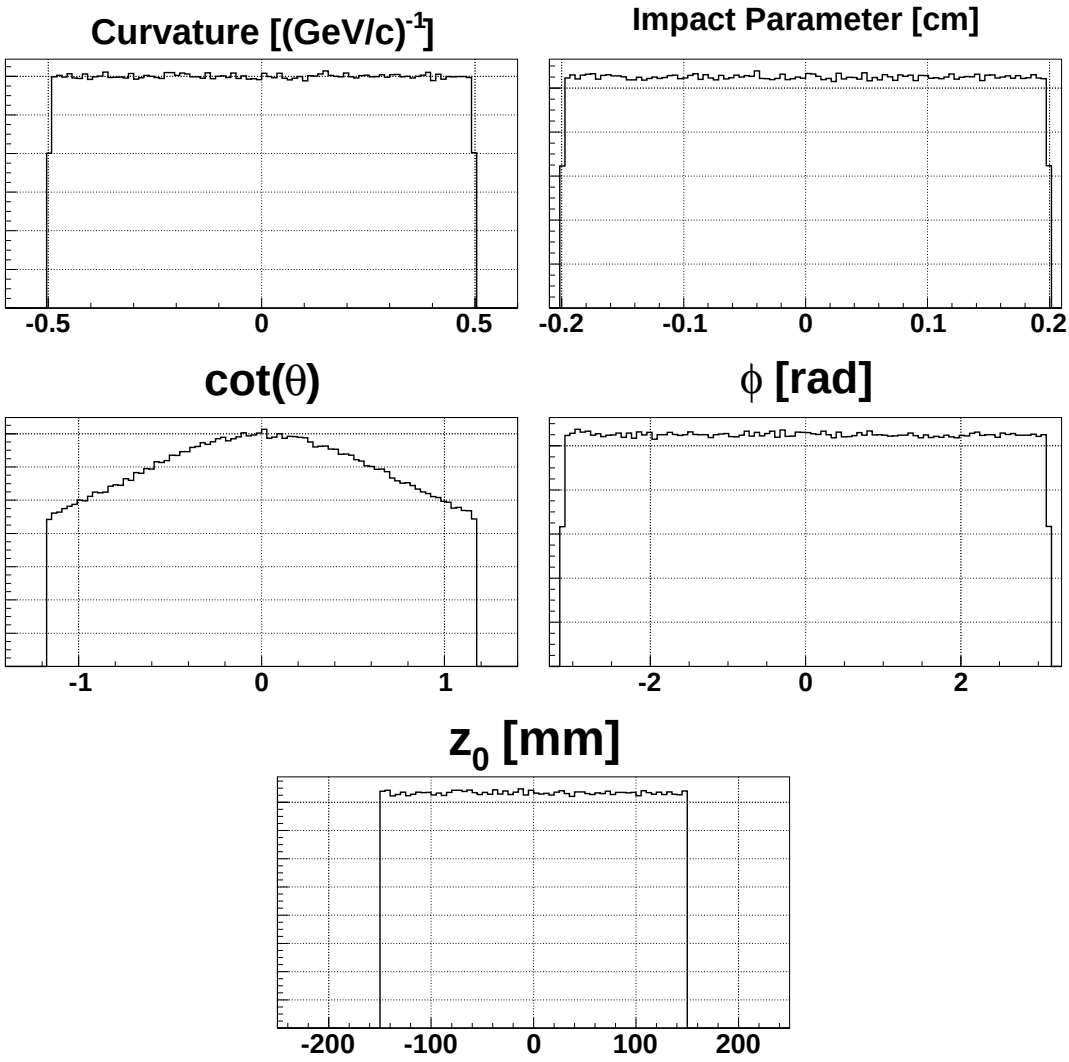

Figure 6.6: Distribution of the track parameters: curvature, impact parameter, $\cot(\theta)$, ϕ, z_0 for the training sample.

In our work we found a list of 157,901 sectors, providing a geometrical coverage of 98.6%.

All sectors are then grouped to form *regions* (see Fig. 6.5). Each region is implemented in hardware as a separate Associative Memory bank, and therefore patterns crossing a region boundary are not allowed by the system. This has no impact on the efficiency, because regions have been defined with a generous overlap: we use 8 regions, each defined by a range of the ϕ coordinate and covering approximately 1/4 of the detector, so that each pair of contiguous regions overlaps

by about 50%. Patterns located in the overlap region are not duplicated because this will generate a fake track, for this reason each of this patterns is arbitrarily assigned to one of the banks. All regions extend along z for the full detector length.

Fit constants and linearity

After the sectors are defined, for each sector the fit constants are determined. The constants will be used to solve the (2.8). They are evaluated by comparing hit positions with the originally generated *true* track parameters. Only tracks hitting at least 7 different layers were used for constants generation.

It has been explicitly verified that each sector covers a region of space small enough to make the linear fitting approximation accurate within the whole sector[48]. The linear approximation, as is shown in the figures 6.5.2, is tested verifying that the difference between track parameters extracted using (2.8) and the real parameter have a distribution centered in 0 for each value of the real parameter. If the linear approximation is not satisfactory will be possible to see deviations from zero for particular values of the parameter. However in this case the linear fit was found a good approximation for all the track parameters.

Majority-logic in FTKSim

In the previous Sec. 6.4 we noticed that requiring a track to have hits on all layers leads to a sizeable efficiency loss. So we need to introduce a technique, compatible with linearization, to recover "incomplete" tracks. Recalling the equation (2.8):

$$p_i = \vec{c_i} \cdot \vec{x} + q_i$$

where $\vec{c_i}$ and q_i represents the fit constants for the sector in which the track is reconstructed. The FC are evaluated using a sample complete tracks, as explained in the previous section, and $\vec{c_i}$ dimension is 14 ($7\ layers \times 2\ coordinates$). An incomplete track will need different sets of Fit Constants, depending on which layers are missing.

In the FTK, with a number of sector about 200,000 and with 7 layers, trying to compute constants for each logical-layer combination would lead to about 1 milion of FC sets, a number too high to handle in the hardware and software. We therefore followed a different approach: when an incomplete track is found, the track is "completed" by estimating the unknown coordinates looking for the values that minimize the χ^2 evaluated from the other measured points. This is possible because the FC set knows the correlation between the coordinates, (2.7), used to evaluate the fit quality parameter χ^2, in (2.9). The minimization of the χ^2 is equivalent to guess for the missing points the most probable values, when keeping the others fixed.

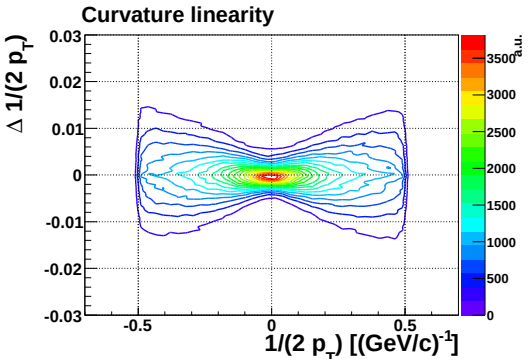

(a) $1/p_T$

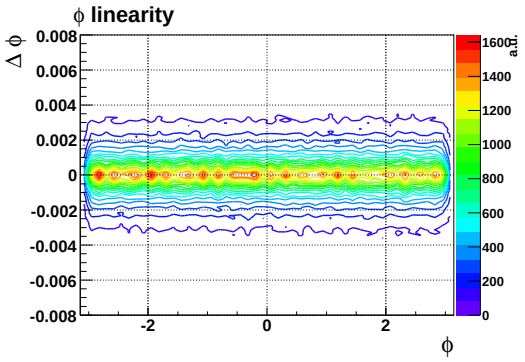

(b) ϕ

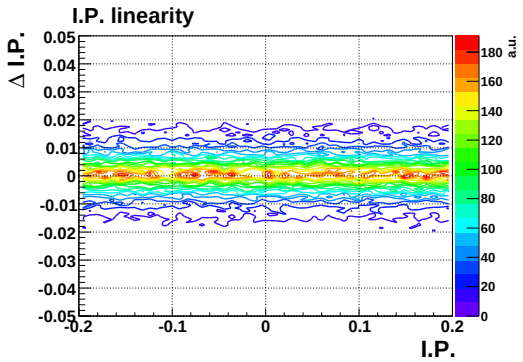

(c) Impact Parameter

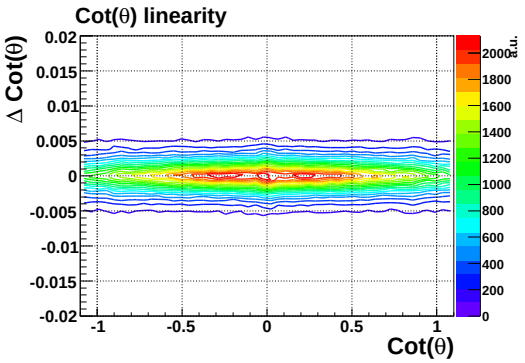

(d) $\cot(\theta)$

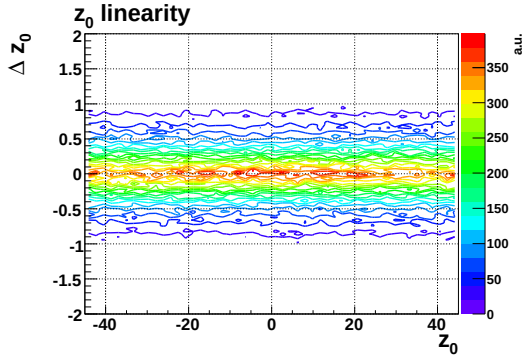

(e) z_0

Figure 6.7: The plots show the difference between the track parameters reconstructed by FTK and the truth parameter as function of the truth parameter itself. As expected if the linear approximation is good the difference are centered in 0 for all truth values.

Using the symbols in Sec. 2.6.3 and making the indexes explicit :

$$\chi^2 = \sum_i \left(\sum_j \hat{S}^{-1}_{ij} x_j - K_i \right)^2 \qquad \begin{matrix} j = 1, \ldots, N \\ i = 1, \ldots, N - N_{par} \end{matrix} \tag{6.1}$$

where N is total number of measured points, the dimension of $\vec{x}$, and N_{par} is the number of track parameters, in this case $N_{par} = 5$. If we introduce the index m running over the missing measurements x_m, the minimum of (6.1) can be found by imposing:

$$\frac{\partial \chi^2}{\partial x_m} = 2 \sum_i \hat{S}^{-1}_{im} \sum_j \left(\hat{S}^{-1}_{ij} x_j - K_i \right) \tag{6.2}$$

imposing (6.2) equal to zero is equivalent to the linear problem:

$$\hat{A} \cdot \vec{y} = \vec{q} \quad \text{where} \quad A_{ij} = \sum_k \hat{S}^{-1}_{ki} \hat{S}^{-1}_{kj}; \quad q_i = - \sum_k \hat{S}^{-1}_{ik} \left(\sum_{j \neq k} \hat{S}^{-1}_{ij} x_j - K_j \right); \tag{6.3}$$

the $\vec{y}$ is a vector representing the missing coordinates x_m, with dimension M; the A is a square matrix, with dimension $M \times M$, and the q_i are constant terms. The missing coordinates are then found by solving (6.3).

After the coordinate vector $\vec{x}$ is completed, the track parameters can be evaluated using the constants evaluated using the complete formula.

Generation of pattern banks

In the second step, valid patterns are determined inside each sector, to be stored in the Associative Memory. Each module is subdivided into a number of bins of equal size (super-bin), each of them a rectangle in the ϕ–z space. A pattern is a combination of 7 such bins, one for each of the 7 modules of the sector being considered. They are generated by the same algorithm used to find valid sectors: the training set of tracks is scanned and the valid patterns are identified as those that have a sizeable probability of being 'hit' by a valid track. The size of the bins has been varied to find a compromise between the size of the pattern bank (see Fig. 6.8) and the hit occupancy within each pattern, which determines the number of track candidates that must be fit. Fig. 6.8 shows the efficiency of the pattern bank as a function of the number of training tracks used to produce the bank. The different curves in the figure correspond to different road sizes. For this work, we have chosen a size in the r–ϕ plane of 5mm for Pixels and 10mm for SCT detectors; both extend in z for the length of a full module. This choice

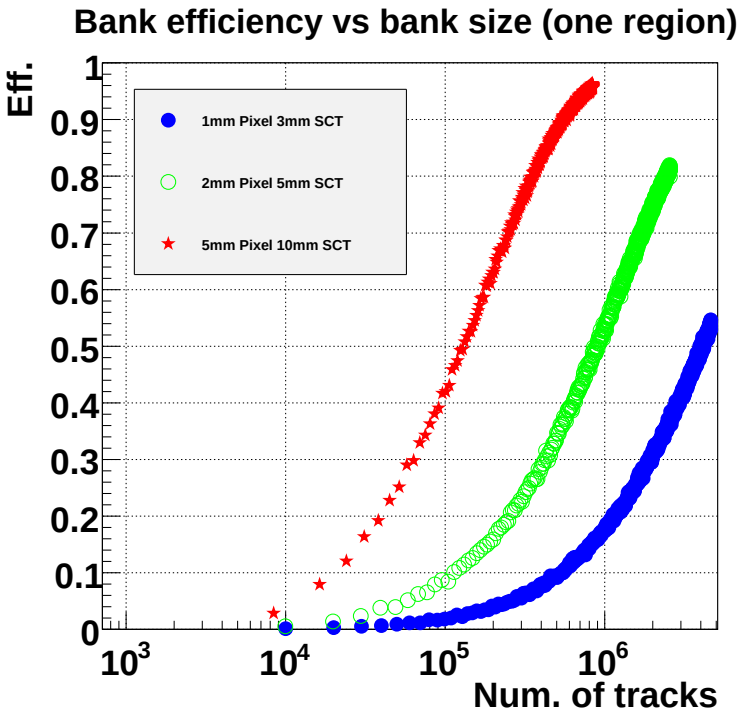

Figure 6.8: Growth of geometric coverage with increasing size of the pattern bank for each region.

Bank	Patterns	Muon eff.	Pions eff.
0	1053348	95.8 ± 0.4	95.9 ± 0.2
1	983741	95.7 ± 0.3	95.8 ± 0.2
2	1017193	96.0 ± 0.3	95.5 ± 0.2
3	1026228	96.1 ± 0.4	95.3 ± 0.2
4	1019529	95.8 ± 0.4	95.2 ± 0.2
5	1029316	96.1 ± 0.3	95.7 ± 0.2
6	1044599	96.4 ± 0.3	95.6 ± 0.2
8	1008758	96.7 ± 0.3	95.2 ± 0.2

Table 6.1: Size and coverage of FTK pattern banks.

yields a bank size of $\sim 10^6$ patterns for each of the 8 regions (see Tab. 6.1). In this case only the barrel detector (central region) is included in the calculation. This is compatible with implementation in 2 AM boards of the type currently in use in the CDF SVT.

6.6 FTK tracking performance

After the generation of the pattern banks and the fit constants it is now possible to evaluate the performance of FTK and compare it with the full off-line reconstruction program (iPatRec v10.0.6). Results are shown in Fig. 6.9, and demonstrate that the FTK is able to provide at the trigger level a resolution comparable with the full–fledged off-line tracking program. The Fig. 6.10 shows the impact parameter resolution as function of the transverse track momentum. The FTK measured resolution has a shape similar to the off-line, with an additional $30\,\mu$m added in quadrature. The reason of this distance is not completely understood, but the precision is enough for the trigger purposes.

The reconstruction efficiency on the single muon sample is also good (Fig. 6.11), with performance very close to the off-line. The small differences can be ascribed to the fact that the off-line reconstruction is based on the complete tracker, while FTK only uses the silicon-based part. The FTK algorithm is actually expected to yield a performance very close to the theoretical maximum when non–linearities are small.

In this document we analyze in detail a specific application: reconstruction of rare B_s^0 decays in the mode $B_s^0 \to \mu^+\mu^-$.

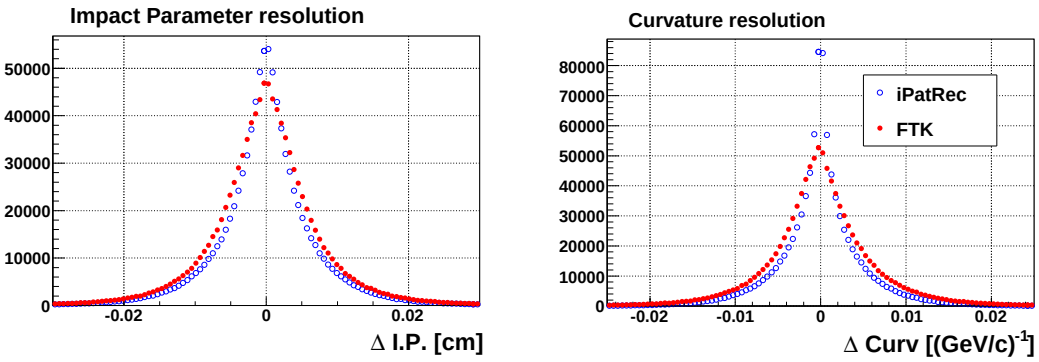

(a) Impact Parameter

(b) Curvature

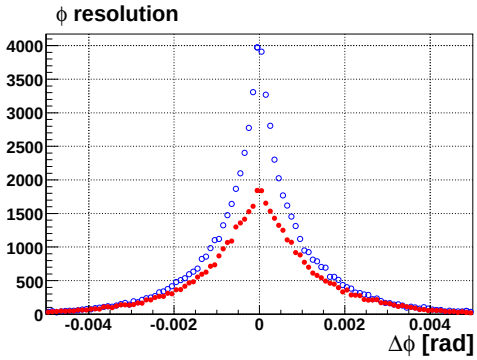

(c) ϕ

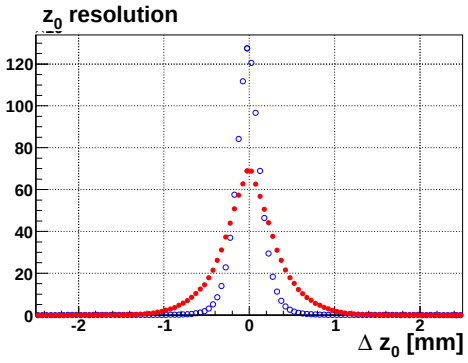

(d) z_0

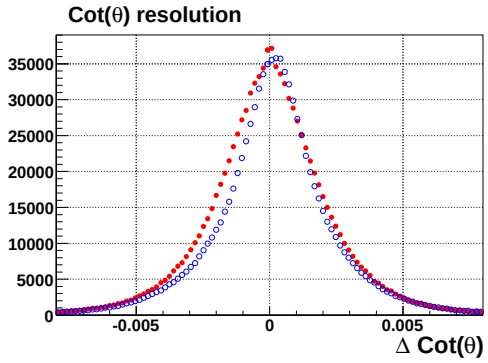

(e) $\cot(\theta)$

Figure 6.9: Comparison of resolution obtained by the off-line reconstruction code iPatRec (blue) and FTKSim (red) for the track parameters.

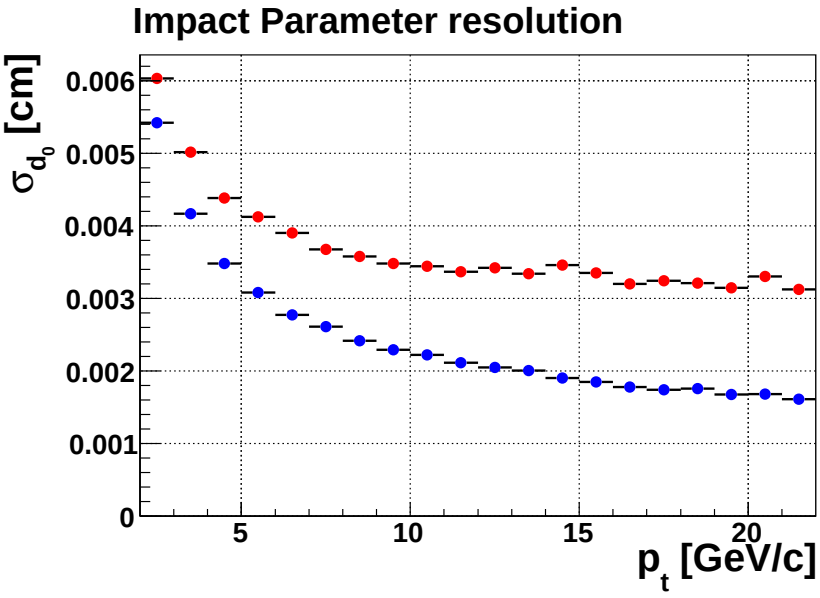

Figure 6.10: Resolution on the impact parameter as function of the track inverse momentum.

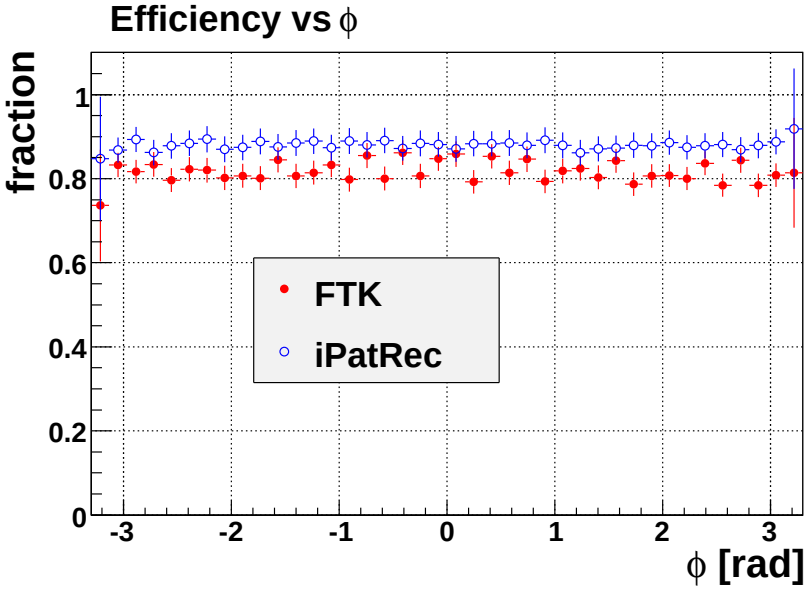

Figure 6.11: Efficiency vs azimuthal angle ϕ.

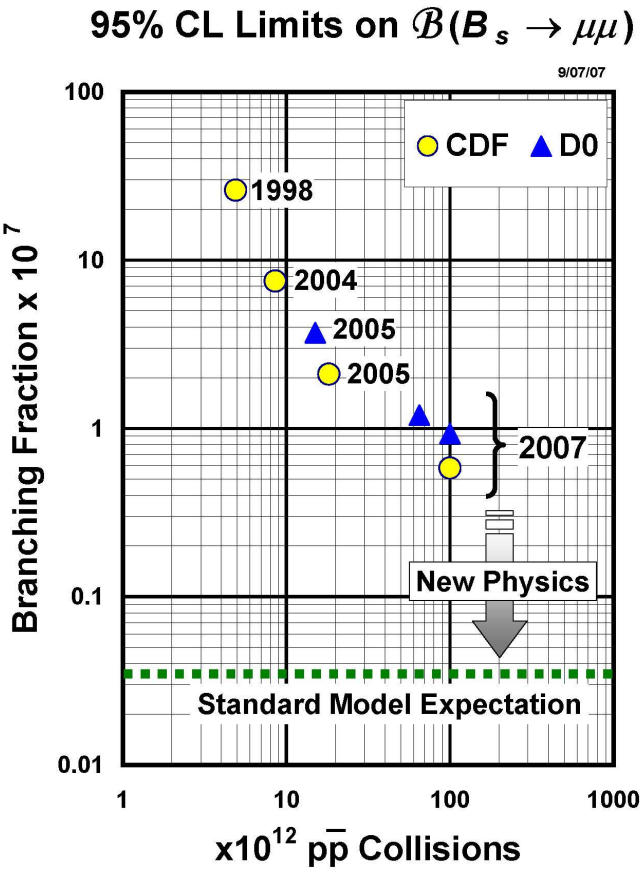

Figure 6.12: The plot shows the progression of the limit on the search on both B_s^0 and B^0 decay modes.

Source	Barrel	EndCap	Barrel+EndCap
π/K	7.0	9.8	16.8
b	1.9	2.1	4
c	1.1	1.3	2.4
W	0.004	0.005	0.009
Total	10.0	13.2	23.2

Table 6.2: Level–1 rates (kHz) for the MU6 trigger (one muon with $p_T > 6\,\mathrm{GeV/c}$ and $|\eta| < 2.5$), estimated for instantaneous luminosity $1 \times 10^{33}\,\mathrm{cm^{-2}s^{-1}}$ [107].

6.7 Application to $B_s^0 \to \mu^+\mu^-$

The small yields makes this mode only accessible in hadron collisions. The current best limits are from the Tevatron (CDF 1.9 $\mathrm{fb^{-1}}$: $< 5.8 \times 10^{-8}$, [102]). The power of this channel in searching for super-symmetry is comparable with direct searches: this is a possible candidate for the first detection of physics beyond the SM. The Tevatron searches proved that this mode can be separated from background and measured in spite of the complexity of the hadronic collisions, provided a good tracking and a strong trigger are available. In this section will not treated the $B^0 \to \mu^+\mu^-$ case because with the expected mass resolution of ATLAS, $60\,\mathrm{MeV/c^2}$[103, 104], will not be possible to separate the two signals in the search.

The presence of muons allows selection at Level–1 of the trigger. The current ATLAS strategy [105] is mainly based on requiring both muons to pass the threshold $p_t > 6\,\mathrm{GeV/c}$ and be within $|\eta| < 2.5$ The possibility of triggering on a single muon has only been considered for low–luminosity periods [106] due to its high rate [107]. As can be seen in table 6.2, the main background comes from in–flight decay of light mesons (π e K); this is strongly suppressed at Level–2 by matching with Inner Detector tracks and improved p_T measurement [105]. The residual background is mainly from semi-leptonic decay of bottom and charmed hadrons. However, this high rate is not a problem if the next level of selection is fast: the presence of FTK allows performing offline–type selections in a small fraction of the time needed by a CPU farm, thus allowing to handle much larger Level–1 rates, provided the Level-2 output rate from the selection is low enough.

We studied the performance of the following Level–2 selection based on FTK, assuming a Level–1 trigger asking for just one muon with $p_T > 6\,\mathrm{GeV/c}$

1. Find a second muon with a $p_T > p_{T_{min}}$
2. Both muons having impact parameter[1] from $100\,\mu m$ to $2\,mm$

[1]This upper limit derives from the training sample distribution for the I.P., see Fig. 6.6

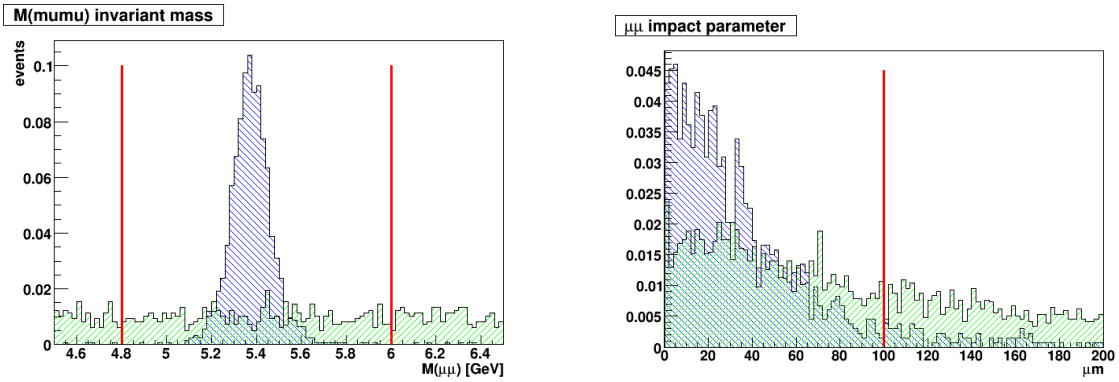

Figure 6.13: The plots show the distribution of mass and impact parameters, evaluated using the FTK variables, for the signal and the background. The applied cuts are shown by the red vertical bars.

3. The reconstructed B_s^0 candidate is required to point to the beam spot in the transverse plane, by applying a cut to its impact parameter: $d_{B_s^0} < 100\,\mu m$
4. $4.8\,\mathrm{GeV/c^2} < M(\mu\mu) < 6\,\mathrm{GeV/c^2}$

These cuts had been performed on signal and background samples generated using Pythia. The background samples was formed by $b\bar{b}$ QCD production that is assumed to be the main background, at least at trigger level. The pile-up and minimum bias events were not considered, processed by the fully detailed ATLAS simulation, of the tracking (code version 10.0.6), followed by our FTK simulator; the noise in the detector was added in the simulation using the standard values. In this version of the code only an older, 6–layer implementation of FTKSim was available, which has a lower performance of the current version, so the results are conservative in this contest. Since the ATLAS muon reconstruction capability has been shown to be very good, detailed muon reconstruction was not deemed necessary, and it is simply assumed that the muons are always correctly identified; this is not expected to influence the results significantly.

The Fig. 6.13 shows the distributions for the quantities chosen to apply cuts. In the plots are compared the distributions for the background (green) and the signal (blue) of reconstructed $B_s^0 \to \mu\mu$ mass and impact parameters. These are the most effective cuts.

The final result of this study is shown in fig 6.14 and detailed in table 6.3 as a function of the cut p_{Tmin}. The plots show that the efficiency for collecting $B_s^0 \to \mu^+\mu^-$ events increase by a factor of 3 when lowering the second muon threshold from 6 to 3 GeV/c.

Even considering the lower efficiency of the muon system below 6 GeV/c (80% at 3 GeV/c), these results imply an improvement of the size of the collected samples

	2 GeV/c	3 GeV/c	4 GeV/c	5 GeV/c	6 GeV/c
2 μ FTK in $\|\eta\| < 1$	0.385				
$\sigma(\mu) > 100\,\mu$m	0.295				
$\sigma(Bs) < 100\,\mu$m	0.360				
$4.8\,GeV/c^2 < M(\mu\mu) < 6\,GeV/c^2$	0.353				
p_t cut on second μ	0.344	0.228	0.170	0.116	0.081
Efficiency relative to L1	0.234	0.150	0.107	0.074	0.053
Total efficiency	0.041	0.029	0.020	0.013	0.009

Table 6.3: Signal efficiencies

	CDF 780pb^{-1}	ATLAS 30fb^{-1}	FTK 30fb^{-1} $p_{t1} > 6$GeV $p_{t2} > 6$GeV	FTK 30fb^{-1} $p_{t1} > 6$GeV $p_{t2} > 3$GeV
	off-line		Level2	
Signal	0	27	178	546
Background	1	93		
L2 Rate			Few Hz	10 Hz
Limit	$< 10^{-7}$ @95% CL	$< 6.6 \times 10^{-9}$ @95% CL		

Table 6.4: Expected event yields from the FTK trigger, under Standard Model assumptions for the branching fraction of $B_s^0 \to \mu^+\mu^-$.

with the respect the original di-muon trigger scenario, this raise sensitivity to low branching fractions even with a limited integrated luminosities.

Given the similarity between FTK and off-line tracking performances, it can be expected that FTK selection efficiencies will be similar also for regions where they have not been explicitly simulated in this study, as in the forward region, but could be included in FTK as well by simply adding further regions. With this assumptions we can evaluate the total number of $B_s^0 \to \mu^+\mu^-$ events collected and make a comparison with previous studies (Tab. 6.4).

A crucial point is obviously the amount of background passing this selection. This was evaluated by simulating generic $b\bar{b}$ events with exactly the same procedures adopted for the $B_s^0 \to \mu^+\mu^-$ signal. The sample contained about 20k events, which is sufficient for a first–order evaluation.

The efficiencies observed on background are reported in Tab. 6.5.

These numbers allow estimating the output Level–2 rate, knowing that the Level–1 rate is $\sim 3.5\,kHz$ at $L = 10^{33} cm^{-2} s^{-1}$. With the $p_T > 3\,GeV/c$ cut, the efficiency is of order 10^{-3}, yielding rates of the order of 10 Hz. This has a large statistical uncertainty due to the small number of events passing the cuts (6), but

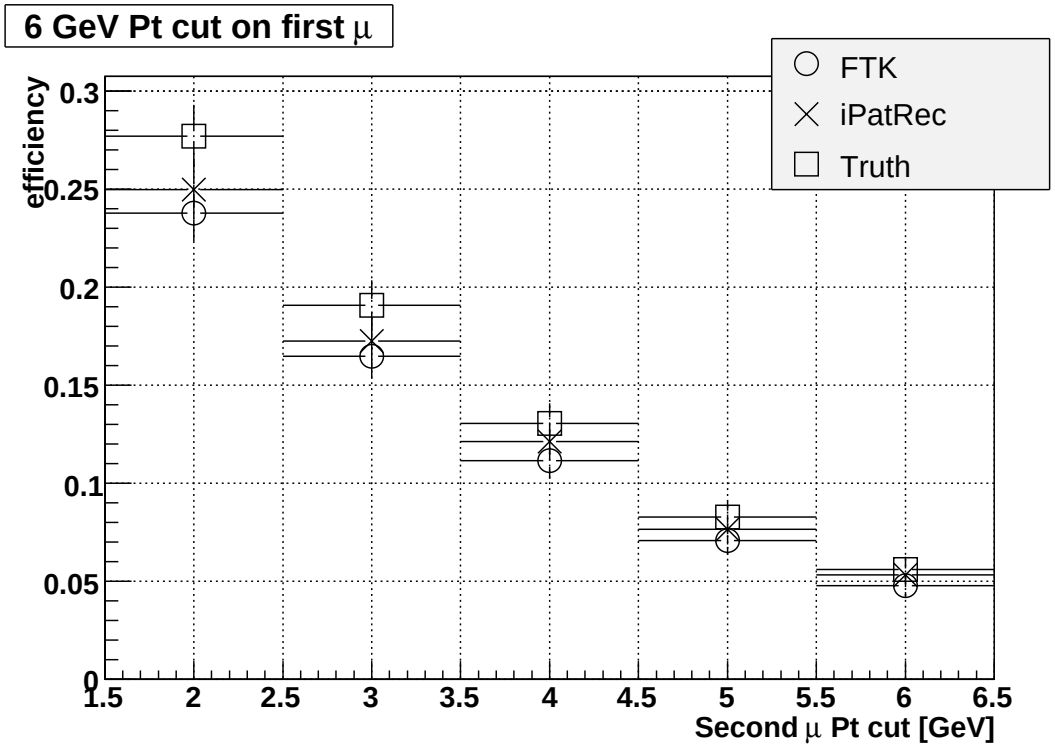

Figure 6.14: Efficiency of the proposed Level–2 selection as a function of the second muon threshold p_{Tmin}. The efficiencies are relative to the Level–1 selection.

this doesn't affect the conclusion that the rate is very reasonable. It can be further reduced if necessary by bringing to Level–2 other cuts that have been proposed for off-line analysis, like isolation or 3D vertexing. They can all be implemented at earlier selection stages thanks to the prompt availability of the FTK track list.

$p_T(\mu_2)$ cut	2 $^{\mathrm{GeV}}/_{\mathrm{c}}$	3 $^{\mathrm{GeV}}/_{\mathrm{c}}$	4 $^{\mathrm{GeV}}/_{\mathrm{c}}$	5 $^{\mathrm{GeV}}/_{\mathrm{c}}$	6 $^{\mathrm{GeV}}/_{\mathrm{c}}$
$\lvert\eta(\mu_2)\rvert < 1$	0.508				
$\sigma(\mu) > 100\,\mu$m	0.375				
$\sigma(Bs) < 100\,\mu$m	0.266				
$M \in [4.8, 6.0]^{GeV}/_{c^2}$	0.014				
$p_T(\mu_2)$	0.491	0.312	0.174	0.100	0.045
LVL1 Eff.	5.25×10^{-3}	2.82×10^{-3}	8.08×10^{-4}	0	0
Total Eff.	6.80×10^{-4}	3.66×10^{-4}	1.04×10^{-4}	0	0

Table 6.5: Efficiency of selection cuts on background events.

6.8 Summary

In this chapter I presented a challenging R&D project with the goal to transfer the technology used in the SVT processor of CDF II to the much more difficult conditions of the ATLAS experiment, to allow the continuation of a strong program of investigation of rare decay modes at hadron colliders.

Using the simulation software I contributed to create, I showed that the FTK processor can reconstruct all five track parameters with resolutions and efficiency close to an off-line algorithm. This is a very important accomplishment for this project and gives good hopes for its positive impact on the experiment. The use on fully-simulated events containing $B_s^0 \to \mu^+\mu^-$ signals and $b\bar{b}$ background has shown that the FTK will be able to improve the acceptance on signal while maintaining an acceptable rate for the ATLAS trigger system.

These early results give good hopes for a brilliant future of the study of rare channels at the LHC.

Bibliography

[1] M. Imbeault, S. Baek, and D. London, "The $B \to \pi K$ Puzzle and Supersymmetry," 2008.

[2] R. Mohanta and A. Giri, "Effects of R-parity violation on CP asymmetry," *Phys. Rev.*, vol. D63, p. 074001, 2001.

[3] R. Mohanta, A. K. Giri, and M. P. Khanna, "Charmless two body hadronic decays of Λ_b^0 baryon," *Phys. Rev.*, vol. D63, p. 074001, 2001.

[4] F. Mandl and G. Shaw, *Quantum Field Theory.* John Wiley & Son.

[5] M. E. Peskin and D. V. Schroeder, "An Introduction to quantum field theory," reading, USA: Addison-Wesley (1995) 842 p.

[6] D. h. Perkins, "INTRODUCTION TO HIGH-ENERGY PHYSICS," reading, Usa: Addison-wesley (1982) 437p.

[7] M. Kobayashi, H. Kondo, and T. Maskawa, "Symmetry breaking of chiral u(3) x u(3) and x → eta pi pi decay amplitude," *Prog. Theor. Phys.*, vol. 49, pp. 634–639, 1973.

[8] N. Cabibbo, "Unitary Symmetry and Leptonic Decays," *Phys. Rev. Lett.*, vol. 10, pp. 531–532, 1963.

[9] L. Wolfenstein, "SYMMETRICAL PARAMETRIZATION OF THE K-M MATRIX," *Phys. Rev.*, vol. D31, p. 2381, 1985.

[10] W. M. Yao *et al.*, "Review of particle physics," *J. Phys.*, vol. G33, pp. 1–1232, 2006. [Online]. Available: http://pdg.lbl.gov

[11] M. Artuso *et al.*, "B, D and K decays," 2008.

[12] A. Abulencia *et al.*, "Measurement of the $B_s^0 - \bar{B}_s^0$ oscillation frequency," *Phys. Rev. Lett.*, vol. 97, p. 062003, 2006.

[13] S. P. Martin, "A supersymmetry primer," 1997.

[14] E. Barberio *et al.*, "Averages of b-hadron properties at the end of 2006," 2007.

[15] R. Fleischer, "New strategies to extract beta and gamma from $B_d \to \pi^+\pi+-$ and $B_s \to K^+K^-$," *Phys. Lett.*, vol. B459, pp. 306–320, 1999.

[16] A. Abulencia *et al.*, "Observation of B^0 $(s) \to K^+K^-$ and Measurements of Branching Fractions of Charmless Two-body Decays of B^0 and B_s^0 Mesons in $\bar{p}p$ Collisions at $\sqrt{s}$ = 1.96-TeV," *Phys. Rev. Lett.*, vol. 97, p. 211802, 2006.

[17] ——, "Observation of $B_s^0 \to KK$ and measurements of branching fractions of charmless two-body decays of b^0 and b_s^0 mesons in p$\bar{p}$ collisions at $\sqrt{s}$=1.96 tev," *Phys. Rev. Lett.*, 2006.

[18] M. Morello, "Measurement of the CP asymmetry and branching fractions of the two-body charmless decays of B^0 and B_s^0 mesons." Ph.D. dissertation, Scuola Normale Superiore, 2007.

[19] H. J. Lipkin, "Is observed direct CP violation in $B_d \to K^+\pi^-$ due to new physics? Check standard model prediction of equal violation in $B_s \to K^-\pi^+$," *Phys. Lett.*, vol. B621, pp. 126–132, 2005.

[20] D. Acosta *et al.*, "Search for $\Lambda_b \to p\pi$ and $\Lambda_b \to pK$ decays in $p\bar{p}$ collisions at $\sqrt{s}$ = 1.96 tev," *Phys. Rev.*, vol. D72, p. 051104, 2005.

[21] A. J. Buras, "Relations between $\Delta(M(s,d))$ and $B_{s,d} \to \mu\bar{\mu}$ in models with minimal flavour violation," *Phys. Lett.*, vol. B566, pp. 115–119, 2003.

[22] A. Sherstnev, "Prospects for b-quark production cross section measurements in p p collisions at the LHC," *Nucl. Phys. Proc. Suppl.*, vol. 167, pp. 21–24, 2007.

[23] D. Acosta *et al.*, "Measurement of the J/ψ meson and $b-$hadron production cross sections in $p\bar{p}$ collisions at $\sqrt{s}$ = 1960 gev," *Phys. Rev.*, vol. D71, p. 032001, 2005.

[24] G. Aubrecht *et al.*, *A Teachers Guide To The Nuclear Science Wall Chart.* Contemporary Physics Education Project, 2003.

[25] M. Popovic, L. Allen, and C. W. Schmidt, "Fermilab linac injector, revisited," prepared for 16th IEEE Particle Accelerator Conference (PAC 95) and International Conference on High-energy Accelerators (IUPAP), Dallas, Texas, 1-5 May 1995.

[26] F. B. Division, *RUN II Handbook*, 1998. [Online]. Available: http://www-bd.fnal.gov/lug/runII_handbook/RunII_index.html

[27] CDF II Collaboration, "The CDF IIb detector: Technical design report."

[28] C. S. Hill, "Initial experience with the CDF layer 00 silicon detector," *Nucl. Instrum. Meth.*, vol. A511, pp. 118–120, 2003.

[29] A. Sill, "CDF run II silicon tracking projects," *Nucl. Instrum. Meth.*, vol. A447, pp. 1–8, 2000.

[30] A. A. Affolder *et al.*, "Status report of the intermediate silicon layers detector at CDFII," *Nucl. Instrum. Meth.*, vol. A485, pp. 6–9, 2002.

[31] ——, "CDF central outer tracker," *Nucl. Instrum. Meth.*, vol. A526, pp. 249–299, 2004.

[32] D. Acosta *et al.*, "A time-of-flight detector in CDF-II," *Nucl. Instrum. Meth.*, vol. A518, pp. 605–608, 2004.

[33] L. Balka *et al.*, "The CDF central electromagnetic calorimeter," *Nucl. Instrum. Meth.*, vol. A267, p. 272, 1988.

[34] S. R. Hahn *et al.*, "Calibration systems for the CDF central electromagnetic calorimeter," *Nucl. Instr. Meth.*, vol. A267, p. 351, 1988.

[35] S. Bertolucci *et al.*, "The CDF central and endwall hadron calorimeter," *Nucl. Instrum. Meth.*, vol. A267, p. 301, 1988.

[36] M. G. Albrow *et al.*, "The CDF plug upgrade electromagnetic calorimeter: Test beam results," *Nucl. Instrum. Meth.*, vol. A480, pp. 524–546, 2002.

[37] ——, "A preshower detector for the CDF plug upgrade: Test beam results," *Nucl. Instrum. Meth.*, vol. A431, pp. 104–111, 1999.

[38] G. Apollinari, K. Goulianos, P. Melese, and M. Lindgren, "Shower maximum detector for the CDF plug upgrade calorimeter," *Nucl. Instrum. Meth.*, vol. A412, pp. 515–526, 1998.

[39] C. M. Ginsburg, "CDF run 2 muon system," *Eur. Phys. J.*, vol. C33, pp. s1002–s1004, 2004.

[40] G. Ascoli *et al.*, "CDF central muon detector," *Nucl. Instrum. Meth.*, vol. A268, p. 33, 1988.

[41] D. Acosta *et al.*, "The CDF Cherenkov luminosity monitor," *Nucl. Instrum. Meth.*, vol. A461, pp. 540–544, 2001.

[42] P. Gatti, "Performance of the new tracking system at CDF II," Ph.D. dissertation, University of Padova, 2001.

[43] S. Menzemer, "TrackingCal - A tracking and alignement software package for the CDF II silicon detector," Ph.D. dissertation, University of Karlruhe, 2002.

[44] G. Gomez-Ceballos *et al.*, "Event builder and level 3 at the cdf experiment," *Nucl. Instrum. Meth.*, vol. A518, pp. 522–524, 2004.

[45] E. J. Thomson *et al.*, "Online track processor for the cdf upgrade," *IEEE Trans. Nucl. Sci.*, vol. 49, pp. 1063–1070, 2002.

[46] A. Rahaman and R. Oldeman, "Level-1 trigger rates of the two-track trigger at high-luminosities," *CDF-Note*, 2005.

[47] R. Oldemam and J. Lewis, "Using the CLC to improve the purity of the Level-1 two-track trigger," *CDF-Note*, December 2004.

[48] S. Belforte *et al.*, "Silicon vertex trigger technical design report," Tech. Rep., 1995, CDF/DOC/TRIGGER/PUBLIC/3108.

[49] H. Wind, "PRINCIPAL COMPONENT ANALYSIS AND ITS APPLICATIONS TO TRACK FINDING," in Bock, R.k. (Ed.) Et Al.: Formulae and Methods In Experimental Data Evaluation, Vol. 3, K1-k16.

[50] R. Brun *et al.*, *GEANT: Simulation Program For Particle Physics Experiments. User Guide and Reference Manual*, 1978.

[51] P. A. Movilla Fernandez, "Performance of the CDF calorimeter simulation in Tevatron Run II," *AIP Conf. Proc.*, vol. 867, pp. 487–494, 2006.

[52] R. Veenhof, "Garfield, a drift chamber simulation program," prepared for International Conference on Programming and Mathematical Methods for Solving Physical Problems, Dubna, Russia, 14-19 Jun 1993.

[53] ——, "GARFIELD, recent developments," *Nucl. Instrum. Meth.*, vol. A419, pp. 726–730, 1998.

[54] D. Tonelli, "First observation of the $B_s^0 \to KK$ decay mode, and measurement of the B^0 and B_s^0 mesons decay-rates into two-body charmless final states at CDF," Master's thesis, University of Pisa, 2006, in Italian, unpublished.

[55] M. Morello, "Decadimenti di mesoni B in due adroni charmless a CDF II," Master's thesis, University of Pisa, 2003.

[56] M. J. Morello, G. Punzi *et al.*, "Disentangling the $B^0 \to hh$ fractions," *CDF/ANAL/BOTTOM/CDFR/6357*, 2003.

[57] D. Ayres *et al.*, "Design report of the fermilab collider detector facility (CDF)," Fermilab, Tech. Rep., August 1981.

[58] F. Abe *et al.*, "The CDF detector: An overview," *Nucl. Instrum. Meth.*, vol. A271, p. 387, 1988.

[59] H. A. Bethe, "Theory of passage of fast corpuscular rays through matter," *Annalen Phys.*, vol. 5, 325, 1930, in German.

[60] F. Bloch, "Stopping power of atoms with several electrons," *Z. Phys.*, vol. 81, 363, 1933.

[61] S. S. Eiko Yu, "COT dE/dx measurement and corrections," *CDF-Note*, 2004.

[62] P. Squillacioti, "Measurement of the branching fraction ratio $\mathcal{B}(B^+ \to \bar{D}^0 K^+)/\mathcal{B}(B^+ \to \bar{D}^0\pi^+)$ with the CDF II detector." *Univ. of Siena*, 2006.

[63] S. Donati, G. Punzi, M. Morello, D. Tonelli *et al.*, "Branching ratios and CP asymmetries in Bhh decays from 180 pb^{-1}," *CDF/ANAL/BOTTOM/CDFR/7066*, 2005.

[64] S. Budroni, M. J. Morello, G. Punzi, and D. Tonelli, "Measurement of direct CP asymmetry in $B^0 \to K\pi$ decays in 355 pb^{-1} of two-track data," *CDF-Note 8057*, 2006.

[65] G. Punzi, "Sensitivity of searches for new signals and its optimization," 2003.

[66] D. Litvintsev, R. J. Tesarek, and S.-S. E. Yu, "Measurement of the Λ_b p_T spectrum in the TTT data using fully reconstructed decay to $\Lambda_b \to \Lambda_c^+\pi$," *CDF/PHYS/BOTTOM/CDFR/8156*, 2005.

[67] H. Albrecht *et al.*, "Search for hadronic b $\to$ u decays," *Phys. Lett.*, vol. B241, pp. 278–282, 1990.

[68] M. J. Morello, G. Punzi, and G. Volpi, "A Fast Monte Carlo for generation of accurate kinematic templates of non-leptonic B and D decay," *CDF-Note 8800*, 2007.

[69] K. Anikeev, P. Christoph, and P. Murat, "Description of Bgenerato II," *CDF-Note 5092*, August 1999.

[70] S. Donati *et al.*, "Measurement of branching fractions and direct CP asymmetries of $B^0_{(s)} \to h^+h'^-$ decays in 1 fb$^-$1," *CDF-Note 8464*, 2006.

[71] E. Barberio and Z. Was, "Photos: A universal monte carlo for QED radiative corrections. version 2.0," *Comput. Phys. Commun.*, vol. 79, pp. 291–308, 1994.

[72] E. Baracchini and G. Isidori, "Electromagnetic corrections to non-leptonic two-body B and D decays," *Phys. Lett.*, vol. B633, pp. 309–313, 2006.

[73] M. Pivk and F. R. Le Diberder, "sPlot: A statistical tool to unfold data distributions," *Nucl. Instrum. Meth.*, vol. A555, pp. 356–369, 2005.

[74] T. J. Rivlin, *Chebyshev Polynomials: From Approximation Theory to Algebra and Number Theory.* Wiley, 1990.

[75] D. Acosta *et al.*, "Measurement of partial widths and search for direct CP violation in D^0 meson decays to K^-K^+ and $\pi^-\pi^+$," *Phys. Rev. Lett.*, vol. 94, 2005.

[76] V. Cirigliano, J. F. Donogue, and E. Golowich, "$K \to \pi\pi$ phenomenology in the presence of electromagnetism," *Eur. Phys. J.*, vol. C18,83, 2000.

[77] E. Baracchini, "Correzioni radiative ai decadimenti in due corpi del mesone B," Tesi di Laurea (Graduation Thesis), University of Rome "La Sapienza", 2005, in Italian, unpublished.

[78] ——, "QED corrections and the $B \to K\pi$ puzzle," prepared for IFAE 2006 (in Italian), Pavia, Italy, 19-21 Apr 2006.

[79] D. Acosta *et al.*, "Measurement of b hadron masses in exclusive J/ψ decays with the CDF detector," *Phys. Rev. Lett.*, vol. 96, p. 202001, 2006.

[80] M. Campanelli and E. Gerchtein, "Calibration of the momentum scale for kalman refitter using J/ψ events," *CDF/ANAL/BOTTOM/CDFR/6905*, 2004.

[81] R. Brun and F. Rademakers, "ROOT: An object oriented data analysis framework," *Nucl. Instrum. Meth.*, vol. A389, pp. 81–86, 1997.

[82] D. Acosta *et al.*, "Measurement of prompt charm meson production cross sections in p$\bar{\text{p}}$ collisions at $\sqrt{s} = 1.96$ TeV," *Phys. Rev.*, 2003.

[83] A. Abulencia *et al.*, "Measurement of the ratio of branching fractions $\mathcal{B}(D^0 \to K^-\pi^+)/\mathcal{B}(D^0 \to K^+\pi^-)$," *Phys. Rev.*, vol. D74, p. 031109(R), 2006.

[84] S. Giagu *et al.*, "BR ratios and direct CP violation in Cabibbo supressed decays of D^0," *CDF/PHYS/BOTTOM/CDFR/6391*, 2003.

[85] M. J. Morello, G. Punzi, and G. Volpi, "Measurement of the efficiency ratio $\epsilon(K - \pi+)/\epsilon(K + pi-)$ from $D^0 \to K\pi$ decays," *CDF/ANAL/BOTTOM/CDFR/8463*, 2006.

[86] M. A. Ciocci, G. Punzi, and P. Squillacioti, "Update of combined PID in 6.1.4," *CDF/PHYS/BOTTOM/CDFR/8478*, 2006.

[87] A. Abulencia *et al.*, "Measurement of $\sigma(\Lambda_b)/\sigma(B^0) \times BR(\Lambda_b \to \Lambda_c\pi^-)/BR(B^0 \to D^+\pi^-)$ in $p\bar{p}$ collisions at $\sqrt{s} = 1.96$ TeV," *Phys. Rev. Let.*, no. 98, 2007.

[88] L. S. G. Collaboration, "The Large Hadron Collider: Conceptual design," CERN, Tech. Rep., 1995.

[89] A. Annovi *et al.*, "The Fast Tracker processor for hadron collider triggers," in *IEEE Trans Nucl. Sci.*, vol. 58, no. 3, June 2001. [Online]. Available: http://www.pi.infn.it/~orso/ftk

[90] A. Bardi *et al.*, "SVT: an online silicon vertex tracker for the CDF upgrade," *Nucl. Instr. Meth.*, vol. A409, pp. 658–661, May 1998.

[91] A. A. et al., "Hadron collider triggers with high-quality tracking at very high event rates," in *IEEE Trans. Vol .51.*, no. 3, 2004.

[92] U. Aglietti *et al.*, "Tevatron-for-LHC Report: Higgs," 2006.

[93] G. Bagliesi, "Tau tagging at Atlas and CMS," 2007.

[94] "ATLAS DAQ, EF, LVL2 and DCS: Technical progress report," CERN-LHCC-98-16.

[95] A. Annovi *et al.*, "Hadron collider triggers with high-quality tracking at very high event rates," *IEEE Trans. Nucl. Sci.*, vol. 51, pp. 391–400, 2004.

[96] J. Adelman *et al.*, "On-line tracking processors at hadron colliders: The SVT experience at CDF II and beyond," *Nucl.Instrum.Phys.*, vol. 581, pp. 473–475, 2007.

[97] The CDF Coll., "SVTSIM web page." [Online]. Available: http://www-cdf.fnal.gov/upgrades/daq_trig/trigger/svt/svtsim.html

[98] The ATLAS Coll, "ATLAS computing technical design report," Tech. Rep., July 2004, ATLAS TDR-017, CERN-LHCC-2005-022.

[99] ——, "ATHENA web page." [Online]. Available: http://atlas.web.cern.ch/Atlas/GROUPS/SOFTWARE/OO/architecture/

[100] R. Brun *et al.*, "ROOT object oriented data analysis framework." [Online]. Available: http://root.cern.ch/

[101] R. Clift and A. Poppleton, "IPATREC: inner detector pattern-recognition and track-fitting," *ATLAS Pub. Doc.*, 1994.

[102] A. Aaltonen *et al.*, "Search for $B_s \to \mu^+\mu^-$ and $B_d \to \mu^+\mu^-$ decays with 2 fb^{-1} of $p\bar{p}$ collisions," 2007. [Online]. Available: http://www.citebase.org/abstract?id=oai:arXiv.org:0712.1708

[103] The ATLAS Coll, "ATLAS detector and physics performance: Technical design report," CERN, Tech. Rep. CERN-LHCC-99-014, ATLAS-TDR-14, 1999, volume 1.

[104] ——, "ATLAS detector and physics performance technical design report," CERN, Tech. Rep. CERN-LHCC-99-014, ATLAS-TDR-14, 1999, volume 2.

[105] ——, "ATLAS High-Level trigger, data acquisition and control technical design report," Tech. Rep., 2003, ATLAS-TDR-016.

[106] S. George, "The ATLAS B-physics trigger," Tech. Rep., 2004, ATL-DAQ-2004-004.

[107] The ATLAS Coll, "Level-1 trigger technical design report," Tech. Rep., 1998, COM-PHYS-2004-053.